Cadi Ayyad University
Faculty of Sciences Semlalia
High Energy Physics & Astrophysics Laboratory

University of Liège
Faculty of Sciences
Space sciences, Technologies & Astrophysics Research Institute

For the degree of Doctor of Science in Astrophysics & Space Sciences

Entitled:

Monitoring the activity and composition of comets with TRAPPIST telescopes

Author
Youssef MOULANE

Supervisors
Dr. Emmanuel JEHIN
Pr. Zouhair BENKHALDOUN

Presented on March 22, 2021 in front of the jury members:

- Pr. Denis Grodent — President, University of Liège (Belgium)
- Dr. Damien Hutsemékers — Secretary, University of Liège (Belgium)
- Dr. Cyrielle Opitom — Member, University of Edinburgh (United Kingdom)
- Dr. Philippe Rousselot — Member, University of Bourgogne Franche-Comté (France)
- Dr. Bin Yang — Member, European Southern Observatory (Chile)
- Pr. Ioan Schneider — Member, Le Havre University (France)
- Dr. Johan De Keyser — Member, Royal Belgian Institute for Space Aeronomy (Belgium)
- Dr. Emmanuel Jehin — Supervisor, University of Liège (Belgium)
- Pr. Zouhair Benkhaldoun — Supervisor, Cadi Ayyad University (Morocco)

2020/2021

Contents

List of Figures

List of Tables

Acknowledgements

Throughout the writing of this dissertation I have received a great deal of support and assistance. First, I would like to express my sincere gratitude to my advisors Prof. Emmanuel Jehin at university of Liège (Belgium) and Prof. Zouhair Benkhaldoun at Cadi Ayyad university (Morocco) for the continuous support during the whole period of my PhD thesis, for their patience, motivation, enthusiasm, and immense knowledge. Their guidance helped me in all the time of research and writing of papers and my thesis. I could not have imagined having a better advisors and mentors for my PhD study and research. Your insightful feedback pushed me to sharpen my thinking and brought my work to a higher level.

I also would like to thank Jean Manfroid, Cyreille Opitom and Damien Hutsemékers at STAR institute, whom helped me continually since the beginning of my PhD. I really appreciate your support and advice that helped me for the reduction and analysis of photometric and spectroscopic data. Thanks for your precious comments, remarks and perspectives on all my work.

My sincere thanks also goes to Prof. Ioan Schneider at the university of Le Havre (France) for accepting me in Erasmus program for the first year of my PhD working on the reactive collision of electrons with molecular cations in cometary coma. A great thanks to you and your group for helping me working on diverse exciting projects. I am extending my thanks to Bin Yang, who supervised me for my 2 years studentship at ESO in Chile. I really appreciate your support, help and guidance during that period of time. I would also like to thank again Cyrielle for helping me to settle down at ESO in Santiago. During these 2 years, I have learned many things and broaden my horizons to different topic in astronomy and astrophysics. Thanks to all the ESO staff for the nice discussion that we have together at science coffees and at regular talks.

I would like to thank the president and the members of my jury Denis Grodent, Damien Hutsemékers, Cyreille Opitom, Philippe Rousselot, Bin Yang, Ioan Schneider and Johan De Keyser for taking the time to read this dissertation and for their useful comments on the first version of my manuscript.

I thank all the observing TRAPPIST team, Emmanuel Jehin, Fran Pozuelos, Khalid Barkaoui, Marin Ferrais, Artem Burdanov and our IT support Sandrine Sohy. It was a pleasure to work with all of you, I have leaned a lot of things and improved my knowledge and skills in observing with TRAPPIST telescopes.

I would like to thank my parents (and my family) for supporting me spiritually throughout my life. Last but not the least, thanks to all my friends and colleagues at High Energy Physics and Astrophysics Laboratory at Cadi Ayyad university, STAR institute at university of Liège and at ESO in Chile for having good times and stimulating discussions as well as happy distractions to rest my mind outside of my research.

Finally, my thanks go to all the people who have supported me to complete the research work directly or indirectly.

Abstract

Comets are remnants of the early stages of the Solar System and the most primitive Solar System bodies. Understanding their nature and evolution history provides important clues about the formation of the Solar System and the planets. Comets contain complex organic molecules, and may have played a key role in delivering water, organics and noble gases from the interstellar medium to the early Earth, contributing to the origin of life. The strong scientific interest in the Solar System small bodies is well demonstrated by numerous space missions in the recent years, such as Stardust, Deep Impact, Dawn and New Horizon etc. Particularly, ESA's very successful Rosetta mission recently visited comet 67P/Churyumov–Gerasimenko and made several ground-breaking discoveries that have dramatically increased our knowledge about comets. However, most of the space missions can only perform short-term studies over a narrow time window of single objects. We are currently lacking long-term observations to study variations in the activity and composition in the coma of a comet and how it evolves along its orbit around the Sun.

We regularly use the two robotic TRAPPIST telescopes to observe relatively bright comets (V $\leq$ 12 mag) that are visible in both hemispheres. These telescopes are equipped with narrow-band cometary filters that allow us to collect images of a comet at wavelengths where the light is emitted by the main gaseous species accessible in the optical (OH, NH, CN, C_2, and C_3). In addition, we observe comets in three continuum windows (scattered sunlight) that allow us to characterize the dust component of the comet. Thanks to the large amount of telescope time available on both telescopes for this project, we collected a unique data set of thousands of photometric measurements of 35 comets including 18 Jupiter-family Comets (hereafter JFCs) and 16 Long Period Comets (hereafter LPCs) in addition to the first active interstellar comet 2I/Borisov which was discovered in 2019. Each comet is monitored along an important part of its inner solar system orbit, starting at 3 au from the Sun (where water start to sublimate) and all the way to its perihelion. Post perihelion, we followed the comet again all the way out to 3 au at least. Then, through cometary coma models, the abundances of the main chemical species (accessible in the optical part of the spectrum) and dust production proxy (known as A$f\rho$) and its color were determined. These measurements, thanks to the high quality and homogeneity of the observations and of the verified analysis procedure, allowed us to address important and long debated questions like the existence of comet compositional classes (comet taxonomy), the changes of molecular abundance ratios with the distance to the Sun and the link between chemical composition and dynamical origins, which is a fundamental step in understanding the formation of comets and the Solar System itself. Among 29 comets for which the gas emissions were detected (at least CN and C_2), we identified three depleted comets in carbon-chain elements. These comets are 21P/Giacobini–Zinner, 260P/McNaught and 398P/Boattini in addition to the first interstellar comet 2I/Borisov. 21P is known as a depleted comet for a long time , but we confirm its depletion in its 2018 passage. The other three comets were found to be depleted in C_2 and C_3 for the first time with TRAPPIST. We made an extensive monitoring of the activity of the first interstellar comet 2I/Borisov. We presented an initial characterization of its activity including magnitude, A$f\rho$ dust parameter and dust colours during our observation period. 2I/Borisov was found to be depleted in C_2 with respect to CN similar to the Solar System comets carbon-depleted group. No LPC was found to be depleted in carbon-chain elements, except for comet C/2019 Y4 which was at the limit of depleted comets before its fragmentation where we see a significant change in its coma composition. We also found four comets (21P, C/2015 V2, C/2017 T2 and C/2018 W2) depleted in NH with respect to OH and CN. In term of dust activity, most comets show a normal dust/gas activity with respect to the heliocentric distance, except for comet C/2017 O1 which shows a higher dust/gas ratio (especially for Afρ/OH) and comet C/2018 Y1 that shows a lower dust/gas ratio (in both Afρ/OH and Afρ/CN) with respect to most comets. We made a follow-up of five JFCs that showed outbursts. These comets include 29P/Schwassmann-Wachmann 1, 123P/West-Hartley, 155P/Shoemaker, 243P/NEAT, and 260P/McNaught. Comet 29P, as usual, shows multiple outbursts with various amplitudes while other comets show an unique outburst. We discussed the evolution of the outbursts for each comet, by measuring the magnitude, Afρ parameter and dust colours.

The dense monitoring of comets allows us to investigate new topics like the heterogeneity of the nuclei composition and the determination of their rotation period through the analysis of the flux variations and of the coma features (jets). We found that the rotation period of comet 41P was surprisingly changed by 26 hr in just two months while the rotation period of comet 46P did not change on both sides of perihelion with an average value of 9.10$\pm$0.05 hr. The regular measurements of the comets activity and composition from optical measurements are also invaluable to support observing programs on larger ground based or space telescopes that we plan with our collaborators or other groups to perform complementary studies of the most interesting objects through optical and IR spectrometers (e.g, 21P and 66P/du Toit).

In this work, we also discussed the reactive collision of electrons with molecular cations in cometary coma. In order to improve our understanding of the kinetics of the cometary coma, theoretical studies of the major reactive collisions in these environments are needed. Deep in the collisional coma, inelastic collisions between thermal electrons and molecular ions result in dissociation and vibrational excitation of the ions, the rates of these processes are especially elevated due to the high ion and electron densities in the inner cometary coma. We presented the study of reactive collisions of electrons with CO^+ and H_2^+ molecular cations using the multi channel quantum defect theory (MQDT), such as dissociative recombination (DR), vibrational excitation (VE) and vibrational de-excitation (VdE), to understand the importance of these reactive collisions in producing carbon, oxygen and hydrogen atoms in cometary activity. The results shows that among all reactive collisions taking place between low energy electrons and CO^+/H_2^+, the dissociative recombination is the most important process at electronic temperatures characteristic of comets, which can be a major source of atoms in the cometary coma at small cometocentric distances.

Chapter 1

General Introduction

1.1 Comets

The word comet originates from the Latin "comēta" and from the Greek “$\kappa o \mu \eta \tau \eta \varsigma$”, which means “the hair of the head” or “long hair”. Comets are among the most primitive bodies of the Solar System. They provide a unique opportunity to study the primitive matter at the origin of the Solar System, material that has been stored in deep freeze for 4.6 billion years. In order to understand the role of comets in the Solar System and its planets formation, we need to address and answer several questions: How did comets form ? What are they made of ? and how do comets work ? Regular and various ground and space based observations, through perihelion and the way back out, are needed to understand how comets behave along their orbital journey around the Sun. This in turn will allow to determine which properties of a given comet are likely primordial and those which are the result of evolution since the Solar System formation.

The first description of comets was made by Chinese astronomers in 2316 BC as transient phenomena, they were the first to create a catalogue listing several forms of comets based on the appearance of their tails with names linked to predictions such that a comet with four tails corresponds to some disease, a comet with two curved tails to a minor war (Ho, 1962). Babylonian and Chaldean astronomers believed that comets were celestial bodies just like planets, and they recorded the observations of comets on tablets. Aristotle (384-322 BC) described comets as atmospheric phenomena due to their impact with the hot atmosphere, and their appearance should be related to weather conditions.

Brahe (1578) measured the distance of a comet for the first time using the parallax method at Uraniborg observatory. Brahe (1578) noticed that the comet’s position in the sky differed very little from similar measurements performed by other astronomers. The difference should have been much larger had the comet been relatively close to the Earth, either at or within the orbit of the Moon. From Brahe’s calculations, the comet appeared to be about five to six times farther than the Moon, and he deduced that it must be then outside of the Earth’s atmosphere (Festou et al., 2004). From this time, a great debate about the nature of comets and their trajectories started. In 1543, the astronomer Copernicus proposed that comets have a heliocentric orbit. This idea was supported by the studies and observations of the astronomer Galileo Galilei in the seventeen century. Kepler observed several comets and tried to study their motion. He proposed that comets are interstellar objects moving along straight lines, and so never fully grasped their dynamics. Based on the work of Kepler and Galileo, Newton (1687) found that comets are attracted by the Sun gravitation and also demonstrated that comets could have elliptical, parabolic, or hyperbolic orbits. In 1688, he calculated the orbit of comet

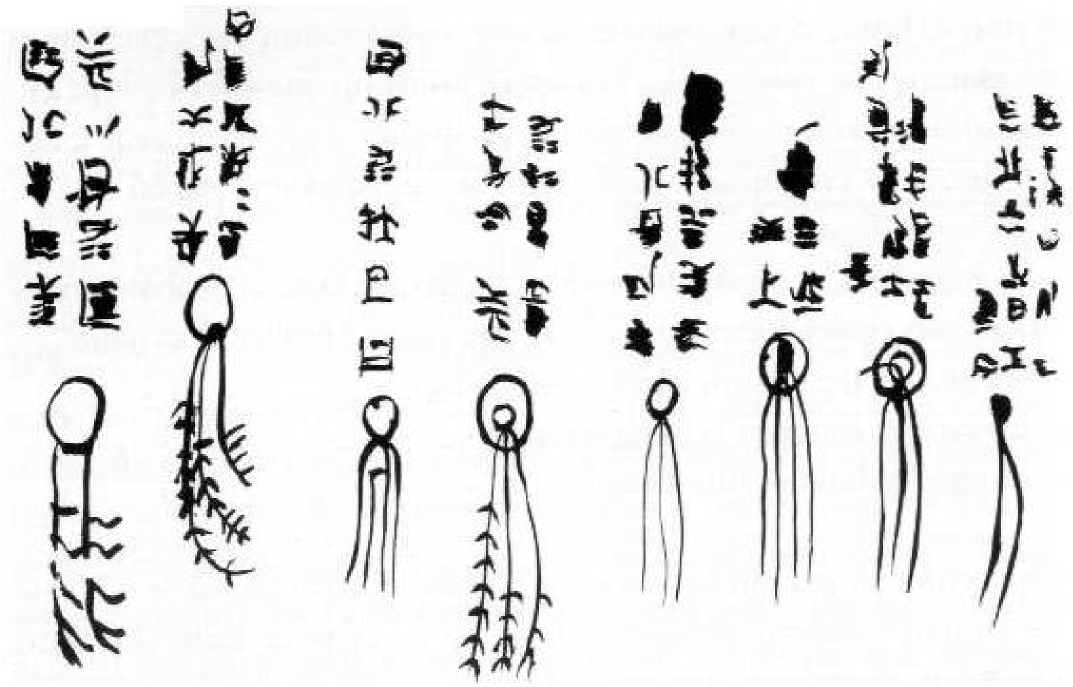

Figure 1.1: Chinese classification of comets according to their appearance (Desvoivres, 1999).

C/1680 V1 (Kirch) and showed that it had a parabolic orbit around the Sun. These results were in good agreement with the observations. Shortly after, Halley (1731) applied Newton's theory to the study of several comets. Halley was the first to suggest that comets may be periodic, moving along very elongated ellipses rather than parabolic paths. He estimated a period of about 76 yr for comet Halley and he expected the comet to be visible again between 1758 and 1759, but he died before these date and his predictions were confirmed.

Since that time, the scientific community started the study of comets and has improved the calculation of their orbits. They were able to determine the orbital period of comets with better precision and were able to predict the next apparition. In the 19th century, astronomers began to investigate the physical nature of comets. Bessel (1836) was the first to establish a link between the tails of comets and the solar radiation. Donati (1864) and Huggins (1868) made the first spectroscopic observations of comets C/1864 (Tempel) and 55P/Tempel-Tuttle, respectively. The spectra were showing three features that are now known to be produced by molecules of diatomic carbon (C_2) in the comet's coma. In the middle of the 20th century, astronomers are interested in the structure and composition of comets through spectroscopic and photometric observations. Wurm (1943) is the first who proposed the concept of "parent" molecules in the nucleus, while "daughter" species would be created in the coma by photochemistry. In 1950, Whipple (1950) proposes a model of the comet nucleus under the name of "dirty snowball", describing it as a conglomerate of ice and dust. From dynamical studies of the distribution of semi-major axes of comets, Oort (1950) identified a distant population of comets known as the Oort cloud comets (see section 1.3). Biermann (1951) gave the correct explanation for the motions of features in cometary plasma tails caused by their interactions with the Solar wind.

1.2 Nomenclature of comets

Based on the International Astronomical Union (hereafter IAU) definition, a comet is a body made of rock and ice with a few kilometres in diameter and it orbits the Sun. As there are many comets visiting the Solar System every year, they must get a number (and a name) to distinguish them. During the 19th century, comets were only given names after their second apparition, while those that had only appeared once were designated by a combination of year of discovery, numbers (both Arabic and Roman) and letters. Sometimes, the name of the discoverer was referred to in parentheses. It was not until the 20th century that comets were routinely named after their discoverers.

Currently, the working group on Small Body Nomenclature (SBN) at the IAU is the responsible committee for strategic matters related to comet naming. Comets get a designation and name according to the following pattern[1]:

- A prefix, alluding to the type of comet, which can be any of the following:
  - P/ for a periodic comet.
  - C/ for a comet that is not periodic.
  - X/ for a comet for which a meaningful orbit cannot be computed.
  - D/ for a periodic comet that no longer exists or is deemed to have disappeared.
  - I/ for an interstellar object.
- The year of discovery.
- An uppercase letter identifying the half-month of observation during that year (A for first half of January, B for second half and so on).
- A number representing the order of discovery within that half month.

As an example, the third comet discovered in the second half of January 2019, and classified as non periodic comet, would be designated as C/2019 B3. The precise method, including exceptions and special cases, is described in the IAU comet-naming guideline[2]. When a periodic comet is observed after its second apparition, the IAU's Minor Planet Center (MPC) gives it a permanent number indicating the order of the discovery. To complete the designation, a comet is given the name of its two first discoverers (last name for an individual or one word or acronym if it has been detected by a specific monitoring project, like LINEAR, Catalina, NEOWISE, PANSTARRS, etc.).

1.3 Origin and classification of comets

Comets formed in the early Solar disk by agglomeration of dust grains and condensation of gas. They were coming from reservoirs that slowly allow comets to leak out to regions where they can be detected. These reservoirs must be stable enough to retain a significant number of objects for billions of years. It is currently believed that there are three main reservoirs: the Oort cloud (OC), the Kuiper Belt (KB) and the Main Asteroids Belt (MAB). The Oort cloud is a very distant reservoir of inactive comet nuclei at heliocentric distances ranging from 10

[1] https://www.iau.org/public/themes/naming/
[2] https://minorplanetcenter.net/iau/info/CometNamingGuidelines.html

000 au to 50 000 au (See section 1.3.1). The Kuiper Belt is a trans-Neptunian disk of inactive comet nuclei at heliocentric distances ranging from 30 au to 50 au (See section 1.3.2). The Main Asteroids Belt is located between the orbits of the planets Jupiter and Mars (See section 1.3.3).

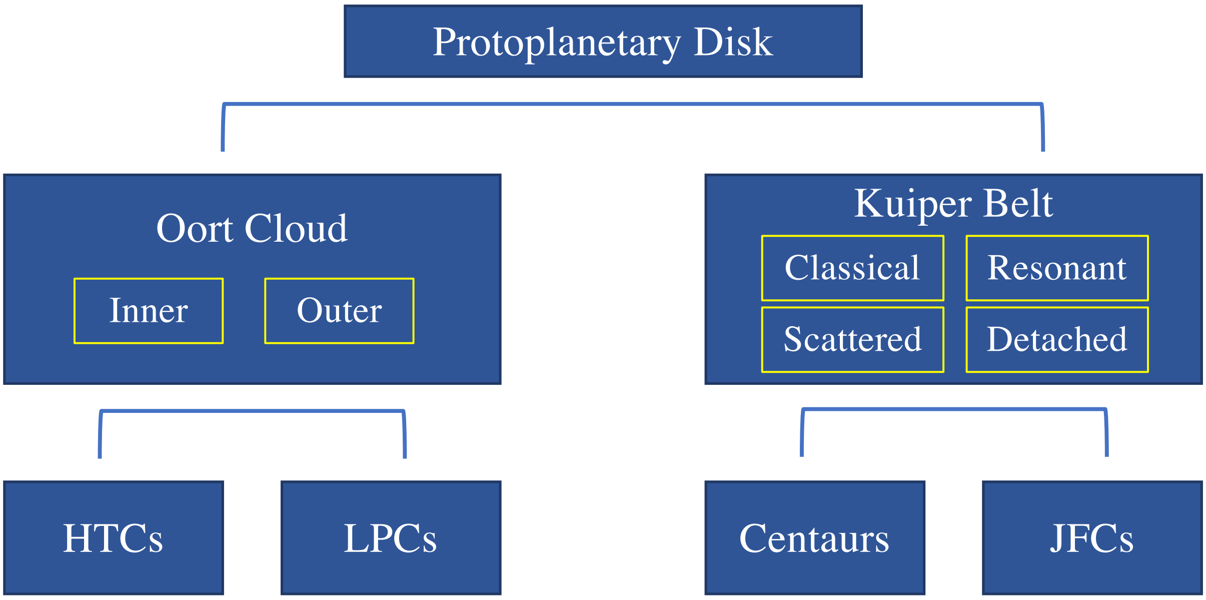

Figure 1.2: Schematic diagram of comets populations based on their dynamical orbits (adapted from Jewitt (2015)).

Historically, cometary taxonomy was based on orbital period which varies wildly. A comet can be either a long-period comet or a short-period comet, depending on whether its orbit is longer or shorter than 200 years. Long-period comets are on trajectories that take them well out past the planets before they return. But this classification could vary during a typical comet's lifetime. Carusi and Valsecchi (1987) suggest a parameter, called the Tisserand parameter, which might be more appropriate for a classification. The Tisserand parameter is a constant of the motion in the restricted, circular three-body approximation, defined with respect to Jupiter by:

$$T_j = \frac{a_j}{a} + 2\sqrt{\frac{a}{a_j}(1-e^2)}cos(i) \tag{1.1}$$

where a, e, and i are the semi-major axes (in au), eccentricity, and inclination (in degrees) of the orbit, respectively, while $a_j = 5.2$ au is the semi-major axis of the orbit of Jupiter.

Comets with $T_i > 2$ are designated ecliptic comets because most of these members have small inclinations. These objects most likely originate in the Kuiper Belt (see section 1.3.2). Ecliptic comets can be further subdivided into three groups: (i) Comets with $2 < T_j < 3$ are mainly on Jupiter-crossing orbits called Jupiter-family comets (JFCs), (ii) comets with $T_j > 3$ and $a > a_j$ are Centaurs as they have an orbit beyond Jupiter and (iii) comets that have $T_j>3$ and $a < a_j$ are Encke-type, in reference to the orbit of comet 2P/Encke. Comets with $T_j<2$, which are believed to be mainly comets from the Oort cloud are designated nearly isotropic comets (NICs), reflecting their inclination distribution (see section 1.3.1). The NICs could be subdivided into two groups: Long Period Comets (LPCs) with semi-major axes $a > 40$ au and Halley-type comets (HTCs), named after the famous 1P/Halley comet, with semi-major axes a

$<$ 40 au (Levison, 1996). Figure 1.2 shows the two main reservoirs of comets, Oort cloud and Kuiper Belt, and their sub-groups and families.

1.3.1 The Oort cloud

Based on the observations of comets orbiting around the Sun with different inclination, and taking into account the number of visible comets and the frequency with which they appeared, Oort (1950) concluded that billions of potential cometary nuclei must exist in a spherical shell surrounding the Solar System. Due to stars perturbation and galactic tides, many comets leave the cloud forever and others enter the planetary system. Among these some may come close to the inner Solar System and are observable as "new" comets. These nearly isotropic comets (NICs) share the following: (i) Their orbits indicate that they did not originate in interstellar space, (ii) they come from all directions, there is no preferred angle of orbital inclination, and (iii) their aphelia tend to group at about 50 000 au. Comets visiting our planetary System for the first time since their placement in the Oort Cloud are called dynamically new comets. These are LPCs which have a semi-major axis larger than 10 000 au and were influenced by gravitational attraction from all the visible and invisible matter in the Galaxy. These comets are particularly interesting since they are some of the most primitive bodies available for a detailed study, and can reveal information about the conditions prevailing in the early solar nebula at the time they formed. The population and mass of the Oort cloud are uncertain, an estimation derived from the measurements of the rate of arrival of new comets suggest a population of 10^{12} comets with radii larger than about 1 km with an average nucleus mass of 10^{13} kg (Neslušan, 2006; Heisler, 1990; Weissman, 1990). Identification of comets orbiting at large heliocentric distances provides useful compositional information and improves our understanding of the formation and evolution of the Solar System.

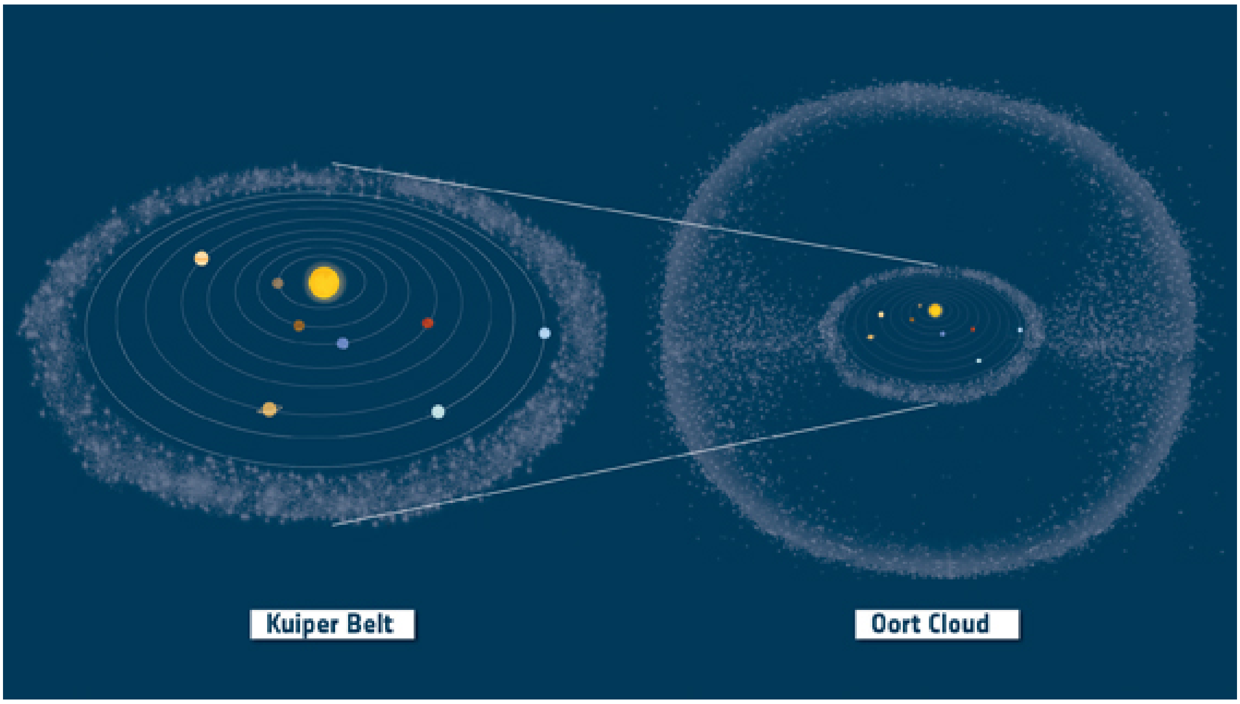

Figure 1.3: Illustration showing the two main reservoirs of comets in the Solar System: the Kuiper Belt, at a distance of 30-50 au; and the Oort cloud, which may extend up to 50 000 - 100 000 au from the Sun. Credit: ESA

1.3.2 The Kuiper Belt

The existence of the Kuiper Belt was confirmed in 1992 with the discovery of the first Kuiper Belt Object (KBO) 1992 QB_1 after Pluto (Jewitt and Luu, 1993). Since then, almost 1 000 more KBOs have been discovered, with the largest having diameters equivalent to or greater than that of Pluto. KBOs can be usefully divided on the basis of their orbits into three distinct families. The resonant objects occupy mean-motion resonances with Neptune that provide long-term dynamical stability. Scattered objects have perihelia close enough to Neptune (q $<$ 40 AU) that they can be dynamically excited by interactions with that planet. It is now believed that the short-period JFCs originate from this scattered disk beyond the Kuiper Belt (Nesvorný et al., 2017). The detached objects are like the scattered objects, but have perihelion distances that are thought to be too large for their orbits to be strongly affected by Neptune in the age of the Solar System (Morbidelli et al., 2008). Current theories have the Kuiper Belt forming along with the rest of the Solar System, though it is still a matter of debate whether it formed in place or was pushed out to its present position as Neptune migrated outwards. If it did form *in situ*, then the region has clearly been heavily depleted, since it contains less than 1% of the mass needed to build the large ice giant planets (Gomes et al., 2005; Morbidelli et al., 2005).

1.3.3 The Main Belt Comets

The Main Belt Comets (hereafter MBCs) are active bodies in the Main Belt of asteroid between Mars and Jupiter, which provides evidence for a possible third reservoir of comets. They are remarkable for having both the orbital characteristics of asteroids and the physical characteristics of comets. They have low inclinations and orbit between about 2 and 4 au from the Sun and a Tisserand parameter of $T_j > 3$. The first such object, 133P/Elst-Pizarro, was discovered in 1996, and the number of known MBCs has increased particularly during the last decade with the new generation of the survey telescopes (e.g. Pan-STARRS, Catalina, etc). At the time of writing, 11 MBCs have been discovered (Snodgrass et al., 2017). Figure 1.4 shows the distribution of these objects in the semi-major axis vs. eccentricity. The activity of these bodies is not necessarily evidence of comet-like, sublimation-driven, activity from surface ices. Several alternative mechanisms have been suggested for the activity of these objects including the impacts between material within the asteroid Belt, rotational instability, electrostatic repulsion, thermal fracture or radiation pressure sweeping (Jewitt, 2012). MBCs present an opportunity to study the nature, extent, and abundance of ice in inner Solar System bodies and have implications for understanding the formation of our Solar System and delivery of water to the early Earth. They are observationally challenging targets not only because they are small and far away from the Sun but also because they exhibit very low activity. Many studies have been done on those objects but they were not able to detect any evidence of gaseous products of sublimation (Snodgrass et al., 2017). In this work, we investigated the originality of comet 66P/du Toit as it has a high probability of coming from the Main Belt of Asteroids (Fernández and Sosa, 2015). Results and discussion about this comet were published in a separate work (Yang et al., 2019) and are given in section 3.6 in chapter 3.

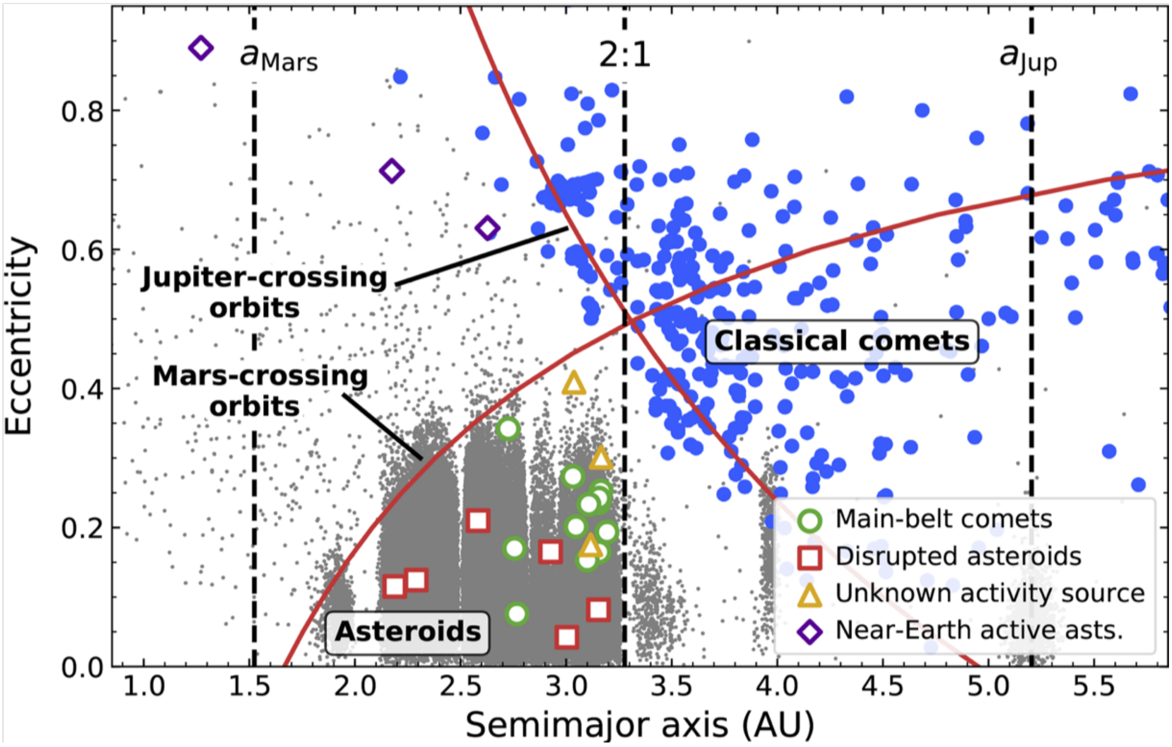

Figure 1.4: Distribution of the known MBCs (green circles) in the semi-major axis vs. eccentricity. The corresponding distributions of asteroids (grey dots) and comets (blue circles) are shown for comparison. Objects above the diagonal arcs cross either the aphelion distance of Mars or the perihelion distance of Jupiter, as marked in red lines. The semi-major axes of the orbits of Mars, Jupiter and the location of the 2:1 mean-motion resonance with Jupiter are shown for reference with dashed lines (Holler et al., 2018).

1.4 Physical characteristics of comets

1.4.1 The nucleus

The nucleus is responsible for most of the observed material in the comet's coma, through the interactions of the solar radiation with the nucleus. It is hard to resolve the nucleus of the comet directly with ground and space-based telescopes because of its small size and the surrounding coma. Nonetheless, unresolved observations remain very important because they can place constraints on the diversity of nuclei including their size, albedo, colour and surface composition (Lamy et al., 2004b; Meech et al., 2004). But the most information with regard to their possible nature, size, density, structure and composition is coming from spacecrafts and *in situ* missions. Several missions have been carried out for comets such as 1P/Halley (Keller et al., 1986), 9P/Tempel 1 (A'Hearn et al., 2005), 81P/Wild 2 (Brownlee et al., 2004), 19P/Borrelly (Soderblom, 2002), 103P/Hartley (Thomas et al., 2013), and recently comet 67P/Churyumov-Gerasimenko with the Rosetta mission (Jorda et al., 2016). These missions reveal different shapes of the nuclei, and many features such as valleys, hills and craters on their surfaces. The gas emission is not uniform over the whole surface of the nucleus but comes out as discrete jets from different locations. Many depressions are found on the nucleus with complex structures, which could have been formed by impact, sublimation or a combination of these processes. Figure 1.5 shows the nuclei of comets visited by different spacecrafts. Studying the composition and structure of cometary nuclei provides the keys to understand the formation and evolution of matter in the early Solar System.

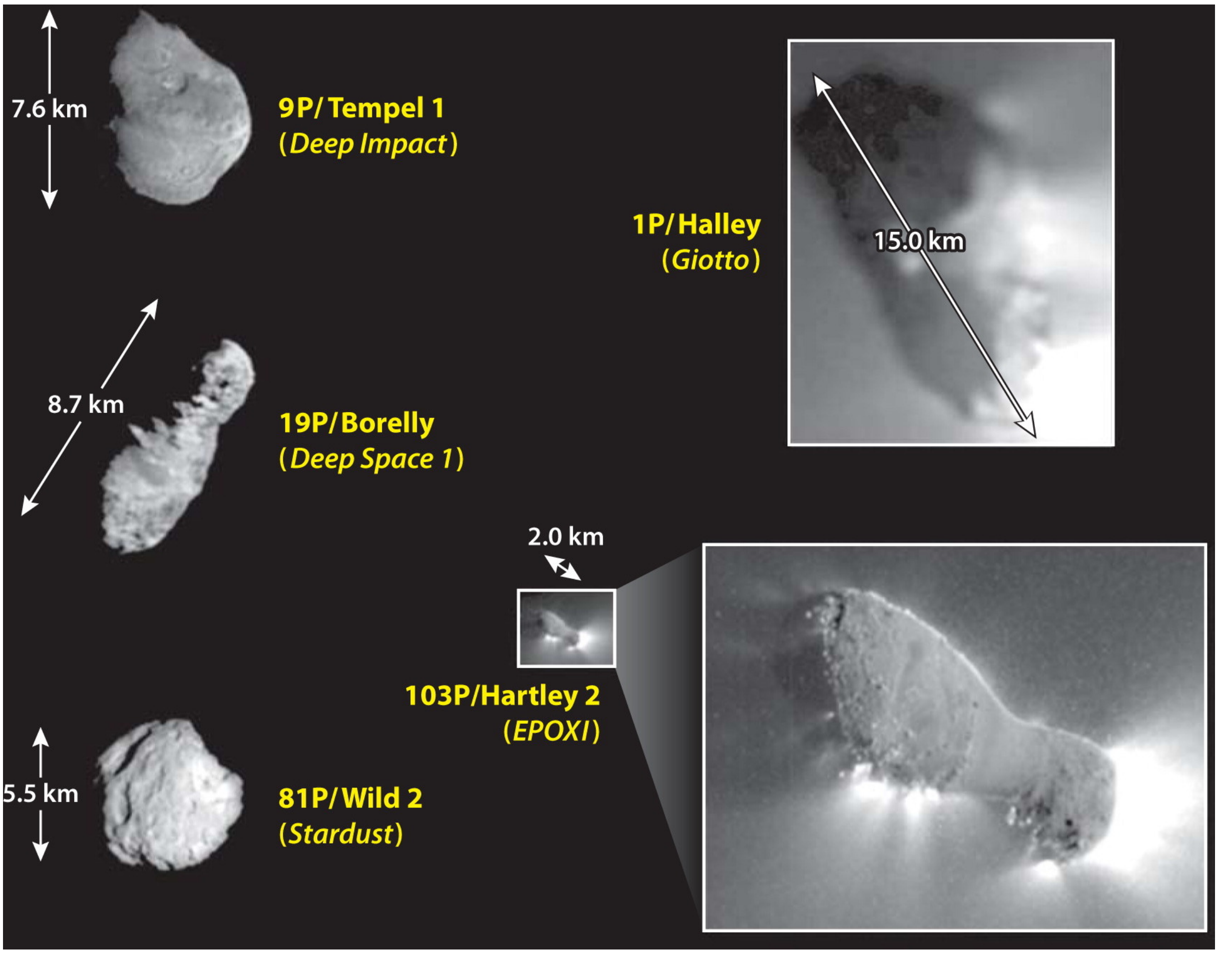

Figure 1.5: Comets nuclei imaged from different spacecrafts. All comets are shown at the same scale, except for the additional expanded view of Hartley 2. Credit: NASA/JPL/UMD.

The rotational state of the nucleus is important for understanding the physical properties of its surface, and also playing a key role in the change of the comet's activity. The rotation period of the nucleus can be estimated from some time dependent property associated with the comet. It could be the observation of a certain repetitive feature (jets), sequence of images of the nucleus (space observations), from an analysis of modelling of light curves. The spin state and rotation period of a nucleus could change for several reasons. Outgassing of volatiles from the nucleus causes a reaction force on the nucleus, and could generate a torque on the nucleus resulting in changes of the nuclear spin state (Whipple, 1982). Another mechanism for altering spin states is via changes to the moment of inertia of the nucleus due to mass loss of volatiles and dust or splitting events of the nucleus (Boehnhardt, 2004). A collision with another Solar System object could change the spin state and rotation period of the nucleus. In chapter 3, we discussed the case of comet 41P/Tuttle-Giacobini-Kresak which has changed its rotation period by 26 hrs in 2 months (Moulane et al., 2018a).

1.4.2 The coma

When a comet gets closer to the Sun, its icy material starts to sublimate due to the solar radiation. The cloud of gas and dust that surrounds the nucleus, the so called coma, formed because of the sublimation of volatile molecules from the nucleus and carryover dust particles that are embedded in the ice towards the anti-solar direction, forming a tail. The coma is known to begin to form at large distance from the Sun (> 3 au) and can reach a size of up to

2-3 million km, which is even larger than the diameter of the Sun. Although occasionally visible at much larger distances due to the sublimation of very volatile species mainly CO and CO_2, this envelope of gas and dust usually gets bigger when the comet gets much closer to the Sun where the Solar radiation heats the surface of the nucleus sufficiently for water to sublimate. The level of a comet's activity depends on its origin and how much it approaches to the Sun. New OCs are Typically more active than the JFCs or HTCs, as they get heated by the Sun for the first time coming from a cold region. Figure 1.6 shows the evolution of the activity of a short period comet as it approaches to the Sun.

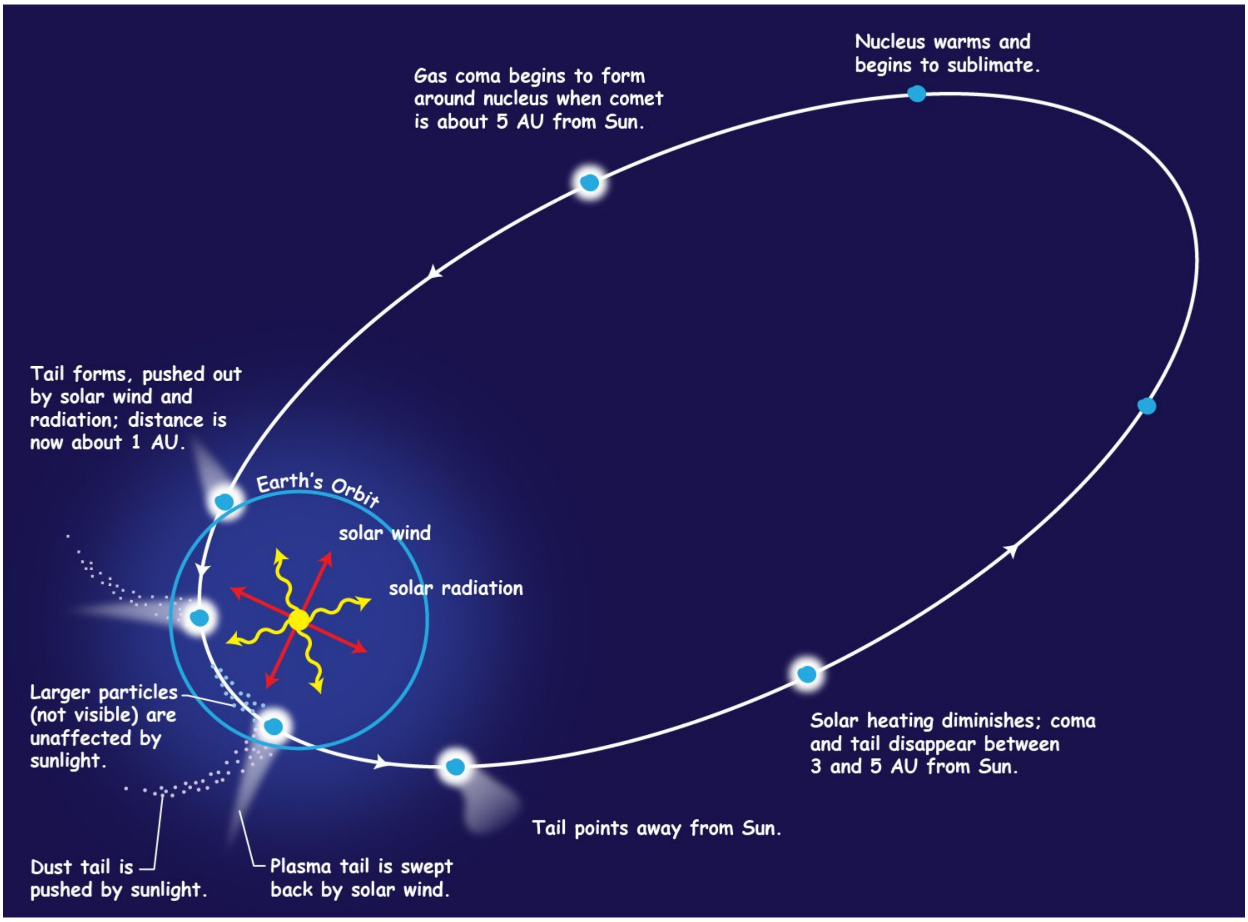

Figure 1.6: Evolution of the activity of a short period comet as it approaches to the Sun. Credit: NASA website

The gas molecules released in the process together with the dust particles escape the nucleus at high speeds, at about 1 km/s and 200 m/s respectively for gas and dust for a comet at 1 au from the Sun, to form a thin coma. The mother molecules coming out from the nucleus break into daughter species due to photo-dissociation by solar photons or by collisions with electrons. The molecules vaporized from the nucleus are subjected to a variety of processes which could dissociate them step by step. The species observed in the spectra of comets could comprise contributions arising out of the dissociated products, released directly from the nucleus or even ejected by dust particles. The complex molecules released from the nucleus, generally known as parent or mother molecules, emit light through fluorescence processes at ultraviolet, infrared, or radio wavelengths. The parent molecules are photo-dissociated by the solar radiation to much smaller molecules, radicals or ions, the so called daughter molecules, like CN, C_2, OH, CH, NH, NH_2, etc, which have been detected in the comet's emission spectra at the optical wavelengths. Photolytic destruction of parent molecules can follow several paths depending on the energy of the incident photons. In fact, there are various processes playing role in the coma

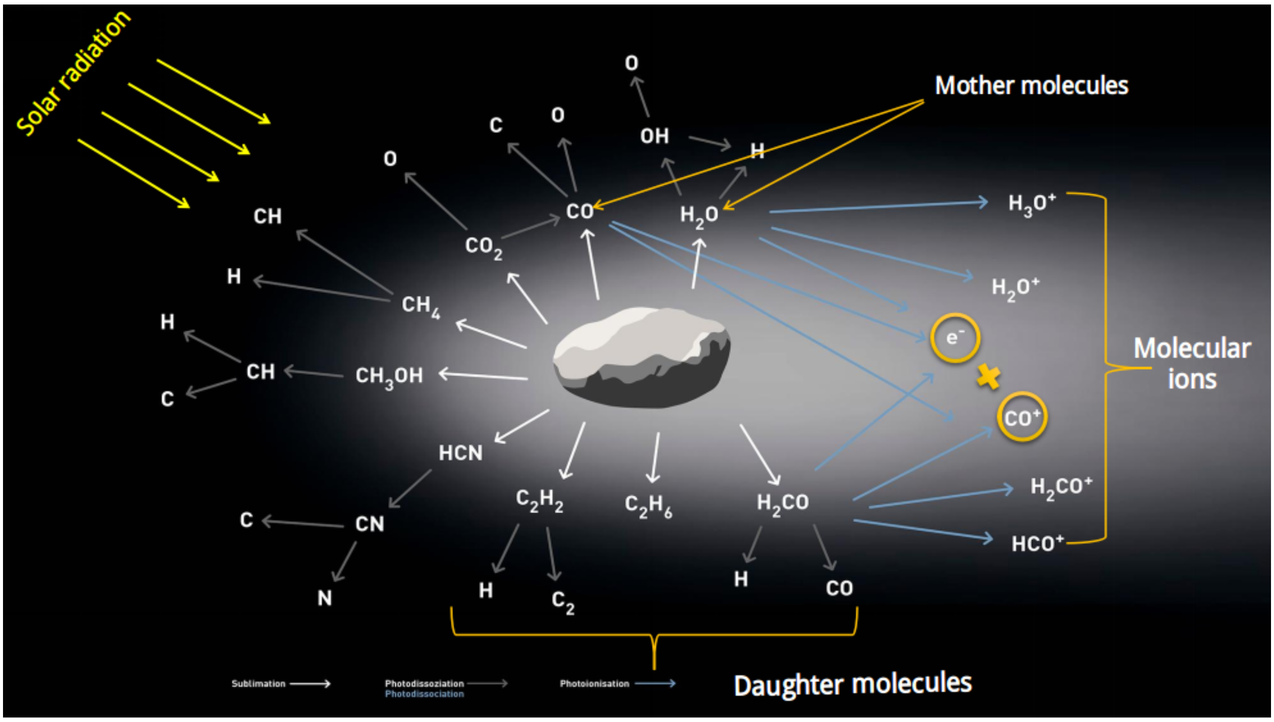

Figure 1.7: Schematic illustration of the main processes (sublimation, photo-dissociation, and photo-ionisation) in the coma. Credit: DLR website

to produce daughter molecules, electrons, ions and atoms. Figure 1.7 provides a simplified overview of these processes. Table 1.1 summarizes different processes taking place in the inner coma in decreasing order of importance (Huebner et al., 1991). Through the study of the radio wavelengths region, a large number of parent molecules of some of the observed species have been identified. Table 1.2 summarizes the probable parent molecules of some observed species in comets. Although chemical and physical processes in the coma alter the molecules, daughter molecules provide important information about the composition of the nucleus.

Observing comets at optical and ultraviolet wavelengths allows to detect the emission lines of electronic transitions of radicals molecules and certain ions and atoms, because of the absorption of solar radiation in their resonance transitions which then trickle down to give the radiation is called the resonance fluorescence process. When molecules absorb a photon at the same wavelength corresponding to one of its possible transitions, they get to an excited state. But they can also return to the ground state via many ways, dissipating energy. We talk about the resonance fluorescence process when a molecule de-energizes by directly emitting a photon at the same wavelength as the one that was absorbed. The molecule thus returns to the ground state in a single step. The fluorescence process is when a molecule goes through different vibrational states before emitting a photon. In this case, the wavelength of the emitted photon is greater than that one initially absorbed, while part of the energy has been dissipated by vibration. The resonance fluorescence process is very successful in explaining the observed band spectra of various molecules in comets. Several molecules, atoms and ions have been identified in the coma of comets at optical, infrared and radio wavelengths. At the optical, the main molecules observed are OH, NH, CN, C_3, C_2,CH, NH and NH_2, etc. Figure 1.8 shows the emission lines of different molecules in a low resolution spectrum of comet 122P/deVico during its apparition in 1995 at a heliocentric distance of 0.69 au. Several ions have been detected in comets such as H_2O^+, OH^+, H_3O^+, CO_2^+, CH^+, N_2^+, etc. Mother and complex molecules have been observed at the infrared and radio wavelengths, like water, CO_2 and CO the most abundant parent species in the coma, CHO-bearing molecules (CH_3OH, H_2CO, $HOCH_2CH_2OH$, etc), hydrocarbons(CH_4,

Table 1.1: Physical and chemical reactions that taking place in the inner coma (Huebner et al., 1991).

Photodissociation	hν + $H_2O \rightarrow$ H + OH
Photoionization	hν + CO $\rightarrow CO^+$ + e
Photodissociative ionization	hν + $CO_2 \rightarrow$ O + CO^+ + e
Electron impact dissociation	e + $N_2 \rightarrow$ N + N + e
Electron impact ionization	e + CO $\rightarrow CO^+$ + e + e
Electron impact dissociative ionization	e + $CO_2 \rightarrow$ O + CO^+ + e + e
Positive ion-atom interchange	CO^+ + $H_2O \rightarrow HCO^+$ + OH
Positive ion charge transfer	CO^+ + $H_2O \rightarrow H_2O^+$ + CO
Electron dissociative recombination	C_2H^+ + e $\rightarrow C_2$ + H
Three-body positive ion-neutral association	C_2H+_2 + H_2 + M $\rightarrow C_2H_4^+$ + M
Neutral rearrangement	N + CH $\rightarrow$ CN + H
Three-body neutral recombination	C_2H_2 + H +M $\rightarrow C_2H_3$ +M
Radiative electronic state deexcitation	$O(^1D) \rightarrow O(^3P)$ + hν
Radiative recombination	e + $H^+ \rightarrow$ H + hν
Radiation stabilized positive ion-neutral association	C^+ + H $\rightarrow CH^+$ + hν
Radiation stabilized neutral recombination	C + C $\rightarrow C_2$ + hν
Neutral-neutral associative ionization	CH + O $\rightarrow HCO^+$ + e
Neutral impact electronic state quenching	$O(^1D)$ + $CO_2 \rightarrow O(^3P)$ + CO_2
Electron impact electronic state excitation	$CO(^1\Sigma) + e \rightarrow CO(^1\Pi) + e$

Table 1.2: Possible parent molecules of the observed ions, molecules and atoms (adapted from (Swamy, 2010)).

Observed species	Possible parent molecules
H_2O,H_2O^+,OH,H	H_2O
CO_2^+	CO_2
CO,CO^+, C	CO,CO_2
CH	CH_4
CN	HCN, C_2N_2
NH_2	NH_3
NH	NH_2, NH_3
C_2	C_2H_2, C_3H_2O
C_3	C_3H_4, C_3H_8
CS	CS_2, OCS
S	S_2, OCS, CS_2, H_2S, SO_2
O	O_2, CO_2, CO, H_2O

C_2H_2, C_2H_6, etc), sulphur bearing molecules (S_2, H_2S, OCS, H_2CS, etc) and nitrogen bearing molecules (NH_3, HCN, HCNO, HC_3N, etc) and many other molecules (Swamy, 2010; Cochran et al., 2015).

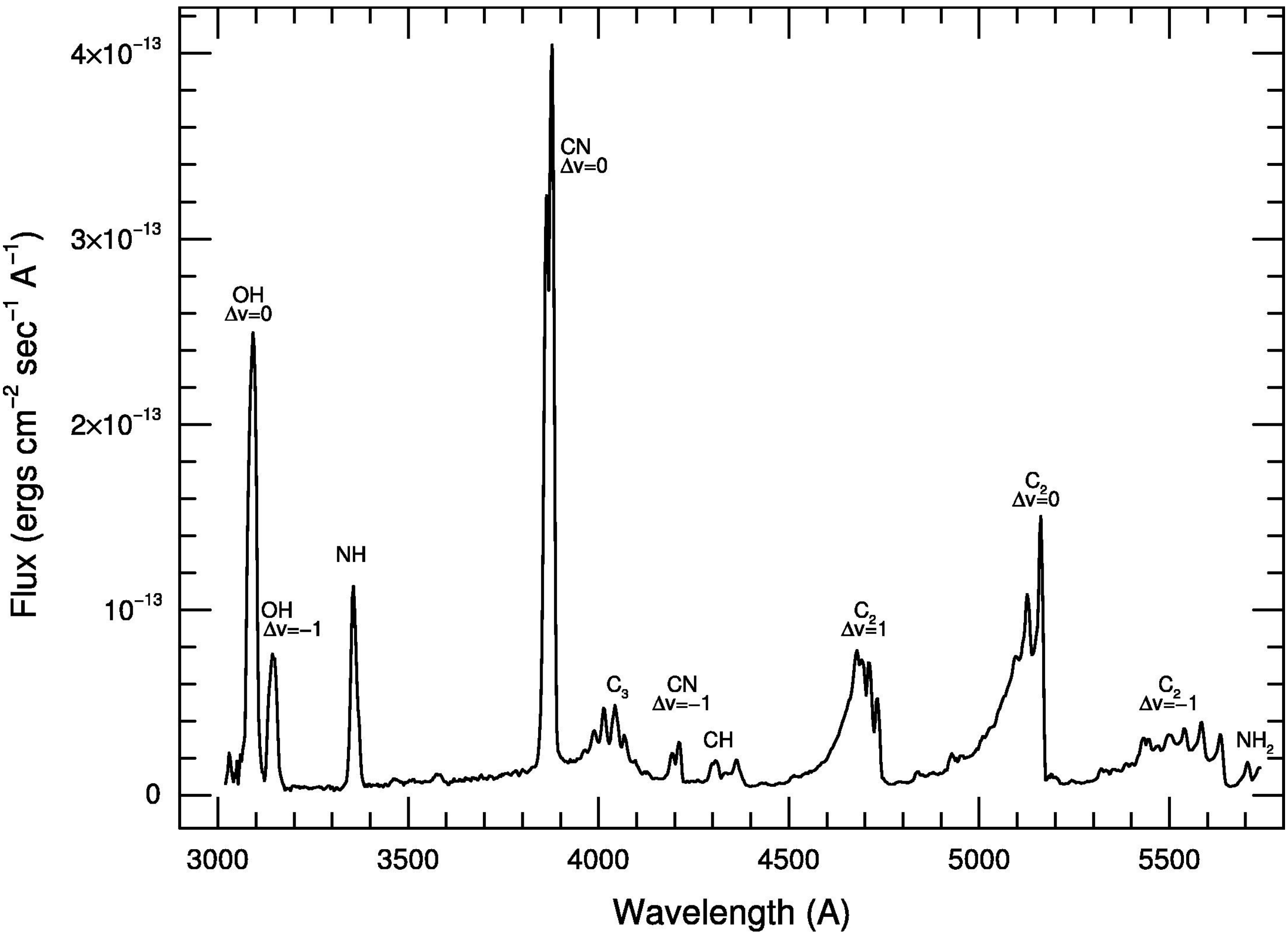

Figure 1.8: Low resolution spectrum of comet 122P/deVico obtained with the Large Cassegrain Spectrograph at the 2.7-m telescope on September 27, 1995 when the comet was at 0.69 au from the Sun (Cochran et al., 2012).

1.4.3 The tails

When the comet is getting close to the Sun, intense heat vaporizes the ice and the radiation pressure releases the dust which streams behind the comet forming two distinct tails: an ion tail carried by the solar wind, the constant flow of charged particles from the Sun, and a dust tail. The coma and, subsequently, plasma and dust tails develop during the comet's approach to the Sun, subside and disappear in reverse order after perihelion passage. The ion tail is formed by the interaction of the Solar wind plasma with the cometary atmosphere. This tail is mainly composed of CO^+, in addition to other molecular ions such as H_2O^+, OH^+, H_3O^+, CO_2^+, CH^+, and N_2^+, and electrons (Flynn, 1994). The ions C^+ and S^+ were also found to be very abundant (Balsiger et al., 1986). The typical velocities of ions in the plasma tail range from 10 km/s near the cometary head to 250 km/s far from it. The solar wind with its magnetic field sweeps these charged ions (primarily CO^+) from the coma into a tail which always points directly away from the Sun. Due to the fast speed at which the solar wind interacts with the comet, this plasma is pushed out into a straight, narrow tail, which may show internal structure as a result of changes in the magnetic field. Figure 1.9 shows an image of both tails of comet C/1995 O1 (Hale-Bopp) during its apparition in 1997.

Large dust tails are a typical characteristic of active comets, they are made of small grains ejected from the nucleus and pushed away by the Solar radiation pressure. The dust grains are controlled by two forces: F_{rad} which is the force of the solar radiation pressure acting on the

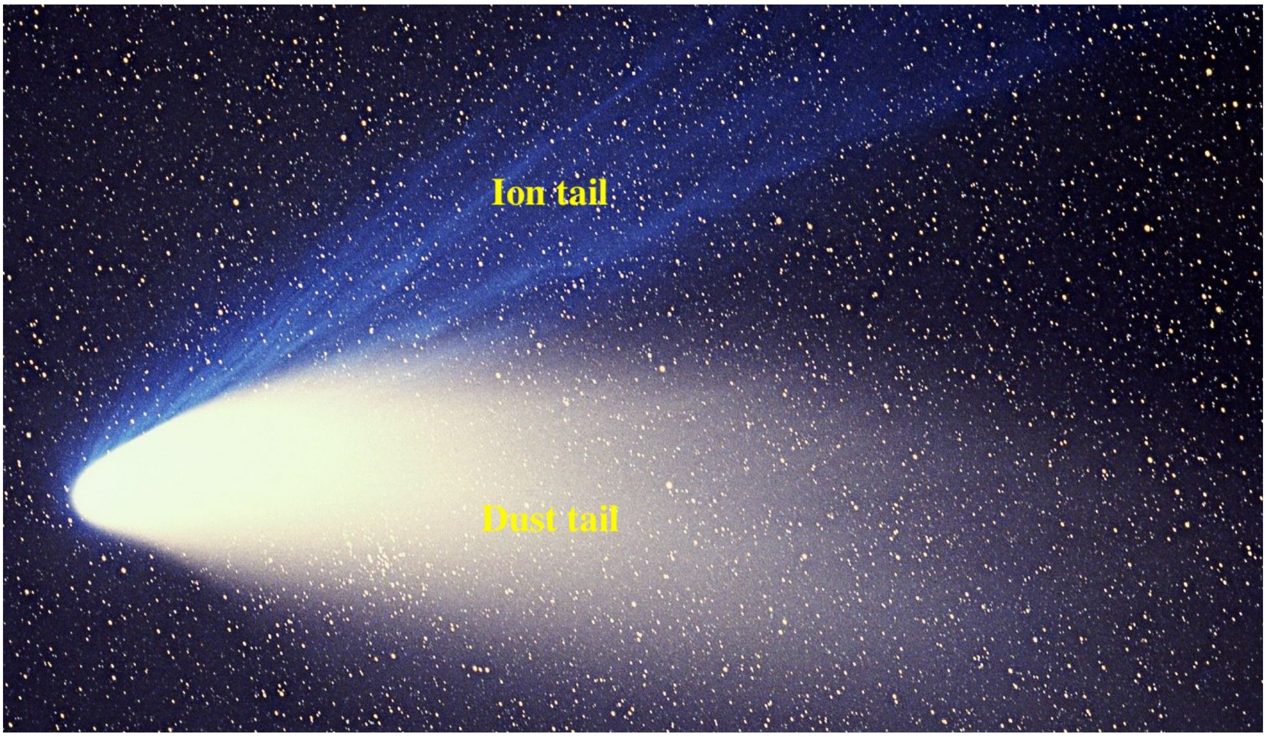

Figure 1.9: Ion and dust tails of comet C/1995 O1 (Hale-Bopp) taken on April 4, 1997. Credit: Johannes-Kepler Observatory.

dust particles pushing it away from the Sun, and F_{grav} is the force of solar gravity pulling the dust particles towards the Sun.

$$F_{rad} = \frac{\pi a^2}{4} \frac{Q_{pr}}{c} \frac{F}{4\pi r_h^2} \tag{1.2}$$

$$F_{grav} = \frac{GM}{r_h^2} \frac{\rho_a \pi a^3}{6} \tag{1.3}$$

where r_h is the heliocentric distance, F is the mean solar radiation, M is the Solar mass, a is the diameter of the grain, ρ_a is the density of grains, Q_{pt} is the efficiency factor for radiation pressure.

These forces vary with the heliocentric distance as r_h^{-2}, and the ratio of radiation pressure to gravitational force is denoted by (1-μ) where :

$$(1-\mu) = \frac{F_{rad}}{F_{grav}} = C\frac{Q_{pr}}{\rho_a a} \tag{1.4}$$

where $C = \frac{3F}{8\pi cGM} = 1.2 \times 10^{-4}$, considering F is the Solar flux at 1 au.

(1-μ) quantity is used to identify the type of the tail curve: (i) *Syndyne* which means that the particles of the same size are emitted by the nucleus. (ii) *Synchrone* which involves the distribution of particles emitted at any particular time, like the case of an outburst.

The observation of comets has clearly shown a wide variation in the chemical and physical nature of grains. The value of Q_{pr} is also not constant but is dependent upon the sizes of the particles. If the grains of various sizes are emitted continuously, it is difficult to separate the effects depending on the time of ejection from those due to the size and properties of the grains. Therefore several studies have been carried out to tackle some of the above limitations. One of these is the Monte Carlo dust model (Moreno et al., 2012), which allows to calculate the orbit of sample dust particles taking into account the anisotropy in dust ejection, and dust ejection velocity for modelling the cometary dust tails. The model also calculates the dust mass rate and the time dependent size distribution function. We have applied this model to some comets described in this thesis (See chapter 3).

In addition to the ion and dust tails, another tail called the sodium tail appeared in some very bright comets. The existence of the neutral tail was confirmed through observations of comet Hale Bopp in 1997 (Cremonese, 1999). Prior to this, neutral sodium atoms had been primarily observed in the coma of comets. The source of the sodium atoms and how the neutral tail forms is still a matter of debate. One idea is that the sodium atoms are formed in the coma and pushed out into the neutral tail through radiation pressure. The neutral tail is therefore formed in a similar way to the dust tail, an idea that is supported by the location of the neutral tail between the dust tail and the ion tail. An alternate idea is that the sodium atoms are created in situ in the tail through either collisions between dust grains or the bombardment of the dust grains with ultraviolet light from the Sun. This releases the sodium atoms in a process called sputtering (Rietmeijer, 1999; Cremonese et al., 2002). In early July 2020, comet C/2020 F3 (NEOWISE) approached the Sun with a perihelion distance of 0.3 au and displayed a sodium tail in addition to both typical ion and dust tails[3].

1.5 Space missions to comets

Several space missions were sent to comets to study their physical and chemical properties in order to improve our understanding of the origin of those objects and how they formed. The first major space adventure was in 1986 when six spacecrafts passed close to the nucleus of comet 1P/Halley (Reinhard, 1986; Mendis, 1988; Sagdeev et al., 1986). Even prior to comet Halley, the first spacecraft that visited a comet was the ICE in 1985, which was sent to study 21P/Giacobini-Zinner (Von Rosenvinge et al., 1986; Cowley, 1987; Mendis, 1988). The mission proved the "dirt-snowball" theory that was proposed by Whipple (1950). These spacecrafts explored the cometary material after its sublimation from the cometary nucleus and exposure to ultraviolet radiation, but none of them had any *in situ* capabilities to explore the nuclei. In the first decade of 2000, the Deep space 1 mission to comet 19P/Borrelly (Soderblom, 2002), Deep Impact and NExT Stardust missions to comet 9P/Tempel 1 (A'Hearn et al., 2005), Stardust mission to comet 81P/Wild 2 (Brownlee et al., 2004), and the EPOXI mission to comet 103P/Hartley 2 (A'Hearn et al., 2011) were able for the first time to look at cometary material in the deeper layers of the nuclei and collect dust to study it in the laboratory. Table 1.3 summarizes all the spacecraft that have encountered comets.

More recently in 2014, the European Space Agency (ESA) spacecraft mission named Rosetta, equipped with a lander named Philae, was the first mission to land on a surface of a comet. Eleven instruments performed measurements of the gas and dust in the coma of comet 67P/Churyumov–Gerasimenko (hereafter 67P) for a large heliocentric distances range. These instruments were designed to study the nucleus and its immediate environment. Figure 1.10 shows an image of 67P's nucleus as seen from Rosetta. More details about the full mission and instruments can be found at the Rosetta mission website[4]. The mission has yielded an important science return, collecting a wealth of data from the nucleus and its environment at various levels of cometary activity. As a result of this unique mission, major and many minor species including their isotopologues were measured as a function of heliocentric distance and as

[3] https://apod.nasa.gov/apod/ap210308.html
[4] http://rosetta.esa.int/

a function of latitude/longitude of the comet nucleus. Rosetta characterized many geological, physical and chemical features of comet 67P during its orbit around the Sun. In terms of composition and chemistry, it more than doubled the known cometary parent species and added many more isotopic ratios to the cometary inventory (Altwegg et al., 2019; Bockelée-Morvan et al., 2015). The instruments on board with Rosetta and Philae lander were able to measure different physical and geological proprieties (density, albedo, size, rotation period, dust porosity, etc) of the nucleus with a high precision (Jorda et al., 2016; Fornasier et al., 2015; Taylor et al., 2017).

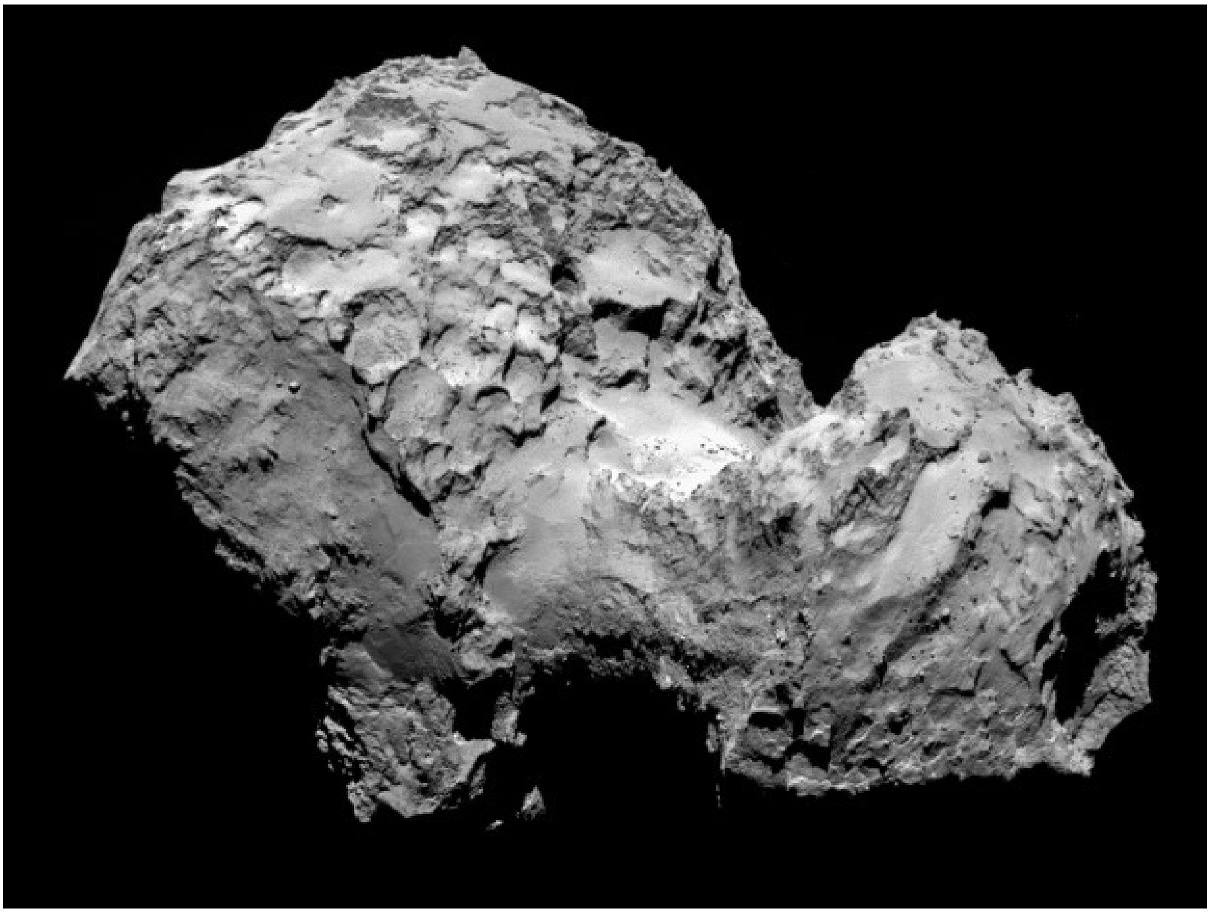

Figure 1.10: Comet 67P/Churyumov-Gerasimenko as seen by Rosetta's OSIRIS narrow-angle camera on August 3, 2014 from a distance of 285 km. The image resolution is 5.3 metres/pixel. Credit: ESA/Rosetta.

The next mission to comets is called Comet Interceptor mission[5] which was selected by ESA in June 2019 as a F-class mission expected to launch in 2028. Comprising three spacecraft, it will be the first to visit a LPC or even an interstellar object that is only just starting its journey into the inner Solar System. The mission is being designed and launched without a specific comet designated as its main target. Comet Interceptor will travel to the Sun-Earth L2 Lagrangian point and wait in hibernation until a suitable LPC is found that will come close enough to the Sun for the spacecraft to maneuver to an encounter trajectory. Its three spacecraft will perform simultaneous observations from multiple points around the comet, creating a 3D profile of a dynamically new object that contains unprocessed material surviving since the Solar System formation. The primary spacecraft will perform a fly-by at $\sim$1000 km from the target and the two smaller probes will travel deeper into the coma, closer to the nucleus. To prepare for all eventualities, the science team has assembled a preliminary set of backup targets from

[5] https://www.cometinterceptor.space/

the known JFCs, where a suitable fly-by trajectory can be achieved during the nominal mission timeline including the possibility of some launch delay (Schwamb et al., 2020).

Table 1.3: Spacecraft that have encountered comets (adapted from Thomas (2020)).

Spacecraft	Agency	Target	Type of encounter	Date of encounter	Closest approach	Reference
ICE (ISEE-3)	NASA	21P/G-Z	Fly-by	September 11, 1985	7800 km	Cowley (1987)
		1P/Halley	Fly-by	End March 1986	28 millions km	Farquhar (1983)
Vega 1	Roscosmos	1P/Halley	Fly-by	March 11, 1986	8889 km	Sagdeev et al. (1986)
Vega 2	Roscosmos	1P/Halley	Fly-by	March 9, 1986	8030 km	Sagdeev et al. (1986)
Sakigake	JAXA	1P/Halley	Fly-by	March 11, 1986	7 millions km	Hirao and Itoh (1986)
Suisei	JAXA	1P/Halley	Fly-by	March 8, 1986	151 000 km	Hirao and Itoh (1986)
Giotto	ESA	1P/Halley	Fly-by	March 13, 1986	596 km	Reinhard (1986)
		26P/G-S	Fly-by	July, 1992	200 km	ESA website
Deep Space 1	NASA	19P/Borrelly	Fly-by	September 22, 2001	2171 km	Boice et al. (2000)
Stardust	NASA	81P/Wild 2	Fly-by	January 2, 2004	237 km	Brownlee et al. (2004)
Deep Impact	NASA	9P/Tempel 1	Fly-by/Impact	July 4, 2005	575 km	A'Hearn et al. (2005)
EPOXI	NASA	103P/Hartley 2	Fly-by	November 4, 2010	700 km	A'Hearn et al. (2011)
NExT (Stardust)	NASA	9P/Tempel 1	Fly-by	February 15, 2011	181 km	Veverka et al. (2013)
Rosetta	ESA	67P/C-G	Rendezvous	August 6, 2014	0 km	Glassmeier et al. (2007)

Chapter 2

Observation and Data Reduction

This chapter describes observations, statistics, reduction and analysis of the comets data collected with both TRAPPIST and spectroscopic instruments on VLTs. Section 2.1 describes the instrumentation of the TRAPPIST telescopes. The statistic of comets data collected with TRAPPIST telescopes in the period of 2017-2020 is given in section 2.2. Photometry techniques, procedures, and methodologies used for the reduction and analysis of the TRAPPIST data are given in section 2.3. Data reduction of spectroscopic observations is given in section 2.4.

2.1 The TRAPPIST telescopes

TRAPPIST (**TRA**nsiting **P**lanets and **P**lanetes**I**mals **S**mall **T**elescope) is a project led by researchers at the Space sciences, Technologies & Astrophysics Research (STAR) Institute, of the University of Liege. It is made of two 60-cm robotic telescopes devoted to the detection and characterization of exoplanets using the transit method and to the study of comets and other small bodies in our Solar System (asteroids and comets) (Jehin et al., 2011). TRAPPIST-South (hereafter TS) was installed at the ESO La Silla Observatory in 2010 (Figure 2.2) and TRAPPIST-North (hereafter TN) was installed in May 2016, at the Oukaimeden Observatory at 2750 m of altitude in the Atlas mountains of Morocco (Figure 2.1) in collaboration with Cadi Ayyad University (Benkhaldoun, 2018). After the installation of TN in the end of 2016, we have access to almost the whole sky on a regular basis. With the two telescopes, we can follow comets over a large part of their orbits from both hemispheres. In 2017, TRAPPIST team announced the discovery a system of 7 exoplanets orbiting around TRAPPIST-1 star, these seven planets are similar in size to Earth and could have liquid water on their surface, particularly the three of them which orbit in the so-called "habitable" zone of their star (Gillon et al., 2017).

Both telescopes are of the Ritchey-Chretien type with a focal ratio of F/8 and mounted on a German equatorial mount NTM-500 built by the *ASTELCO* company. TN is equipped with a thermo-electrically cooled 2K×2K Andor IKONL CCD camera with a $20' \times 20'$ field of view. We bin the pixels two by two giving a resulting plate scale of $1.2''$/pixel. TS is equipped with a 2K×2K FLI PL3041-BB CCD camera with a pixel size of $15 \mu m$, providing a field of view of $22' \times 22'$ with plate scale of $1.3''$/pixel with a binning of two pixels. The CCD cameras have a high sensitivity over the whole range of the optical spectrum. Both cameras are equipped with a double Apogee filter wheel with 15 filters (for TN) and 18 filters (for TS) mounted. Table 2.1 summarized different characteristics of TRAPPIST.

TN is covered by a 4.2m Gambato dome while TS is placed under a 5m Ash-Dome dome, both of domes are in automatic mode linked to the main remote software. More details about the TRAPPIST instruments efficiency are given in Table 2.1. Both of sites are supported with *Diffraction Limited Boltwood Cloud Sensor* weather station and *SBIG* AllSky Camera[1].

Figure 2.1: TRAPPIST-North at Oukaimeden Observatory, Morocco (IAU code Z53).

Figure 2.2: TRAPPIST-South at ESO/La Silla Observatory, Chile (IAU code I40).

Both TRAPPIST are equipped with narrow-band filters designed for the observation of comet Hale-Bopp (HB hereafter) in 1997 at the Lowell Observatory (Farnham et al., 2000). These filters isolate the emission bands of OH[3090 Å], NH[3362 Å], CN[3870 Å], C_3[4062 Å], and C_2[5141 Å] daughter species as well as emission free dust continuum in four regions covering the optical range UC [3448 Å] (only for TS), BC [4450 Å], GC [5260 Å], and RC [7128 Å]. These narrow-band filters are interference filters, whose design was carefully thought to maximize the fraction of the emission bands encompassed while minimizing the continuum contamination for the gas filters. Most of the filters have more than 60% in their transmission spectrum. In the case of OH, the filter isolates the 0-0 band at 3090 Å, while excluding the 1-1 band which starts at 3126 Å. For NH, the entire signal is produced by the 0-0 band, overlapping the 1-1 band. The CN filter includes both the 0-0 band of the B-X system and the overlapping 1-1 band, the latter varying between 5 and 11% of the flux of the 0-0 band. The homonuclear molecules, C_2 and C_3, have relatively broad emission bands because large numbers of rotational levels

[1] http://www2.orca.ulg.ac.be/TRAPPIST/Camera/CamerasTRAPPIST.php

Table 2.1: Characteristics of TN and TS telescopes and instrumentation.

Instruments	TRAPPIST-North	TRAPPIST-South
Telescope		
Diameter	60 cm	60cm
Type	Ritchey-Chretien	Ritchey-Chretien
System focal ratio	F/8	F/8
The mount		
Model	Astelco NTM-500	Astelco NTM-500
Type	German equatorial	German equatorial
Speed	50 deg/s	50 deg/s
Tracking accuracy	1 arcsec/5 min	1 arcsec/5 min
CCD Camera		
Model	Andor IKONL BEX2 DD	FLI ProLine PL3041-BB
Array size	2048×2048 pixels	2048×2048 pixels
Pixel size	13.5 μm	15 μm
Pixel scale	0.60 arcsec/pixels	0.65 arcsec/pixels
Field of view	20×20 arcmin	22×22 arcmin
Full well	100,000 electrons	100,000 electrons
Gain	1.1 él/ADU	1.1 él/ADU
Peak QE	90%	96%
Read-out modes	1MHz, 3MHz, 5MHz	1×1MHz, 1×2MHz, 2×2MHz
Read-out noise	7e, 12e, 32e	9.5e, 14e, 14e
Read-out time	5s, 3s, 1.8s	6s, 4s, 2s
Dark current	0.15 e/s/pixel at -65C	0.1 e/s/pixel
Cooling	-100°C	-55°C
Temperature stability	0.1°C	0.1°C
The filter Wheel		
Filters (wheel 1)	B, V, Rc, Ic, I+z, z, Exo	B, V, Rc, Ic, I+z, z, Exo, H_2O^+, NaI
Filters (wheel 2)	OH, NH, CN, C_3, BC, C_2, GC, RC	OH, NH, CN, CO^+,C_3, BC, C_2, GC, RC, UC
Dome		
Type (Diameter)	Gambato Dome (4.2m)	Ash-Dome REB (5.0m)

are populated in each vibrational level and multiple vibrational bands overlap in wavelength with comparable band intensities. The C_3 filter includes a single band complex whose wings stretch from approximately 3400 to 4400 Å. Only two of the four primary C_3 peaks are included, because the short wavelength cutoff of the C_3 filter was chosen to avoid the CO^+ (3-0) band near 4000 Å. The C_2 filter is slightly wider than the rest of filters at the blue end isolating the $\Delta v = 0$ bands centered around 5141 Å. TS is equipped with more three filters to isolate the ions CO^+[4270 Å] and H_2O^+[7050 Å], to study the ion tail of comets, and NaI[5890 Å] filter to study the sodium tail or observations of the Io moon of Jupiter. The CO^+ 2-0 band at 4260 Å was selected to avoid the stronger band at 4010 Å which overlaps with the C_3 band complex, while other bands either are weaker or have more contamination than the 4260 Å band. The CO^+ filter avoids the CN(Δv=-1) band at the blue end and CH emission at the red end, but is contaminated by the long red-ward wing of C_3. The H_2O^+ was designed to isolate the (0,6,0) band centered near 7010 Å. More characteristics about these filters are given in Table 2.2 and illustrated in Figure 2.4.

The continuum filters have to be large enough to provide significant signal but avoid gas contamination at the same time. The UV continuum (UC) filter was designed and placed at 3448 Å closer to the OH and NH bands, it is contaminated by weak OH and CO_2^+ emission but C_3 remains the primary contaminant. For these reasons, we decided to not use this filter to evaluate the dust proxy in comets included in this work. The red continuum (RC) filter was constructed and centered at 7128 Å, to avoid the H_2O^+ emission at the blue end and a telluric H_2O feature at the red end. The blue continuum (BC) filter was centred at 4450 Å,

Table 2.2: Characteristics of HB narrow-band comet filters.

Species[a]	Filter	Wavelength central[b] (Å)	FWHM[c] (Å)	Transmission[d] (%)
OH (0-0)	OH	3090	62	56
NH (0-0)	NH	3362	58	63
UV Continuum	UC	3448	84	67
CN ($\Delta v = 0$)	CN	3870	62	67
C_3 (Swings system)	C_3	4062	62	62
CO^+ (2-0)	CO^+	4266	64	77
Blue Continuum	BC	4450	67	65
C_2 ($\Delta v = 0$)	C_2	5141	118	85
Green Continuum	GC	5260	56	78
H_2O^+ (0,6,0)	H_2O^+	7020	170	75
Red Continuum	RC	7128	58	80
Sodium	NaI	5890	30	70

[a]Emission band designations in parentheses, [b]Measured center wavelength,[c]Measured full-width power points, and [d]Measured mean peak transmission.

between the CO^+ and C_2 bands, to avoid the C_2 emission. Because it is less contaminated, we decided to use the blue filter (BC) continuum for the subtraction of dust from the gas filters. The green continuum (GC) filter was designed and centered at 5260 Å, just red-ward of the C_2 (Δv = 0) band, to reduce the C_2 contamination and avoids most NH_2 emission. TRAPPIST is also equipped with broad-band B, V, Rc, and Ic Johnson-Cousin filters (Bessell, 1990). The broad-band filters have a large bandpass and contain some gas emission bands. The B filter bandpass encompasses the emissions of CN, C_3 and C_2 and the V filter is contaminated by the emission of C_2, while Rc and Ic are less contaminated by gas emissions. In this work, we use Rc and Ic filters to compute the Afρ parameter (see section 2.3.3). Both TRAPPIST equipped with I+z, z, and Exo filters that we use for exoplanet observations program.

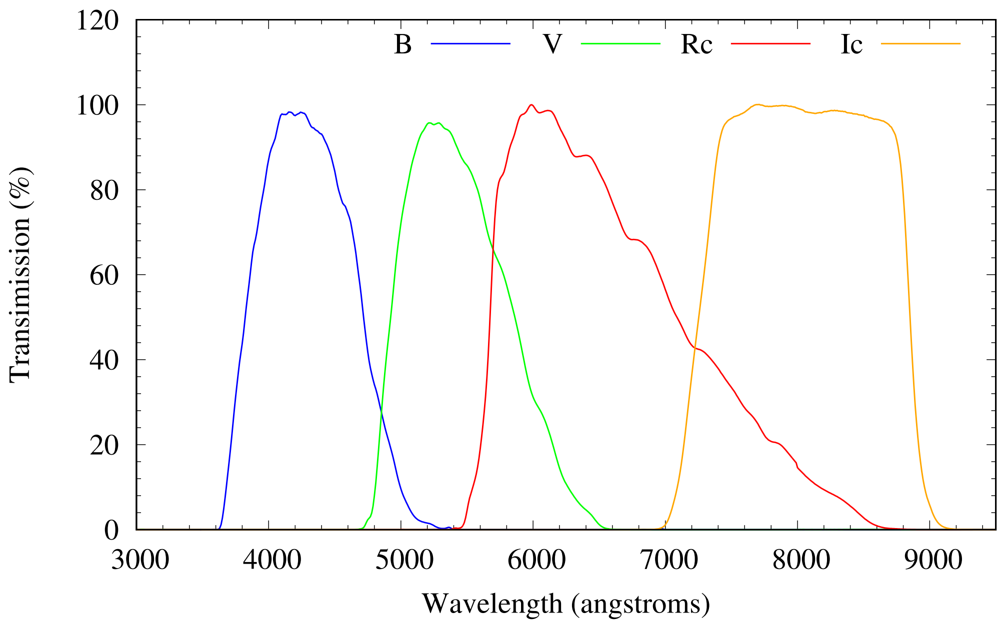

Figure 2.3: Transmission profiles for the Johnson/Cousins B, V, Rc, and Ic filters.

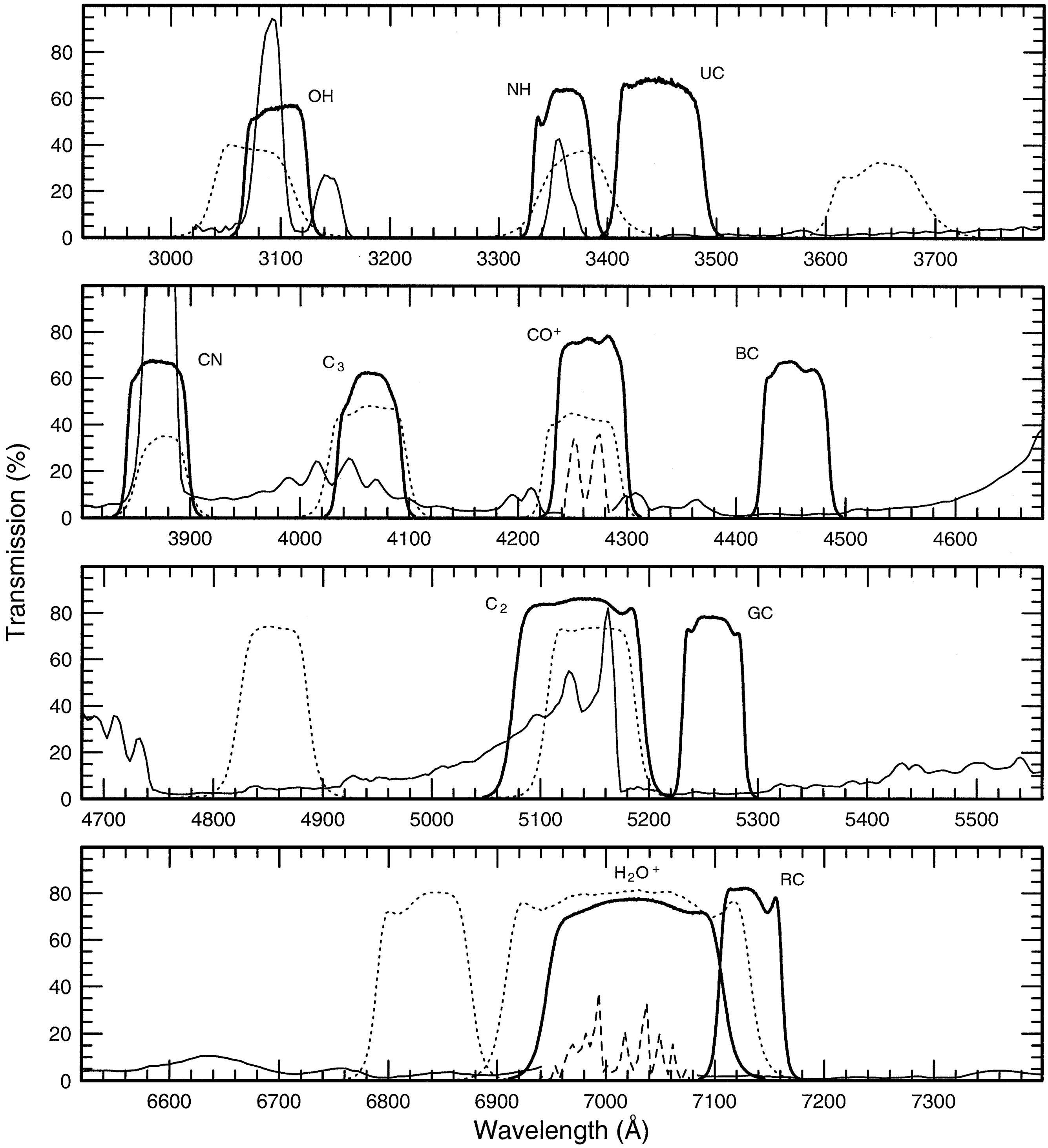

Figure 2.4: Transmission profiles for the HB filters (thick lines) compared to the sets used in the International Halley Watch (IHW) in 1982 (dotted lines). For comparison, some measured comet spectra illustrate the locations of the different emission bands. In the three top panels, a spectrum of comet 122P/deVico (resolution ∼12 Å) is represented (solid lines), while the spectrum of Comet 8P/Tuttle (resolution ∼40 Å) is illustrated in the bottom panel (thin solid lines) (Farnham et al., 2000).

2.2 The TRAPPIST database (2017-2020)

With TRAPPIST telescopes, we collected in the period of 2017-2020 (47 months) a data set of 35 comets including 18 JFCs and 16 LPCs in addition to the first interstellar comet 2I/Borisov. Figure 2.5 shows the number of nights as well as the number of images collected for each comet with the two telescopes. Table 2.2 summarizes the sample of comets observed from 2017 to 2020, their dynamical type, as well as their orbital elements and the ranges of distances and dates over which each comet was observed.

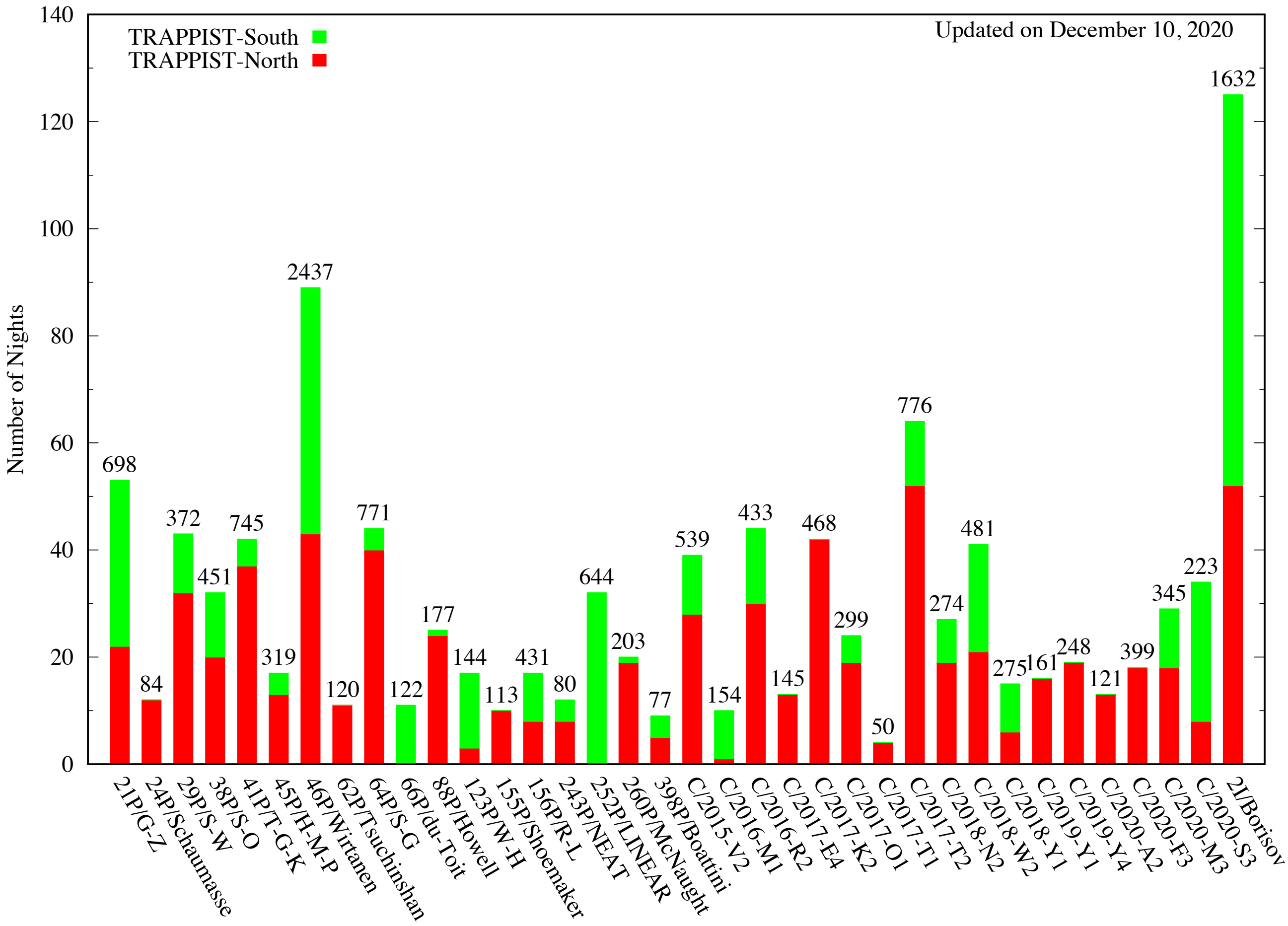

Figure 2.5: Number of comets observed with TRAPPIST telescopes in the period of 2017-2020. The numbers on the top of the bars are the numbers of NB and BB images taken for each comet.

Thanks to the large amount of observing time available for comets program with TRAPPIST, we could follow the evolution of the activity and composition of bright comets ($V_{mag} \leq 12$) for several months around their orbit. As mentioned above, we collected images in both narrow-band and broad-band filters in order to compute the production rates of several gas species (OH, NH, CN, C_3, and C_2) as well as dust proxy (Afρ parameter). With an average of 8 bright comets observed every year, we collected a homogeneous sample of comets (JFCs and LPCs) to study their activity and composition evolution during their journey around the Sun. With this sample of comets, we try to determine their chemical properties and classification in order to understand the origin of their composition. TRAPPIST also provides data of bright and faint comets to support the observations with larger telescopes. With TRAPPIST, we can make a follow-up observations of comets that show suddenly an outburst or fragmentation event. In the next chapter, we will discuss the activity and composition of the individual and ensemble comets observed with TRAPPIST and more details about these observations for each comet will be given later.

It is very important to describe our observing strategy in order to explore any selection effects that could affect our sample. First, we observe the comet with the broad-band filters and try to get the CN and C_2 emission. Since we got these emissions, we collect images in the rest of narrow-band filters (C_3, NH and OH). The observation continues on the comet twice a week with all the filters until the comet gets fainter and no gas emissions are detected. Several comets, including JFCs and LPCs, were monitored extensively given their brightness which allow us to investigate their coma morphology or they made a very close approach to the Earth which allows us to reveal their rotation period. CN, C_2 and Rc images series were taken, for many hours at the same night, for several comets (41P, 46P, 252P, etc) in order to derive the rotation period of the nuclei from the flux light-curve variation or from the rotation of jets in their coma. Some very bright comets were observed simultaneously with observations made at different wavelengths with large telescopes (i.e, 21P and 46P). During 4 years of observations with both TRAPPIST, we collected more than 15 000 broad- and narrow-band images of 35 comets with different dynamical types. These comets were observed over more than 680 nights with TN and 420 nights with TS. The number of observations and nights of a given comet varies considerably. As an example, we collected more than 2400 images of comet 46P/Wirtanen over 90 nights with both telescopes as it was well visible in both hemispheres. 2I/Borisov was the most observed comet in our database with more than 1600 images taken over 120 nights. The interstellar comet was observed almost every night from the time of its discovery. Some comets were observed only for few nights due to their lower visibility and brightness. We observed comets over a wide range of heliocentric distances from 0.55 au for comet C/2017 E4 (Lovejoy) to 12.90 au for the most distant active comet C/2017 K2 (PANSTARRS). But 80% of the observations are concentrated between 1 and 2 au.

Comets	Type	e	i (°)	P (yr)	T_j	Peri (au)	tp (UTC)	r_h-range Pre/Post	Dates Start/End	Telescope TN/TS
21P/Giacobini-Zinner	JFC	0.71	31.99	6.54	2.46	1.01	2018 Sep. 10	1.61-1.01-2.10	09.06.18/04.02.19	TN & TS
24P/Schaumasse	JFC	0.70	11.73	8.26	2.50	1.20	2017 Nov. 16	1.23-1.20-1.47	30.10.17/22.01.18	TN
29P/Schwassmann-Wachmann 1	JFC	0.04	9.39	14.66	2.98	5.72	2019 Mar. 07	[5.77-5.78	25.10.18/07.11.19	TN & TS
38P/Stephan-Oterma	HTC	0.86	18.36	37.84	1.89	1.58	2018 Nov. 10	1.64-1.59-1.92	07.10.18/09.03.19	TN & TS
41P/Tuttle-Giacobini-Kresak	JFC	0.66	9.23	5.42	2.83	1.04	2017 Apr. 12	1.27-1.05-1.63	16.02.17/20.07.17	TN & TS
45P/Honda-Mrkos-Pajdusakova	JFC	0.82	4.23	5.26	2.58	0.53	2016 Dec. 31	[0.97-1.56	10.02.17/25.03.17	TN & TS
46P/Wirtanen	JFC	0.66	11.74	5.44	2.82	1.05	2018 Dec. 12	2.08-1.06-1.30	13.07.18/08.02.19	TN & TS
62P/Tsuchinshan 1	JFC	0.59	9.70	6.39	2.79	1.38	2017 Nov. 18	1.40-1.38-1.57	31.10.17/21.01.18	TN
64P/Swift-Gehrels	JFC	0.68	8.94	9.40	2.49	1.39	2018 Nov. 04	1.70-1.39-2.09	15.08.18/20.03.19	TN
66P/du Toit	JFC	0.78	18.66	14.77	2.12	1.28	2018 May. 20	1.30-1.28-1.49	06.05.18/14.07.18	TS
88P/Howell	JFC	0.56	4.38	5.48	2.94	1.35	2020 Sep. 28	1.87-1.35-1.54	25.05.20/02.12.20	TN & TS
123P/West-Hartley	JFC	0.44	15.35	7.58	2.83	2.12	2019 Feb. 05	2.13-1.12-2.31	17.01.19/01.06.19	TS
155P/Shoemaker 3	JFC	0.72	6.39	16.94	2.32	1.80	2019 Nov. 14	1.83-1.80]	16.10.19/06.11.19	TN
156P/Russell-LINEAR	JFC	0.62	18.44	6.43	2.71	2.12	2020 Nov. 12	1.40-1.30-1.38	10.11.20/15.12.20	TN & TS
243P/NEAT	JFC	0.36	7.63	7.50	2.94	2.45	2018 Aug. 26	[2.56-2.72	15.12.18/26.02.19	TN & TS
252P/LINEAR	JFC	0.67	10.42	5.32	2.82	0.99	2016 Mar. 15	1.14-1.00-1.50	04.02.16/08.06.16	TS
260P/McNaught	JFC	0.59	15.75	7.05	2.71	1.49	2019 Sep. 09	[1.45-1.83	06.10.19/25.12.19	TN
398P/Boattini	JFC	0.58	10.97	5.56	2.90	0.40	2020 Dec. 26	1.40-1.30-1.32	10.11.20/24.12.20	TN & TS
C/2015 V2 (Johnson)	HPC	1.00	49.89	-	3.34	1.63	2017 Jun. 12	2.25-1.64-1.80	13.02.18/06.08.18	TN
C/2016 R2 (PANSTARRS)	LPC	1.00	58.22	>200	1.06	2.60	2018 May. 09	2.95-2.60-5.58	26.12.17/03.10.19	TN & TS
C/2016 M1 (PANSTARRS)	LPC	1.00	91.00	>200	-0.02	2.21	2018 Aug. 10	2.45-2.21-2.40	09.05.18/11.08.18	TS
C/2017 E4 (Lovejoy)	LPC	1.00	88.18	>200	0.03	0.49	2017 Apr 23	[0.82-0.55	26.03.17/13.04.17	TN
C/2017 K2 (PANSTARRS)	HPC	1.00	87.54	-	0.17	1.80	2022 Dec. 20	12.89-7.62]	06.11.18/07.12.20	TN
C/2017 O1 (ASASSN)	LPC	1.00	39.85	>200	1.17	1.50	2017 Oct 14	1.83-1.50-1.93	31.01.17/12.01.18	TN & TS
C/2017 T1 (Heinze)	HPC	1.00	96.83	-	3.03	0.58	2018 Feb. 21	1.29-0.58-0.88	27.12.17/21.01.18	TN
C/2017 T2 (PANSTARRS)	HPC	1.00	57.23	-	0.85	1.61	2020 May. 05	3.70-1.61-2.11	04.08.19/15.08.20	TN
C/2018 N2 (ASASSN)	HPC	1.00	77.53	-	0.47	3.12	2019 Nov. 10	3.28-3.12-3.23	28.07.19/04.02.20	TN & TS
C/2018 Y1 (Iwamoto)	LPC	0.98	160.40	>200	-1.28	1.28	2019 Feb 07	1.38-1.28-1.43	05.01.19/21.03.19	TN & TS
C/2018 W2 (Africano)	LPC	1.00	116.61	>200	-0.66	1.45	2019 Sep. 05	1.71-1.45-1.55	03.07.19/14.10.19	TN & TS
C/2019 Y4 (ATLAS)	LPC	1.00	45.38	>200	0.45	0.25	2020 May. 31	2.50-0.81]	27.01.20/03.05.20	TN
C/2020 A2 (Iwamoto)	LPC	1.00	120.74	>200	1.12	0.98	2020 Jan. 08	[1.05-1.70	30.01.20/01.04.20	TN
C/2020 F3 (NEOWISE)	LPC	1.00	128.93	>200	-0.40	0.29	2020 Jul. 03	[0.63-1.61	22.07.20/10.09.20	TN
C/2020 M3 (ATLAS)	LPC	1.00	23.47	>200	1.46	1.26	2020 Oct. 25	1.43-1.26-1.54	11.09.20/24.12.20	TN & TS
C/2020 S3 (Erasmus)	LPC	1.00	19.86	>200	0.76	0.40	2020 Dec. 12	1.68-0.84]	27.09.20/01.12.20	TN & TS
2I/Borisov	ISO	3.35	44.05	-	2.38	2.00	2019 Dec. 08	2.80-2.00-3.04	11.09.19/21.03.20	TN & TS

Note: JFC: Jupiter Family Comet, HPC: Hyperbolic Comet, HTC: Halley Type Comet, LPC: Long Period Comet, ISO: Interstellar Object, e: Eccentricity, i: Inclination, P: Orbital period, T_j: Jupiter Tisserand invariant, Peri: Perihelion distance, t_p: Time of perihelion passage. For r_h-range, "]" for pre-perihelion and "[" for post-perihelion. The format of the date is Day.Month.Year

2.3 Data reduction and analysis of the TRAPPIST data

2.3.1 Basic reduction and flux calibration

We followed the standard procedures to reduce all the TRAPPIST comet images, and we used custom-made routines based on the Image Reduction and Analysis Facility (IRAF) software (Tody, 1986, 1993) to correct the bias, dark, and sky flatfield frames. Bias is the term used to describe a CCD camera's electronic offset above the zero level. Each pixel has a slightly different base value, due to read out noise. This zero level is removed using a bias frame which is taken with an exposure of zero second. Dark frames are used to correct the CCD image so called thermal dark current, which is dependent primarily on the temperature of the camera. A dark frame is taken at the same temperature as the science image and with the same exposure time, making it possible to subtract this thermal signal from the image. Sky flats images are used to remove image artifacts due to the optical system. Vignetting and shadows from out-of-focus dust specks are the most common aberrations which flats eliminate. A flat is a blank, evenly illuminated image which will show the variations in brightness due to the optical system. We combine calibration frames over a week, by taking the median to create master bias, flat, and dark frames, to reduce the noise introduced by the data reduction and avoiding changes in the flatfield frames aspect due to the apparition of new specks of dust. Figure 2.6 shows the three calibration images taken with TRAPPIST-North.

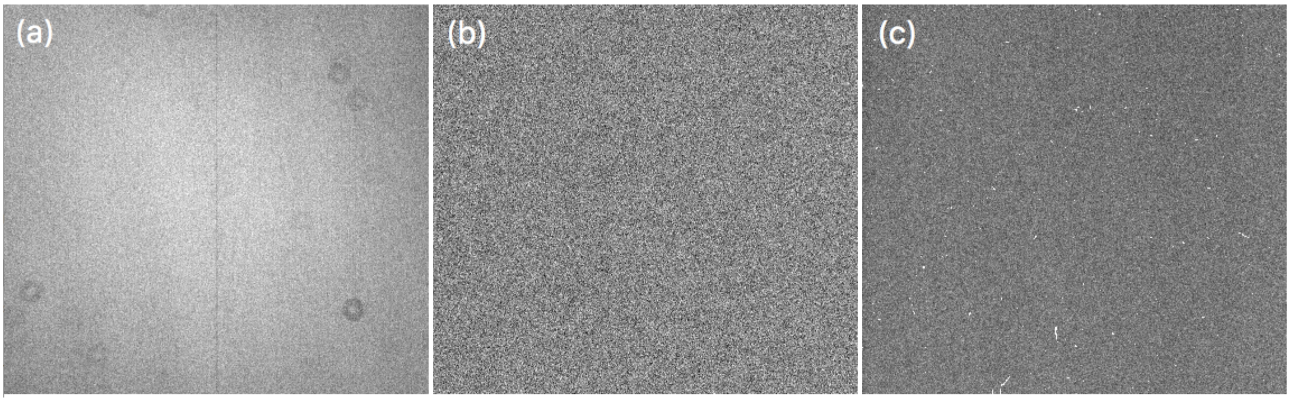

Figure 2.6: Examples of TRAPPIST-North calibration images: (a) Flatfield in C_2 filter, (b) Bias and (c) Dark.

The first basic reduction of the images is to subtract the master bias and the master dark from the raw images of the comet and then divide by the master flatfield (normalized to 1) corresponding to the filter used. The final images must be cleaned from the instrumental effects. Figure 2.7 shows two Rc images of comet 398P/Boattini before and after the basic reduction.

The next step is to remove the sky contribution which is coming mainly from atmospheric activity and moon contamination, which are variable and depend on the wavelength. The subtraction of the sky background has to be done with great care for extended objects, especially when the comets extend over the whole field of view and it is then difficult to determine the value of the sky background in the image. As TRAPPIST has a large field of view ($22' \times 22'$), it was always possible to determine the sky contribution from parts of the image which did not contain any cometary contribution. After determining the center of the coma, we search for the closest parts that is free of cometary emission around the coma in the same image. Then, we measure the median sky level in this area and subtract it from the whole image.

We derive the median radial brightness profiles from the gas and dust images. Usually, we acquired images in the continuum dust filter during the same night as the gas images to avoid

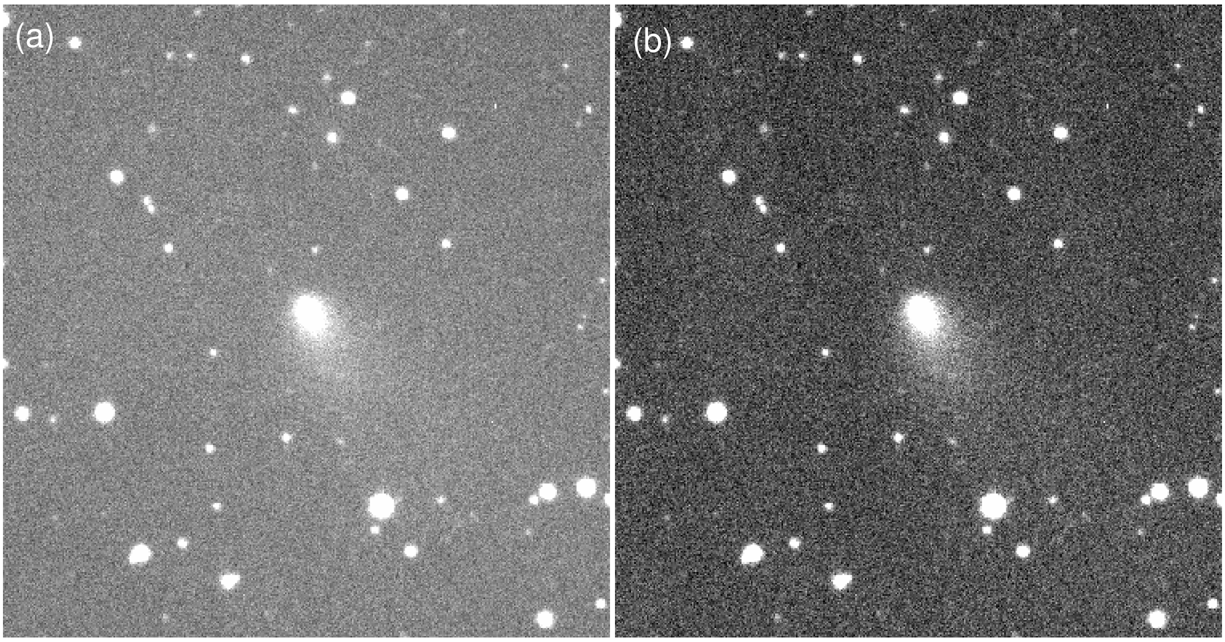

Figure 2.7: Rc image of comet 398P/Boattini before (a) and after (b) the basic reduction.

changes in the observing conditions. For the dust subtraction, we used BC images which is less contaminated by cometary gas emission compared to other dust filters. Then, we subtract the dust radial profile from the gas radial profiles by scaling it with a factor (f_c) depending on the degree of the contamination in the gas filter. The C_3 and C_2 filters are the most contaminated, while the dust contamination in the OH, NH, and CN filters is much lower.

In order to compute the physical flux in our images, we need to convert the pixel values (in ADU/s) to flux in a physics unit $erg/cm^2/s/\text{Å}$. More details on the flux calibration process using standard stars were explained by Farnham et al. (2000). They observe stars whose magnitudes and flux are known in the spectral band of the cometary filters. They generated the coefficients to convert the flux from $ADU/arsec^2/s$ to $erg/cm^2/s/\text{Å}$.

$$F_c = F_0 * F * 10^{0.4(K*am-25+ZP)} \tag{2.1}$$

where am is the airmass, K is the extinction coefficients, ZP aree the Zero Points of a star at magnitude 0 for the corresponding filter. F_0 is the star flux at magnitude 0 in $erg/cm^2/s/\text{Å}$. F is the molecule flux in $ADU/arcsec^2$/s, and F_c is the molecule flux in $erg/cm^2/s/\text{Å}/arcsec^2$. Table 2.3 shows the quantities of the different parameters for each filter. Note that the ZP values shown in the table 2.3 correspond to February 2017. We frequently observed standard stars provided by Farnham et al. (2000) to compute and update the new zero points for different filters. We use median values of these coefficients over a month, since we have noticed that zero points values were not changing over these timescales. Figures 2.8 and 2.9 show the long-term evolution of the zero points measured for TN and TS, respectively. Generally, the zero points do not vary significantly on large time-scales for both telescopes.

Table 2.3: Narrow-band filters calibration coefficients from Farnham et al. (2000). F_{0XX} is the flux of star at magnitude 0 in erg cm^{-2} s^{-1} Å. $m_{\odot xx}$ is the solar color index. γ' is the fraction of the emission band encompassed in the filter and γ its normalization by the filter width and transmission characteristics. f_c is the scaling factor for dust subtraction, K is the extinction coefficient, Zero points are given for broad- and narrow-band filters of TN and TS on September 2019.

Species	F_{0XX} ($\times 10^{-9}$)	$m_{\odot XX}$	$\gamma_{XX/XX}$	$\gamma'_{XX/XX}$	K	Zero points TN	TS
OH	10.56	1.791	1.698×10^{-2}	0.98	1.60	7.540	7.005
NH	8.42	1.188	1.907×10^{-2}	0.99	0.65	7.081	6.522
CN	8.60	1.031	1.812×10^{-2}	0.99	0.36	5.716	5.994
C_3	8.16	0.497	3.352×10^{-3}	0.19	0.29	5.552	5.936
C_2	3.88	-0.423	5.433×10^{-3}	0.9	0.15	4.990	5.223
BC	6.21	0.000	–	–	0.25	5.651	6.170
GC	3.61	-0.507	–	–	0.14	5.900	6.175
RC	1.31	-1.276	–	–	0.05	6.251	6.668
B	6.40	0.000	–	–	0.25	2.262	2.631
V	3.67	-0.649	–	–	0.14	2.434	2.752
Rc	1.92	-1.019	–	–	0.098	2.068	2.543
Ic	0.94	-1.375	–	–	0.043	2.567	3.177

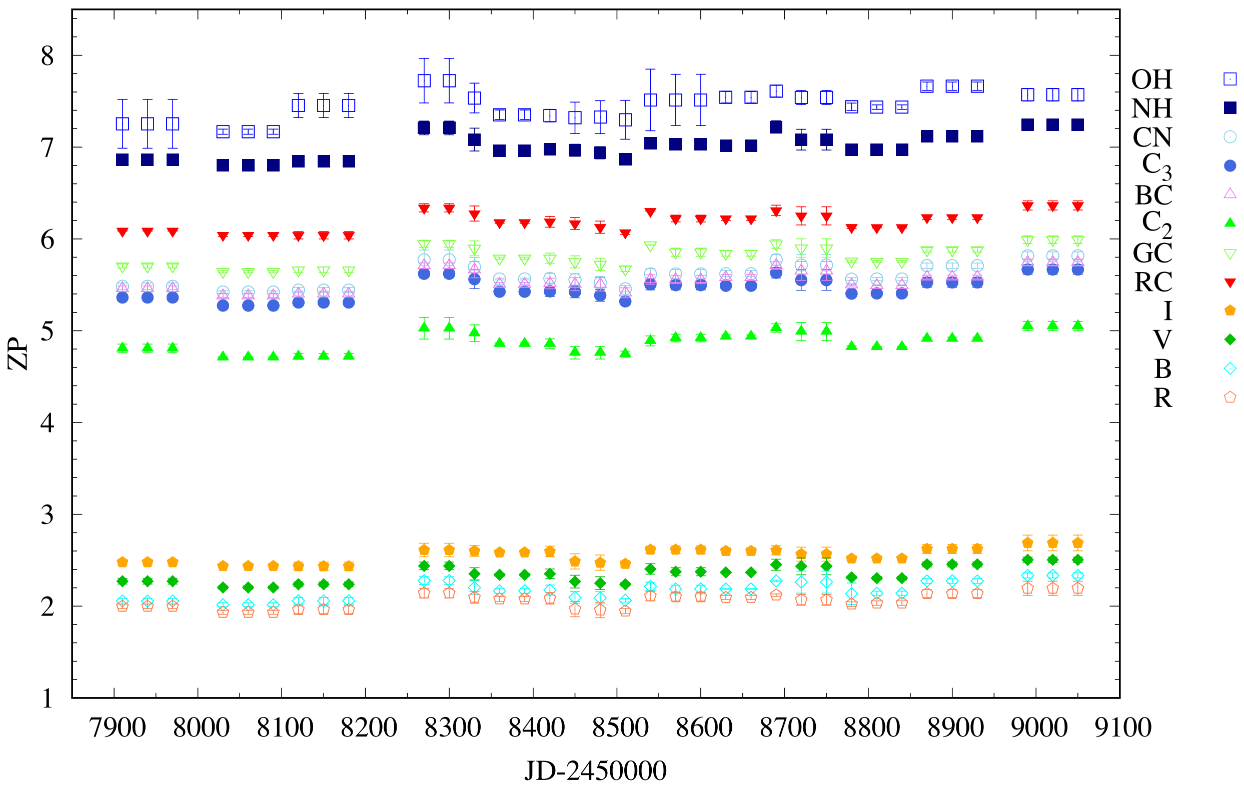

Figure 2.8: Evolution of zero points of broad- and narrow-band filters equipped with TN between June 2017 and July 2020.

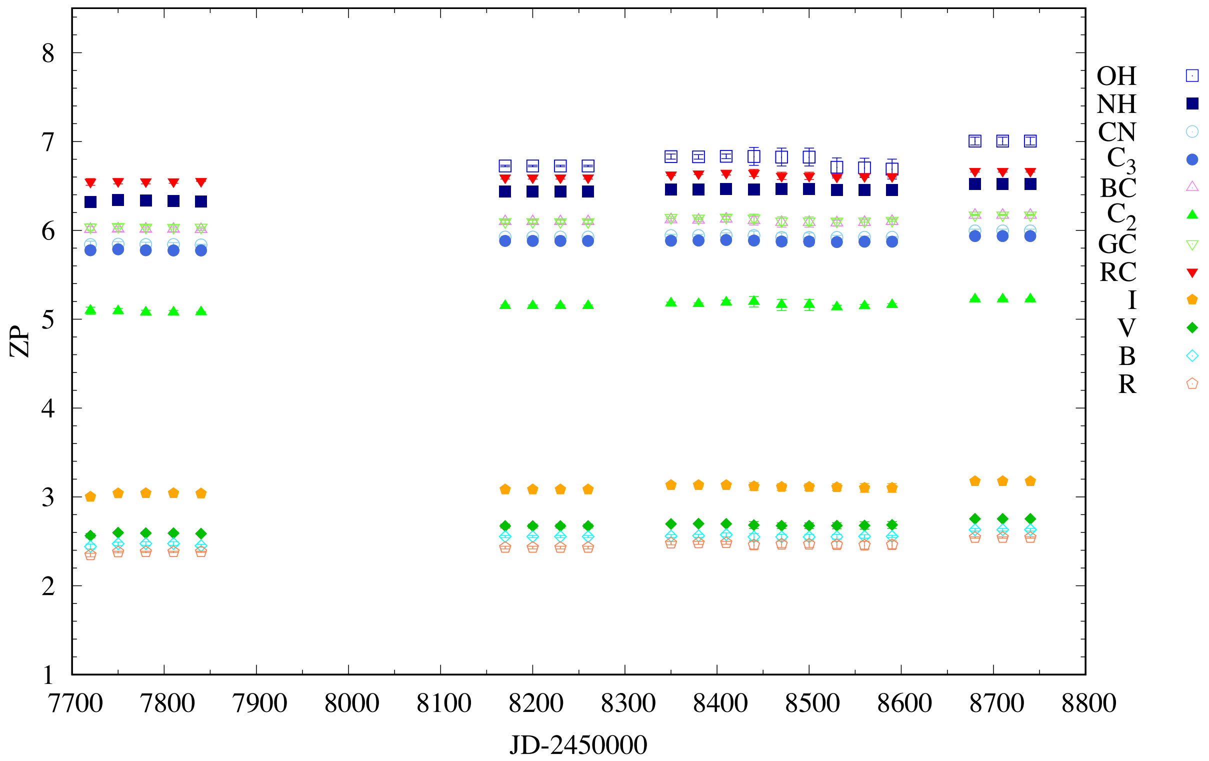

Figure 2.9: Evolution of zero points of broad- and narrow-band filters equipped with TS between January 2017 and October 2019.

2.3.2 The production rates with the Haser Model

In order to derive the production rates for different daughter molecules, we adjust the column densities profiles with a Haser model (Haser, 1957). This rather simple model is based on a number of assumptions. The comet has a spherical nucleus of radius r_n, its activity is due to the solar radiation. The molecules are ejected from the nucleus's surface in radial direction with a constant radial velocity v_0. The parent molecules are photo-dissociated in a one-step process to form daughter molecules, and each daughter molecule corresponds to only one parent molecule. The molecules are disintegrated by photo-dissociation following the law :

$$n = n_0.e^{\frac{-t}{\tau_p}} \tag{2.2}$$

where n_0 is the number of molecules at a time zero and τ_p is the molecule lifetime.

First, we compare the gas production rate with the molecules flux on the surface, so we have:

$$Q_n = \phi(0) \tag{2.3}$$

The coma symmetry is considered spherical and the molecules velocity follow the radial direction. The molecules flux at the distance r from the nucleus is given by the integration of the quantity $n_p(r).\vec{v}_p$ on the sphere of radius r.

$$\phi(r) = v_p.n_p(r).4\pi r^2 \tag{2.4}$$

The flux $\phi(r)$ is not conservative. So, the flux at distance r from the nucleus is given by :

$$\phi(r) = \phi(0)e^{\frac{-t}{\tau_p}} \tag{2.5}$$

According to equality of equations (2.5) and (2.4), the distribution of parent molecules density is :

$$v_{exp}.n_p(r).4\pi r^2 = Q_n e^{\frac{-t}{\tau_p}} \tag{2.6}$$

$$n_p(r) = \frac{Q_n}{4\pi r^2 v_p} e^{\frac{-t}{\tau_p}} \tag{2.7}$$

Or

$$n_p(r) = \frac{Q_n}{4\pi r^2 v_p} e^{\frac{-r}{L_p}} \tag{2.8}$$

where L_p is the parent molecules scale-lengths given by $L_p = v_p \tau_p$, τ_p is the parent molecules life time, proportional to the square of the heliocentric distance r_h^2.

$N_p(r_n)$ is the number of parent molecules produced at a distance r$_n$ from the nucleus per second and per cm, $N_p(\rho)$ is the same quantity at distance ρ from the nucleus. Using (2.2), the total number of parent molecules at ρ is given by:

$$4\pi\rho^2 N_p(\rho) = 4\pi r_n^2 N_p(r_n) e^{-\frac{\rho - r_n}{L_p}} \tag{2.9}$$

The daughter molecules are then photo-dissociated by the UV solar radiation with a scale-length of $L_d = v_d.\tau_d$.

For the daughter molecules, we derive the equation (2.9) with respect to the ρ :

$$-\frac{d}{d\rho}(4\pi\rho^2 N_p(\rho)) = 4\pi r_n^2 N_p(r_n) \frac{1}{L_p} e^{-\frac{\rho - r_n}{L_p}} \tag{2.10}$$

The number of daughter molecules produced at a distance ρ from the nucleus has decreased by a factor $e^{-\frac{r-\rho}{L_d}}$. Then, the molecules flux in $[\rho, \rho + d\rho]$ is given by:

$$d\phi_p(r) = 4\pi r_n^2 N_p(r_n) \frac{1}{L_p} e^{-\frac{\rho - r_n}{L_p}} e^{-\frac{r-\rho}{L_d}} \tag{2.11}$$

By integration on $d\rho$

$$\phi_p(r) = 4\pi r^2 N_p(r) = \int_{r_n}^{r} 4\pi r_n^2 N_p(r_n) \frac{1}{L_p} e^{-\frac{\rho - r_n}{L_p}} e^{-\frac{r-\rho}{L_d}} d\rho \tag{2.12}$$

and using :

$$N_d(r) = v_d n_d(r) \qquad\qquad Q_n = 4\pi r_n^2 N_p(r_n)$$

The daughter molecules density is :

$$n_d(r) = \frac{Q_n}{4\pi v_d r^2} \frac{L_d}{L_p - L_d} (e^{\frac{-r}{L_p}} - e^{\frac{-r}{L_d}}) \tag{2.13}$$

Generally, the density distribution of molecules in the coma of comet is given by:

$$n(r) = \frac{Q}{4\pi v r^2} \frac{\beta_0}{\beta_1 - \beta_0} (e^{-\beta_0 r} - e^{-\beta_1 r}) \tag{2.14}$$

where $\beta_0 = \frac{1}{L_d}$ for parent molecules and $\beta_1 = \frac{1}{L_p}$ for daughter species

Equation 2.14 must then be integrated along the line of sight to obtain the column density $N(r)$ that can in turn be linked to the brightness profile. This integration can be done in two different ways: analytic integration or numeric integration.

For the analytic method, the column density $N(r)$ is the density distribution of molecules $n(r)$ integrated along the line of sight (Biver, 2011).

For the parent molecules :

$$N(r) = \frac{2Q}{4\pi v}\frac{1}{r}\int_{\beta_1 r}^{\infty} K_0(x)\,\mathrm{d}x \tag{2.15}$$

For the daughter molecules :

$$N(r) = \frac{2Q_n}{4\pi v}\frac{\beta_0}{\beta_1 - \beta_0}\frac{1}{r}\int_{\beta_1 r}^{\beta_0 r} K_0(x)\,\mathrm{d}x \tag{2.16}$$

where ρ is the distance from the nucleus, and $K_0(x)$ is the modified Bessel function of the second kind with $\int_0^{\infty} K_0(x)\,\mathrm{d}x = \frac{\pi}{2}$.

The numeric method consists of a direct numeric integration along the line of sight of the molecules density.

$$N(r) = \frac{Q}{4\pi v}\int_{-z}^{z} e(r)\,\mathrm{d}z \tag{2.17}$$

where $e(r)$ is the emissivity defined by :

$$e(r) = \frac{1}{r^2}\frac{\beta_0}{\beta_1 - \beta_0}(e^{-\beta_1 r} - e^{-\beta_0 r}) \tag{2.18}$$

The column density is linked to the flux per solid angle unit by:

$$N(r) = \frac{4\pi}{g}\frac{1}{\Omega}F \tag{2.19}$$

where F is the flux observed in solid angle Ω, g (or g-factors) represents the number of photons per second scattered by a single atom or molecule exposed to the unattenuated sunlight (Swamy, 2010) which is used to convert the flux to column density :

$$g_\lambda = \lambda^2 f_\lambda F_\lambda \frac{\pi e^2}{m_e c^2}\frac{A_{ik}}{\sum_k A_{ik}} \tag{2.20}$$

where F_λ is the solar flux per unit of wavelength at 1 au and f_λ is the oscillator strength. A_{ik} are the Einstein coefficients. The term $\frac{A_{ik}}{\sum_k A_{ik}}$ represents the fraction of photons emitted from the energy level i to the energy level k relative to all the photons emitted from the energy level i. Factors e and m_e are the charge and mass of an electron, respectively.

The fluorescence efficiency values used in this work for the different gas filters are taken from Schleicher's website[2]. The C_2 g-factors have a single value for the Δv=0 band sequence with a band head near 5160 Å, and it is scaled by r_h^{-2} (A'Hearn et al., 1984). The C_3 g-factor has a single value for the C_3 band complex which peaks near 4030 Å and extends from 3300 to

[2]Comet fluorescence efficiency: http://asteroid.lowell.edu/comet/gfactor.html

4400 Å. The C_3 fluorescence efficiencies are scaled by r_h^{-2} and are taken from A'Hearn (1982). The CN and NH fluorescence efficiencies vary with both the heliocentric velocity and distance because of the strong change in the number of rotational levels populated with heliocentric distance. The CN and NH g-factors are taken from Schleicher (2010) and from Meier et al. (1998), respectively. The OH g-factor value of the 0-0 band centered near 3090 Å varies with the heliocentric velocity and also depends on whether or not the lambda-doublet ground state is quenched; scaled by r_h^{-2} (Schleicher and A'Hearn, 1988).

Table 2.4 shows the scale-lengths, lifetimes and g-factors of the different molecules at 1 au scaled by r_h^{-2}. The scale lengths are equivalent to the lifetimes of molecules as we are using a constant radial velocity of 1 km/s. We decided to use those given in A'Hearn et al. (1995) for two reasons: First, these values were used for the previous TRAPPIST data analysis and we have to keep the homogeneity of the parameters to allow comparison with previous data sets. Secondly, we compare our production rate ratios for different gas species to those given in the largest sample analysed and published so far (A'Hearn et al., 1995). Figure 2.10 show original CN image of comet 46P/Wirtanen its corresponding radial profile after dust subtraction with Haser Model fit.

Table 2.4: The scale lengths, lifetimes and the fluorescence efficiencies of different molecules at 1 au scaled by r_h^{-2}. The fluorescence efficiencies are taken from Schleicher's website [3].

Molecules	Parent (km)	Daughter (km)	Lifetime (s)	g-factors erg s^{-1} mol^{-1}
OH(0,0)	2.4×10^4	1.6×10^5	1.6×10^5	1.49×10^{-15}
NH(0,0)	5.0×10^4	1.5×10^5	1.3×10^4	6.27×10^{-14}
CN(Δv=0)	1.3×10^4	2.1×10^5	2.1×10^5	2.62×10^{-13}
C_3(λ=4050 Å)	2.8×10^3	2.7×10^5	2.7×10^5	1.00×10^{-12}
C_2(Δv=0)	2.2×10^4	6.6×10^4	6.6×10^4	4.50×10^{-13}

Several models have been proposed to describe the coma, from the most simple models to more complicated physically realistic models. One of these is the Vectorial model which was introduced by Festou (1981a,b). It considers the collisions in the inner coma producing a non-radial motion of the molecules and becomes less important when the cometocentric distance increases. Furthermore, the release of energy when daughter molecules are produced may result in an additional non-radial motion throughout the entire cometary coma. It is noted that a vectorial model appears to be required to represent the density distribution of some radicals. But the Vectorial model has more free parameters, which are usually poorly determined and may be a major source of uncertainty in the determination of the gas-production rates. Most authors are still using the Haser model to derive the production rates. In this work, we decided to use this model to compute the production rates in order to compare our results with others.

Figure 2.11 shows the comparison of Vectorial and Haser models for a similar OH production rate Q(OH)=2.21×10^{27} molecules/s computed for comet 41P/Tuttle–Giacobini–Kresak when it was at 1.12 au from the Sun and at 0.17 au from Earth. The Vectorial model column density can be retrieved online[4]. In order to derive the OH column density profile from the Vectorial model website, we set different parameters. We used the same scale lengths and lifetimes for the Haser model given in Table 2.4. We set the velocities of the parent and daughter molecules to 1 km/s for a heliocentric distance of 1 au. The program internally adjusts the parent molecule velocity with the factor of r_h^{-2}, while the model considered that the daughter molecule velocity

[4]Vectorial model: `http://www.boulder.swri.edu/wvm-2011/`

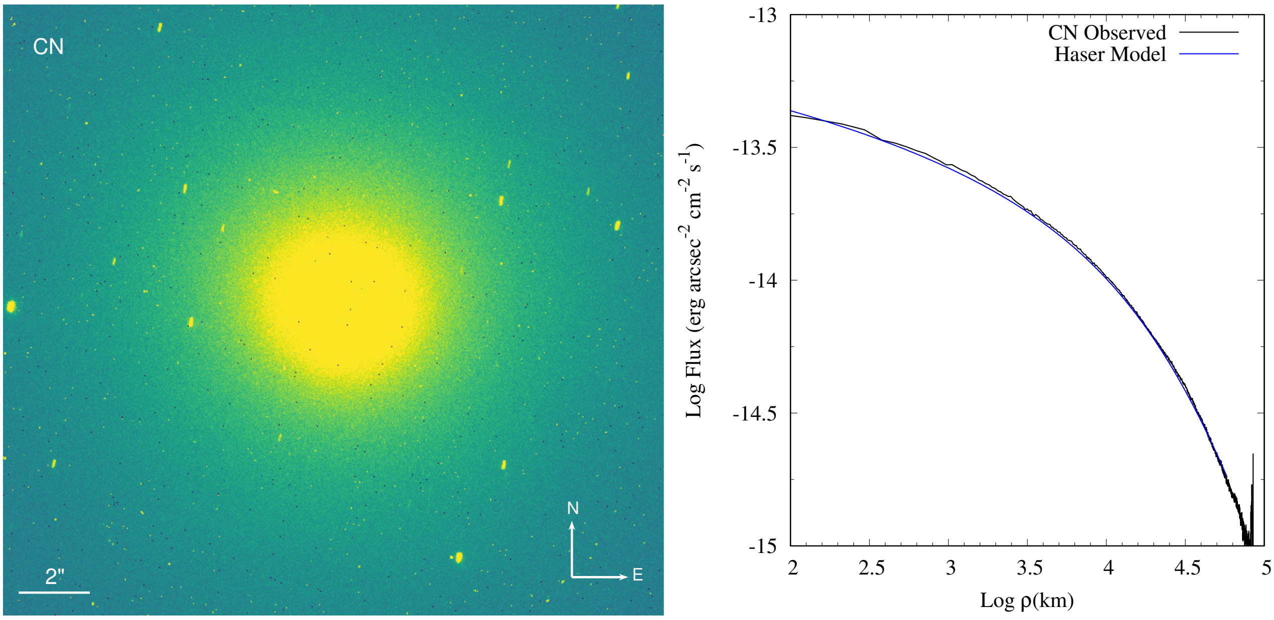

Figure 2.10: Original CN image of comet 46P/Wirtanen taken with TS on December 9, 2018 and its corresponding radial profile after dust subtraction with Haser Model fit.

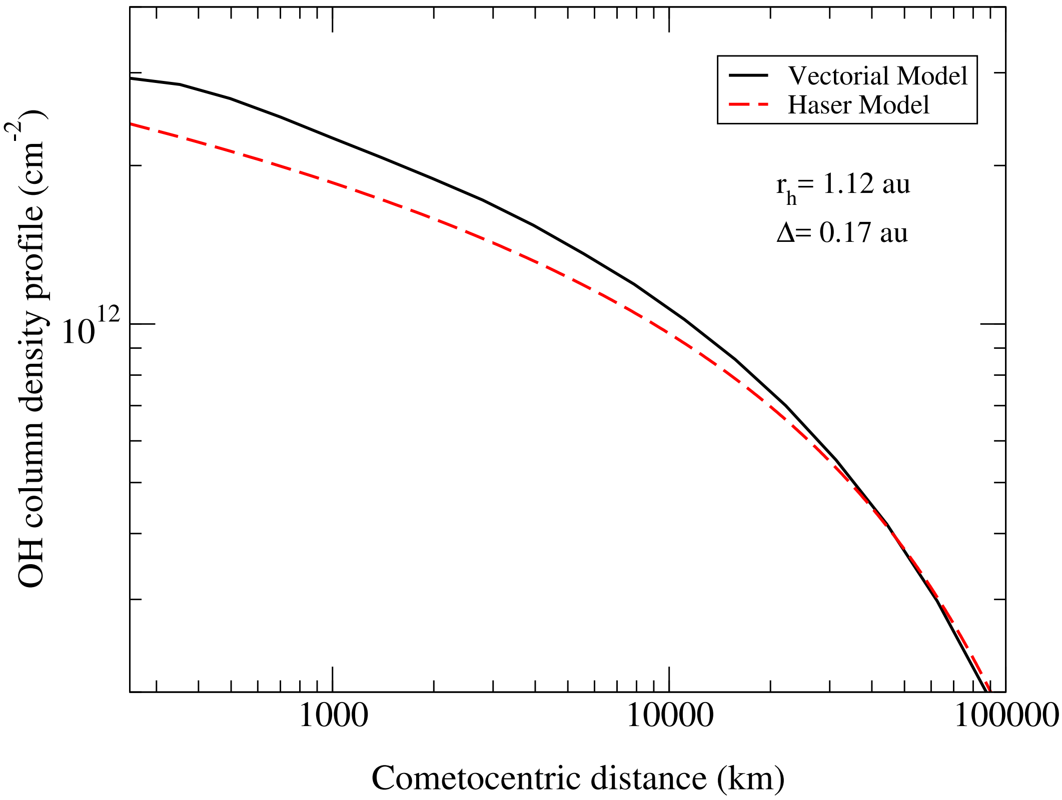

Figure 2.11: Comparison of the OH column density profile of 41P from the Vectorial and the Haser models for a production rate of 2.21×10^{27} molecules/s obtained on March 14, 2017.

is independent of the heliocentric distance and no scaling for distance is made. We followed the same procedure and technique described above to reduce all TRAPPIST images, which provide a high homogeneous data set to study the evolution and composition of comets along their orbits.

2.3.3 The Afρ parameter

We derived the Afρ parameter, introduced by A'Hearn et al. (1984) as a proxy for the dust production, from the dust profiles in the cometary dust continuum BC, GC, and RC filters and the broad-band Rc and Ic filters. $A(\theta)f\rho$ is defined by a product of three parameters. (i) Albedo $A(\theta)$ which depends on the phase angle θ, which is the ratio between the reflected flux in a direction and the incident solar flux; (ii) the filling factor (f) which is defined by the total cross section of grains (red in Fig. 2.12) within the field of view divided by the surface of the aperture ($\pi\rho^2$); (iii) the radius of the aperture (ρ).

$$A(\theta)f\rho = \frac{(2\Delta r_h)^2}{\rho}\frac{F_{com}}{F_{\odot}} \tag{2.21}$$

Δ and r_h are the geocentric and heliocentric distance, respectively. F_{com} is the Solar flux reflected by the dust grains in the aperture for a corresponding band filter ($erg/cm^2/s/$Å) and $F_{\odot}$ is the Solar flux at 1 au[5].

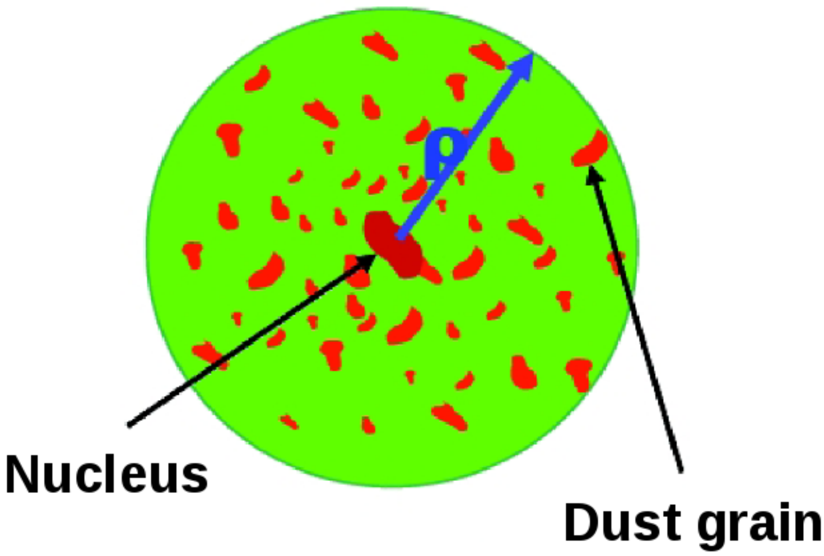

Figure 2.12: Illustration of the dust gains in the coma and the nucleus of a comet. The red features present the grains in the coma with a radius ρ (adapted from Jorda (2010)

In the cometary coma, the brightness of the continuum is affected by the dependence on the solar phase angle of the scattering of sunlight by cometary grains. In all cases, there is a strong increase in the forward direction of scattering, and a much smaller peak at small backscattering angles. In practice these effects can reach up to a factor of three over a range of phase angles between 0° and 110°, and much more at higher phase angles (Schleicher et al., 1998). An early phase function for cometary dust was constructed by Divine (1981), which appears to provide a reasonable match to comet observations between phase angles of ∼15° and 70°. But this phase function is too shallow at smaller phase angles (Ney and Merrill, 1976; Hanner and Newburn, 1989; Schleicher et al., 1998), and does not increase sufficiently fast at large phase angles (Marcus, 2007). In this work, we decided to use the phase function normalized at θ=0° given by Schleicher (2010)[6] to correct for the phase angle effect.

[5]The Solar radiation for each band emission that we used in this work are given at: http://rredc.nrel.gov/solar/spectra/am1.5/ASTMG173/ASTMG173.html

[6]http://asteroid.lowell.edu/comet/dustphase.html

We used the A(0)fρ values obtained with the narrow-band filters which are not contaminated by the gas emissions to derive the dust colours. The normalized reflectivity gradients between wavelength λ_1 and λ_2 is defined as (A'Hearn et al., 1984; Jewitt and Meech, 1986):

$$S_v(\%/1000) = \frac{Af\rho_1 - Af\rho_2}{Af\rho_1 + Af\rho_2} \times \frac{2000}{\lambda_1 - \lambda_2} \tag{2.22}$$

where λ_1 and λ_2 are the effective wavelengths of the filters: BC[4450 Å], GC[5260 Å] and RC[7128 Å].

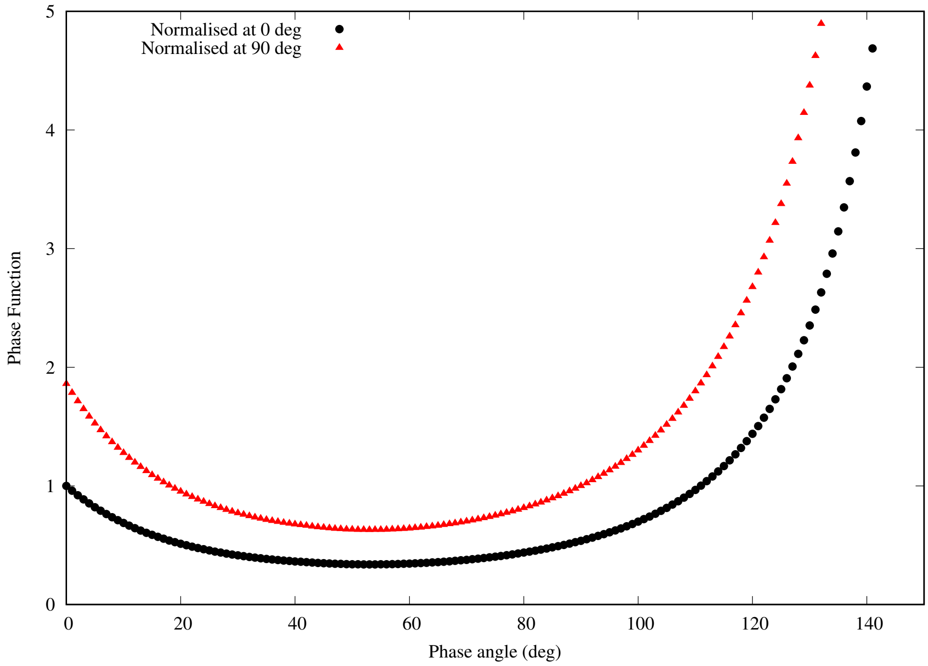

Figure 2.13: Phase function used to correct the A(θ)fρ from the phase angle effect.

2.3.4 Coma image enhancement techniques

The coma is dominated by the overall brightness distribution, and many individual features are not easily recognisable. This makes analysing the spatial structure of comet images difficult, as important structural information is contained both near the coma centre and in the dimmer outer regions. The study of coma morphology can give us information about the rotation period, active areas, and homogeneity of the nucleus. Among the features most commonly observed, there are jets, fans, arcs, spirals, or simple spatial asymmetries. We discuss here the techniques that we tested to enhance TRAPPIST images for several comets that showed an important activity. The first technique is the rotational gradient filters provided by MaximDL software[7], which is useful for enhancing low contrast structures. They are particularly suited to bringing out details such as comet near-nucleus jets and tail structure. Two types are provided: the Simple Subtraction filter takes the difference between two oppositely-rotated copies of the image from each other, while the Larson-Sekanina filter (Schleicher and Farnham, 2004) adds the two and subtracts the result from twice the original image. In either case, a constant is added so as to make the minimum pixel in the result zero. For both cases, it requires an angle by which the image is rotated clockwise and counter-clockwise prior to calculating the difference. We tested several rotation angles, and they always revealed the same features. Finally we

[7] https://diffractionlimited.com/product/maxim-dl/

adopted a 40° angle, which provided the highest contrast images. The technique presented here is very sensitive to the centering of the nucleus, which we can set as the centroid of the profile or put manually. We tested both techniques on several images and they give similar results, using different angles of rotation. Other enhancements techniques of comet images and tools have been developed by the community. Martin et al. (2015) developed a web-tool[8] to enhance comets images using different techniques. The description and comparison for each technique is explained in Samarasinha and Larson (2014). We tested all these techniques for several comets images to find the most appropriate ones for our data. Figure 2.14 shows CN image of comet 46P/Wirtanen enhanced by different techniques. We decided to use the simple rotational filter technique for all the comets enhanced in this work.

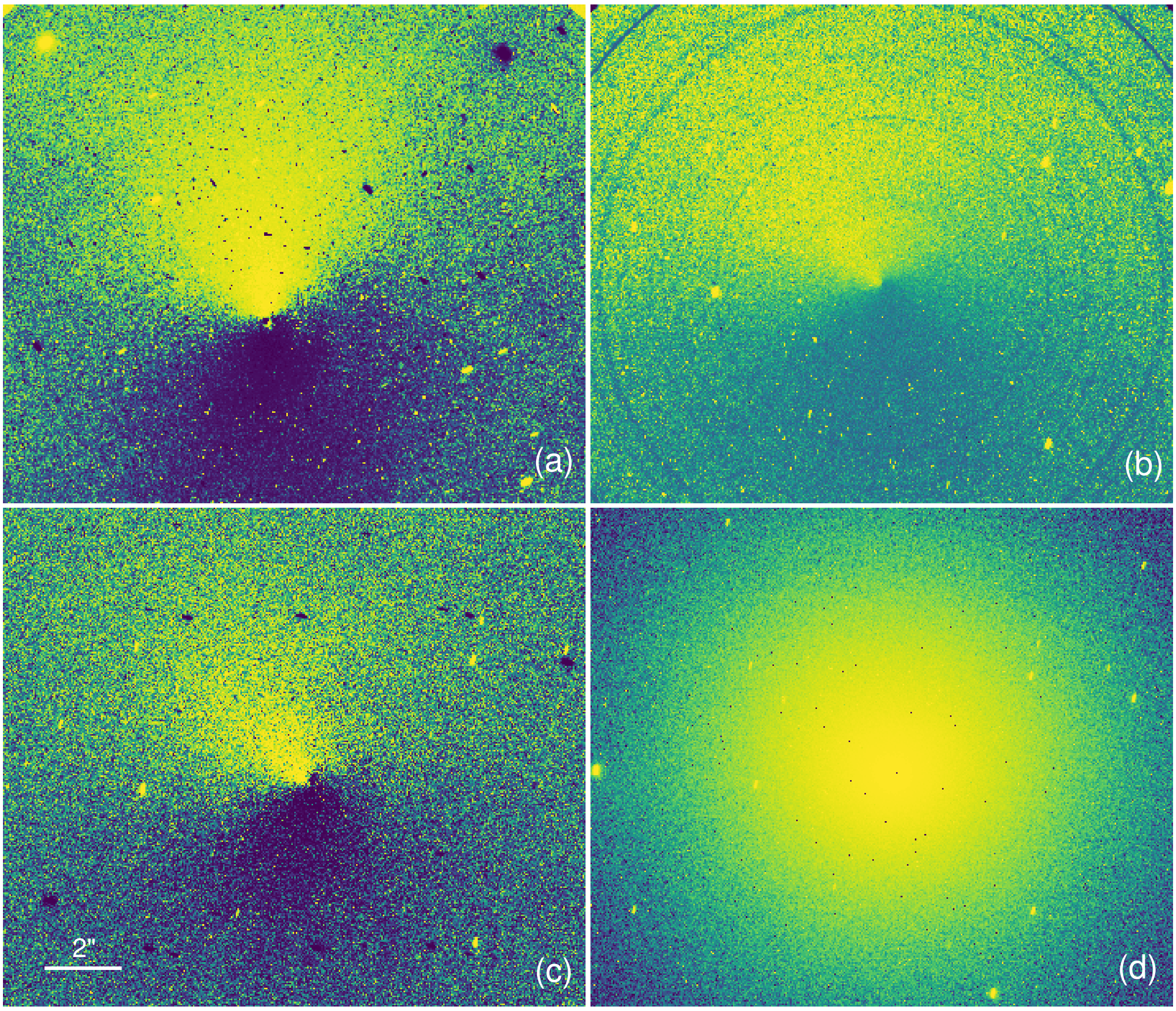

Figure 2.14: CN image of comet 46P/Wirtanen taken on November 16, 2018 with TS enhanced by different techniques. (a) simple rotational filter, (b) division by an azimuthal average, (c) Larson-Sekanina filter and (d) the original image of the comet. The scale of the images is given in the frame (c).

[8] https://www.psi.edu/research/cometimen

2.4 Spectroscopic observations and data reduction

2.4.1 UVES

UVES (**UV**-**V**isual **E**chelle **S**pectrograph) is the ESO high-resolution optical spectrograph mounted on UT2 Kueyen Very Large Telescope (VLT) at the Paranal Observatory (Dekker et al., 2000). It is a cross-dispersed Echelle spectrograph designed to operate with high efficiency from the atmospheric cut-off at 3000 Å to the long wavelength limit of the CCD detectors (about 11000 Å). The maximum (two-pixel) resolution is 80 000 or 110 000 in the Blue- and the Red arm, respectively. The instrument is built for maximum mechanical stability and allows for accurate wavelength calibration. The blue CCD detector format is 2048×4096 pixels, windowed to 2048×3000. The red CCD is a mosaic of two 4096×2048 pixels CCDs, separated by about 1 mm. Several standard setting are available for UVES to facilitate the preparation of observation and adapt the the database calibration. In this work, we will discus the UVES settings used for each observation in chapter 3. More details about the standard setting are given in the UVES user manual corresponding to the period concerned, and can be found at the ESO website[9]. For data reduction, we used the ESO UVES pipeline through the ESO Recipe Flexible Execution Workbench (Reflex), an environment to run pipelines which employs a workflow engine to provide a real-time visual representation of a data reduction cascade. Reflex and the data reduction workflows have been developed by ESO and instrument consortia and they are fully supported (Freudling et al., 2013). The ESO UVES pipeline has been used to reduce the spectra in its two-dimensional (2D) mode, keeping the spatial information. The spectra are corrected for the extinction and flux calibrated. One-dimensional spectra are then extracted by averaging the 2D spectra with simultaneous cosmic ray rejection and then corrected for the Doppler shift. More details about the UVES data reduction are given in the UVES manual[10]. The dust-reflected sunlight was removed using a reference solar spectrum BASS2000[11]. More in depth description of the steps for the solar spectrum subtraction is given in Manfroid et al. (2009) and references therein. In this work, we obtained high resolution spectroscopic data with UVES only for two comets 21P/Giacobini-Zinner and comet 66P/du Toit.

2.4.2 XSHOOTER

XSHOOTER is the first of the second generation instruments at the VLT, it has the capabilities of obtaining, in highly efficient way, high quality spectra over a broad wavelengths range of faint targets. It is a multi-wavelength (300-2500 nm), medium resolution spectrograph mounted at the UT2 Cassegrain. It consists of three spectroscopic arms, each with optimized optics, dispersive elements, and detectors. The acquisition and guiding camera can be used to obtain complementary images: (i) UVB with a wavelength range of 300-559.5 nm; (ii) VIS with a wavelength range of 559.5-1024 nm and (iii) NIR with a wavelength range of 1024-2480 nm. More details and description about XSHOOTER are available in the ESO instrument website[12] and published in Vernet et al. (2011). For the data reduction, we used the ESO XSHOOTER pipeline through the ESO Reflex program (Freudling et al., 2013). The same as for UVES, the pipeline provide a two dimensional reduced spectra with flux and wavelength calibration. To extract one dimensional spectra, we used self-developed IDL routines (Yang et al., 2019). In this work, we only have XSHOOTER data for comet 66P/du Toit.

[9] https://www.eso.org/sci/facilities/paranal/instruments/uves/doc.html
[10] ftp://ftp.eso.org/pub/dfs/pipelines/uves/uves-pipeline-manual-22.17.pdf
[11] http://bass2000.obspm.fr/solar_spect.php
[12] https://www.eso.org/sci/facilities/paranal/instruments/xshooter.html

Chapter 3

Monitoring the activity and composition of comets with TRAPPIST

In this chapter, we present the narrow-band photometry analysis of several comets observed with both TRAPPIST telescopes between 2017 and 2020. During this period, we observed 35 comets including 18 short period comets, 16 long period comets in addition to the first interstellar comet 2I/Borisov discovered in 2019. Some comets of our sample have been observed with both telescopes at the same time, which allow us to demonstrate the high quality and synergy of our measurements. Thanks to both TRAPPIST telescopes, we were able to observe some comets continuously for a long time in order to study their activity evolution over a large range of heliocentric distances. We also were able to observe some comets many hours over the same night in order to derive the rotation period of their nucleus. Each comet has been monitored as long as possible, depending on its brightness and its visibility on both sites. Some comets were particularly bright and remained observable for a long time from both hemispheres. All these comets have been observed with the same instruments (See Table 2.1 in chapter 2), the observations have been reduced with the same pipeline, and gas production rates have been computed using the same model and parameters (See section 2.3 in chapter 2). This provides an homogeneous and coherent comparison between all the observed comets observed with TRAPPIST over the last 10 years.

In this work, we study the activity evolution and composition of the coma based on the gas production rates and dust production rate proxy (A(0)fρ parameter). We derived and followed the evolution of the relative abundances of different molecular species with respect to the heliocentric distance. We compared the activity level and coma composition of comets at the current passage with the previous apparitions. We study the coma morphology and we derived the rotation period of certain periodic comets. Our regular measurements of the comets activity and composition from optical measurements were also invaluable to support observing programs on larger ground based or space telescopes. In this chapter, we chose to present a detailed study of 18 comets: 12 JFCs (including 5 comets that showed an outburst), 5 LPCs and the first interstellar comet 2I/Borisov. For the JFCs, we include comets 21P/Giacobini–Zinner, 41P/Tuttle-Giacobini-Kresak, 45P/Honda-Mrkos-Pajdusakova, 46P/Wirtanen, 64P/Swift-Gehrels, 66P/du Toit, and 252P/LINEAR. Comets 21P and 66P were observed in parallel with high and medium-resolution spectroscopy instruments at Very Large Telescope (hereafter VLT). The work presented here about comets 21P and 66P have been published in Moulane et al. (2020) and Yang et al. (2019), respectively. Comets 41P, 45P, 46P and 64P made a very close approach to the Earth during the 2017-2018 apparition and they were monitored intensively over a wide ranges of heliocentric distances on both sides of perihelion with both telescopes. The results of analysis of comets 41P and 45P have been published in Moulane et al. (2018a), while the work about comet 46P is still in progress (Moulane et al. in preparation). We also monitored comets 29P/Schwassmann-Wachmann, 123P/West-Hartley, 155P/Shoemaker 3, 243P/NEAT, and 260P/McNaught that all showed outburst activity. For the LPCs, we include C/2017 O1 (ASASSN), C/2017 T2 (PANSTARRS), and C/2018 W2 (Africano) because they were monitored for a long period of time on both sides of perihelion. Comet C/2019 Y4 (ATLAS) was a very bright comet before its disintegration. C/2020 F3 (NEOWISE) was the brightest comet in the northern hemisphere since comet Hale–Bopp in 1997. Finally 2I/Borisov was particularly interesting as it was the first active interstellar comet discovered.

3.1 Comet 21P/Giacobini–Zinner

Comet 21P/Giacobini-Zinner (hereafter 21P) is a JFC with a short period of 6.5 yr. 21P was discovered in 1900 by Michel Giacobini and rediscovered by Ernst Zinner in 1913[1]. After its discovery, 21P was observed in most of its apparitions and many photometric and spectroscopic measurements were reported. In September 1985, 21P was the first comet visited by the International Cometary Exporer (ICE) spacecraft to study the interaction between the solar wind and the cometary atmosphere (Von Rosenvinge et al., 1986; Scarf et al., 1986). 21P is also known as the parent body of the Draconids meteor shower (Beech, 1986; Egal et al., 2019). Many spectroscopic-photometric studies at various wavelength ranges have been performed since its discovery (Schleicher et al., 1987; Cochran and Barker, 1987; Fink Uwe and Hicks, 1996; Weaver et al., 1999; Lara et al., 2003; Combi et al., 2011) including production rates measurements, atomic and molecular abundances. 21P is the prototype of depleted comets in C_2 and C_3 with respect to CN and to OH (Schleicher et al., 1987; A'Hearn et al., 1995). C_2 and C_3 relative abundances are about 5 and 10 times smaller than those measured in "typical" comets (A'Hearn et al., 1995). 21P was found to be also depleted in NH (Schleicher et al., 1987; Kiselev et al., 2000) and NH_2 (Konno and Wyckoff, 1989; Beaver et al., 1990; Fink, 2009).

The physical properties of 21P were investigated in the previous apparitions. Its nucleus size is not well determined, the average estimate of its radius is about 1-2 km (Tancredi et al., 2000; Królikowska et al., 2001; Pittichová et al., 2008). Its rotation period is not well constrained, a large range from 9.5 hr to 19 hr was estimated (Leibowitz and Brosch, 1986). 21P activity has shown an asymmetric light-curve with respect to perihelion in the previous apparitions. In 1985, the production rates pre-perihelion were two times larger than post-perihelion at heliocentric distances of 1.0-1.5 au (Schleicher et al., 1987). The gas and dust maximum production was observed about one month pre-perihelion for the previous apparitions (Schleicher et al., 1987; Hanner et al., 1992; Lara et al., 2003). Both its unusual composition and the behavior of its activity during multiple apparitions make 21P an object of great interest. In addition, as it is the parent body of the Draconids, a study of its dust properties might be valuable. The 2018 apparition was very favorable for ground-based observations since the comet was close both to the Sun and the Earth at the same time and reaching high elevation. Many observed the comet again for the 2018 return using various state of the art instrumentation (IR and optical spectrographs on large telescopes) in order to better understand these peculiarities.

We started monitoring 21P with TN at the beginning of June 2018 when the comet was at 1.55 au from the Sun. The comet was observed three months pre-perihelion to four months after perihelion. The comet reached perihelion on September 10, 2018 at a heliocentric distance of 1.01 au and a geocentric distance of 0.39 au. In total the comet was observed over 50 different nights with both telescopes, 13 nights pre-perihelion and 37 after. The pair of TRAPPIST telescopes is in such a case very useful as it allowed a continuous monitoring of the comet

[1] https://ssd.jpl.nasa.gov/sbdb.cgi?sstr=21P;old=0;orb=0;cov=0;log=0;cad=0#discovery

before and after perihelion. We collected images with the cometary HB narrow-band filters (Farnham et al., 2000) to measure the production rates of the radicals OH, NH, CN, C_3, and C_2. We also acquired images with the dust continuum filters BC, GC, and RC for blue, green and red (Farnham et al., 2000). We used the broad-band filters B, V, Rc, and Ic (Bessell, 1990) to compute the A(0)fρ parameter which is a proxy of the dust production rate (A'Hearn et al., 1984) and to derive the dust colours. Throughout the passage of the comet, we acquired a high cadence monitoring of 21P with images taken about twice a week. On photometric nights, we also obtained long series of observations with the gas narrow-band filters, especially CN and C_2 filters, to measure the variations of the production rates during the same night due to the rotation of the nucleus. We chose the exposure time of the different filters depending on the brightness of the comet. We used exposure times between 60 s and 240 s for the broad-band filters and between 600 s and 1500 s for the narrow-band filters.

We obtained one spectrum of comet 21P with the Ultraviolet-Visual Echelle Spectrograph (UVES) mounted on the ESO 8.2m UT2 telescope of the VLT on September 18, 2018 (a week after perihelion, $r_{\rm h}$=1.01 au and Δ=0.40 au) under Director's Discretionary Time. We used the UVES standard settings DIC1 346+580 covering the range 3030 to 3880 Å in the blue and 4760 to 6840 Å in the red. We used a 0.44″ wide slit, providing a resolving power R$\sim$80 000. We obtained one single exposure of 3000 s at 8h35 UT with a mean airmass of 1.7. This exposure provided two different spectra, both of them covering one of the above mentioned spectral ranges.

3.1.1 Composition and activity

Along with our monitoring of comet 21P with the TRAPPIST telescopes, we derived the OH, NH, CN, C_3, and C_2 production rates. They are summarized in Table A.1 and their evolution as a function of the heliocentric distance are compared with two previous passages in Figure 3.1. We started to detect most of the radicals in the coma by the end of June 2018 (except NH one month later). The various production rates and the dust activity have been increasing slowly as the comet was getting closer to the Sun (from 1.52 to 1.07 au). The maximum of the activity was reached at 1.07 au from the Sun, on August 17, 24 days pre-perihelion. It then started to decrease rapidly after perihelion. CN was detected in our data until the end of 2018 at 1.66 au, while OH, C_3, and C_2 were not detected anymore after the beginning of November at 1.4 au and NH early October at 1.2 au. We found that like for the previous apparitions (Schleicher et al., 1987), the production rates pre-perihelion are larger by more than a factor two than post-perihelion. It is clear from Figure 3.1 that the asymmetric activity is seen for all species and this behaviour does not change over the various apparitions (Schleicher et al., 1987; Combi et al., 2011) as shown also in Figure 3.2 for the water-production rate. The same behavior has been reported for the parent molecules (H_2O, CO, CH_4, C_2H_2, C_2H_6, NH_3 and CH_3OH) production rates derived at Infrared wavelengths during the 2018 passage (Faggi et al., 2019; Roth et al., 2020). This might be due to the shape of the nucleus and its spin-axis orientation. This effect has been observed in several comets such as 9P/Tempel 1 (Schleicher, 2007), 81P/Wild 2 (Farnham and Schleicher, 2005) and also for comet 67P/Churyumov-Gerasimenko (Schleicher, 2006; Opitom et al., 2017). It has been shown very clearly by the Rosetta mission that the maximum activity of 67P well associated with the illumination of the most southern regions, which were receiving the maximum solar flux, and were subject to intense erosion (Lai et al., 2019). Recently, Marshall et al. (2019) has shown for those three comets that the nucleus shape, the spin axis orientation, and the distribution of activity on the comet's surface can explain the water-production rate light-curve as a function of the heliocentric distance.

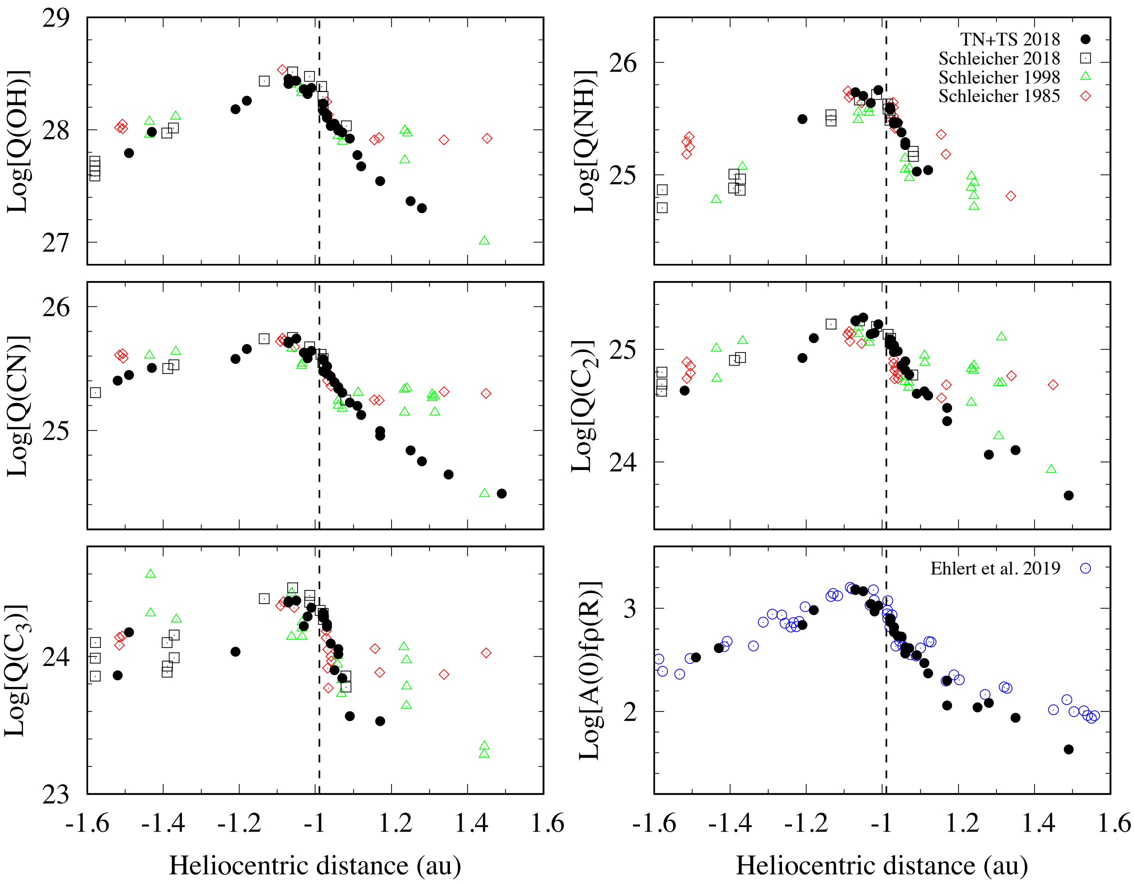

Figure 3.1: The logarithm of the production rates (in molec/s) of each species and of the A(0)fρ dust parameter (in cm), of comet 21P during its 2018 return (this work and Schleicher and Knight (2018)) are compared with two previous apparitions in 1985 and 1998 (Schleicher and Knight, 2018) as a function of the heliocentric distance. The dashed vertical line represents the perihelion distance on September 10, 2018. The maximum of the gas and dust activity was reached at 1.07 au from the Sun, on August 17, 2018, 24 days pre-perihelion.

Around the maximum of the activity, the production rates are almost the same as those measured in the previous apparitions indicating that there is no decrease of the activity level of 21P over the last five orbits. Our production rates mostly agree very well with those derived by Schleicher and Knight (2018) who used the same technique, while we noticed a discrepancy at large heliocentric distance and post-perihelion in the 1985 and 1998 apparitions data (Schleicher et al., 1987; Schleicher and Knight, 2018). This could be due to a sensitivity issue in their data as the production rates seem to level off on both sides of perihelion while the distance increases or to a higher activity level of the comet after perihelion in the past. It has been also found that there is no significant change in the production rates of hypervolatile molecules (CO, CH_4, and C_2H_6) in comet 21P over the three different apparitions, 1998 (Weaver et al., 1999; Mumma et al., 2000), 2005 (DiSanti et al., 2012) and 2018 (Faggi et al., 2019; Roth et al., 2020).

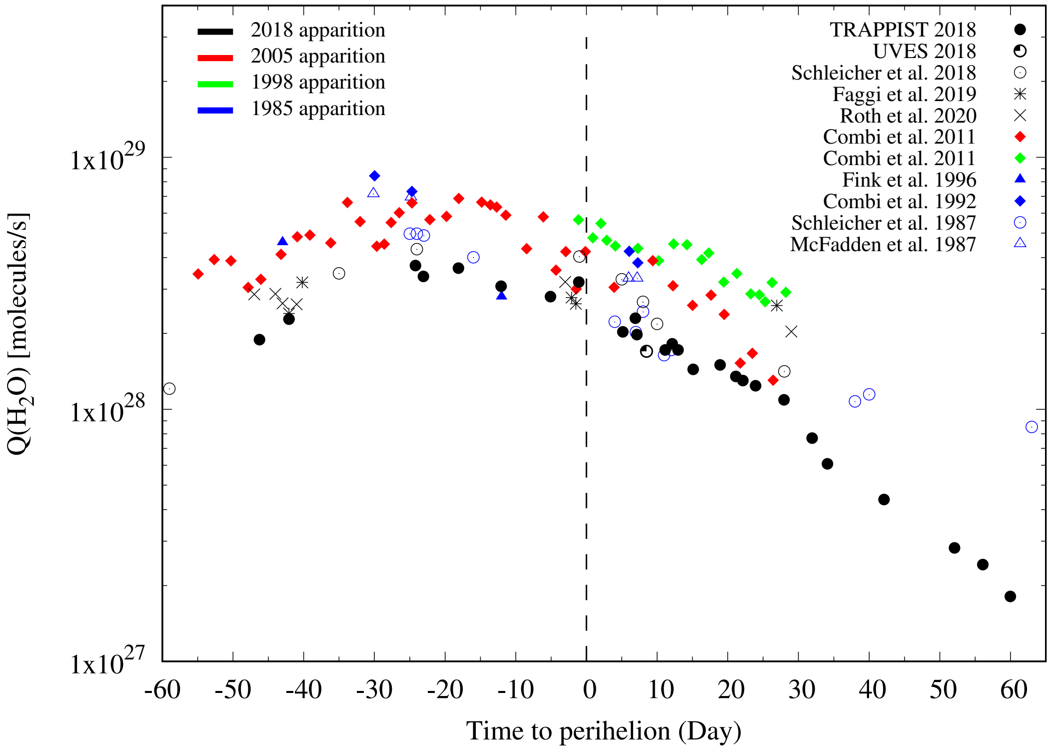

Figure 3.2: H_2O production rates of comet 21P as a function of days to perihelion in 2018 compared to the previous apparitions (1985, 1998 and 2005). More description about the data is given in section 3.1.1.1.

3.1.1.1 H_2O production rate

The water-production rate is the most significant indicator of the activity of a comet. It can be measured directly from near-Infrared observations or derived from OH emission at 3090 Å and radio wavelengths or from H Lyman-α emission at 1216 (Combi et al., 1986) assuming that both OH and H arise from the dissociation of H_2O. In this work, we computed the vectorial-equivalent water-production rates according to an empirical procedure based on a comparison of OH and water-production rates derived from the mean lifetimes, velocities, and scale lengths given by Cochran and Schleicher (1993). Schleicher et al. (1998) built an empirical relationship:

$$Q(H_2O) = 1.361 \times r_h^{-0.5} \times Q(OH) \tag{3.1}$$

This correlation was based on a $r_h^{-0.5}$ dependence of the H_2O outflow velocity, a photodissociation branching ratio for water to OH of 90%, and the heliocentric distance. Figure 3.2 shows the water production we derived compared to previous apparitions (with different techniques) as a function of days to perihelion. We used the formula given above to convert Q(OH) to water-production rates for Schleicher and Knight (2018) data. Combi et al. (2011) derived the production rates from the H Ly-α emission observed by the SWAN instrument on board SOHO in 1998 and in 2005. Combi and Feldman (1992) values are derived from H Ly-α emission observed by the IUE mission for the 1985 apparition. From the Pioneer Venus Orbiter ultraviolet system (UVS) instrument, McFadden et al. (1987) derived the water-production rates from OH (3090 Å) emission. Fink Uwe and Hicks (1996) derived the water-production rates from the [OI](^{1}D) forbidden line doublet using a correlation between the water-production rates and the total photon luminosity. Faggi et al. (2019) and Roth et al. (2020) measured directly the water-production rates from near-Infrared spectra. TRAPPIST and UVES data points are from this work (see section 3.1.1.1 and 3.1.3.1). The maximum in the last four apparitions was reached about one month pre-perihelion and does not change over all apparitions, but we observe a clear systematic difference between the narrow band and spectroscopic methods in the optical on one hand and the measurements made from the space observations of the H Ly-α emission in the UV on the other hand. The maximum of the water production we measured was on August 17, 24 days before the perihelion, and it reached $(3.72\pm0.07)\times10^{28}$ molec/s in good agreement with Schleicher and Knight (2018) measurement of 4.20×10^{28} molec/s at the heliocentric distance 1.07 au. Using the same technique for the 1985 apparition, Schleicher et al. (1987) reported Q(H_2O)=4.85×10^{28} molec/s when the comet was at 1.05 au from the Sun. Using high resolution Infrared spectroscopy, Weaver et al. (1999) measured $\sim$2–3×10^{28} molec/s at r_{h}=1.10 au in 1998. For the 2005 apparition, Combi et al. (2011) found a value of 5.80×10^{28} molec/s from the H Ly-α emission observed by the SWAN/SOHO at r_{h}=1.08 au. Comparing these data, we found that the water-production rates measured by Combi and Feldman (1992) in 1985 and Combi et al. (2011) in 2005 are systematically higher by a factor of about two with respect to our results in 2018. Such an offset between various techniques has been reported in previous studies and as early as comet 1P/Halley (Schleicher et al., 1998). The origin of this discrepancy is not clear but it is obvious that there is a good agreement when the same technique is used. This indicates that the level of activity of 21P was the same over the past four decades and did not decrease like comet 41P/Tuttle–Giacobini–Kresak which has been losing as much as 30% to 40% of its activity from one orbit to the next (Moulane et al., 2018a).

3.1.1.2 Active area of the nucleus

To estimate the active area of the nucleus' surface, we modelled the water production using the sublimation model of Cowan and A'Hearn (1979). Due to the low thermal inertia of cometary nuclei (Gulkis et al., 2015), the slow-rotator approach was adopted in a number of cases as the most appropriate way to compute the cometary outgassing (see e.g., Bodewits et al., 2014; Lis et al., 2019). The slow-rotator model assumes every facet of the nucleus is in equilibrium with the solar radiation incident upon it, with the rotational pole pointed at the Sun. As mentioned previously, the size of 21P's nucleus, necessary to convert the active area to the active fraction of the whole surface, is not well constrained so far, with a radius ranging from 1 to 2 km. Hence, to estimate the active fraction of the surface we assumed a radius of 1.5±0.5 km. Moreover, we assumed a bond albedo of 5% and a 100% Infrared emissivity (see e.g., A'Hearn et al., 1989; McKay et al., 2019). We found that the active area of 21P during our monitoring campaign varied from $\sim$5 km^2 at 1.49 au pre-perihelion, reached a maximum of $\sim$12 km^2 at 1.07 au pre-perihelion, and decreased to $\sim$1 km^2 at 1.31 au post-perihelion. Table 3.1 shows the minimum and maximum active areas and active fraction for 21P using the slow-rotator model at some interesting heliocentric distances. We obtained different values in comparison with previous estimations given by Combi et al. (2019). The reason is twofold; first, the already mentioned discrepancy in the water-production rates found via different observational techniques (see Section 3.2), and secondly, the model used by the authors (fast-rotator), which is less appropriate to describe the cometary outgassing.

3.1.2 Abundances ratios

Studying the molecular abundances and their ratios with respect to the distance to the Sun gives information about the homogeneity of a comet's nucleus and the chemical processes involved in the coma. Based on the relative abundance of 41 comets, A'Hearn et al. (1995)

Table 3.1: Active area (km^2) and active fraction of the surface (%) for 21P using the slow-rotator model at some interesting heliocentric distances.

Date UT	r_h (au)	Active Area (km^2)	Active fraction (%)
(a) 2018 Jun 22	-1.49	4.9±0.1	18±12
(b) 2018 Aug 17	-1.07	12.0±0.2	43±28
(c) 2018 Sep 09	-1.01	9.0±0.2	32±21
(d) 2018 Sep 15,16,17	+1.02	6.9±0.1	22±14
(e) 2018 Nov 09	+1.31	0.90±0.04	4±2

Note. (a) The first measurement during our monitoring campaign, (b) the maximum activity during our monitoring campaign, (c) the last measurement pre-perihelion passage, (d) the mean of the first measurements after perihelion passage with similar heliocentric distances of 1.02 au, and (e) the last and minimum measurements during our monitoring campaign. Large errors in the active fractions of the surface came from the large uncertainties in the radius of the nucleus, which we adopted as 1.5±0.5 km (see section 3.1.1.2 for details).

classified comets into two groups based on their C_2/CN ratio. Typical comets are defined as those having a Log[Q(C_2)/Q(CN)] $\geq$ -0.18 while the carbon-chain depleted comets are those below that value. This classification was confirmed later by other photometric and spectroscopic studies of large data sets (Schleicher, 2008; Fink, 2009; Langland-Shula and Smith, 2011; Cochran et al., 2012) and must reflect some differences between the formation conditions (the pristine scenario) or a change of relative composition with time (several perihelion passages) of these comets (the evolutionary scenario). Figure 3.3 shows the evolution of the 21P abundance ratios of the various radicals with respect to OH (a proxy of water) and CN, as a function of heliocentric distance. It is clear that 21P abundance ratios in the 2018 return agree with the mean values of depleted comets given in A'Hearn et al. (1995). Table 3.2 summarizes the relative abundances in 2018 compared to 1985 and 1998 data using the same technique and the same Haser model parameters (Schleicher and Knight, 2018). Our 2018 ratios are the mean values for all the data obtained (see Table A.1). Like for the activity level over the past passages, the relative abundances did not change over the last 5 orbits. Note that the A(0)fρ values derived in 1985 and in 1998 by Schleicher and Knight (2018) were computed for the narrow band GC[5260 Å] filter while we used the BC[4450 Å] filter. After correcting their A(0)fρ values for the phase angle effect using the same function as for the TRAPPIST data (see chapter 2), both data sets are in agreement. This indicates that there is no evidence of changes in the chemical composition in the coma of the comet at different heliocentric distances (in the range 1.0 to 1.5 au) and over the five orbits, which is an argument to reject the evolutionary origin of the carbon chain depletion in that comet at least.

As seen in the bottom panel of Figure 3.3, there is also no evidence that the dust/gas ratio represented by A(0)fρ/Q(CN) and A(0)fρ/Q(OH) depends on the heliocentric distance. We found that this ratio in 21P is consistent with the average value of depleted comets and higher than the mean value of the typical comets as defined in A'Hearn et al. (1995). Lara et al. (2003) obtained a value of Log[A(0)fρ/Q(CN)]=-22.91±0.10 in 1998 which is in agreement with our measurement. Like for the relative gas abundances, we conclude that 21P coma does not show significant variation in the dust/gas ratio over the previous apparitions and it has a similar ratio as the depleted comets defined by A'Hearn et al. (1995).

The comparison with abundances of parent molecules derived from Infrared data (Faggi et al., 2019; Roth et al., 2020) allows us to investigate the origin of the radicals observed in 21P atmosphere. Using high-resolution Infrared spectra obtained in 1998, Weaver et al. (1999) reported upper limits for different species relative to H_2O such as C_2H_6 (2-3%), HCN(0.3-

Table 3.2: Relative molecular abundances of comet 21P over the last passages compared to the mean values for depleted and typical comets.

	Log production rate ratio				
	1985	1998	2018	Depleted comets	Typical comets
	Schleicher and Knight (2018)		This work	A'Hearn et al. (1995)	
C_2/CN	-0.64	-0.50	-0.52±0.10	-0.61±0.35	0.06±0.10
C_3/CN	-1.42	-1.30	-1.39±0.12	-1.49±0.14	-1.09±0.11
CN/OH	-2.59	-2.67	-2.62±0.08	-2.69±0.14	-2.50±0.18
C_2/OH	-3.23	-3.17	-3.16±0.21	-3.30±0.35	-2.44±0.20
C_3/OH	-4.02	-3.98	-4.03±0.16	-4.18±0.28	-3.59±0.29
NH/OH	-2.66	-2.87	-2.68±0.14	-2.48±0.34	-2.37±0.27
A(0)fρ/CN	-22.74	-22.73	-22.70±0.10	-22.61±0.15	-23.30±0.32
A(0)fρ/OH	-25.33	-25.42	-25.32±0.12	-25.30±0.29	-25.82±0.40

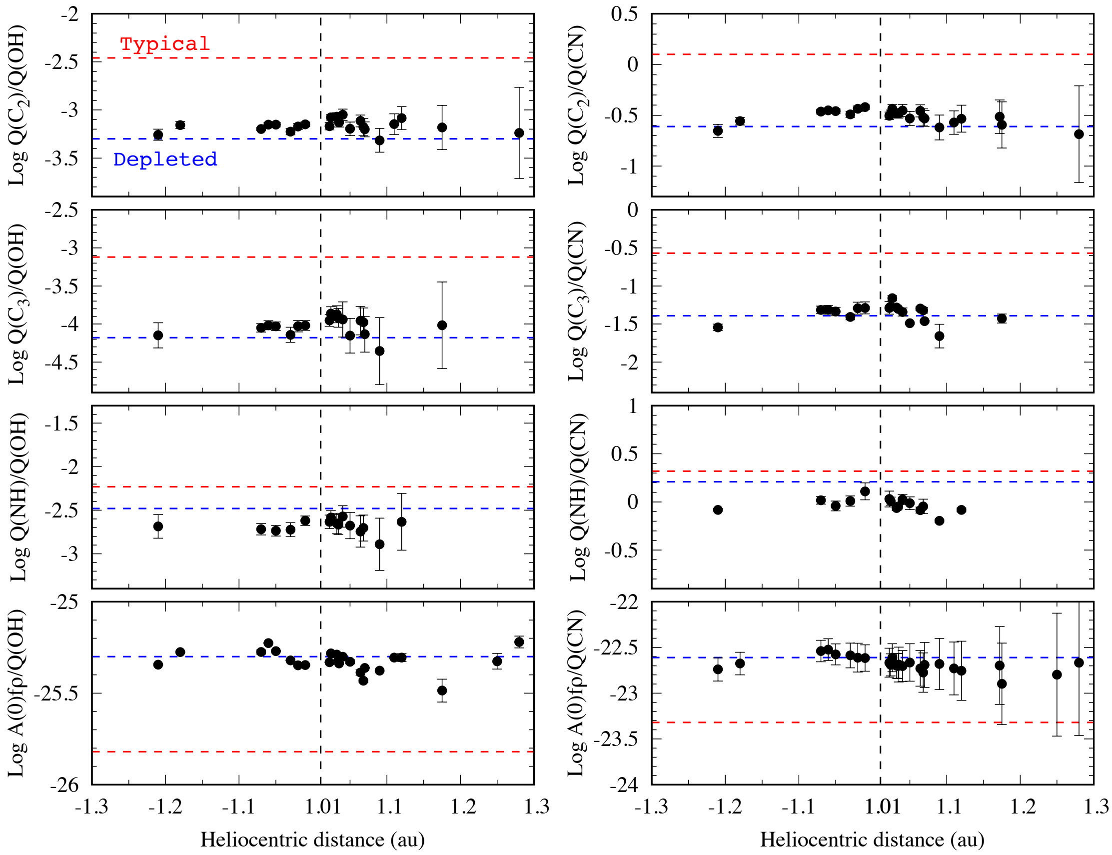

Figure 3.3: Evolution of the logarithmic production rates ratios of each species with respect to OH and to CN as a function of heliocentric distance. The red dashed line represents the mean value of typical comets as defined in A'Hearn et al. (1995) while the blue one represents the mean value of the depleted group. The bottom panels shows the dust/gas ratio represented by A(0)fρ/Q(OH) and A(0)fρ/Q(CN). The vertical dashed line shows the perihelion distance on September 10, 2018 at r_{h}=1.01 au.

0.4%) and C_2H_2(0.5-0.8%) assuming that all species are parent molecules. C_2H_2 has been

Table 3.3: Comparison of daughter molecules and possible parent molecules production rates derived from optical and Infrared data of comet 21P in the 2018 passage.

Date 2018	r_h (au)	$\triangle$ (au)	Q(OH)	Q(H_2O)	Q(CN)	Production rates (10^{25}molec/s) Q(HCN)	Q(C_2)	Q(C_2H_2)	Q(C_2H_6)	Q(NH)	Q(NH_3)	Reference
Jul 30	1.17	0.61	1810±28		4.55±0.07	-	1.26±0.07	-	-	3.13±0.50	-	This Work
Jul 30	1.17	0.61	-	2401±394	-	<3.20	-	<4.52	4.49±1.45	-	<63.72	Faggi et al. (2019)
Jul 31	1.16	0.59	-	2503±385	-	6.16±0.12[(a)]	-	<1.80[(a)]	6.05±0.77	-	<16.19[(a)]	Roth et al. (2020)
Sep 07	1.01	0.39	3036±357	3206±112	-	-	-	-	10.60±1.10	-	-	Roth et al. (2020)
Sep 09	1.01	0.39	-	2623±586		4.30±0.32		<0.62	8.30±1.38		<12.59	Faggi et al. (2019)
Sep 09	1.01	0.39	2360±33		4.39±0.07	-	1.67±0.06	-	-	5.66±0.38	-	This Work
Oct 07	1.07	0.49	-	2583±864	-	-	-	-	4.55±1.44	-	-	Faggi et al. (2019)
Oct 08	1.08	0.49	834±25	-	1.68±0.05	-	0.40±0.06	-	-	1.07±0.35		This Work
Oct 10	1.10	0.51	-	2028±255	-	-	-	-	2.92±0.39	-	-	Roth et al. (2020)

Note. [(a)] From Roth et al. (2018) measured on July 29, 2018. Upper limits are 3σ for both Roth et al. (2020) and Faggi et al. (2019) results.

found depleted with respect to HCN by a factor five compared to other comets like Hyakutake and Hale–Bopp, a result that has been confirmed at this apparition by Faggi et al. (2019). We derived a Q(C_2)=1.26×10^{25} molec/s which is consistent with the upper limit of Q(C_2H_2) <4.52×10^{25} molec/s reported by Faggi et al. (2019) and <1.80×10^{25} molec/s reported by Roth et al. (2018) at 1.18 au from the Sun. This agreement indicates that C_2 could be a daughter species of C_2H_2. C_2 also has the possibility to come from C_2H_6 and HC_2N (Helbert et al., 2005; Weiler, 2012; Hölscher, 2015) or released from organic-rich grains (Combi and Fink, 1997), but a detailed chemical model of the coma would be needed to go in more details. We also found a very good match between Q(CN)=4.40×10^{25} and Q(HCN)=4.30×10^{25} molec/s (Faggi et al., 2019) at 1.01 au, showing that HCN could be the main parent molecule of CN in 21P. This result is known for several comets using different methods, including comparison between HCN and CN production rates (Rauer et al., 2003; Opitom et al., 2015), coma morphologies (Woodney et al., 2002), and also carbon and nitrogen isotopic ratios in both species (Manfroid et al., 2009; Bockelée-Morvan et al., 2015). We should note however that in some cases both abundances do not agree and that other sources, for instance extended sources, have been claimed for the CN origin (Fray et al., 2005).

Some molecules such as C_4H_2, $CH_2C_2H_2$, and CH_3C_2H are proposed to be the parent molecules of C_3 (Helbert et al., 2005; Mumma and Charnley, 2011; Hölscher, 2015), but these complex species were not observed at Infrared or at radio wavelengths. NH and NH_2 were found to be depleted in 21P in the previous apparitions (A'Hearn et al., 1995; Fink, 2009). New Infrared observations in 2018 show very low NH_3 in 21P, with an upper limit ratio of Q(NH_3)/Q(H_2O) < 0.6% (Faggi et al., 2019). In this work, we derive Q(NH)/Q(OH)=0.2% which is consistent with Q(NH_3)/Q(H_2O).

3.1.3 Optical high-resolution spectrum

3.1.3.1 Water-production rate

The UVES spectrum offered the possibility of computing independently the water-production rate at the time of observation. We first measured the overall flux for the OH (0,0) band near 309 nm, integrated over the whole slit. We found 1.47×10^{-13} erg s^{-1} cm^{-2} arcsec^{-2}. The fluorescence efficiency computed for this band and the heliocentric distance and velocity at the time of observation was 2.62×10^{-4} s^{-1} (or 1.71×10^{-15} erg s^{-1} molecule^{-1} if scaled to 1 au; see details on the fluorescence model in Rousselot et al. (2019)). From these values and a Monte-

Carlo simulation of the water molecules creating OH radicals in the inner coma (model based on equations given by Combi and Delsemme (1980)) it is possible to compute the corresponding water-production rate for the number of OH radicals observed in the slit (0.44×9.5 arcsec) centered on the nucleus. Using the parameters of H_2O radial velocity, OH and H_2O lifetimes given in Cochran and Schleicher (1993) and assuming that 91.8% of water molecules dissociate to OH (Crovisier, 1989), we found Q(H_2O)=1.7×10^{28} molec/s. This result is in excellent agreement with the water-production rates computed from TRAPPIST observations in the same period (see Figure 3.2). It must, nevertheless, be pointed out that it depends of the different parameters and can change a bit with them, especially with the water lifetime.

3.1.3.2 The ^{12}C/^{13}C and ^{14}N/^{15}N isotopic ratios

The study of the isotopic ratios in comets has attracted considerable attention as it contains information about the conditions which prevailed at the time of formation of these objects in the early Solar System (Jehin et al., 2009; Hyodo et al., 2013). The carbon ^{12}C/^{13}C ratio has been determined for several comets from the analysis of the C_2 Swan band and CN B-X system in the optical (Manfroid et al., 2009; Bockelée-Morvan et al., 2015, and references therein). Some in situ measurements have also been obtained in comet 67P by the ROSINA mass spectrometer on-board the Rosetta spacecraft for C_2H_4, C_2H_5, CO (Rubin et al., 2017) and CO_2 molecules (Hässig et al., 2017). All derived values are compatible with the terrestrial ratio of 89, except for CO that could possibly be slightly enriched in ^{13}C. The nitrogen ^{14}N/^{15}N isotopic ratio was measured for the first time from high resolution spectra of the CN violet band in comets C/2000 WM1 (LINEAR) and C/1995 O1 (Hale-Bopp) and found to be enriched by a factor of two in ^{15}N with respect to the Earth value (Arpigny, 2003). The same ratio was found later from sub-millimeter observations of HCN in comet 17P/Holmes during its outburst and archival data of C/1995 O1 (Hale-Bopp) (Bockelée-Morvan et al., 2008). It has also been recently possible to measure the ^{14}N/^{15}N ratio in ammonia via the NH_2 radical (Rousselot et al., 2014). The values obtained are similar to the one found in HCN and CN, which was confirmed by subsequent works (Shinnaka et al., 2014; Rousselot et al., 2015; Shinnaka and Kawakita, 2016; Shinnaka et al., 2016; Yang et al., 2018). Recent measurements performed by the ROSINA mass spectrometer in comet 67P provided a ratio ^{14}N/^{15}N=118±25 for NH_3 and 130±30 for N_2 molecules (Altwegg et al., 2019).

We used the ^{12}C^{14}N B-X (0,0) band to estimate the ^{12}C/^{13}C and ^{14}N/^{15}N isotopic ratios of 21P. We used a CN fluorescence model to create synthetic spectra of ^{13}C^{14}N, ^{12}C^{15}N, and ^{12}C^{14}N. More details of the model are given in Manfroid et al. (2009). Figure 3.4 shows the observed CN spectrum compared to the synthetic one made under the same observational conditions. The ratios found for ^{12}C/^{13}C and ^{14}N/^{15}N are 100±10 and 145±10, respectively. These values are consistent with those of about 20 comets with different dynamical origins, 91.0±3.6 and 147.8±5.7 for ^{12}C/^{13}C and ^{14}N/^{15}N respectively (Manfroid et al., 2009; Bockelée-Morvan et al., 2015).

3.1.4 NH_2 and NH_3 ortho-para ratios

We measured the ortho-to-para abundance ratio (OPR) of NH_2 from the three rovibronic emissions bands (0,7,0), (0,8,0) and (0,9,0), see Figure 3.5, following the method described in Shinnaka et al. (2011). The derived OPRs of NH_2 and of its parent molecule NH_3, are listed for each band in Table 3.4 and have average values of 3.38 ± 0.06 and 1.19 ± 0.03, respectively. The latter is in very good agreement with the Subaru/HDS determination (NH_3 OPR = 1.16 ± 0.02; (Shinnaka et al., 2020)). A nuclear spin temperature ($T_{\rm spin}$) for ammonia of 27 ± 1 K

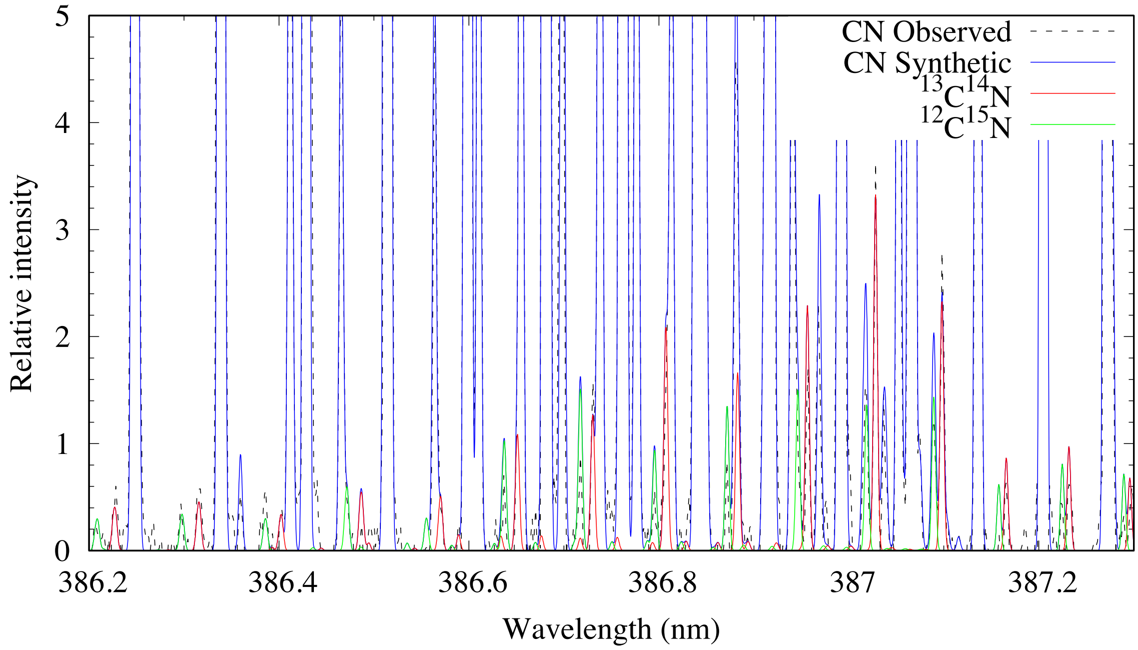

Figure 3.4: The observed and synthetic CN spectra of the R branch of the B-X (0, 0) violet band in comet 21P.

was derived. The 21P value is consistent with typical values measured in comets (see Figure 3.6). 21P cannot then be distinguished from other comets based on its NH_2 OPR (see Figure 3.7), a possible cosmogonic indicator linked to the formation temperature of the molecule.

Table 3.4: Derived NH_2 and NH_3 OPRs in comet 21P

NH_2 band	NH_2 OPR	NH_3 OPR	T_{spin}(K)
(0,7,0)	3.30±0.13	1.15±0.07	$28^{+5}/_{-3}$
(0,8,0)	3.55±0.08	1.28±0.04	$23^{+2}/_{-1}$
(0,9,0)	3.15±0.10	1.08±0.05	$34^{+8}/_{-4}$
Average	3.38±0.06	1.19±0.03	27±1

Note that recent laboratory experiments demonstrate that the OPR of water does not keep the memory of its formation temperature (Hama et al., 2011; Hama et al., 2016; Hama and Watanabe, 2013). It is likely that this is also the case for ammonia. The OPRs of cometary volatiles might have been modified by an ortho-para conversion process in the inner coma or other catalyst activities of dust crust surfaces of the nucleus rather than reflected by a formation temperature in the solar nebula 4.6 Gy ago. OPRs might be a diagnostic of the physico-chemical conditions in the inner-most coma or beneath the surface.

3.1.5 Dynamical evolution

In this section we analyse the dynamical evolution of the comet within the last 10^5 yr. JFCs are highly chaotic objects, whose dynamic evolution must be studied in terms of statistics (Levison and Duncan, 1994). With this in mind we analysed the evolution of the original object, i.e., comet 21P, by considering the nominal values of its orbital parameters as they are defined in JPL-HORIZONS (orbital solution JPL K182/3). In the analysis, 200 clones

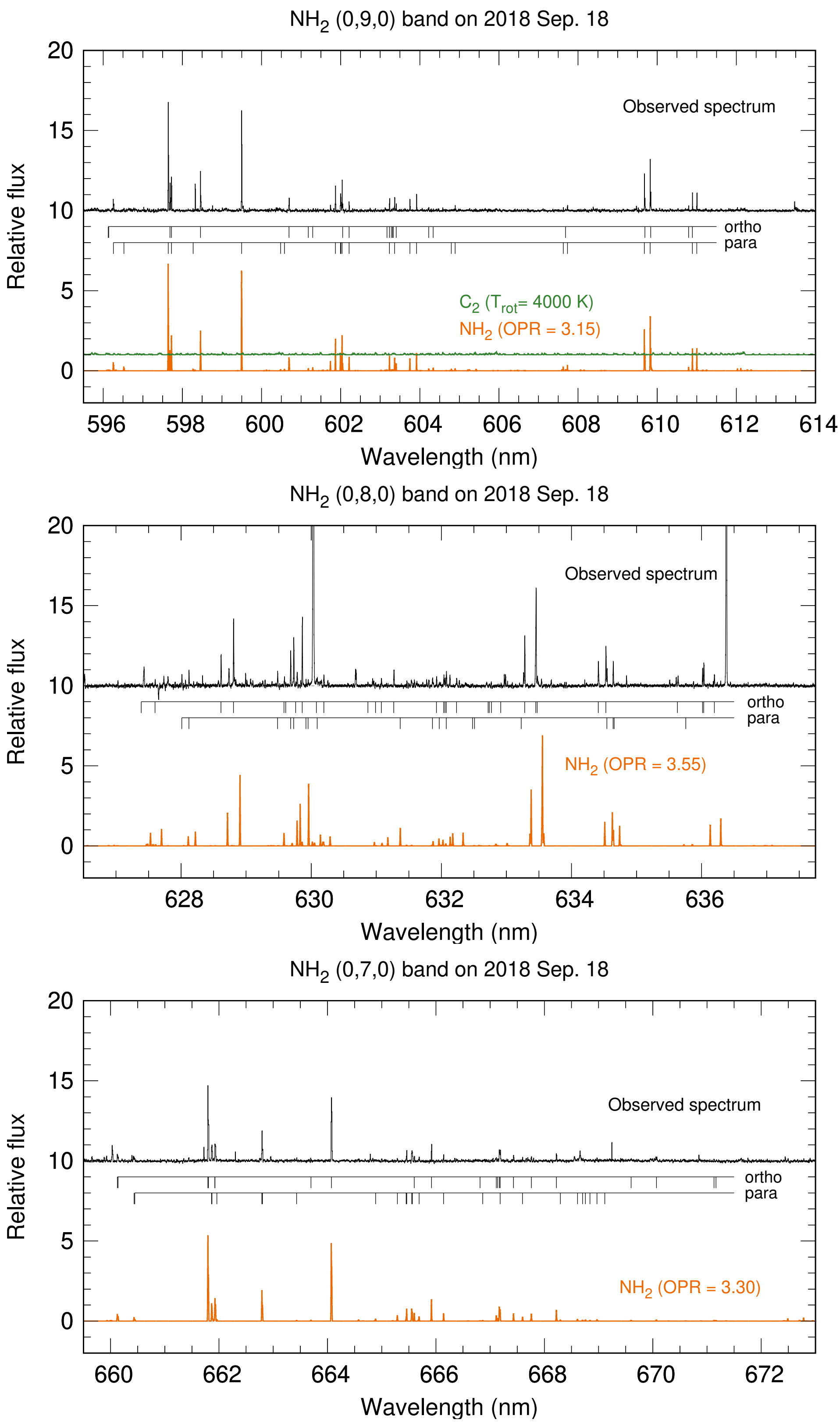

Figure 3.5: Comparison between the observed and modeled spectra of the NH_2(0,9,0), (0,8,0), and (0,7,0) bands. The modeled spectrum of C_2 is also plotted on the NH_2 (0,9,0) band panel, but due to the depleted nature of 21P, the C_2 lines are not affecting the NH_2 spectrum. The ortho- and para-lines of NH_2 are labeled in these modeled spectra. The two strong emission lines at 6300 Å and 6364 Å are the forbidden oxygen lines [OI] in the NH_2 (0,8,0) band panel. Note that the intensity ratio among bands is not correct because we scaled intensity for each plot independently.

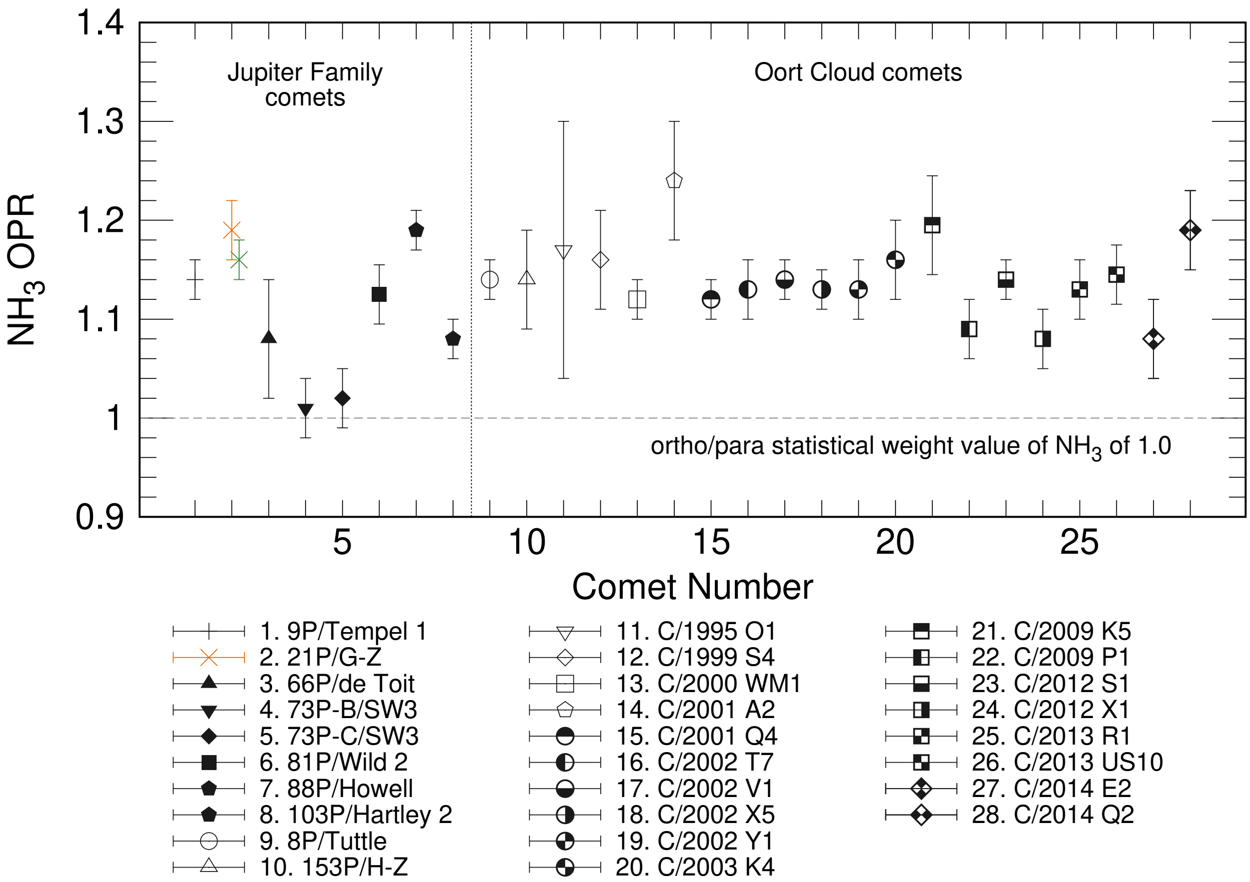

Figure 3.6: Summary of NH_3 OPRs in comets. The orange and green cross symbols symbols are the NH_3 OPR of 21P by VLT/UVES (this work) and by Subaru/HDS (Shinnaka et al. 2020), respectively.

were generated following the covariance matrix of its orbital parameters[2] . We performed the integrations with the numerical package MERCURY (Chambers, 1999), using the integration algorithm Bulirsch-Stoer with a time-step of 8 d and we included the Sun, all planets and Pluto in the simulation. In addition, we also included non-gravitational forces. The results of the simulations are displayed in Figure 3.8.

We find that the orbits of all the clones in the simulation are very compact for a period of ∼1650 yr. After that period, the orbits started to scatter, which was provoked by a close encounter with Jupiter, at mean distance of 0.1 au. Due to the chaotic nature of JFCs, a comparison of results from different authors who applied different methods (e.g., integration algorithm used, the number of clones, how their clones were generated etc.) is difficult to perform, and any superficial comparison might yield wrong conclusions. Only one analysis identical to that performed here has been carried out: for the comet 66P/du Toit by Yang et al. (2019). In that study it was found that the comet belonged to the Jupiter Family for at least $\sim 60\times10^3$ yr, and the stable nature of its orbit was evident. This result hints that 21P is likely a young member of the Jupiter Family, which has crossed its perihelion ∼230 times with similar distances of q∼1.013 au. The youth of 21P could explain its unusual composition. However, the lack of a statistic sample prevents us from robustly confirming this hypothesis.

[2]Both sets of the orbital parameters and the covariance matrix of the orbit for 21P are published together in the NASA/JPL small-body browser: https://ssd.jpl.nasa.gov/sbdb.cgi?sstr=21P;old=0;orb=0;cov=1;log=0;cad=0#elem

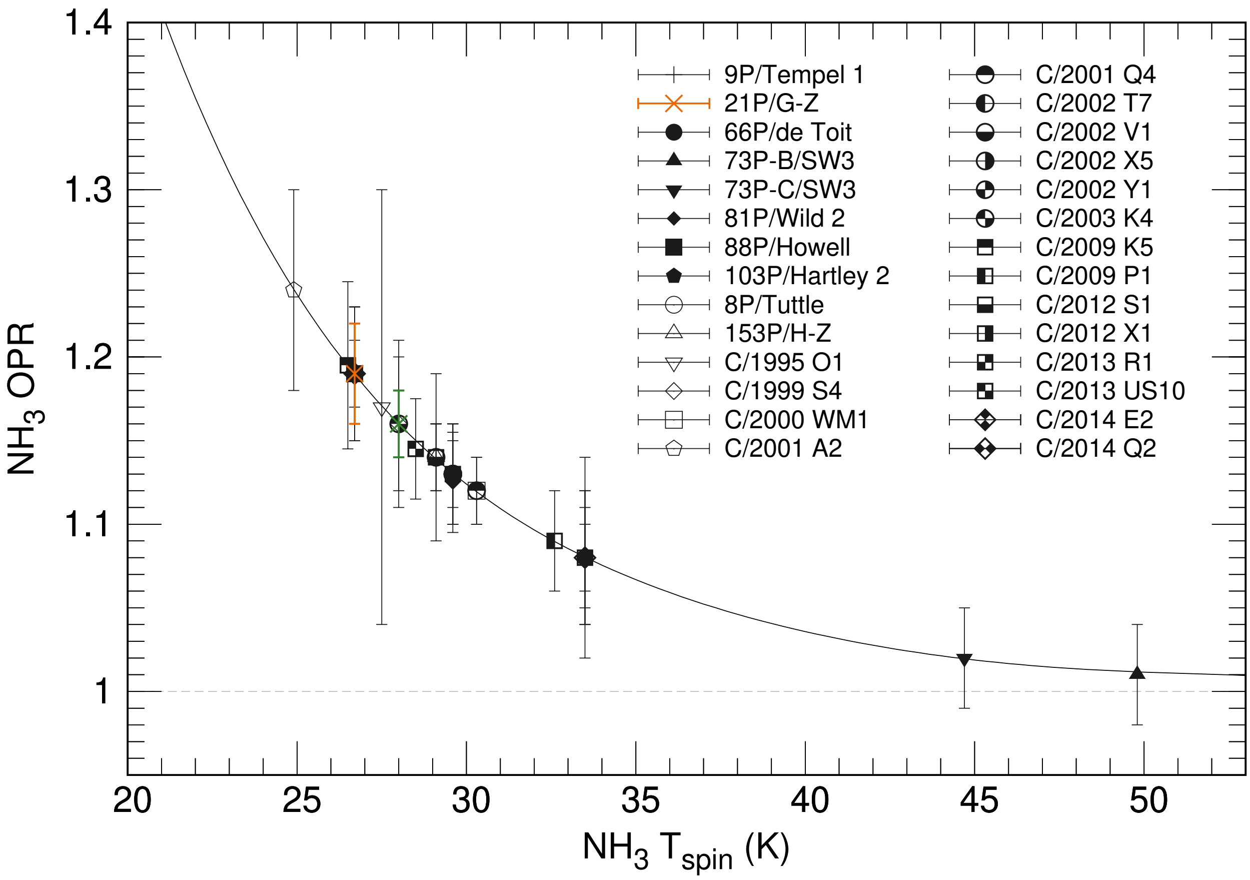

Figure 3.7: Summary of the NH_3 T_{spin} in 28 comets of various origins. The orange and green cross symbols are the NH_3 T_{spin} of 21P by VLT/UVES (this work) and by Subaru/HDS (Shinnaka et al. 2020), respectively.

Table 3.5: Orbital elements and relevant parameters of 21P at epoch 2458309.5 (July 10, 2018). Reference: JPL (K182/9)

Parameter	Value±Uncertainty (1-σ)
Epoch of perihelion passage (t_p)	2458371.77 (Sept. 10.27, 2018)
Perihelion distance (q)	$1.01281 \pm 4.2080 \times 10^{-7}$ (au)
Semi-major axis (a)	$3.49774 \pm 1.1045 \times 10^{-5}$ (au)
Eccentricity (e)	$0.71043 \pm 8.1113 \times 10^{-7}$
Inclination (i)	$31.99742 \pm 1.3367 \times 10^{-5}$ (deg)
Longitude of the ascending node (Ω)	$195.39123 \pm 3.2585 \times 10^{-5}$ (deg)
Argument of perihelion (ω)	$172.86224 \pm 6.6485 \times 10^{-5}$ (deg)
Mean anomaly (M)	$350.61663 \pm 4.7926 \times 10^{-5}$ (deg)
Jupiter Tisserand invariant (T_{jup})	2.466

3.1.6 Discussion

As mentioned above, C_2 and C_3 had been found depleted as compared to CN in 21P already more than 50 yr ago (Mianes et al., 1960; Herbig, 1976; Schleicher et al., 1987). In A'Hearn et al. (1995) data set, 21P was classified as the prototype of the group depleted in carbon-chain molecules. About 30% of the comets analyzed were found to be depleted in carbon-chain elements by varying amounts including different dynamical types of comets, two thirds are

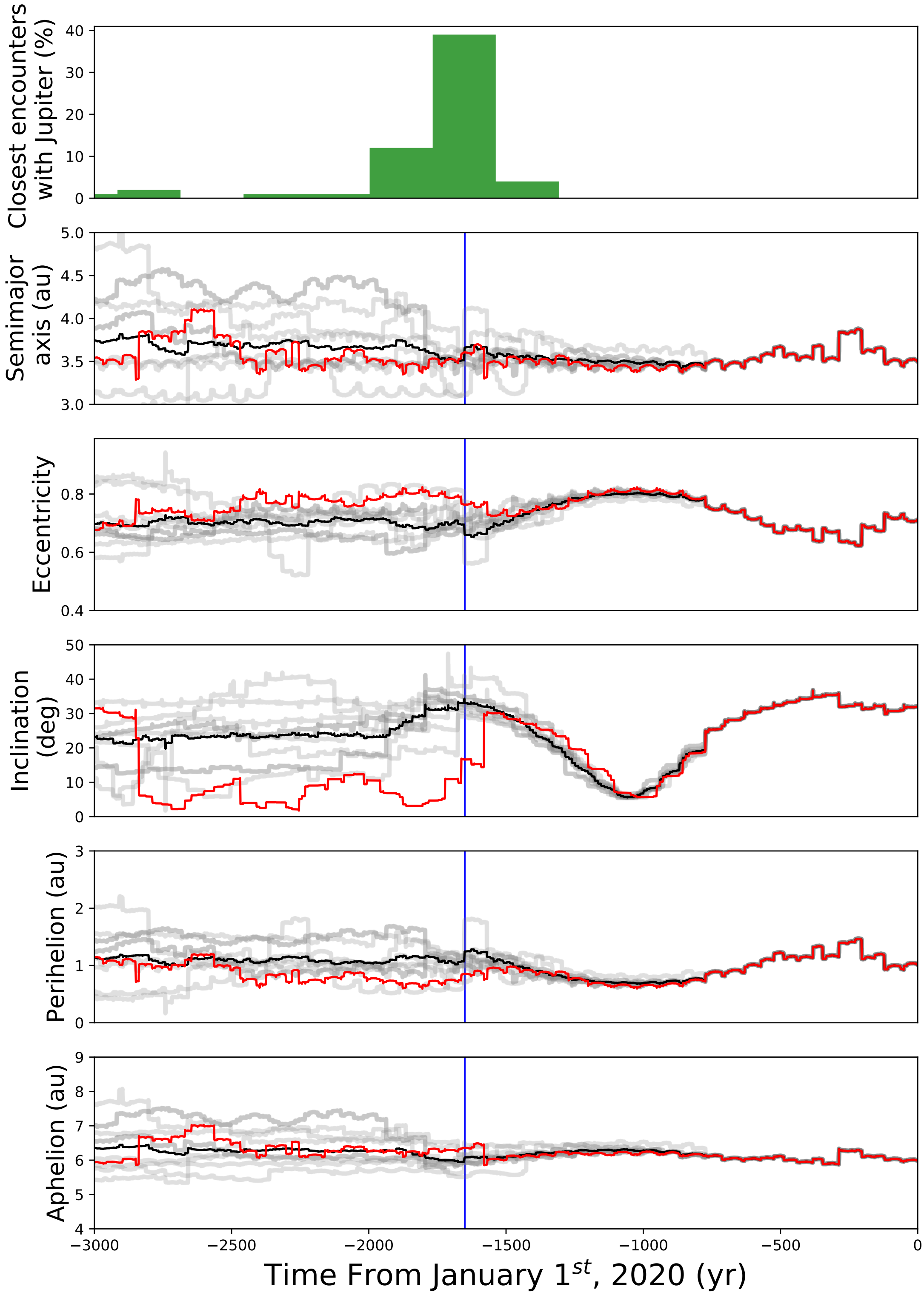

Figure 3.8: Orbital evolution of 21P and its 200 clones for 3000 yr backward in time from January 1, 2020. From top to the bottom: the closest approaches with Jupiter, semi-major axis, eccentricity, inclination, perihelion, and aphelion distance. In all panels, the gray lines correspond to the evolution of each clone, the black line is the mean value of the clones, and the red line is that of the nominal comet 21P. The blue-vertical line corresponds to the time of the closest encounter with Jupiter. The initial orbital elements were taken from the JPL Small-Body Data Browser (orbital solution JPL K182/3).

JFCs and one third are LPCs (A'Hearn et al., 1995; Schleicher, 2008; Fink, 2009; Cochran et al., 2012). 21P was found to be also depleted in NH with respect to OH (A'Hearn et al., 1995), this result was confirmed by its depletion in NH_2 using spectro-photometric observations by Konno and Wyckoff (1989) in 1985 apparition and later by Fink Uwe and Hicks (1996) in 1998 passage. This depletion in both NH and NH_2 indicates that 21P is likely depleted in the parent molecule NH_3 which was recently confirmed by (Faggi et al., 2019). 21P is not the pnly case of a comet depleted in both carbon chain and ammonia daughter species. A few others have been found, but with a lesser degree of depletion like 43P/Wolf–Harrington and the split comet 73P/Schwassmann–Wachmann 3 (A'Hearn et al., 1995; Fink, 2009; Cochran et al., 2012). This indicates that there might be a small group of similar comets that formed under similar conditions and different from other comets. But according to taxonomy studies, no clear grouping associated with NH abundance has been identified.

Our long monitoring of the abundance ratios combined with previous studies (Schleicher and Knight, 2018; Combi et al., 2011) rules out the evolutionary scenario (peculiar composition due to repeated passages to perihelion). Indeed our observations show remarkably constant abundance ratios of the different species, especially the depleted C_2 and NH, before and after perihelion, and over months. The fact that these ratios are still the same after five orbits, is in favor of a pristine composition rather than compositional changes due to repeated passages of the comet at perihelion.

It was argued that this peculiar composition might be linked to a higher formation temperature, closer to the sun (Schleicher et al., 1987), or in a local disk around Jupiter as it was proposed for comet 73P (Shinnaka et al., 2011). We obtained high resolution, high SNR optical spectra in order to investigate the C and the N isotopic ratios, as well as the NH2 OPR. 21P appears to have a normal $^{14}N/^{15}N$ ratio and a normal NH_3 OPR, similar to other comets. This is in contrast with comet 73P which has both peculiar $^{14}N/^{15}N$ and OPR (see Figure 3.7 and Shinnaka et al. (2011)). It does not seem then that both comets are related and the peculiar composition of 21P still needs to be explained. These peculiarities are clearly linked to the ice composition of the nucleus, as the Infrared studies of the mother molecules are also showing the same kind of depletion, with an obvious link to the daughter species.

3.1.7 Summary and conclusion

We performed an extensive monitoring of comet 21P on both sides of perihelion with TRAPPIST. The gas species production rates as well as the dust proxy, A(0)fρ, were measured until the detection limit. We derived the water-production rates for this apparition and we compared it, as well as the various abundance ratios, to previous passages. Using a sublimation model for the nucleus and the water-production rates, we constrained the active area of the nucleus surface using slow-rotator approach. An accurate determination of the 21P nucleus parameters is needed to better constrain the active area fraction. Comet 21P shows an asymmetric activity with respect to perihelion which might be due to the nucleus shape, the spin axis orientation, and the distribution of activity on the comet's surface. The maximum of the gas and dust activity was about 24 days pre-perihelion similar to the previous apparitions. According to the molecular abundance relative to CN and OH, we confirm that 21P is depleted in C_2, C_3 and NH with respect to CN and to OH. A very good agreement between the abundance of the potential mother molecules measured in the Infrared (HCN, C_2H_2 and NH_3) and the daughter species from our optical observations has been found. We obtained a high resolution UVES spectrum of 21P a week after perihelion and we derived $^{12}C/^{13}C$ and $^{14}N/^{15}N$ isotopic ratios of 100$\pm$10 and 145$\pm$10 from the CN R-branch of the B-X (0, 0) violet band. The ammonia OPR was found equal to 1.19$\pm$0.03 corresponding to spin temperature of 27$\pm$1 K. All these values are in agreement with those found for several comets of different dynamical types and origins and do not show any peculiarity that could be related to the low carbon chain species and ammonia abundances. Our observations are favouring a pristine origin for this composition, rather than heterogeneity or evolutionary scenarios of the surface composition.

3.2 Comet 41P/Tuttle-Giacobini-Kresak

The comet 41P/Tuttle–Giacobini–Kresak (hereafter 41P) is a JFC discovered by Horace Parnell Tuttle on May 3, 1858, and re-discovered independently by Michel Giacobini and Ubor Kresák in 1907 and 1951, respectively. The comet had two close encounters with Jupiter in 1975 and 1988 that have altered its orbit slightly. Its perihelion distance is 1.05 au and its orbital period 5.42 yr[3]. Comet 41P is famous for major outbursts that makes it highly variable in brightness. During its 1973 apparition, 41P briefly reached magnitude 4 after a major outburst (Kresak and Kresakova, 1974). The apparition of the comet in late 2000 and early 2001 was not expected to be one of the best, with a magnitude of about 12 by early January 2001. During that period, 41P was observed by the Solar and Heliospheric Observatory (SOHO). The water-production rate was $(5.20\pm0.07)\times10^{28}$ molec/s at perihelion (r_h=1.05 au, January 6, 2001). This rate was derived by modelling the observed distribution of atomic hydrogen in the cometary coma (Combi, 2017). During its 2006 apparition, the water-production rate obtained from SOHO decreased to $(1.60\pm0.08)\times10^{28}$ molec/s at perihelion (r_h=1.05 au). The last perihelion of the comet was on November 12, 2011, but it was not observed because it was on the far side of the Sun. The heliocentric light-curve of Tancredi et al. (2000) indicates that 41P has a small nucleus. Lamy et al. (2004a) estimate the nucleus radius to be about 0.7 km, but even this may only be an upper limit. The radius of 41P is less than 70% of all measured radii of JFCs (Fernández et al., 2013), so 41P can be considered as a small comet.

We have obtained 600 images of comet 41P with TN over 5 months from February 16, when the comet was at 1.27 au from the Sun and at 0.29 au from the Earth, until July 27, 2017, when the comet was at 1.69 au. Its perihelion was on April 12 at 1.0 au and the comet was at its closest distance to Earth on April 1 at only 0.14 au. We also observed 41P with TS pre-perihelion on February 25 and on March 8, 2017, with narrow- and broad-band filters. In the OH, NH, and RC filters, no signal was detected. Exposure times range from 60 to 240 s for the broad-band filters, and from 300 to 1200 s for the narrow-band filters. Most Rc, CN, and C_2 images were obtained in sets of 4-12 images per night whereas most images in other filters were obtained as single images.

3.2.1 Composition and activity

The derived production rates for each gas species and A(0)fρ values for the green, blue, and red continua are given in Table A.2 with their errors. We started to detect CN, C_2, and C_3 species at the beginning of the second half of February, 2017 (r_h=1.27 au), when the OH and NH species were detected for the first time on March 11 and March 26, respectively. The gas production rates relatively increase towards perihelion. We continued to monitor 41P until the perihelion when the comet was at 1.05 au from the Sun. The OH, NH, CN, C_2 and C_3 production rates did not vary much between March 26 and May 27, 2017. We also monitored 41P after perihelion, the CN and C_2 were detected until July 20, when the comet was at 1.63 au from the Sun, and C_3 was not detected after June 22 (r_h=1.39 au). The CN, C_2, and C_3 production rates start to decrease from May 27 until the end of monitoring. Hydroxyl (OH) was detected until May 24 (r_h=1.18 au) with a production rate of $(1.57\pm0.08)\times10^{27}$ and NH reached $(1.91\pm0.10)\times10^{25}$ molec/s on April 27. Figure 3.9 shows the production rates for all gas species in logarithmic scale as a function of time to perihelion. The OH, CN, C_3 and C_2 production rates from TN are in agreement with the few measurements obtained with TS at the beginning of the monitoring.

[3] https://ssd.jpl.nasa.gov/sbdb.cgi#top

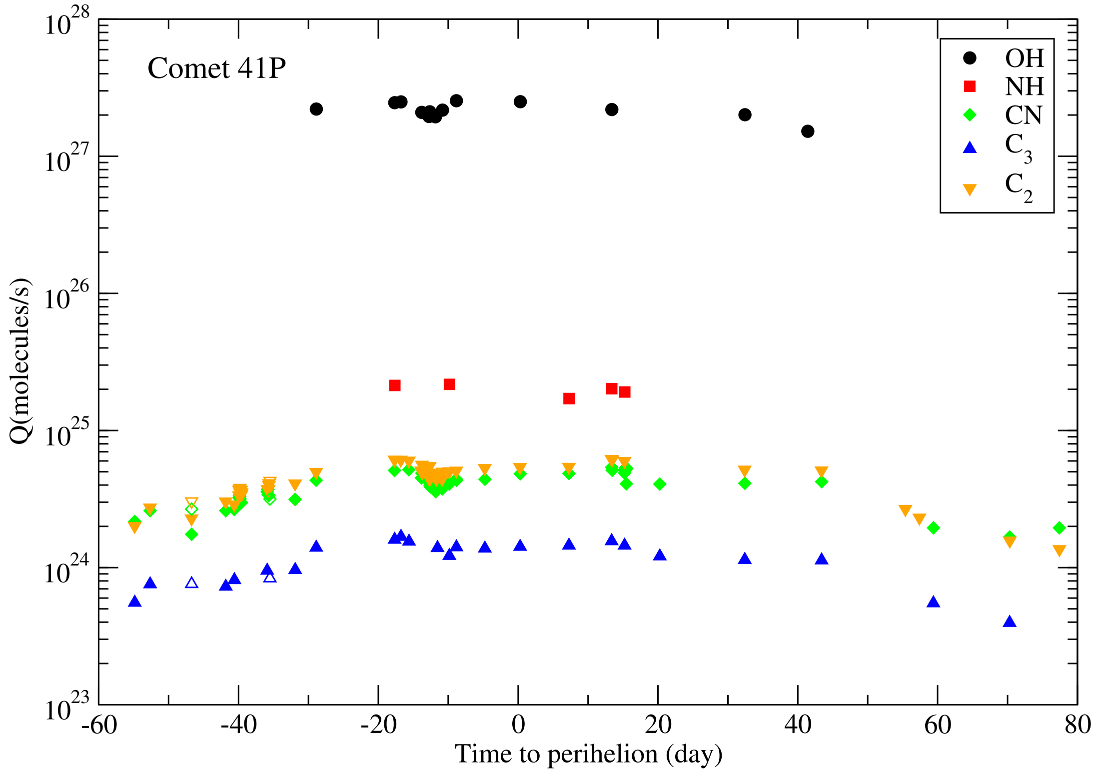

Figure 3.9: Production rates of comet 41P for each molecular species as a function of time to perihelion. The TN data are represented with filled symbols and TS data with open symbols. The values and their uncertainties are given in Table A.2.

In order to estimate the dust activity, we observed 41P with the BC, RC, and GC continuum filters in addition to the ones regularly performed with the broad-band Rc filter. The values of the A(0)fρ parameter are shown in Figure 3.10 in a logarithmic scale as a function of time from perihelion. The present paper focuses on the analysis of the activity and the gas composition. The analysis of the dust coma of 41P has been done in Pozuelos et al. (2018). These latter authors performed Monte Carlo simulations to characterise the dust environment as a function of the heliocentric distance using the model described in Moreno et al. (2012). The total amount of dust produced was roughly 7.5×10^8 kg, with a peak of activity of 110 kg/s a few days pre-perihelion. They concluded that 41P is a dust-poor comet compared to other JFCs.

Figure 3.11 presents the comparison of the water-production rates of 41P at different apparitions as a function of time to perihelion. The water-production rates, corresponding to the apparition in 2001 (black circles) and 2006 (red squares), were derived from the hydrogen Lyman-α emission observed with the SWAN instrument on board the SOHO spacecraft. For the SWAN data, 1σ stochastic errors are shown; systematic uncertainties are at the 30% level (Combi et al., 2006, 2011). Bodewits et al. (2018) used recent Swift/UVOT observations of OH emission to determine the water-production rate in 2017 (green triangles). These values are in good agreement with our TRAPPIST water-production rates. Using our data, we computed vectorial-equivalent water-production rates (blue diamonds) from our Haser-model OH production rates using equation 3.1 (Cochran and Schleicher, 1993; Schleicher et al., 1998). The water-production rate peaked around $(1.83\pm0.26)\times10^{29}$ molec/s on December 21, 2000, when the comet was at 1.07 au from the Sun and $(2.22\pm0.67)\times10^{28}$ molec/s on May 15, 2006, when 41P was at 1.10 au from the Sun (Combi, 2017). As shown in Figure 3.11, two outbursts have been detected at optical wavelengths as peaks 33 and 15 days pre-perihelion in 2001 (Kronk, 2017; Combi, 2017). However, no outburst was detected during the 2017 perihelion passage. From the data shown in Figure 3.11, we conclude that there was a $\sim$3.5$\times$ decrease in water

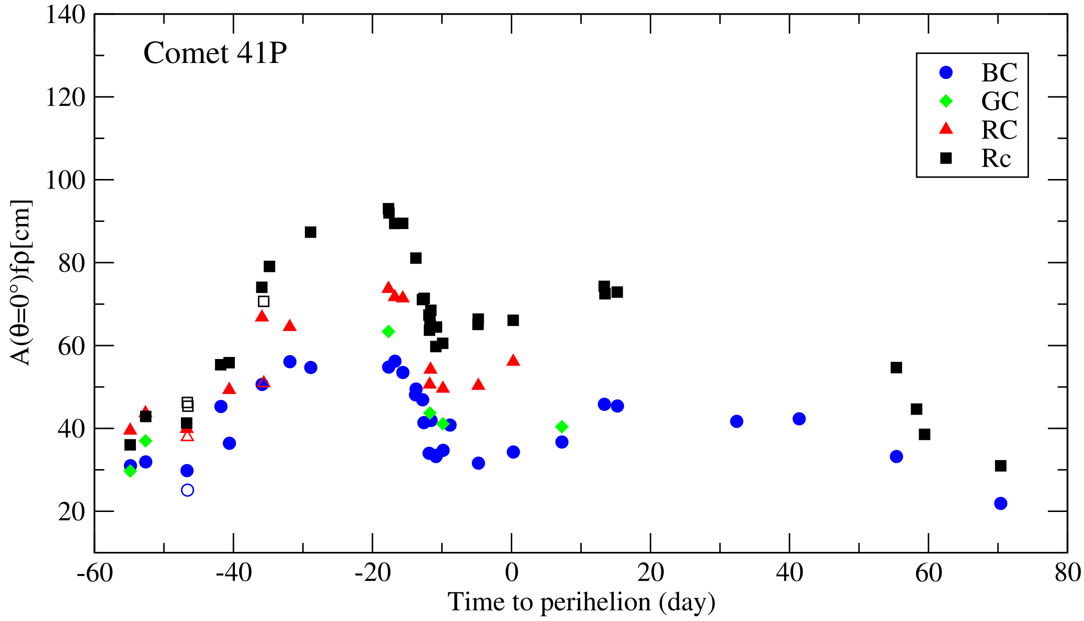

Figure 3.10: The A(0)fρ dust parameter of comet 41P for the narrow-band filters (BC, RC and GC) and for the broad-band filter Rc as a function of time to perihelion. We normalized the A(0)fρ values at 0° phase angle. The TN data are represented with filled symbols and TS data with open symbols. The values and their uncertainties are given in Table A.2.

outgassing between 2001 and 2006, for two continuous orbits (∼5 yr), and a ∼5× decrease between 2006 and 2017, an interval of two orbits. This implies a relatively consistent drop of about 30 to 40% from one apparition to the next. Generally, the distribution of active surface areas of comets correlate with the smaller nuclei (A'Hearn et al., 1995). As 41P has a small nucleus, Bodewits et al. (2018) claims that more than 50% of the surface of 41P could be active, while studies show that less than 3% of the surface of most comets is active (A'Hearn et al., 1995). We note that the water-production rates are coming from different techniques and observations at different wavelengths, which means the comparison of the results should be taken with caution.

A'Hearn et al. (1995) presented a chemical classification for 85 comets observed between 1976 and 1992 using production rate ratios with respect to CN and to OH. In order to compare 41P and 45P to this taxonomy, we computed those ratios for all the gas species. Our results show that 41P is 'typical' comets of the JF. Typical comets are defined in A'Hearn et al. (1995) as those with log[Q(C_2)/Q(CN)]$\geq$ -0.18, which was updated by Schleicher (2008) to log[Q(C_2)/Q(CN)]$\geq$ -0.11. The mean value of this quantity during our monitoring of 41P is 0.06±0.03, respectively, in agreement with the mean value given in A'Hearn et al. (1995)for JFCs (see Table 3.6). Preliminary results from the Near-Infrared Spectrograph indicate that 41P has typical C_2H_2 and HCN abundances compared to other JFCs, while the C_2H_6 abundance is similar to that of nearly isotropic comets (NICs), but is enriched compared to other JFCs (McKay et al., 2018). The logarithm of the production rate ratios with respect to CN and to OH as well as ratios of A(0)fρ/Q(OH) and A(0)fρ/Q(CN) for comet 41P are shown in Figure 3.12. Generally, the ratios do not vary significantly on both sides of perihelion, but they vary significantly more with respect to OH than with respect to CN. The C_2/CN production rate ratio (Figure 3.12(d)) stays nearly constant with perihelion distance.

We computed the A(0)fρ values in the coma at 5000 km from the nucleus and we corrected it for the phase angle effect. The mean values for log[A(0)fρ/Q(CN)] and log[A(0)fρ/Q(OH)] are -23.00±0.06 and -25.46±0.03 cm molec. s^{-1}, respectively, for comet 41P, and -22.88±0.12 and

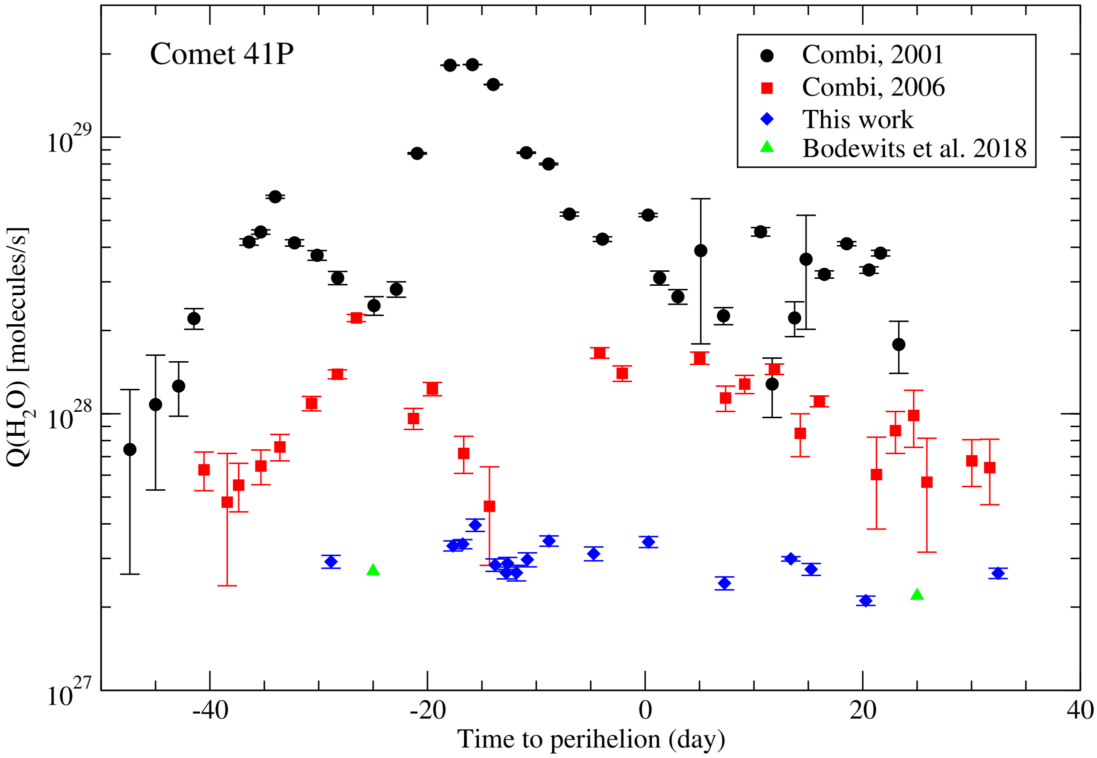

Figure 3.11: The logarithm of the water-production rate for different apparitions of comet 41P in 2001, 2006 and 2017 as a function of time to perihelion. Combi (2017) derived the production rates from hydrogen Lyman-α emission observed by the SWAN instrument onboard SOHO in 2001 (black circles) and 2006 (red squares). Our water-production rates (blue diamonds) were derived from the OH production rates using equation 3.1 given in Cochran and Schleicher (1993). The water-production rates given in Bodewits et al. (2018) are derived from the Swift/UVOT observations of OH emissions (green triangles) and are in good agreement with the TRAPPIST measurements.

-25.66±0.11 for comet 45P. As shown in Figure 3.12(e) and (j), the evolution of the dust/gas ratios of 41P is symmetric on both sides of perihelion. The relatively low dust/gas ratios for 41P is consistent with the trend of an increasing dust/gas ratio as a function of the perihelion distance found by A'Hearn et al. (1995), which they assume to be associated with thermal processing of the surfaces of cometary nuclei.

3.2.2 Coma morphology and rotation period

In this section, we discuss the morphology of the coma of 41P, which showed an important activity on both sides of perihelion. Figure 3.14 shows an example of CN, C_3, C_2, and Rc features on March 31, 2017. Even though it is slightly contaminated by the gas, we decided to use the broad-band dust filter (Rc) to show the dust features in our data because the S/N is too small in the narrow-band dust filter images for such processing. These images were obtained one week pre-perihelion. Usually, we acquired one or two C_2 and C_3 images per night, while we acquired more than six images for CN. Over most of the nights we saw CN and C_2 with sufficient S/N to detect variations of the jet positions in the coma caused by a variation of the viewing geometry. We started to detect the CN features at the beginning of March but we only saw one main jet, due to the low S/N of the images at that time. At the end of March, and as shown in Figure 3.14, we were able to see a second jet more clearly with the relative intensity and position of the jets varying with rotation. This allowed us to measure the rotation period

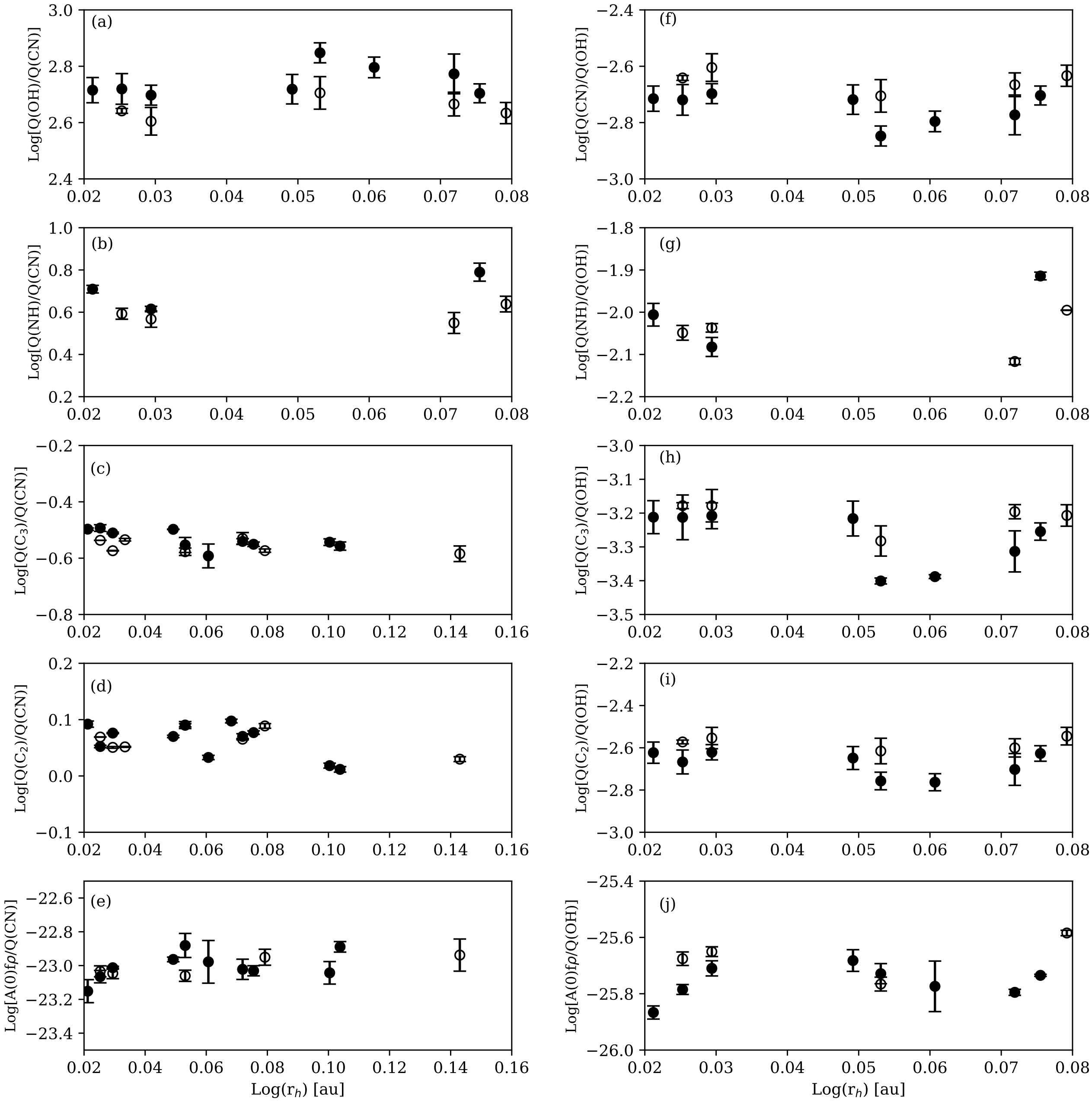

Figure 3.12: The logarithm of the production rates and A(0)fρ ratios with respect to CN and to OH as a function of the logarithm of the heliocentric distance of comet 41P. Pre-perihelion values are represented with filled symbols and post-perihelion values with open symbols.

of 41P's nucleus. This is more or less the same feature that we saw in April with an additional variation of jet position and brightness over the night. The C_3 and C_2 features are weaker than CN; they both display two short jets in opposite directions with different brightness compared to CN. These features are also weaker than the dust jet (frame Rc), and are not detected in every image during our observations. The features are not detected in OH and NH filters, due to the lower S/N in these bands. The Rc image shows an enhancement of the coma in the dust tail direction.

The changes of orientation and morphology of the features is not necessarily a direct representation of the rotation period of the nucleus. The coma morphology depends on the shape, activity, and rotational state of the nucleus of the comet, but can also be influenced by the orientation of the active regions on the nucleus, changing viewing geometry, and seasonal changes

Table 3.6: Mean of the logarithm of production rates and A(0)fρ ratios with respect to OH and to CN for comet 41P compared to those presented in A'Hearn et al. (1995).

	Log production rate ratio		
	41P	Typical comets	Depleted comets
	This work	A'Hearn et al. (1995)	
C_2/CN	0.06±0.03	0.06±0.10	-0.61±0.35
C_3/CN	-0.55±0.05	-1.09±0.11	-1.49±0.14
CN/OH	-2.70±0.04	-2.50±0.18	-2.69±0.14
C_2/OH	-2.64±0.04	-2.44±0.20	-3.30±0.35
C_3/OH	-3.25±0.03	-3.55±0.29	-4.18±0.28
NH/OH	-2.03±0.02	-2.37±0.27	-2.48±0.34
A(0)fρ/CN	-23.00±0.12	-23.30±0.32	-22.61±0.15
A(0)fρ/OH	-25.70±0.10	-25.80±0.40	-25.30±0.29

in activity (Belton et al., 1991; Jewitt, 1997; Davidsson, 2001; Keller et al., 2015). However, observing repeating changes in the morphology of the coma is still one of the best ways to determine the rotation period of a comet nucleus from ground-based observations (Samarasinha et al., 2004; Samarasinha and Larson, 2014).

We enhanced the CN narrow-band images of 41P using a simple rotational filter, as described in the section 2.3.4. Often, CN images are used to investigate the gas coma features because those images have a better S/N and are less contaminated by the underlying dust continuum. This technique has been used to measure the rotation period of several comet nuclei such as 1P/Halley (A'Hearn et al., 1986), C/2004 Q2 Machholz (Farnham et al., 2007), 8P/Tuttle (Waniak et al., 2009) and C/2012 F6 Lemmon which was observed with TS (Opitom et al., 2015).

The first two series of CN images were obtained during the nights of March 3 and 7, 2017, but it is hard to distinguish the jets in the coma because of the faint signal. Following these, we have no further long series until March 31, when we took a series of 16 images with exposure time of 600 s spanning over 8 h. Figure 3.13 shows an example of the CN coma features obtained. Two jets labelled J1 and J2 are clearly detected like partial spirals in a counter-clockwise rotation. The jets are rotating, with a position angle difference of 90° between the first and the last image of the series. Dividing the measured position angle difference by the time between the measurements, and considering that the jet is moving at the same rate throughout the entire rotation, we obtain a rotation period of about (30±5) h. The last long series is on April 27. We collected 25 images in the CN filter over 5 h. Figure 3.15 shows two examples of CN-enhanced images for this date. Two jets are detected (J2 brighter than J1) moving slowly in a counter-clockwise rotation. The change of the jets' position angle is 40° over 5 h which gives a rotation period of (50±10) h. In conclusion, with these two long series that we obtained during one month, we found a change in the rotation period of about 20 h with an average increase of 0.68 hr per day.

Several authors reported on the rotation period of the nucleus of 41P. Farnham et al. (2017) reported a rotation period of 19.75-20.05 h during March 6-9 using images of CN coma features taken with the Large Monolithic Imager on Lowell Observatory's 4.3-m Discovery Channel Telescope (DCT). Using the Lowell Observatory's 31" telescope and the same method, Knight et al. (2017) reported a change of the rotation period from 24 to 27 h during the period of March 19-27. Using the aperture photometry technique, Bodewits et al. (2018) found that the rotation

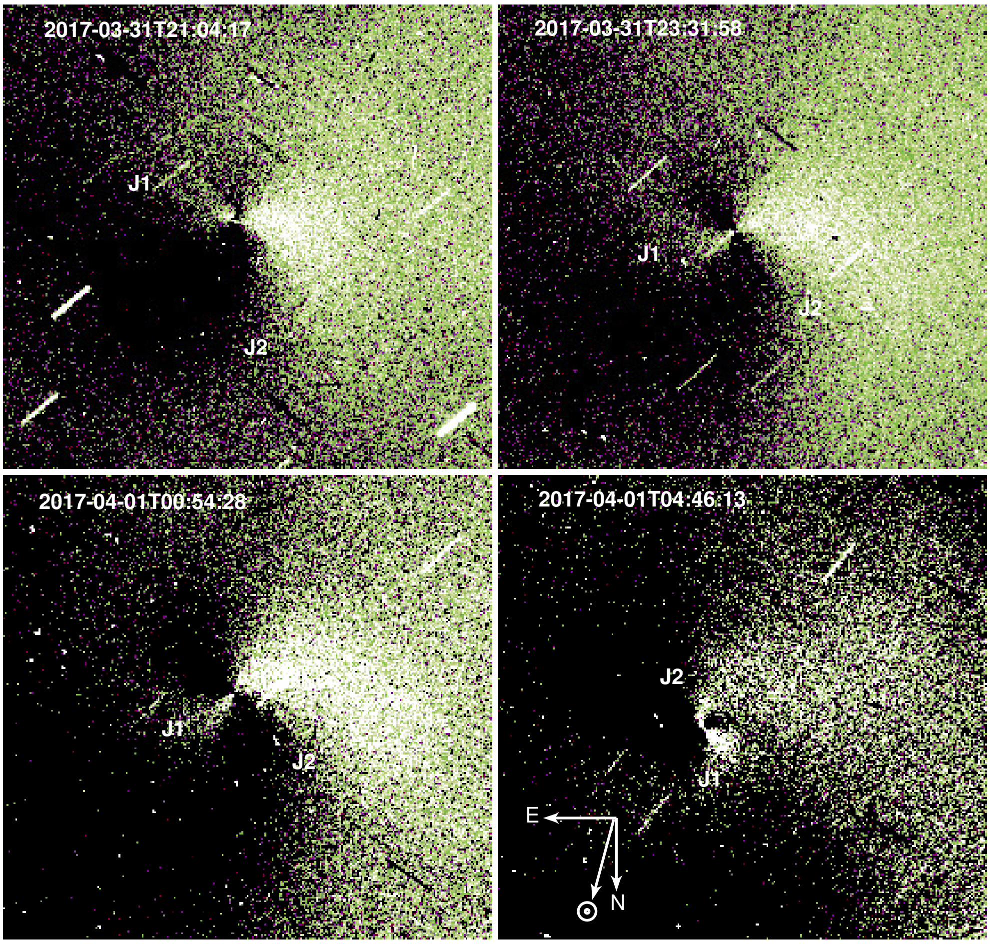

Figure 3.13: CN coma morphology of 41P on March 31, 2017 (pre-perihelion). Each image is centred on the nucleus, and has been enhanced by a simple rotational filter. The date (in UT) is indicated at the top of each frame. In all images north is down and east to the left with the direction of the Sun indicated in the bottom right frame. The field of view of each image is 8.5′× 9.8′, which covers 53120 × 26520 km.

period was changing from 46 to 60 h, with an average increase of 0.40-0.67 hr per day, during the period of May 7-9 using Swift/UVOT data (Gehrels et al., 2004). Schleicher et al. (2017) measured a rotation period of approximately 48 h on April 28. The rotation period of 41P therefore more than doubled between March and May 2017, increasing from 20 to 50 h. Our measurements are in agreement with these data. Figure 3.16 shows the evolution of the rotation period of 41P's nucleus as a function of time to perihelion. Bodewits et al. (2018) extrapolated the rotation period of the comet in time to investigate the past and future behaviour assuming that the activity level and torques, as well as the water-production rates and orientation of spin axis did not change significantly in the past. The authors found that before 2006 the comet could have been rotating with a period of only about 5 h, which is near the fragmentation limit. In the future they assume that the rotation period could exceed 100 h. They hypothesise that the rapid rotation might be linked to the bright outburst that occurred during the perihelion passage in 2001 (see Figure 3.11). This is the fastest rate of change ever measured for a comet nucleus. Pozuelos et al. (2018) found a complex ejection pattern which started as full isotropic, switched to anisotropic about 1.21-1.11 au inbound (February 24 - March 14, 2017), and then switched again to full isotropic around 1.3-1.45 au outbound. During the anisotropic ejection, they found that two strong active areas took over the dust emission, ejecting at least 90% of particles. The same authors related this result with the spin down found by Bodewits et al. (2018), in the sense that those active areas could act as brakes. All of this may suggest the

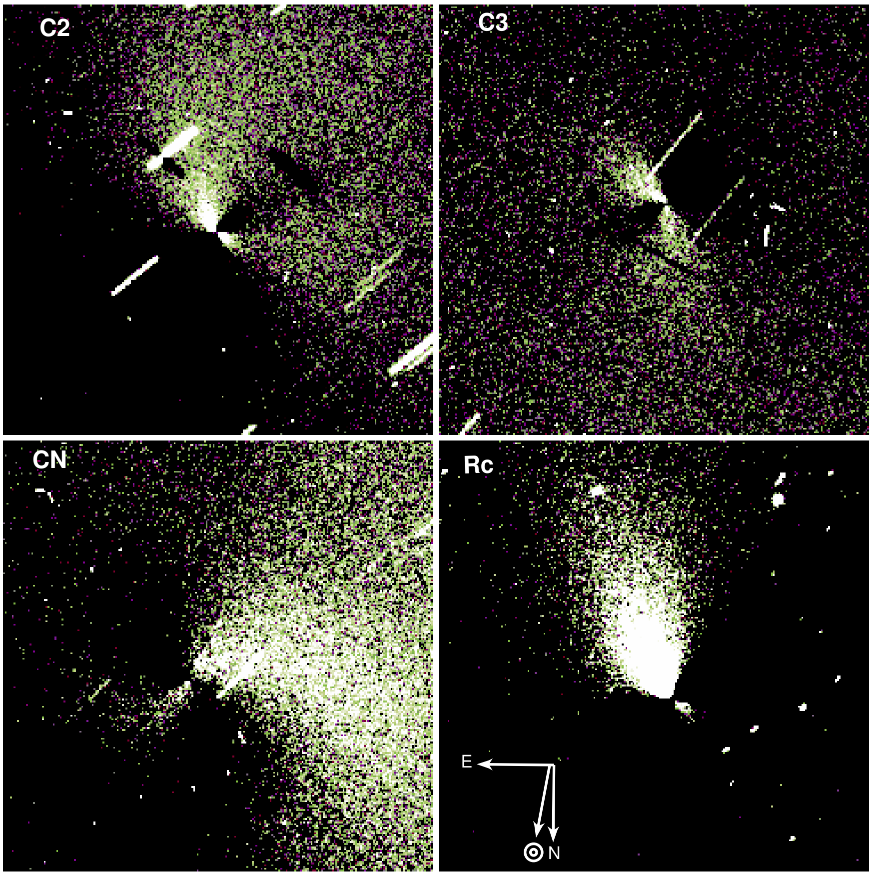

Figure 3.14: Gas and dust coma morphology of 41P on March 31, 2017. Each image is centred on the nucleus and enhanced by a simple rotational filter. The filter name is indicated at the top of each frame. All images are oriented with north down and east left with the direction of the Sun as indicated in the Rc frame. The field of view of each image is $5.8' \times 5.9'$, which covers 36600 $\times$ 37800 km.

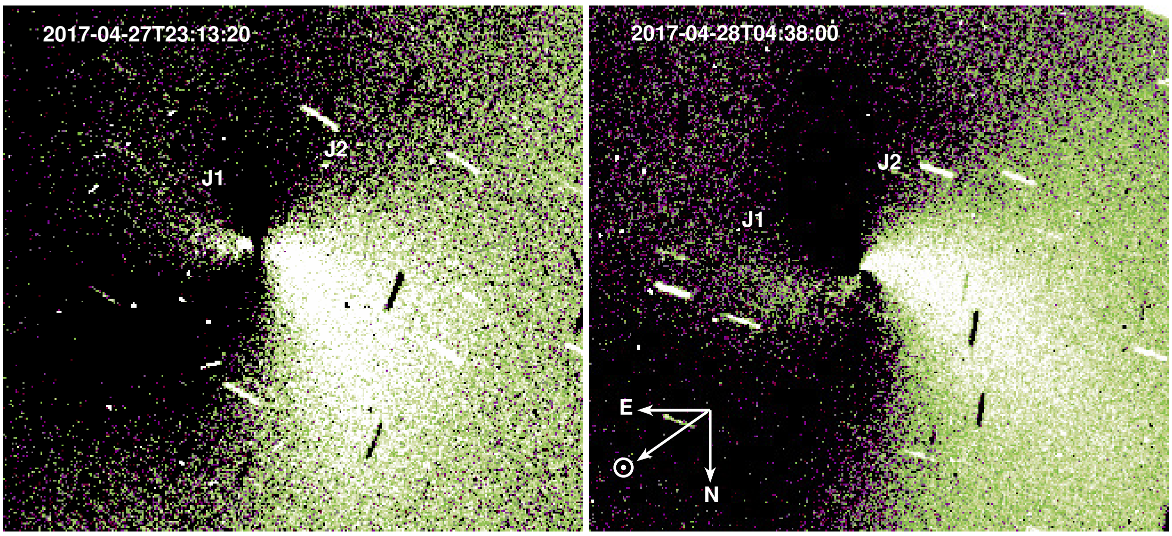

Figure 3.15: CN coma morphology of 41P on April 27, 2017 (after perihelion). The images are enhanced by a simple rotational filter. The date (in UT) is indicated at the top of each frame. In all images north is down and east to the left with the direction of the Sun as indicated in the right frame. The field of view of each image is $8.4' \times 7.6'$, which covers 67500 $\times$ 62800 km.

nucleus rapidly changes its rotation period as a result of changes in cometary activity and the strong active areas.

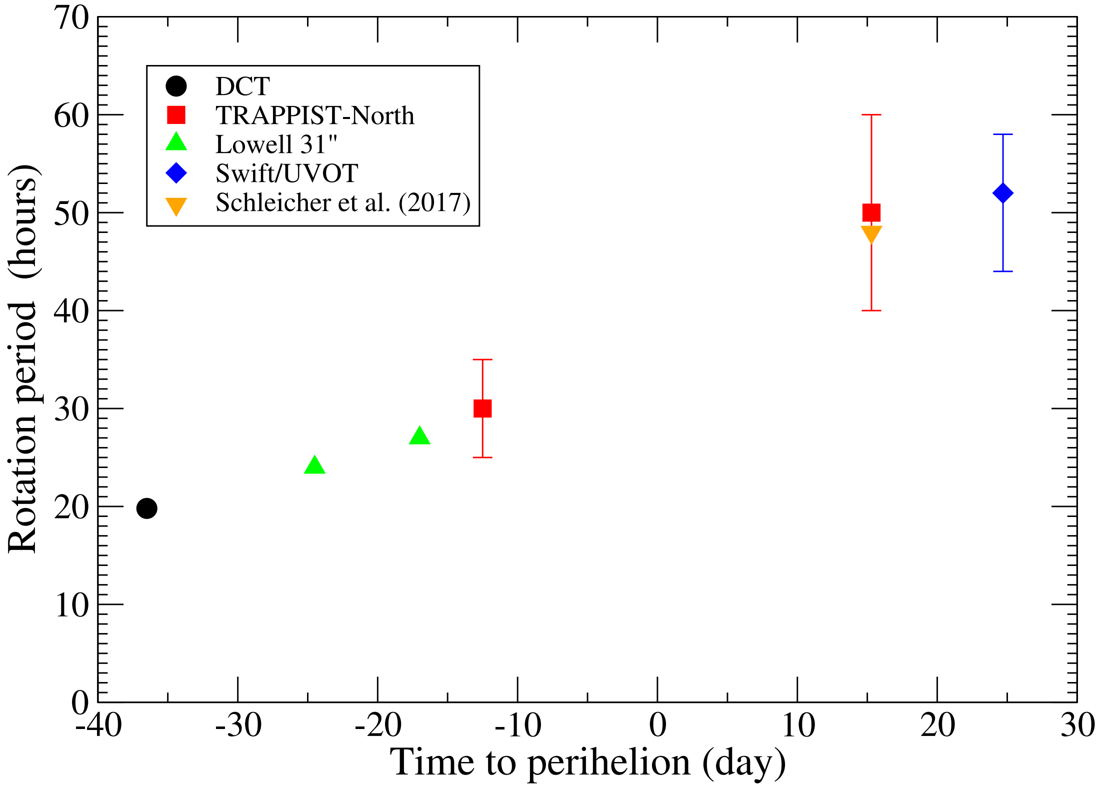

Figure 3.16: Rotation period evolution of comet 41P as a function of time to perihelion. The DCT value (black circle) is from Farnham et al. (2017). The Lowell values (green triangles) are from Knight et al. (2017). The triangle down value is from Schleicher et al. (2017). The Swift value (blue diamond) is from Bodewits et al. (2018). The error bar on the Swift observation indicates the range of possible solutions due to the uncertainty in the change of activity as a function of heliocentric distance.

Several JFCs have also shown variation of their rotation periods. The best example is 103P/Hartley 2, the target of NASA's EPOXI mission, which has a nucleus of 0.57 km in diameter and a rotation period of 17 h (A'Hearn et al., 2011). This comet showed a variation of its rotation period of 2 h in the three months around perihelion (October 28, 2010) during its return in 2010 (Knight and Schleicher, 2011; Belton et al., 2013; Samarasinha and Mueller, 2013; A'Hearn et al., 2011). However, 103P had a peak water-production rate three times higher than 41P (Jehin et al., 2010; Knight and Schleicher, 2011). In this context, we can also mention 9P/Tempel 1 (P_{rot}= 41 h), whose rotation was shown to decrease by 0.2 hr over a period of 50 days (A'Hearn et al., 1995; Belton et al., 2011; Samarasinha and Mueller, 2013; Manfroid et al., 2007). The target of ESA's Rosetta spacecraft, 67P (P_{rot}= 12 h) shows a decrease of $\sim$0.4 hr over 10 months after its perihelion passage (Mottola et al., 2014; Keller et al., 2015). Non-periodic comets have also shown changes in their rotation such as C/2001 K5 (LINEAR) (Drahus and Waniak, 2006) and C/1990 K1 (Levy) (Schleicher et al., 1991; Feldman et al., 1992). Many have shown a rotation period change, even though the amplitude in the case of 41P is rather unusual.

3.3 Comet 45P/Honda-Mrkos-Pajdusakova

The comet 45P/Honda-Mrkos-Pajdusakova (hereafter 45P) is a JFC with an orbital period of 5.25 yr. It was discovered on December 3, 1948, by Minoru Honda, Antonín Mrkos, and Ludmila Pajdušáková. Since then, it has been observed on every apparition except for its 1959 and 1985 passages, when it was too close to the Sun. Over the last few apparitions, it was close to Jupiter in 1935 and in 1983. The comet reached its perihelion on December 31, 2016 at 0.53 au from the Sun. The recent apparitions of 45P were in 2006 when the comet was on the far side of the Sun around the time of perihelion. The last apparition was in 2011 when it was well positioned for pre-perihelion observations. At that time, the comet approached the Earth within 0.06 au on August 15, 2011. Its perihelion was on September 28, 2011, and the comet reached a peak of magnitude of 7.5. The water-production rate obtained from the SOHO observatory was around 9×10^{28} molec/s when the comet was 0.54 au from the Sun and at 0.87 au from the Earth (Combi, 2017). Many authors reported on the radius of the comet nucleus, Lowry et al. (2003) obtained a mean value of r_n=0.34±0.01 km using observations performed in June 1999 with the Hubble Space Telescope. The HST snapshot observation of Lamy et al. (1999) gives a much larger value of r_n=1.34±0.55 km, but the large error bar means that r_n could be as small as 0.8 km. Using radar observations, Lejoly and Howell (2017) estimated the effective radius of 45P's nucleus to be in the range of 1.2-1.3 km with a rotation period of about 7.5 h.

We started to collect data for 45P as soon as the comet was visible from the northern hemisphere, on February 10, 2017. It was about one month after perihelion and at a distance of 0.97 au from the Sun and at its closest distance to Earth, only 0.08 au. With a perihelion at 0.53 au, the comet had a small solar elongation ($<30°$) around perihelion. Most ground-based telescopes were not able to observe this close to the Sun, which leads to a limited of data for this comet at perihelion. The comet was rising fast and it was soon visible all night. Comet 45P faded rapidly and NH was not detected during our observations. We continued to observe 45P about twice a week until the end of March when the comet was at 1.62 au. The comet was also observed with TS on February 25 and on March 8, 20-21, 2017, with narrow- and broad-band filters. No signal was detected in the OH and NH filters at that epoch.

The mean OH, CN, C_2 and C_3 production rates that we obtained for 45P during our observations were $(1.07\pm0.46)\times10^{27}$, $(1.77\pm0.05)\times10^{24}$, $(1.93\pm0.06)\times10^{24}$, and $(0.65\pm0.04)\times10^{24}$ molec/s, respectively. While NH was not detected, the OH, CN, C_2 and C_3 production rates and A(0)fρ in the broad- and narrow-band filters are given with their uncertainties in Table A.3. The evolution of comet 45P gas and dust activity as functions of time to perihelion are summarized in Figs. 3.17 and 3.18, respectively. As shown in Figure 3.17, the gas species production rates decrease after perihelion (from 0.97 au to 1.62 au from the Sun). The lack of data for this comet prevents us from computing the production-rate slopes, but the gas-production rates still show a dependence on heliocentric distance. The A(0)fρ parameter, corrected from the phase angle effect, shows a peak of 33 cm in the Rc filter around 50 days after perihelion. Subsequently, the A(0)fρ starts to decrease with heliocentric distance. 45P phase angle changes from 110° to 20° during the entire observing period. The TRAPPIST-North and -South results show a good agreement.

Comet 45P was observed by numerous observers at different wavelengths to detect the parent molecules (H_2O, NH_3, HCN and C_2H_2). DiSanti et al. (2017) reported various molecule production rates of 45P on 6-8 January, 2017 (r_{h}=0.55 au, one week after perihelion), using the high-spectral-resolution cross-dispersed facility, iSHELL, at the NASA Infrared Telescope Facility on Mauna Kea. The authors obtained a mean value of the water-production rate of 1.5×10^{28} molec/s noting a decrease during these two days. We have a mean water-production

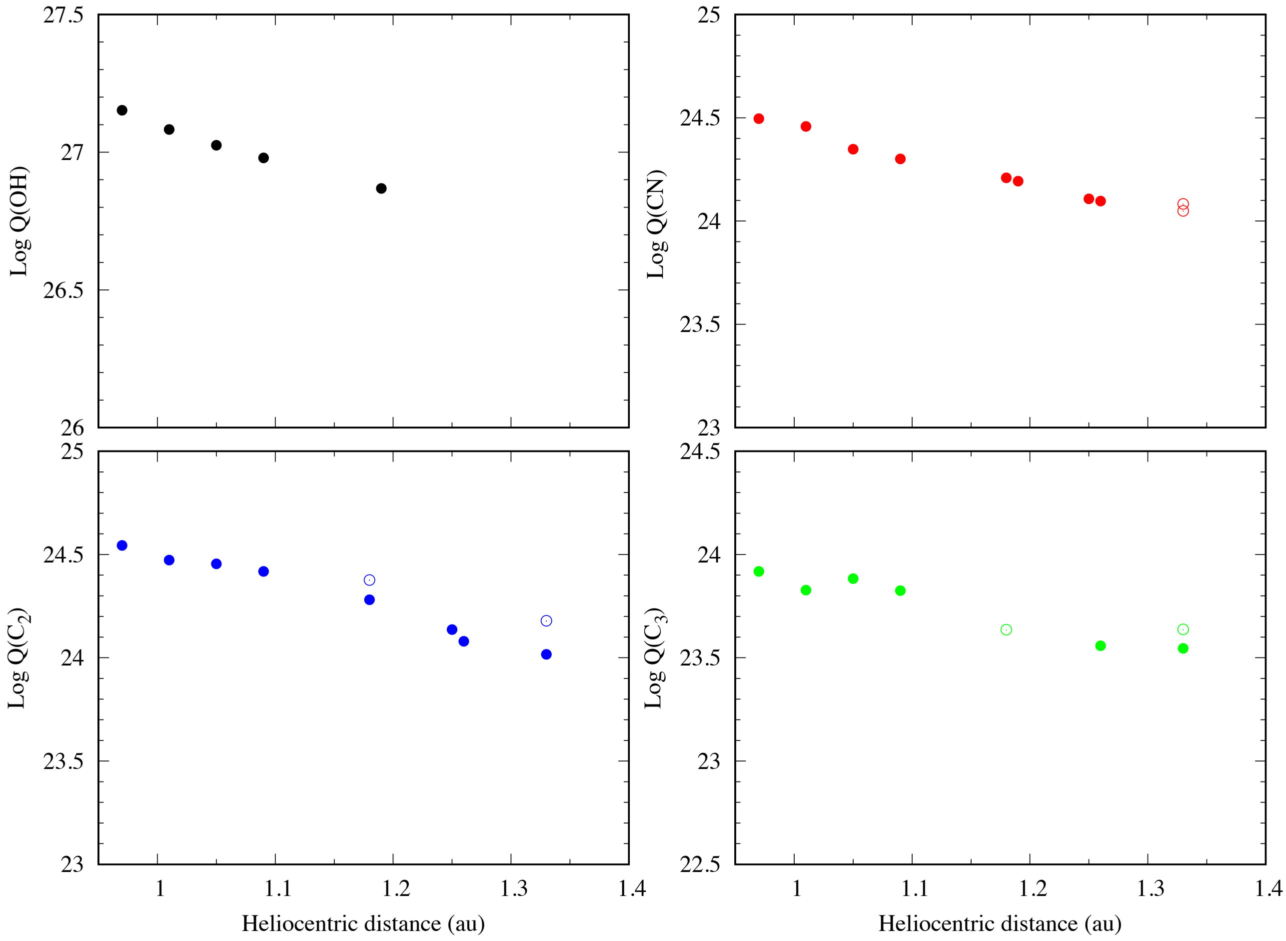

Figure 3.17: Logarithmic evolution of the production rates of comet 45P for each molecular species with the heliocentric distance. The TN data are represented with filled symbols and TS data with open symbols. The values and their uncertainties are given in Table A.3.

rate of 1.5×10^{27} molec/s. Possible reasons for this large discrepancy could be the different size of the field of view and also the technique used to derive the water-production rate. Moreover, (DiSanti et al., 2017) had observed 45P around the perihelion, while we started to observe this comet 40 days after perihelion. Using radar observations made on February 9, 2017, Lejoly and Howell (2017) detected a skirt of material around the nucleus of the comet, indicating that there is a large population of centimetre-sized grains being emitted from the comet.

Comet 45P has been observed in the past. During its passage in July 1990, it was observed from the Lowell Observatory when the comet was at 1.15 au from the Sun and 0.36 au from the Earth. The production rates obtained for five gas species were: Q(OH)=6.16×10^{26}, Q(NH)=3.80×10^{24}, Q(CN)=8.12×10^{23}, Q(C_2)=9.12×10^{22}, Q(C_3)=1.38×10^{24} molec/s and the A(0)fρ parameter was 11 cm measured at 5000 km from the nucleus. At this time, the water-production rate was about 8×10^{26} molec/s (Randall et al., 1992; Osip et al., 1992; A'Hearn et al., 1995). The comparison of these results with our mean production rate values of 45P in 2017 shows that OH and CN production rates increased by a factor 2 and C_2 increased by 20, while the production rate of C_3 decreased by 2. We conclude that 45P increased its activity between the passage in 1999 and 2017.

We computed the production rate ratios with respect to CN and to OH. Our results show that 45P is a typical comet. Typical comets are defined in A'Hearn et al. (1995) as those with log[Q(C_2)/Q(CN)]$\geq$ -0.18, which was updated by Schleicher (2006) to log[Q(C_2)/Q(CN)]$\geq$-

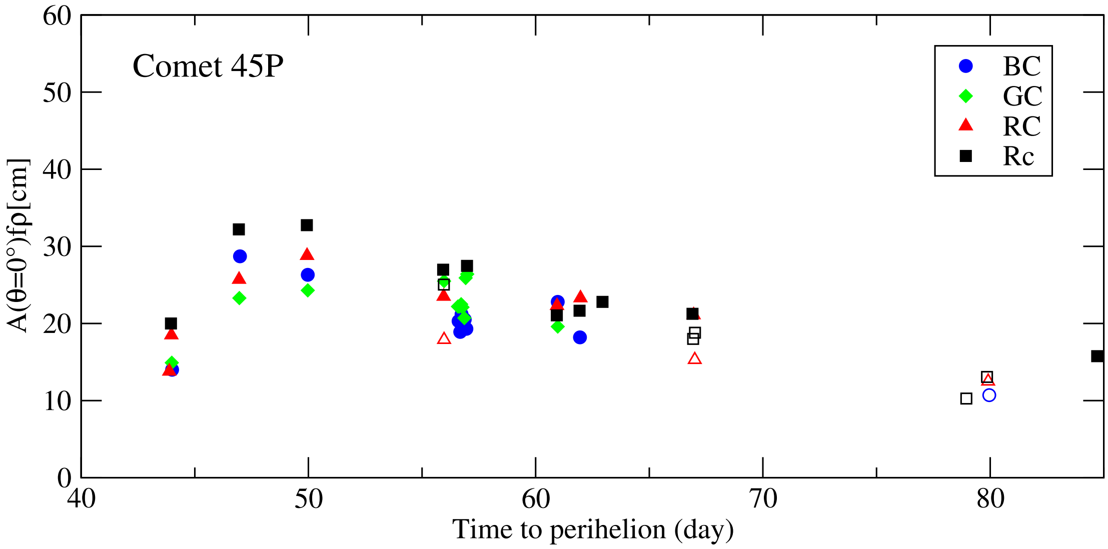

Figure 3.18: The A(0)fρ dust parameter of comet 45P for the narrow-band filters (BC, RC and GC) and for the broad-band filter Rc as a function of time to perihelion. We normalized the A(0)fρ values at 0° phase angle. The TN data are represented with filled symbols and TS data with open symbols. The values and their uncertainties are given in Table A.3.

0.11. The mean value of this quantity during our monitoring of 45P is 0.04±0.03 in agreement with the mean value given in A'Hearn et al. (1995) for JFCs (see Table 3.7). The mean values for log[A(0)fρ/Q(CN)] and log[A(0)fρ/Q(OH)] for comet 45P are -23.01±0.28 and -25.71±0.34, respectively. The relatively low dust/gas ratios for 45P is consistent with the trend of an increasing dust/gas ratio as a function of the perihelion distance found by A'Hearn et al. (1995), which they assume to be associated with thermal processing of nuclei surfaces.

Table 3.7: Mean of the logarithm of production rates and A(0)fρ ratios with respect to OH and to CN for 45P compared to the mean values presented in A'Hearn et al. (1995). The A(0)fρ values were derived from BC filter and corrected for the phase angle effect.

	Log production rate ratio		
	45P	Typical comets	Depleted comets
	This work	A'Hearn et al. (1995)	
C_2/CN	0.04±0.03	0.06±0.10	-0.61±0.35
C_3/CN	-0.45±0.04	-1.09±0.11	-1.49±0.14
CN/OH	-2.78±0.02	-2.50±0.18	-2.69±0.14
C_2/OH	-2.75±0.02	-2.44±0.20	-3.30±0.35
C_3/OH	-3.21±0.03	-3.55±0.29	-4.18±0.28
A(0)fρ/CN	-23.01±0.28	-23.30±0.32	-22.61±0.15
A(0)fρ/OH	-25.71±0.34	-25.80±0.40	-25.30±0.29

3.4 Comet 46P/Wirtanen

Comet 46P/Wirtanen (hereafter 46P) was discovered in 1948 by Carl Wirtanen. It is a JFC with a current orbital period of 5.4 yr and a perihelion distance of 1.05 au. Comet 46P was the target of the Rosetta spacecraft (Rickman and Jorda, 1998), which was re-targeted to comet 67P/Churyumov-Gerasimenko after its original launch was delayed. It was also the target of the Comet Hopper Discovery mission, which progressed through the Phase A proposal, but was not selected. Given its accessibility, it is likely that 46P will be the target of future missions as well. During the 2018 apparition, 46P made a very close approach to the Earth at 0.07 au (∼30 Lunar distances). 46P is a hyperactive comet, belonging to a small family of comets (e.g, 41P, 45P and 103P) with activity levels higher than expected based on their size. The perihelion distance of comet 46P decreased from 1.26 to 1.06 au between 1972 and its current apparition. Many studies have been done in the previous apparitions of comet 46P to determine its physical properties, including its nucleus size, shape, rotation period, albedo and colours as well as the gas and dust activity. Lamy et al. (1998) reported on the nucleus proprieties using HST images taken on August 28, 1996. They derived a nucleus radius of (0.60±0.02) km using the comet's brightness profile. They found that the colour of the nucleus is moderately red with a gradient of 10 %/1000 Å. During the 2018 passage, radar observations provided the first definitive measurements of the nucleus diameter of 1.4 km[4]. Figure 3.19 shows images of comet 46P as observed by ground and space-telescopes at different wavelengths.

46P's return was long expected, as it did an unusually close approach to Earth (0.07 au) in December 2018, about 30× the distance to the moon only and with an excellent visibility from both hemispheres. This allowed observer around the world to observe the comet in great detail with a large set of ground and space-based telescopes[5]. This closest approach provided a spatial scales of about 50 km/arcsec, which offered very nice conditions to study the inner coma of the comet in great details. Using both TN and TS, we collected observation of comet 46P over almost a year. We started monitoring the comet at the beginning of August 2018 (r_h=1.88 au) until the end of March 2019 (r_h=1.70 au). More than 2400 broad- and narrow-band images of the comet were collected over 45 nights with TS and 40 nights with TN. 46P reached its perihelion on December 12, 2018 with a distance of 1.06 au from the Sun and only at 0.08 au from the Earth. Because the comet was near opposition during its apparition, it was observable for many hours during the night in both hemispheres. This allowed us to perform series of Rc and CN images to investigate the rotation period of the nucleus using both morphology and photometric measurements.

3.4.1 Composition and activity

We followed the production rates evolution of different gas species in comet 46P over a year. The derived production rates for each gas species and A(0)fρ parameter and their uncertainties are given in Table A.4. Figure 3.20 shows the logarithmic evolution of OH, NH, CN, C_2 and C_3 production rates as a function of the distance to the Sun. Figure 3.21 shows the A(0)fρ parameter evolution for different narrow- and broad-band dust filters with respect to days from the perihelion. The gas and dust activity of the comet was increasing slightly as the comet was approaching the Sun and but decreased rapidly after the perihelion. The peak of activity of the comet occurred right at perihelion. This asymmetric activity could be due the orientation of the active regions on the comet with respect to the observer after the perihelion.

[4] https://uanews.arizona.edu/story/ua-researcher-captures-rare-radar-images-comet-46pwirtanen
[5] http://wirtanen.astro.umd.edu/46P/index.shtml

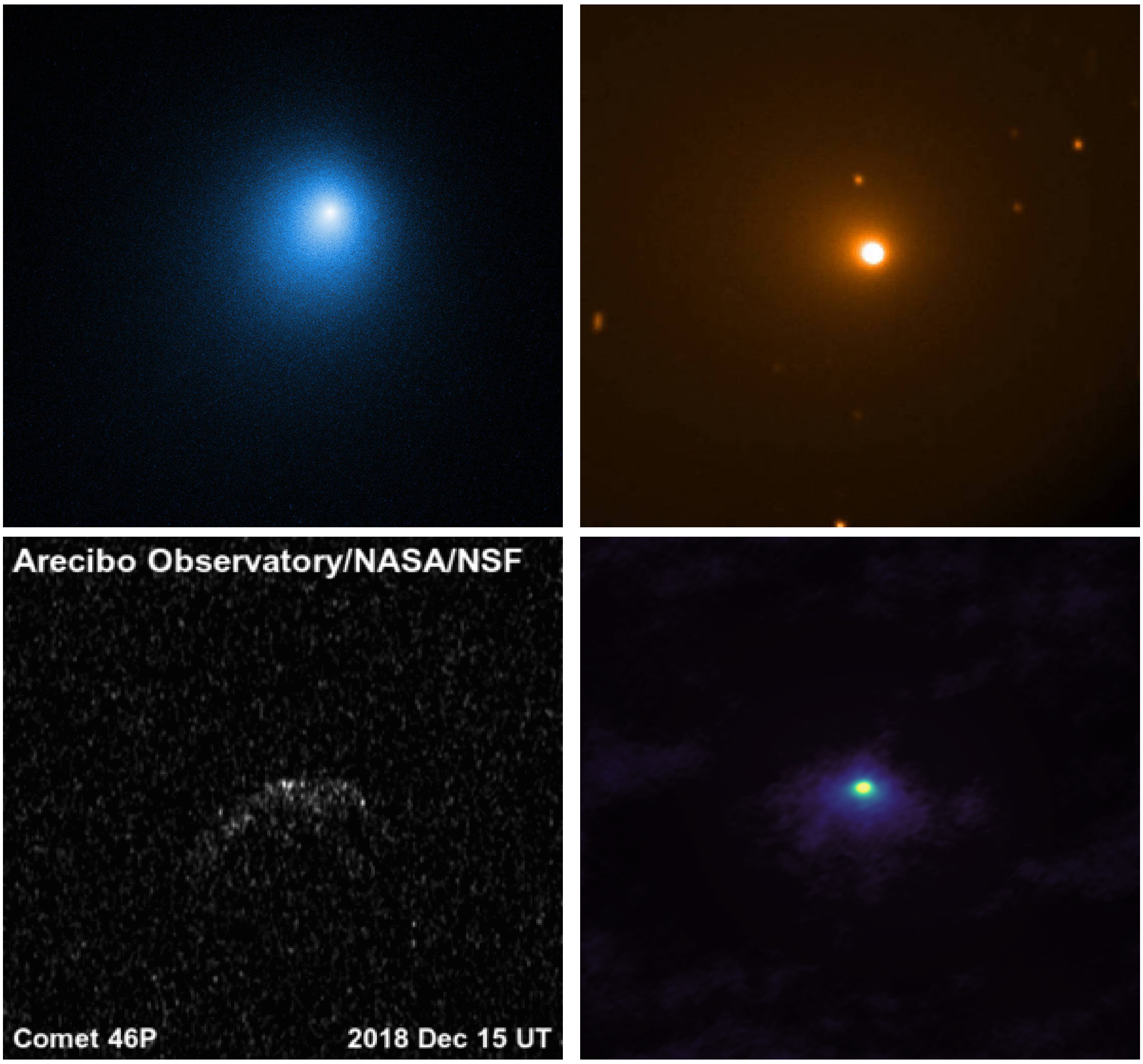

Figure 3.19: Images of comet 46P taken by the Wide Field Camera 3 (WFC3) of the HST on December 13, 2018 (top-left), by the Stratospheric Observatory for Infrared Astronomy (SOFIA) on December 16, 2018 (top right), with the Arecibo Radar Observatory on December 15, 2018 (lower left) and with ALMA observatory on December 2, 2018 (lower right).

We derived the water-production rate from the OH production rates using an empirical correlation (see equation 3.1) proposed by Cochran and Schleicher (1993) and Schleicher et al. (1998). Figure 3.22 shows the water-production rates evolution with respect to time to perihelion in 1997 and 2018 apparitions. Data shows a good agreement between the TRAPPIST and the Lowell Observatory measurements (Schleicher et al. 2018, private communication). The offset between 1997 and 2018 measurements is a systematic difference between the narrow-band and spectroscopic measurements in the optical and the measurements made from the space observations of the H Ly-α emission in the UV. We have seen this systematic offset between various techniques in previous studies of comets like 1P/Halley (Schleicher et al., 1998) and 21P/Giacobini-Zinner (Moulane et al., 2020). The maximum water-production rate in the 2018 apparition was measured on December 2 (10 days pre-perihelion) with Q(H_2O)=$(8.00\pm0.30)\times10^{27}$ molec/s, while the water-peak activity was $(1.70\pm0.20)\times10^{28}$ molec/s in 2008 apparition (Kobayashi and Kawakita, 2010) and $(1.00\pm0.10)\times10^{28}$ molec/s in 1991 and 1997 apparitions (Farnham and Schleicher, 1998; Fink et al., 1998; Bertaux et al., 1999; Crovisier et al., 2002). This result implies that there is no decrease or change in the activity of the comet over the last three decades 1991–2018, taking into account the uncertainties and

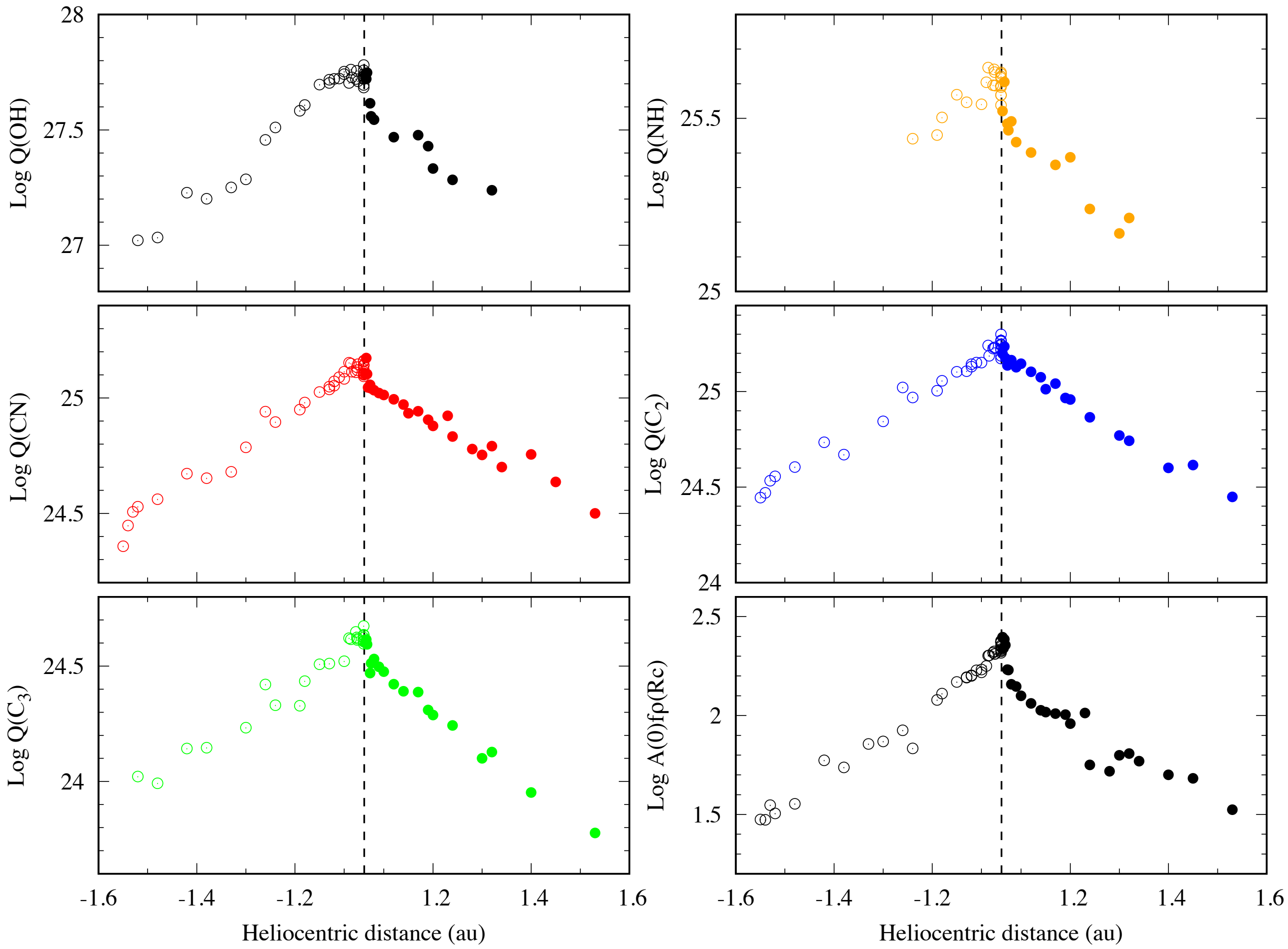

Figure 3.20: Logarithmic evolution of the production rates for each molecular species and A(0)fρ dust parameter with Rc filter as a function of the heliocentric distance. The vertical dashed line indicates the perihelion at 1.06 au. The values and their uncertainties are given in Table A.4.

systematic offset between different techniques used to derive the water-production rates. Taking the opportunity of this close approach of the comet to the Earth, Lis et al. (2019) used the GREAT spectrometer aboard the Stratospheric Observatory for Infrared Astronomy (SOFIA) to measure the D/H ratio of 46P. They derived a D/H ratio of $(1.61 \pm 0.65) \times 10^{-4}$ which is similar to that measured in the Earth's oceans 1.56×10^{-4}. This result is consistent with other measurements performed in hyperactive comets such as 103P/Hartley (Hartogh et al., 2011) and 45P/Honda-Mrkos-Pajdušáková (Lis et al., 2013).

Table 3.8 summarizes different relative molecular abundances measured in 2018 (this work) and in 1997 apparition (Farnham and Schleicher, 1998), compared to those for typical comets given in A'Hearn et al. (1995). Both measurements in 2018 and in 1997 show that 46P has a typical coma composition and a normal dust/gas ratio. Given the uncertainties on the ratios, no significant change was observed in the molecular abundances of comet 46P over the last four orbits. TRAPPIST data in 2018 passage did not show any variation in these ratios along the heliocentric distance range where the comet was observed. This implies that comet 46P has an homogeneous composition along its orbit around the Sun and over the previous apparitions. We will provide a detailed photometric analysis for the 2018 passage in a separate work (Moulane et al. in preparation).

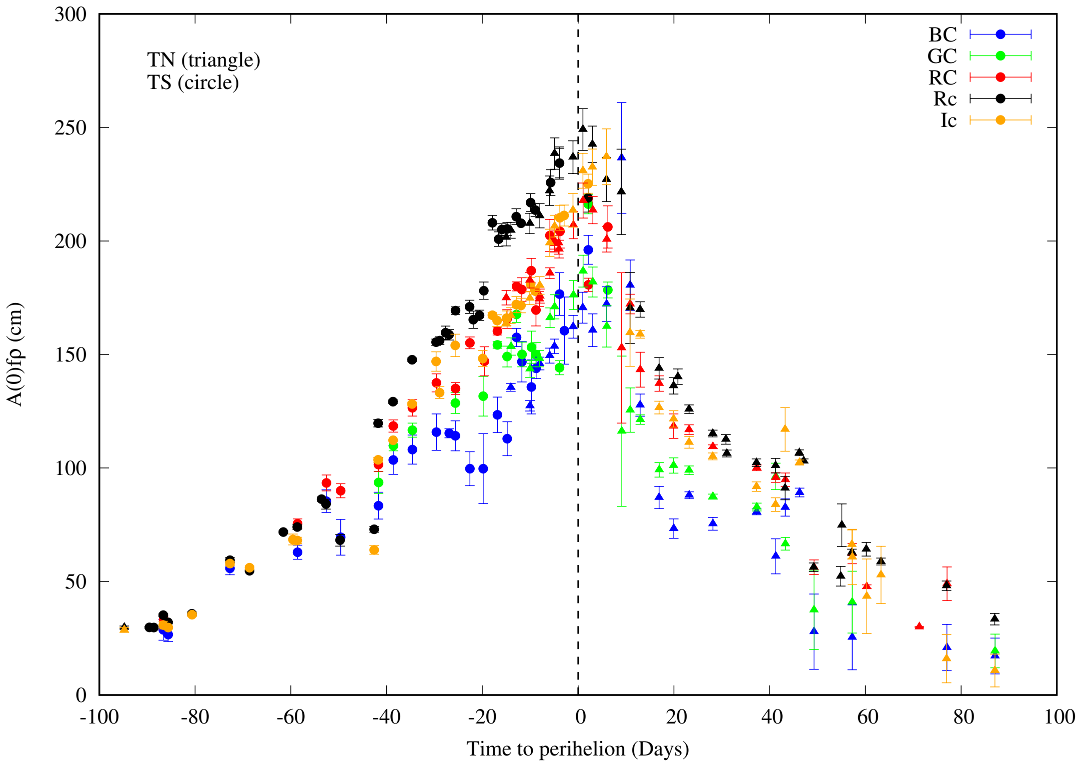

Figure 3.21: The A(0)fρ parameter in the broad- and narrow-band filters as a function of time from perihelion in days. Filled symbols for TS and open ones for TN.

Table 3.8: Mean relative molecular abundance of comet 46P for the 1997 and 2018 passages compared to those of typical and depleted comets.

	Log production rate ratio			
	1997 passage	2018 passage	Typical comets	Depleted comets
	Farnham and Schleicher (1998)	This work	A'Hearn et al. (1995)	
C_2/CN	0.10±0.10	0.08±0.04	0.06±0.10	-0.61±0.35
C_3/CN	-1.05±0.10	-0.54±0.08	-1.09±0.11	-1.49±0.14
CN/OH	-2.50±0.12	-2.57±0.06	-2.50±0.18	-2.69±0.14
C_2/OH	-2.36±0.30	-2.49±0.06	-2.44±0.20	-3.30±0.35
C_3/OH	-3.49±0.12	-3.10±0.08	-3.59±0.29	-4.18±0.28
NH/OH	-2.36±0.30	-2.10±0.06	-2.37±0.27	-2.48±0.34
A(0)fρ/CN	-23.55±0.38	-23.05±0.20	-23.30±0.32	-22.61±0.15
A(0)fρ/OH	-25.92±0.21	-25.62±0.25	-25.82±0.40	-25.30±0.29

3.4.2 Rotation period

We took the opportunity of the very close approach of comet 46P to the Earth during this apparition to investigate the rotation period of its nucleus, using long CN series images collected during the same night and at different epochs on both sides of the perihelion. Thanks to the visibility of the comet in both hemispheres, we collected long series of CN images for many hours on several nights with both telescopes. These series were taken over 12 nights with TS and 8 nights with TN, at different epochs. We determined the rotation period using the CN flux variation with the time. We tested different size apertures and we used 20″ which gave the largest amplitude of the light-curve. We phased multiple nights data to construct more extensive light-curves and searched for the best alignment of the overlapping segments.

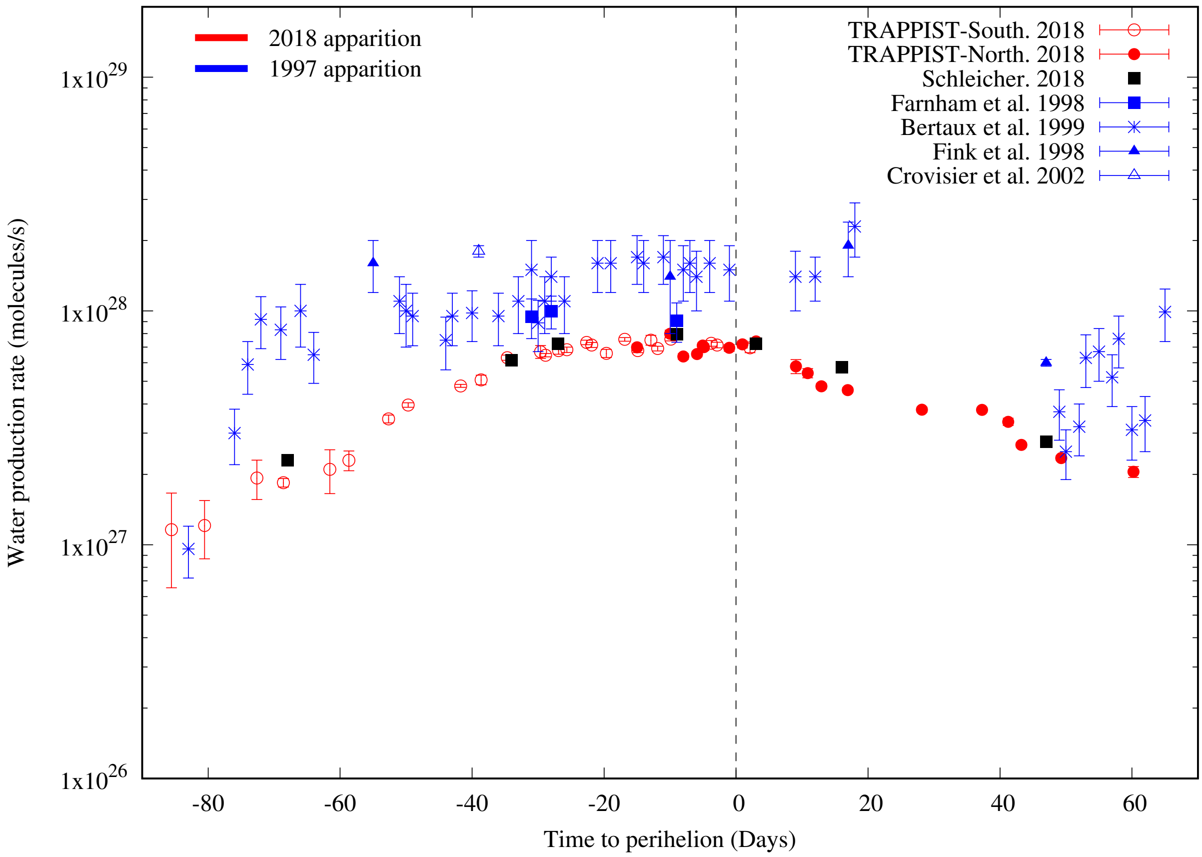

Figure 3.22: Water-production rates of comet 46P as a function of time from perihelion in days in 1997 (in blue) and in 2018 (in red) apparitions. Our measurements and those of Schleicher and Knight (2018); Farnham and Schleicher (1998) were derived from the OH production rates using equation 3.1. Fink et al. (1998) derived the water-production rate from the [OI](^{1}D) forbidden line doublet emission in the optical, Bertaux et al. (1999) values were derived from the H Ly-α emission observed by the SWAN instrument on board SOHO and Crovisier et al. (2002) values were derived from the OH emission observed at the radio wavelengths.

We derived a rotation period of 9.10±0.05 hr in late November and early December (pre-perihelion), 9.15±0.05 hr between December 7 and 10 (perihelion time) and 9.10±0.10 hr at mid January 2019 (post-perihelion). These results are in agreement, within the error-bars, with those derived by Farnham et al. (2020) from the CN coma morphology and photometry series. Table 3.9 summarizes the comparison between both measurements. Figure 3.23 shows the CN light-curves at different epochs. In all these light-curves, we detected two asymmetric maxima and minima in the light-curve which could be due to two primary active areas on the surface of the nucleus. This was confirmed by two CN spiral structures detected by Farnham et al. (2020). Given the uncertainties on the measurements, we did not detected any significant change in the rotation period of the nucleus on both side of the perihelion. During the 1997 apparition, Lamy et al. (1998) derived a rotation period of the nucleus of 6.0±0.3 using data from HST while Meech et al. (1997) found a possible rotation period of 7.6 hr and a very small amplitude variation of 0.09 mag using ground-based telescope. Based on these results, we conclude that the rotation period of the 46P nucleus might have increased by 16% to 45% over the last four orbits. These changes might be due to some unusual activity in the previous apparitions. There is some evidence for potentially significant outburst activity during the 2002 apparition (Combi et al., 2020b) that could explain these changes.

Table 3.9: Rotation period of 46P nucleus at different epochs.

Epoch	Date UT	Rotation period (hour)	
		This work	Farnham et al. (2020)
Pre-perihelion	November 23-28, 2018	9.10±0.05	9.03±0.04
Perihelion	December 7-10, 2018	9.15±0.05	9.14±0.02
Post-perihelion	January 12-15, 2019	9.00±0.10	9.01±0.01

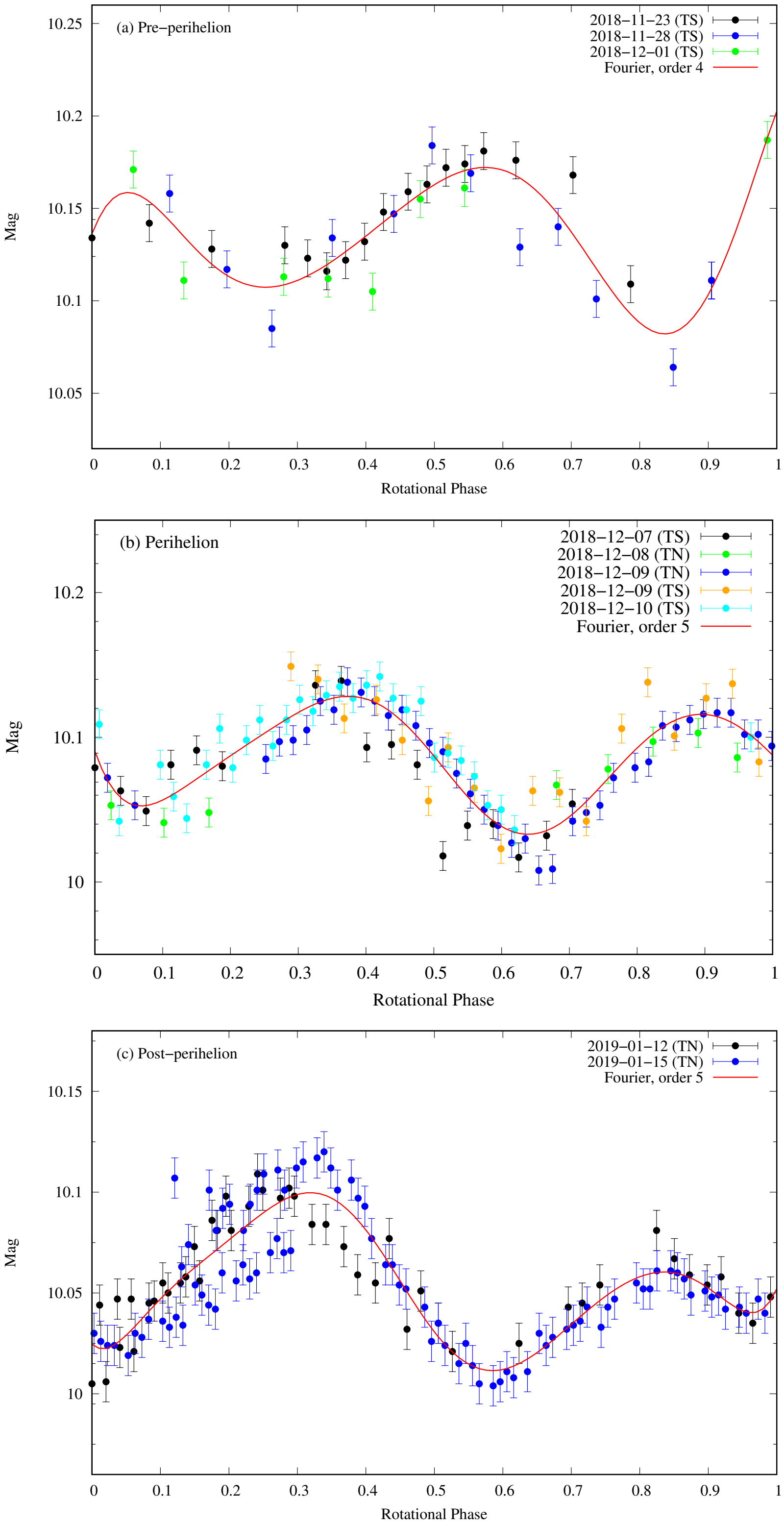

Figure 3.23: Phased CN light-curves for the rotation period of comet 46P at different epochs. (a) pre-perihelion with 9.10±0.05 h, (b) perihelion with 9.15±0.05 h and (c) post-perihelion with 9.00±0.10 h. The red curve shows the Fourier fit, at given order, of the data.

3.4.3 Coma morphology

We investigated the coma morphology of comet 46P using narrow- and broad-band filters using the simple rotational filter technique (see section 2.3.4). We detected a clear spiral jet in both the gas and dust images. Figure 3.24 shows the evolution of the CN jet at different epochs on both sides of perihelion. We did not detect any clear rotation of this jet with the time in our images for many hours during the same night, this could be due the orientation of the jet towards the Earth (geometry view). Around November 16, another small jet appeared in the CN images but it disappeared in the following nights. This could suggest that 46P nucleus could be in a non-principal axis (NPA) rotation state as was argued previously by Samarasinha et al. (1996). The orientation of the jet remains at the same direction before the perihelion while it changed by $\sim$ 95 degrees counterclockwise after perihelion, because of the viewing geometry of the comet with respect to Earth. Farnham et al. (2020) used the 4.3-m Lowell Discovery Telescope to investigate the CN coma morphology features of 46P. They were able to reveal two spiral jets in the coma. The first one appears to have been active (at varying levels) throughout most of a rotation, corresponding to the bright jet detected in our data. The second seems to turn on and off with time, and it could correspond to the small jet that appears around mid November in our images.

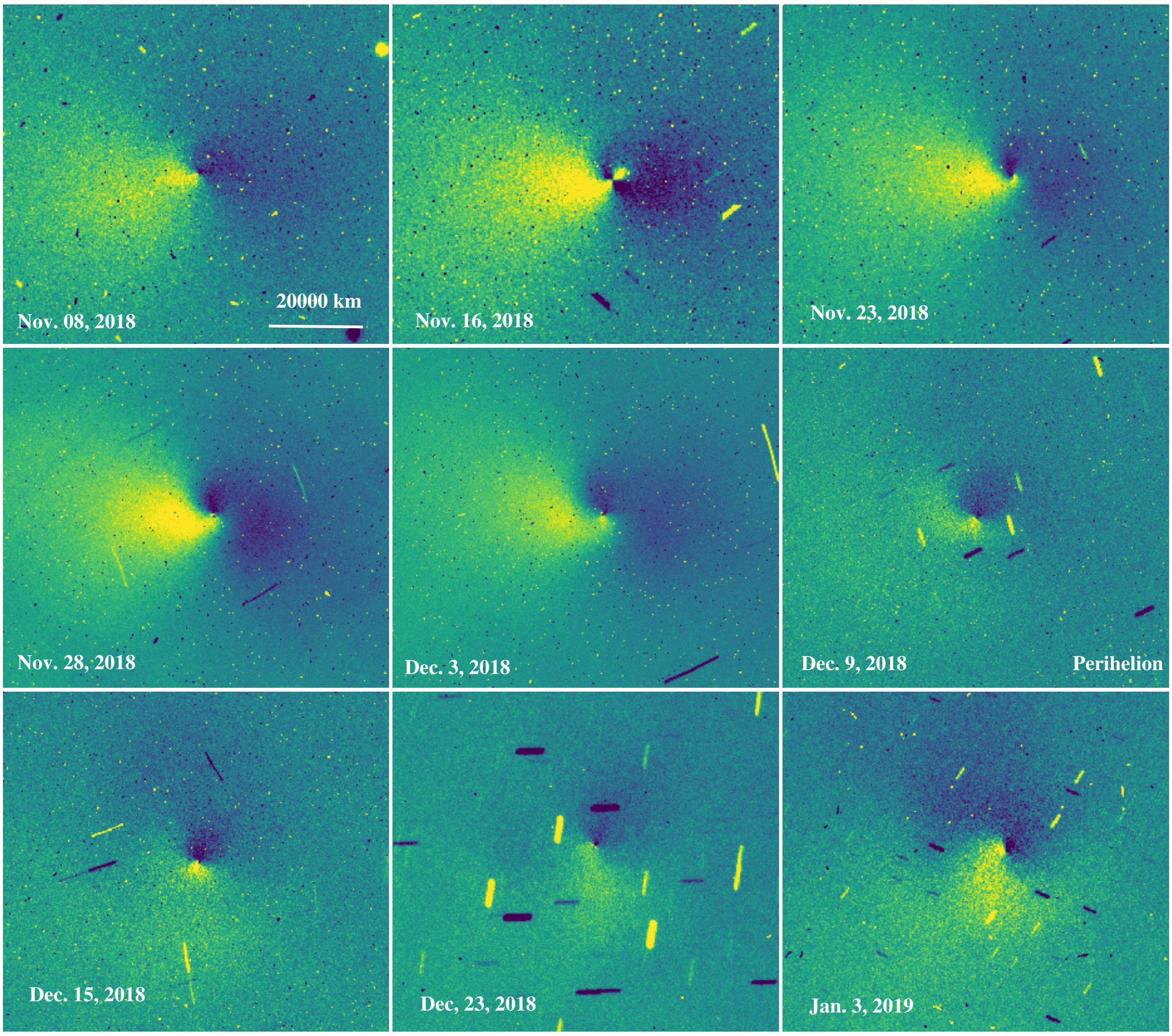

Figure 3.24: Evolution of the CN jets of comet 46P along its orbit around the Sun. The images are oriented north up and east right.

3.5 Comet 64P/Swift-Gehrels

Comet 64P/Swift-Gehrels (hereafter 64P) was discovered on November 17, 1889 by Lewis Swift at the Warner Observatory. The comet was re-discovered later by Tom Gehrels on February 8, 1973 at the Palomar Observatory at magnitude 19 with a compact coma, but no tail could be detected at the time of discovery[6]. 64P is a member of the JFCs with an orbital period of 9.41 yr. The comet reached its perihelion on November 3, 2018 at a heliocentric distance of 1.39 au. During this apparition, an outburst of 2.7 magnitude was discovered in the Zwicky Transient Facility (hereafter ZTF) data on August 14.41, 2018 when the comet was at 1.7 au (Kelley et al., 2018). Three other small outbursts have been identified following this event. These outbursts occurred on August 27.37 (0.48 mag), September 7.33 (0.23 mag), and 10.33 UTC (0.23 mag) (Kelley et al., 2019a). After its first large outburst, we started collecting observations of 64P with TN on August 15, 2018 when the comet was at 1.70 au from the Sun and at 0.82 au from the Earth. We collected only images for three nights on August 15, 17, and 20, and we did not observe the comet until October 21, 2018. CN and C_2 have been detected since the first observation after the outburst in mid August, while OH, NH and C_3 were detected later in October and the beginning of November, respectively.

The derived production rates for each gas species and A(0)fρ parameter and their uncertainties are summarized in Table A.5. Figure 3.25 shows the logarithmic evolution of OH, NH, CN, C_2 and C_3 production rates and the A(0)fρ parameter with BC filter as a function of heliocentric distance. The comet reached its maximum activity on December 14, a month after the perihelion, with a water-production rate of $(7.80\pm0.25)\times10^{27}$ molec/s. Then, its activity started decreasing slightly until the end of the monitoring on March 9, 2019 (r_h=2.00 au). The dust and gas activity have the same behavior over the period of our monitoring. During its apparition in 2009, Ootsubo et al. (2012) derived production rates of $Q(H_2O)=(6.04\pm0.65)\times10^{26}$, $Q(CO_2)=(1.46\pm0.15)\times10^{26}$ and an upper limit of $Q(CO)< 3.16\times10^{26}$ molec/s from Infrared observations when 64P was at 2.27 au from the Sun. This provides a production rate ratio $Q(CO_2)/Q(H_2O)=$ 24%, which is comparable with the comets observed within 2.5 au (Ootsubo et al., 2012; Bockelée-Morvan et al., 2004).

We derived the production rates ratios for different gas species with respect to CN and to OH as well as the dust/gas ratios represented by A(0)fρ/CN and A(0)fρ/OH. Table 3.10 summarizes these ratios compared to those of typical and depleted comets presented in A'Hearn et al. (1995). Based on the criteria of typical comets defined in A'Hearn et al. (1995) and later in Schleicher (2008), comet 64P has a typical composition and a normal dust/gas ratio with respect to mean value of typical comets. We did not see any significant changes in the molecular abundances ratios along the heliocentric distance range (1.40 au - 2.00 au) where the comet was observed.

[6] http://cometography.com/pcomets/064p.html

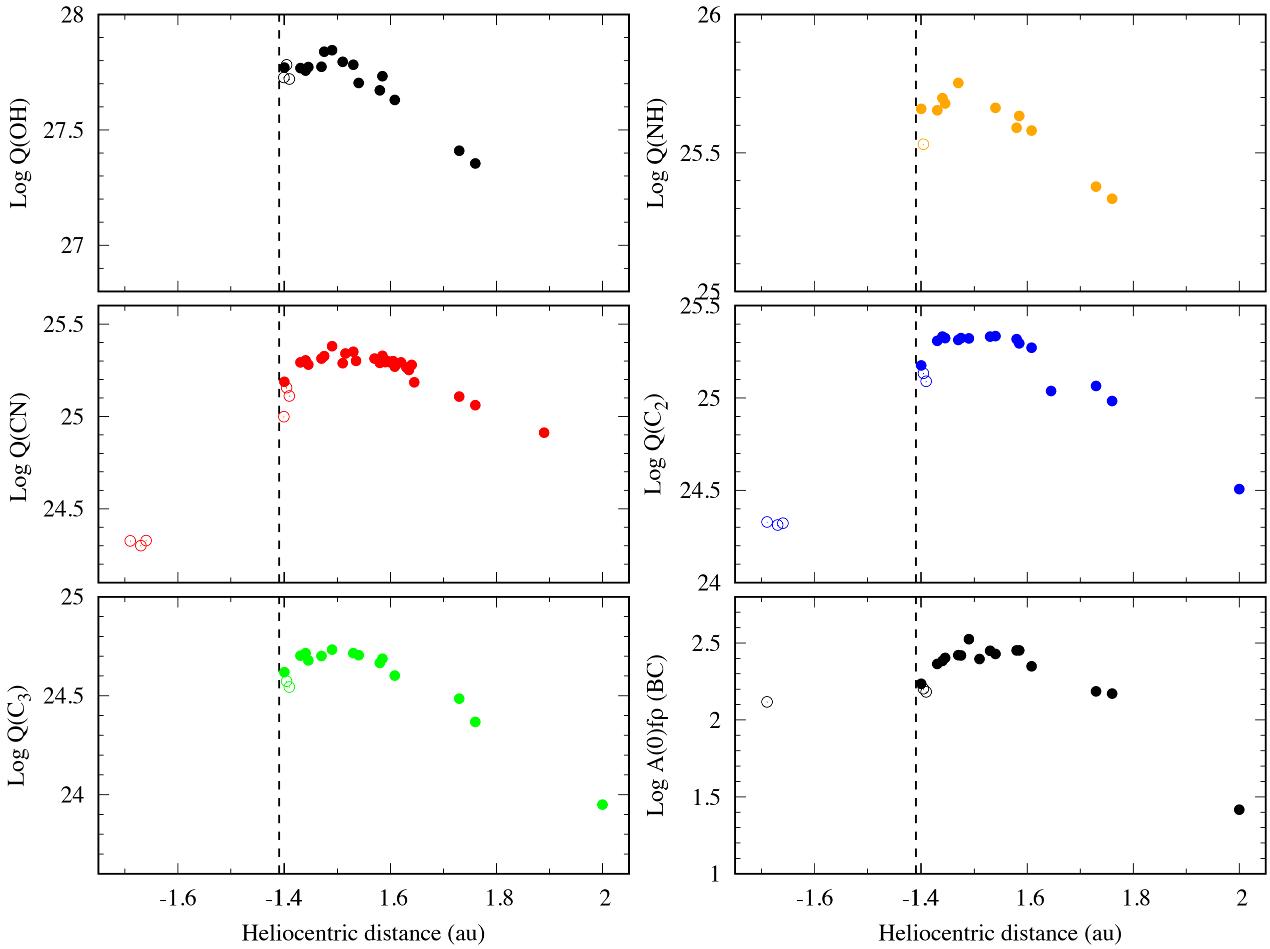

Figure 3.25: Logarithmic evolution of the production rates for each molecular species and A(0)fρ dust parameter from the BC filter of comet 64P as a function of the heliocentric distance. The vertical dashed line indicates the perihelion at 1.39 au. The values and their uncertainties are given in Table A.5.

Table 3.10: Mean relative molecular abundances of comet 64P compared to those of typical and depleted comets.

	Log production rate ratio		
	64P	Typical comets	Depleted comets
	This Work	A'Hearn et al. (1995)	
C_2/CN	0.05±0.04	0.06±0.10	-0.61±0.35
C_3/CN	-0.65±0.15	-1.09±0.11	-1.49±0.14
CN/OH	-2.47±0.11	-2.55±0.65	-2.69±0.14
C_2/OH	-2.46±0.09	-2.46±0.39	-3.30±0.35
C_3/OH	-3.06±0.07	-3.12±0.68	-4.18±0.28
NH/OH	-2.07±0.06	-2.23±0.22	-2.48±0.34
A(0)fρ/CN	-22.91±0.27	-23.30±0.32	-22.61±0.15
A(0)fρ/OH	-25.36±0.12	-25.82±0.40	-25.30±0.29

3.6 Comet 66P/du Toit

Comet 66P/du Toit (hereafter 66P) was discovered by D. du Toit on May 17, 1944 at Harvard College Observatory (South Africa) with a magnitude 10, and it is confirmed by H. van Gent (Union Observatory, South Africa) on May 23, 1944 with an estimation of magnitude of 11[7]. 66P is a JFC Near-Earth Object(NEO) with an orbital period of 14.78 yr. Fernández and Sosa (2015) identified that comet 66P is one of a group of comets that might originate from the main asteroid belt, regarding to their dynamical stability and weaker activity. We performed a detailed spectroscopic, photometric and dynamical evolution study of this object in Yang et al. (2019). In this section, we focus on the composition and activity evolution of the comet with TRAPPIST. We monitored the activity of 66P around its perihelion (r_{h}=1.29 au) with TS. Since its discovery in 1944, 66P showed a highly variable appearance during its previous perihelion passages with its visual brightness varying between 10th and 20th magnitude. We monitored the activity of this comet for 2 months, from May 6 to July 13, 2018. During this period, we detected the strong CN, C_2, and C_3 emissions on most of the nights while OH was only detected two times with a low SNR. NH was not detected due to the weak activity of this comet.

The OH, CN, C_2, and C_3 production rates as well as the A(0)fρ values of 66P are given in Table A.6. 66P's activity did not change much around perihelion (1.30-1.29 au) but it started to decrease at 1.37 au. We estimate a water-production rate of about $(3.24\pm0.17)\times10^{27}$ molec/s around perihelion derived from the mean values of Q(OH). We computed the mean production rate ratios of CN/OH, C_2/OH, and C_2/CN as well as the A(0)fρ/gas ratios such as A(0)fρ/OH and A(0)fρ/CN. Table 3.11 summarizes these ratios and the comparison to the typical values of comets based on narrow-band photometry survey over 100 comets, given in A'Hearn et al. (1995). Our results show that the mixing ratio of various carbon-chain molecules of 66P are compatible with the composition of typical comets.

Table 3.11: Mean production rate ratios and A(0)fρ/gas ratios for comet 66P compared to those of typical and depleted comets given in A'Hearn et al. (1995).

	Log production rate ratio		
	66P/du Toit	Typical comets	Depleted comets
	This work	A'Hearn et al. (1995)	
C_2/CN	0.04±0.02	0.06±0.10	-0.61±0.35
C_3/CN	-0.56±0.09	-1.09±0.11	-1.49±0.14
CN/OH	-2.51±0.04	-2.55±0.65	-2.69±0.14
C_2/OH	-2.50±0.03	-2.46±0.39	-3.30±0.35
C_3/OH	-3.02±0.02	-3.12±0.68	-4.18±0.28
A(0)fρ/CN	-23.02±0.03	-23.30±0.32	-22.61±0.15
A(0)fρ/OH	-25.53±0.03	-25.82±0.40	-25.30±0.29

Although 66P is a weakly active comet, thanks to its close distance to the Earth at the time of observations, several gas species were detected both with X-shooter/VLT and TRAPPIST. Figure 3.26 shows the OH, NH, CN, C_2 and C_3 emission features in the UV and optical spectra taken with X-shooter/VLT on July 08 and 14, 2018. The reflectance spectrum of 66P closely resembles the mean spectrum of the D-type asteroids, which is much redder than the spectra of the known MBCs. The Q(CN)/Q(OH) and Q(C_2)/Q(OH) of 66P are slightly lower than

[7] http://cometography.com/pcomets/066p.html

for other JFCs. However, its relative abundance ratios are within the normal values of over 85 typical comets studied in (A'Hearn et al., 1995). We note that 66P was observed only within a narrow time window. Nevertheless, the TRAPPIST observations were made at typical heliocentric distances for other JFC observations, so it is reasonable to compare our results with them.

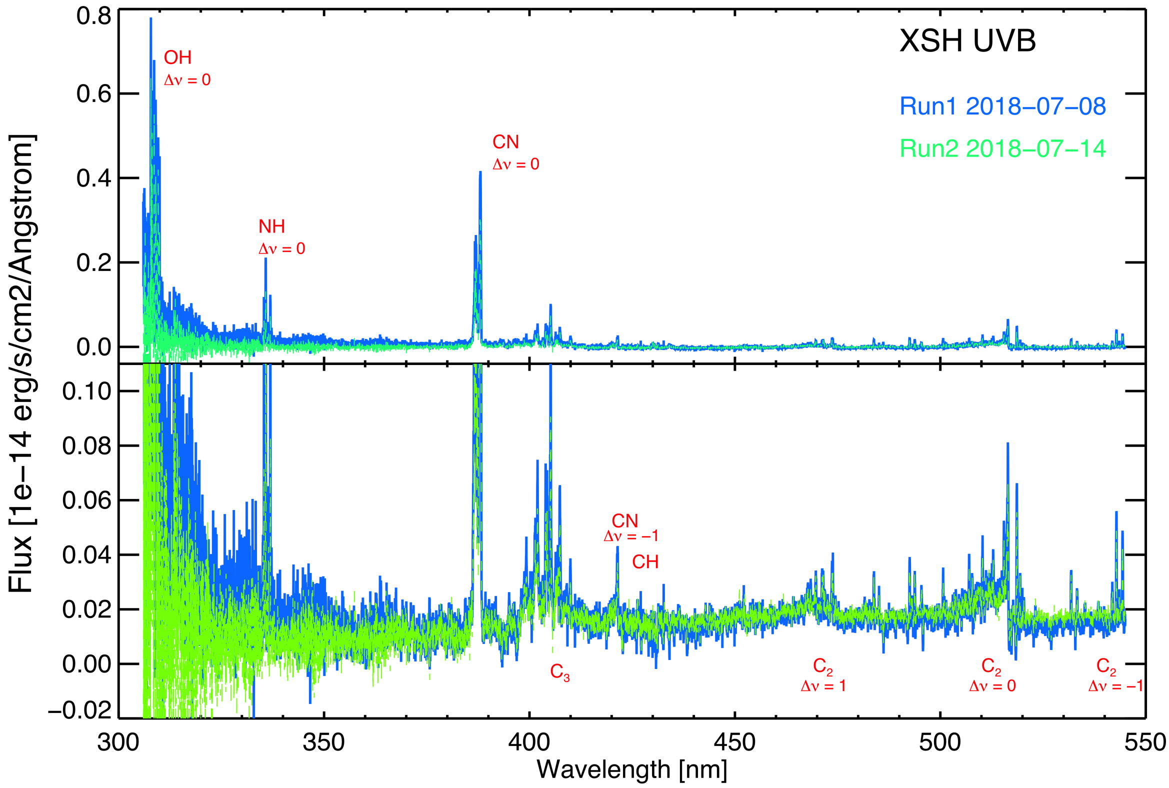

Figure 3.26: Medium resolution spectra of comet 66P taken with X-shooter/VLT on July 08 and 14, 2018. The strongest cometary emission features in the UV and optical range (OH, NH, CN, C_2 and C_3) are identified (Yang et al., 2019).

A'Hearn et al. (1995) noted that for a typical comet all gaseous species vary at a similar rate with the heliocentric distance, which can be described as Q(gas)$\propto r_h^{-2.7}$. Given that the activity of MBCs is likely to be driven by water ice sublimation, we scaled the upper limits of water and CN production rates of the known MBCs to r_h=1.29 au, where most observations were made for 66P. The scaled values as well as the original upper limits are listed in Table 3.12. The water-production rate Q(H_2O) of 66P is about an order of magnitude higher than those of known MBCs. One caveat of this comparison is that most upper limits of Q(H_2O) of MBCs are scaled from Q(CN) assuming a cometary ratio Q(CN)/Q(H_2O) $\sim$ 0.001. MBCs are closer to the Sun than LPCs, therefore CN could be depleted in MBCs (Prialnik and Rosenberg, 2009). However, for 176P and 358P, the Q(H_2O) rates were derived observing the H_2O and OH lines directly (de Val-Borro et al., 2012; O'Rourke et al., 2013), which are comparable to the limits derived using Q(CN).

As discussed widely in Yang et al. (2019), our dust models found remarkable differences between 66P and the MBCs, the latter in general show much lower values for both dust production rates (0.2-1.4 kg s^{-1}) and ejection velocities (0.5-2.0 m s^{-1} for particles of 100 μm). In comparison, the JFCs have typical dust productions rates of 40-250 kg s^{-1}, and ejection velocities for particles of 100 μm ranging from 5-10 m s^{-1}. Previous statistical study of 85 comets found the average variation of the dust production rate can be expressed as A(θ)fρ $\propto r_h^{-2.3}$ (A'Hearn et al., 1995). Using the latest orbital elements, our dynamical simulation confirmed

Table 3.12: Upper limits of the CN and H_2O production rates and dust production rates of MBCs (Snodgrass et al., 2017) compared to 66P.

Objects	$Q(H_2O)_s^a$ ($\times 10^{26}$)	$Q(CN)_s^a$ ($\times 10^{24}$)	$\frac{dM}{dt}_s^b$ (kg/s)	r_h (au)	$Q(H_2O)$ ($\times 10^{26}$)	$Q(CN)$ ($\times 10^{24}$)	$\frac{dM}{dt}$ (kg/s)	References
133P	0.1	0.1	7.2	2.64	0.02	0.01	1.4	Licandro et al. (2011)
176P	2.6	-	0.5	2.58	0.40	-	0.1	de Val-Borro et al. (2012)
259P	1.3	0.4	-	1.86	0.50	0.14	-	Jewitt et al. (2009)
288P	6.1	2.6	2.3	2.52	1.00	0.42	0.5	Hsieh et al. (2012a)
313P	3.2	1.6	1.7	2.41	0.60	0.18	0.4	Jewitt et al. (2015)
324P	7.1	1.9	1.1	2.66	1.00	0.30	0.2	Hsieh et al. (2012b)
358P	2.7	0.8	4.3	2.42	0.50	0.15	1.0	Hsieh et al. (2013)
P/2013 R3	1.9	1.2	<3.5	2.23	0.43	0.12	<1.0[c]	(Jewitt et al., 2014)
66P	27.1	7.5	55.0	1.29	27.1	7.5	55.0	This Work

[a]Scaled water and CN production rates to r_h=1.29 au, using Q(gas)$\propto r_h^{-2.7}$ (A'Hearn et al., 1995)
[b]Scaled dust production rates to r_h=1.29 au, using the proxy relationship: $\frac{dM}{dt} \propto r_h^{-2.3}$ (A'Hearn et al., 1995)
[c]The empirical limit to the mass loss (Jewitt et al., 2017).

that the orbit of 66P is no longer highly asteroidal but moderately asteroidal due to the shorter capture time. Considering all the available observations as well as the results of the dust model and the dynamical model, we conclude that 66P is much more similar to typical JFCs than MBCs and therefore it is unlikely to have originated from the asteroid main belt and is not related to MBCs (Yang et al., 2019).

3.7 Comet 252P/LINEAR

Comet 252P/LINEAR (hereafter 252P) was discovered by the LINEAR (Lincoln Near-Earth Asteroid Research) survey on April 7, 2000 at 1.11 au from the Sun when its magnitude was about 17.9 (Shelly et al., 2000). 252P is a JFC with an orbital period of 5.32 yr. It made a very close approach to the Earth on March 22, 2016 at just 0.04 au, providing a rare opportunity to investigate its activity, composition and morphology in detail. The activity level of 252P in the 2016 apparition increased by two orders of magnitude compared to its previous apparitions, making this apparition unusual (Shelly et al., 2000). The nucleus radius of 252P is estimated to be around 0.3 km, and it has a rotation period estimated between 5.41h and 7.24h, measured at different epochs, suggesting that its nucleus is in a non-principal axis rotation (Li et al., 2017). According to dynamical evolution studies, 252P became a near-Earth object (NEO) 400 yr ago and it could produce meteor activity (Ye et al., 2016). Analysis of observations of its morphology have resulted in several possible rotational periods. Knight and Schleicher (2016) found a rotation period of 7.35±0.05 hr from repetition of features in narrow-band images, while Li et al. (2018) obtained 7.24 hr using the same technique and 5.4 hr from the light-curve flux variation. Li et al. (2018) suggested that the two different periodicity derived from coma morphology and the light-curve is a strong indication that the nucleus of 252P is in a non-principal axis (NPA) rotation, like other comets such as 1P/Halley, 103P/Hartley 2 (Knight et al., 2015; Samarasinha et al., 2017) and 2P/Encke (Belton, 2000; Fernandez et al., 1998; Luu and Jewitt, 1990; Jewitt and Meech, 1987).

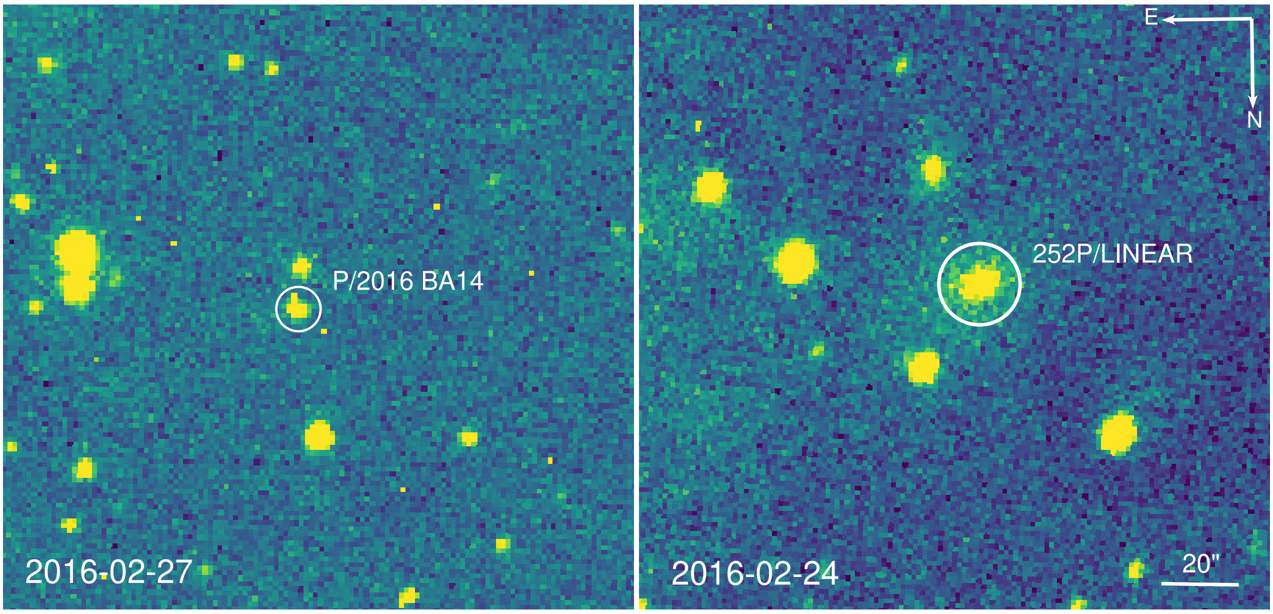

Figure 3.27: Rc images of 252P and BA14 taken with TS on February 27, 2016.

The similarity between the orbits of 252P and P/2016 BA14 (PANSTARRS) (hereafter BA14) suggests that they might be a pair of fragments from one common parent body (Rudawska et al., 2016; Li et al., 2017; Sosa and Fernández, 2016). BA14 was discovered by the Pan-STARRS survey on January 21, 2016 when it was at 0.02 au from the Earth (Naidu et al., 2016). We observed BA14 with TS using BVRI filters on February 27, 2016. BA14 did not show any coma activity compared to 252P and had an asteroidal aspect (see Figure 3.27). The radar images show that the nucleus of BA14 has an irregular shape with a radius of 0.45 km (Naidu et al., 2016). Infrared data confirmed that it reflects less than 3% of the sunlight (Reddy and Li, 2016). Warner (2016) estimated the rotation period of comet BA14 of (36.6±0.1) h. BA14 was selected as potential backup target of Comet Interceptor mission which is expected to be launched in 2028 (Schwamb et al., 2020).

We performed a dynamical analysis of the motion of 252P and BA14 in the past to clarify how likely these objects are originating from a common parent body. The results of this work will be published separately in a regular paper (Moulane et al. in preparation).

We started following the activity and composition of 252P from February until June 2016 with TS telescope. We started using the Rc and Ic filters on February 4 when the comet was not very active with a magnitude of 17 at 1.14 au from the Sun. At the beginning of March, its activity increased rapidly in a few days when it reached perihelion (March 15, r_h=1.00 au). At that time, we started detecting gas emissions in all the narrow-band filters. We continued observing the comet until June 8, 2016 when the comet was at 1.50 au from the Sun. We followed the production rates evolution of different gas species over more than two months. The derived production rates for different gas species, A(0)fρ parameter and their uncertainties are given in Table A.7. Figure 3.28 shows the logarithmic evolution of the various gas species production rates and A(0)fρ parameter as a function of heliocentric distance. The activity of the comet was increasing rapidly towards the perihelion, reaching its maximum activity on April 10, 2016 (a month after perihelion). At that time, we derived a water-production rate of $(8.42\pm0.08)\times10^{27}$ molec/s. Afterwords, the activity decreased slowly until 2.0 au from the Sun. We derived the relative molecular abundances for each observed species with respect to CN and to OH as well as the dust/gas ratio. We summarize all the abundances compared to the mean values of typical and depleted comets in Table 3.13. The C_2/CN and C_3/CN ratios in 2016 apparition were above the limits of depleted comets as defined in A'Hearn et al. (1995). This makes 252P a typical comet with a dust/gas ratios similar to those of typical comets.

Table 3.13: Mean relative molecular abundances of comet 252P compared to those for typical and depleted comets.

	Log production rate ratio		
	252P/LINEAR	Typical comets	Depleted comets
	This work	A'Hearn et al. (1995)	
C_2/CN	0.08±0.03	0.06±0.10	-0.61±0.35
C_3/CN	-0.59±0.07	-1.09±0.11	-1.49±0.14
CN/OH	-2.64±0.09	-2.55±0.65	-2.69±0.14
C_2/OH	-2.56±0.06	-2.46±0.39	-3.30±0.35
C_3/OH	-3.23±0.03	-3.12±0.68	-4.18±0.28
NH/OH	-2.14±0.05	-2.23±0.22	-2.48±0.34
A(0)fρ/CN	-23.26±0.10	-23.30±0.32	-22.61±0.15
A(0)fρ/OH	-25.90±0.12	-25.82±0.40	-25.30±0.29

Comet 252P was also observed at radio and at Infrared wavelengths as it made a very close approach to the Earth. Paganini et al. (2019) used Near-infrared Spectrograph (NIRSPEC) at the Keck Observatory to measure the production rates of several parent molecules (H_2O, CH_3OH, C_2H_6, NH_3, H_2CO, C_2H_2, CO, CH_4, and HCN) on April 12, 17, 26 and 29, 2016. Coulson et al. (2017) used JCMT to derive the HCN production rate on March 27, 2016 (12 days post-perihelion). Li et al. (2017) used the Hubble Space Telescope (HST) to derive the OH and CN production rates on April 17, 2016. H_2O, HCN, C_2H_6 and NH_3 were considered the main source of molecules OH, CN, C_2, and NH, respectively (Crovisier et al., 1997; Helbert et al., 2005; Mumma and Charnley, 2011; Hölscher, 2015). Table 3.14 summarizes the comparison of the daughter molecules production rates of comet 252P derived at the optical from TRAPPIST images with the possible parent molecules production rates derived from the Infrared and radio

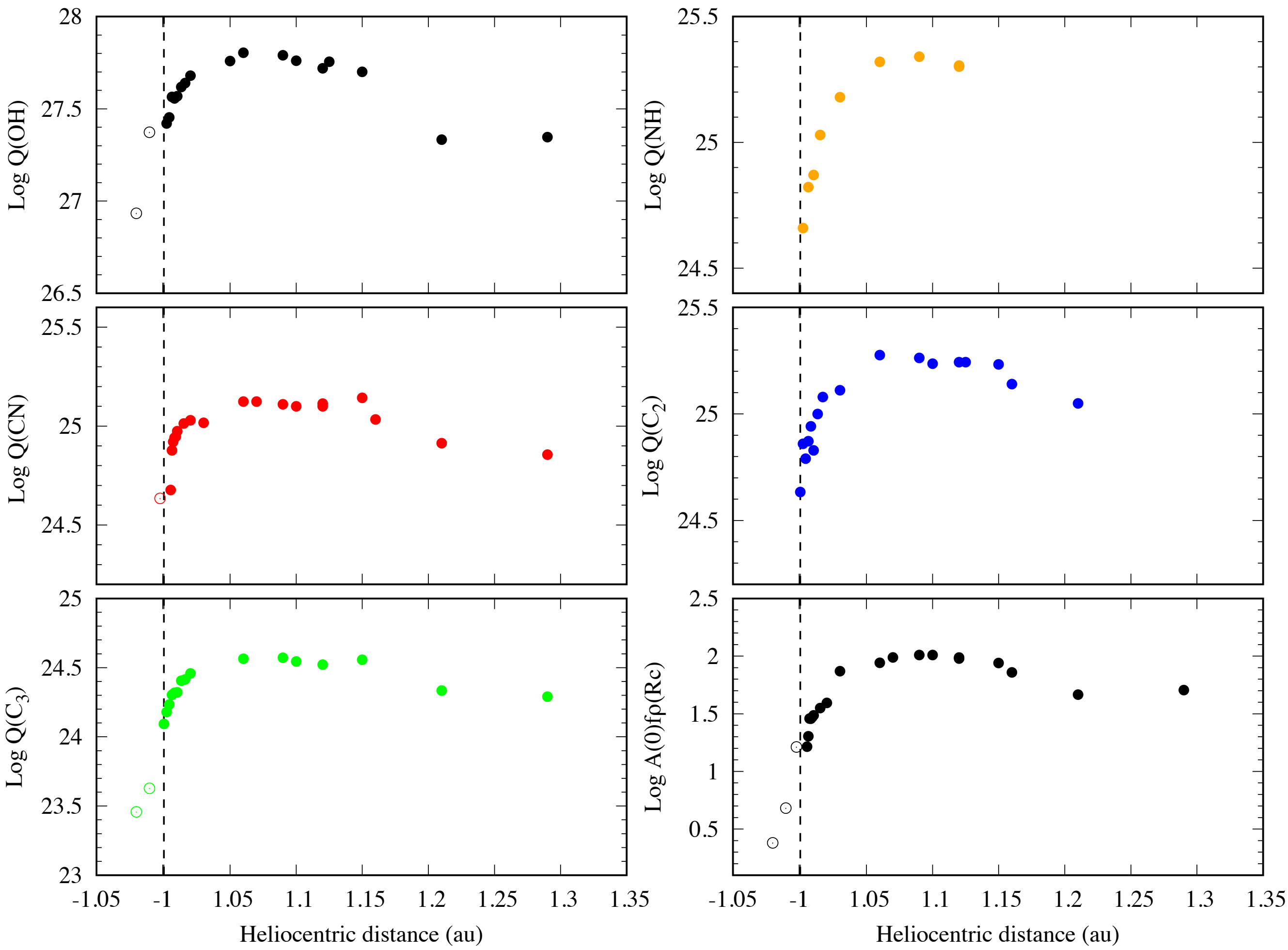

Figure 3.28: Logarithmic evolution of the production rates for each molecular species and A(0)fρ dust parameter with Rc filter of comet 252P as a function of the heliocentric distance. The dashed line refers to the perihelion on March 15, 2016 (r_h=1.00 au, Δ=0.05 au). The values and their uncertainties are given in Table A.7. 252P activity increased rapidly after perihelion to decrease only slowly after.

wavelengths (Coulson et al., 2017; Li et al., 2017; Paganini et al., 2019). The CN and OH production rates derived from HST are in agreement with those obtained with TRAPPIST around the same dates. We found an agreement between the production rates of daughter molecules and of the possible parent molecules. This confirms the correlation between these molecules found in several comets observed at different wavelengths (Opitom, 2016).

Table 3.14: Production rates of daughter molecules and possible parent molecules derived form different instruments for comet 252P.

Date UT	r_h (au)	$\triangle$ (au)	Q(OH)	Q(H_2O)	Q(CN)	Q(HCN)	Q(C_2)	Q(C_2H_6)	Q(NH)	Q(NH_3)	Reference
			Production rates ($\times10^{24}$molec/s)								
2016 Mar 27	1.01	0.05	4150±111	5615±150	10.00±0.36		10.00±0.36				This Work
2016 Mar 27	1.01	0.05				6.45±1.1					Coulson et al. (2017)
2016 Apr 01	1.02	0.07	4780±110	6436±148	10.40±0.20		2.90±0.31		15.10±0.29		This Work
2016 Apr 01	1.02	0.07				6.56±1.2					Coulson et al. (2017)
2016 Apr 10	1.06	0.12	6370±56	8414±78	13.30±0.12		18.90±0.14		20.90±0.27		This Work
2016 Apr 12	1.07	0.14		4960±200				52±2			Paganini et al. (2019)
2016 Apr 16	1.09	0.16	5770±66		12.60±0.12		17.20±0.20				This Work
2016 Apr 17	1.09	0.16	5810±110	7933±137	12.5±0.1						Li et al. (2017)
2016 Apr 19	1.11	0.18		5470±330				46±2			Paganini et al. (2019)
2016 Apr 26	1.16	0.22	5020±114	6339±144	13.90±0.13		17.10±0.17				This Work
2016 Apr 26	1.16	0.22		4560±220		11±2		46±2		<35	Paganini et al. (2019)
2016 Apr 29	1.18	0.23		4380±430		9±1				<30	Paganini et al. (2019)
2016 May 04	1.21	0.26	2150±46	2658±56	8.20±0.05		11.20±0.08				This Work

Note. We note that all DCT photometry is within a 19.2" (2260 km) radius aperture and all HST photometry are for 0.2" (13 km) radius aperture (Li et al., 2017). The DCT production rates are computed with the vectorial model. The DCT calibration uncertainties for the HB filters and derived gas fluxes are 5%–10% (Li et al., 2017). We used equation 3.1 to derive the H_2O production rate from the Q(OH). The mean production rate Q(HCN) is derived from spectral line integrated intensities of HCN(J=4–3) (Coulson et al., 2017).

3.8 Comet C/2017 O1 (ASASSN)

Comet C/2017 O1 (ASASSN), hereafter ASASSN, was discovered by the All Sky Automated Survey for SuperNovae (ASAS-SN) on July 19, 2017 when it was at 2.00 au from the Sun and at 1.75 au from the Earth (Green, 2017). At the time of discovery, the comet was at magnitude 15 and in just a few days the comet had a strong outburst brightening by ∼5 magnitudes (Prieto et al., 2017). Figure 3.29 shows the discovery image on July 19 and 2 more epochs of ASASSN on July 22 and 25, 2019. The sudden brightening of ASASSN could have several origins. Such outbursts can be indicative of splitting, in particular if Δm>3. But no fragments were observed during and after the outburst. Splitting can be caused by tidal breakup, rotational spin up, thermal stresses, and internal gas pressure due to heat reaching volatiles are also other possible outburst mechanisms (Gronkowski and Wesołowski, 2016). Using a photometric follow up and measuring the H_2O and CO_2 production rates, Brinkman (2020) constrained the nucleus size of ASASSN to 0.92 km which is in agreement with 0.92±0.09 km derived from the brightness profile of the comet (Paradowski, 2020).

We started monitoring comet ASASSN with TRAPPIST from July 31, 2017 ($r_{\rm h}$=1.83 au), a few days after the outburst event, until January 12, 2018 ($r_{\rm h}$=1.93 au). The comet reached its perihelion on October 14, 2017 at 1.50 au from the Sun. Due to the large outburst detected, we were able to detect all the gas species pre- and post-perihelion, NH was observed only two nights around perihelion. The comet was mostly monitored with TN, and additional data was also obtained with TS for four nights on August 1, 5 and September 4 and 16. The OH, NH, CN, C_2 and C_3 production rates and A(0)fρ parameter were derived and summarized in Table A.8. The logarithmic evolution of the gas and dust activity are shown in Figure 3.30. After the outburst, we obtained high production rates values when the comet was at 1.83 au from the Sun, which decreased slightly crossing perihelion. This strong outburst did not allow us to see the usual activity behavior of the comet with respect to perihelion. The comet was observed by NEOWISE satellite near-infrared sky survey (Mainzer et al., 2011) between July

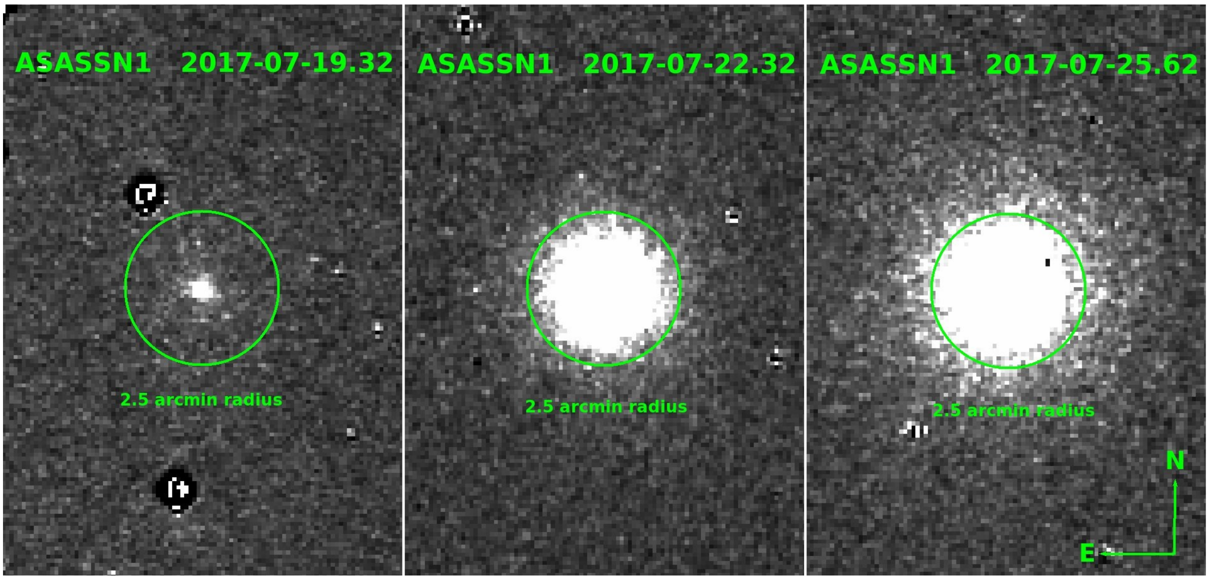

Figure 3.29: Discovery image comet C/2017 O1 (ASASSN) compared with images at two more epochs. Credit ASAS-SN1 Survey.

31 and August 2, 2017. Brinkman (2020) obtained a CO_2 production rate of 2.9×10^{27} molec/s which is comparable to the modeled value for the massive outburst (Δm=14.5 mag) of comet 17P/Holmes in 2007, with a CO_2 production rate of 3.3×10^{27} molec/s (Hillman and Prialnik, 2012). Brinkman (2020) obtained an upper limit of $Q(H_2O) < 8\times10^{26}$ molec/s on July 21, 2017 which is similar to $Q(H_2O)=(1.08\pm0.05)\times10^{27}$ molec/s derived from Q(OH) with TN on July 31, 2017.

We derived the relative abundances of the different species with respect to OH and to CN. Table 3.15 summarizes the mean relative molecular abundances of comet ASASSN compared to those obtained for 85 comets in A'Hearn et al. (1995). We obtained $\mathrm{Log}[Q(C_2)/Q(CN)]=-0.03 > -0.18$ which makes comet ASASSN a typical gas coma composition but with a high dust/gas ratio compared to typical comets. This could be caused by the outburst which is responsible for the overabundance, creating fine dust grains, which increase the scattering cross section dramatically. Over a range of heliocentric distances from 1.50 au to 1.93 au pre- and post-perihelion, we did not detect any significant variation in all the relative molecular abundances. Brinkman (2020) obtained an optical spectrum on July 21, 2017 with the Magellan 6.5m Clay telescope. They derived a ratio $\mathrm{Log}[Q(CN)/Q(OH)]=-2.5$ which is in agreement with the mean ratio of -2.55 ± 0.65 of typical comets (A'Hearn et al., 1995) and lower than our derived value -1.57 ± 0.10.

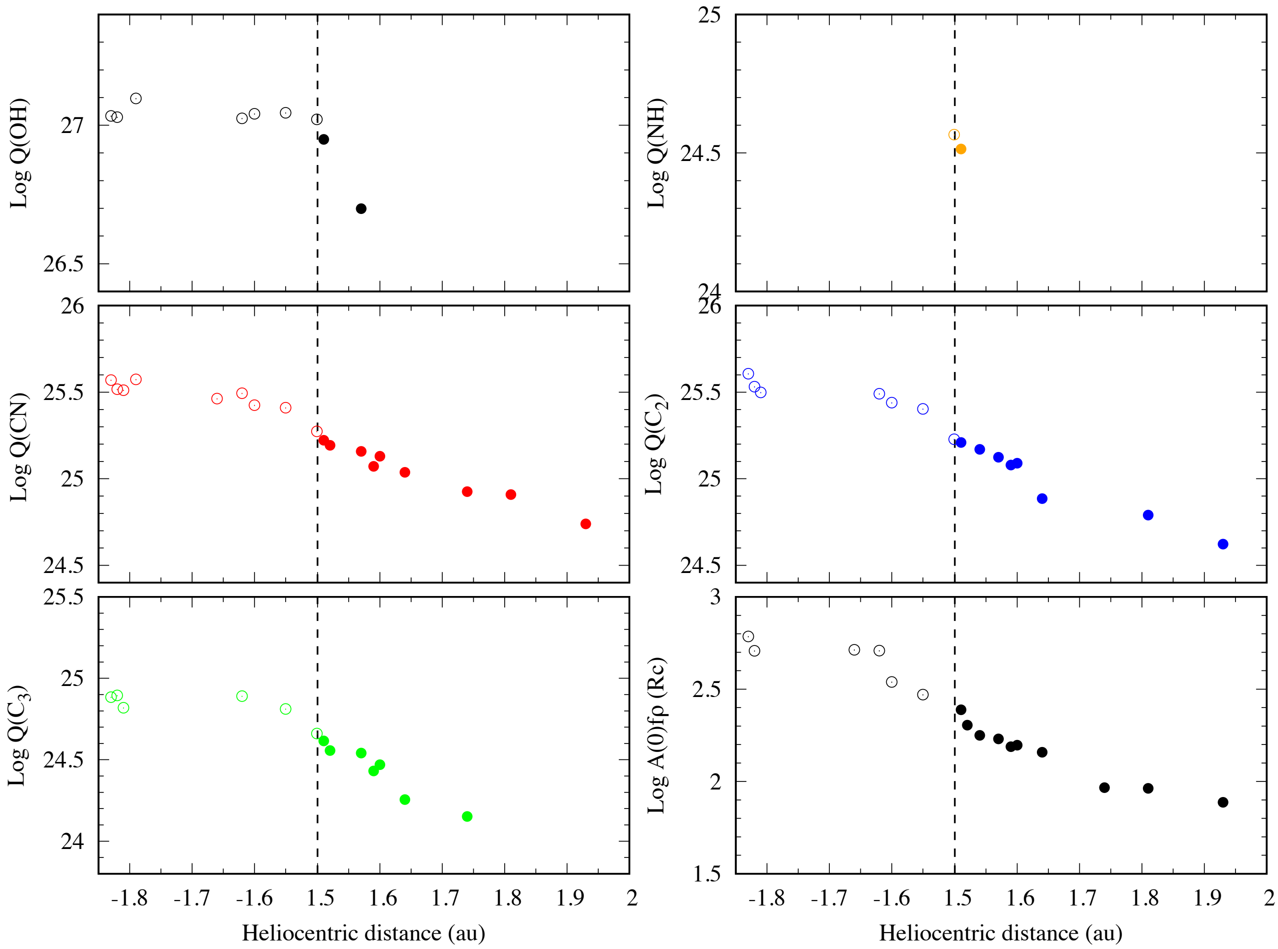

Figure 3.30: Logarithmic evolution of the production rates for each molecular species and A(0)fρ dust parameter with Rc filter of comet C/2017 O1 as a function of the heliocentric distance. The vertical dashed line indicates the perihelion at 1.50 au. The values and their uncertainties are given in Table A.8

Table 3.15: Mean relative molecular abundances of comet ASSASN compared to those of typical and depleted comets.

	Log production rate ratio		
	C/2017 O1 This work	Typical comets A'Hearn et al. (1995)	Depleted comets A'Hearn et al. (1995)
C_2/CN	-0.03±0.05	0.06±0.10	-0.61±0.35
C_3/CN	-0.66±0.06	-1.09±0.11	-1.49±0.14
CN/OH	-1.57±0.10	-2.55±0.65	-2.69±0.14
C_2/OH	-1.58±0.12	-2.46±0.39	-3.30±0.35
C_3/OH	-2.21±0.10	-3.12±0.68	-4.18±0.28
NH/OH	-2.44±0.03	-2.23±0.22	-2.48±0.34
A(0)fρ/CN	-22.94±0.10	-23.30±0.32	-22.61±0.15
A(0)fρ/OH	-24.50±0.22	-25.82±0.40	-25.30±0.29

3.9 Comet C/2017 T2 (PANSTARRS)

Comet C/2017 T2 (PANSTARRS), hereafter 17T2, is an Oort cloud comet discovered on October 2, 2017 by the PANSTARRS survey when it was 9.2 au from the Sun. The closest approach to Earth was on December 28, 2019 at a geocentric distance of 1.52 au and it reached its perihelion on May 4, 2020 at 1.61 au from the Sun. The comet reached a maximum magnitude of 8 by the end of April 2020. We started monitoring its activity with TN from September 5, 2019 (r_h=2.81 au, Δ=2.00 au) until August 15, 2020 (r_h=2.11 au, Δ=2.42 au). We started detecting CN, C_2 and C_3 at the beginning of November while OH and NH were detected at the end of the month. C_3, NH and OH were still detected in TRAPPIST images until the beginning of June 2020 (1.80 au) while we still have CN and C_2 signal until mid August when the comet was at 2.11 au. We did not observe the comet from March 10 to April 1, 2020 as it was too low at Oukaimeden observatory.

The derived production rates for each gas species, A(0)fρ dust parameter and their uncertainties are summarized in Table A.9. Their logarithmic evolution as a function of the heliocentric distance are shown in Figure 3.31. The production rates of different species were increasing lightly since the the beginning of our monitoring until February 26, 2020 where the comet reached its maximum activity with water-production rate peak of $(5.50\pm0.12)\times10^{29}$ molec/s two months pre-perihelion. Then, the activity of the comet decreased rapidly post-perihelion. Schleicher et al. (2020) derived a water production of 6×10^{28} molec/s in early October 2019 at a distance of 3.15 au from the Sun, while we obtained $Q(H_2O)=(1.73\pm0.11)\times10^{29}$ molec/s a month later (r_h=2.60 au). Relative abundances for different species were derived and summarized in Table 3.16. We obtained a logarithmic ratio of C_2/CN of 0.07±0.05 in agreement with the mean value of typical comets (A'Hearn et al., 1995). We conclude that the LPC 17T2 comet has a typical coma composition, but it has a dust/gas ratio higher than that of typical comets. This makes comet 17T2 one of the most dust-rich comets reported in our database. Regarding the variation of the relative molecular abundances with respect to the heliocentric distance, we did not notice any significant change.

Table 3.16: Mean relative molecular abundances of comet C/2017 T2 compared to those of typical and depleted comets.

	Log production rate ratio		
	C/2017 T2	Typical comets	Depleted comets
	This work	A'Hearn et al. (1995)	
C_2/CN	0.07±0.05	0.06±0.10	-0.61±0.35
C_3/CN	-0.70±0.08	-1.09±0.11	-1.49±0.14
CN/OH	-2.71±0.09	-2.55±0.65	-2.69±0.14
C_2/OH	-2.64±0.09	-2.46±0.39	-3.30±0.35
C_3/OH	-3.41±0.12	-3.12±0.68	-4.18±0.28
NH/OH	-2.85±0.19	-2.23±0.22	-2.48±0.34
A(0)fρ/CN	-22.31±0.11	-23.30±0.32	-22.61±0.15
A(0)fρ/OH	-25.06±0.12	-25.82±0.40	-25.30±0.29

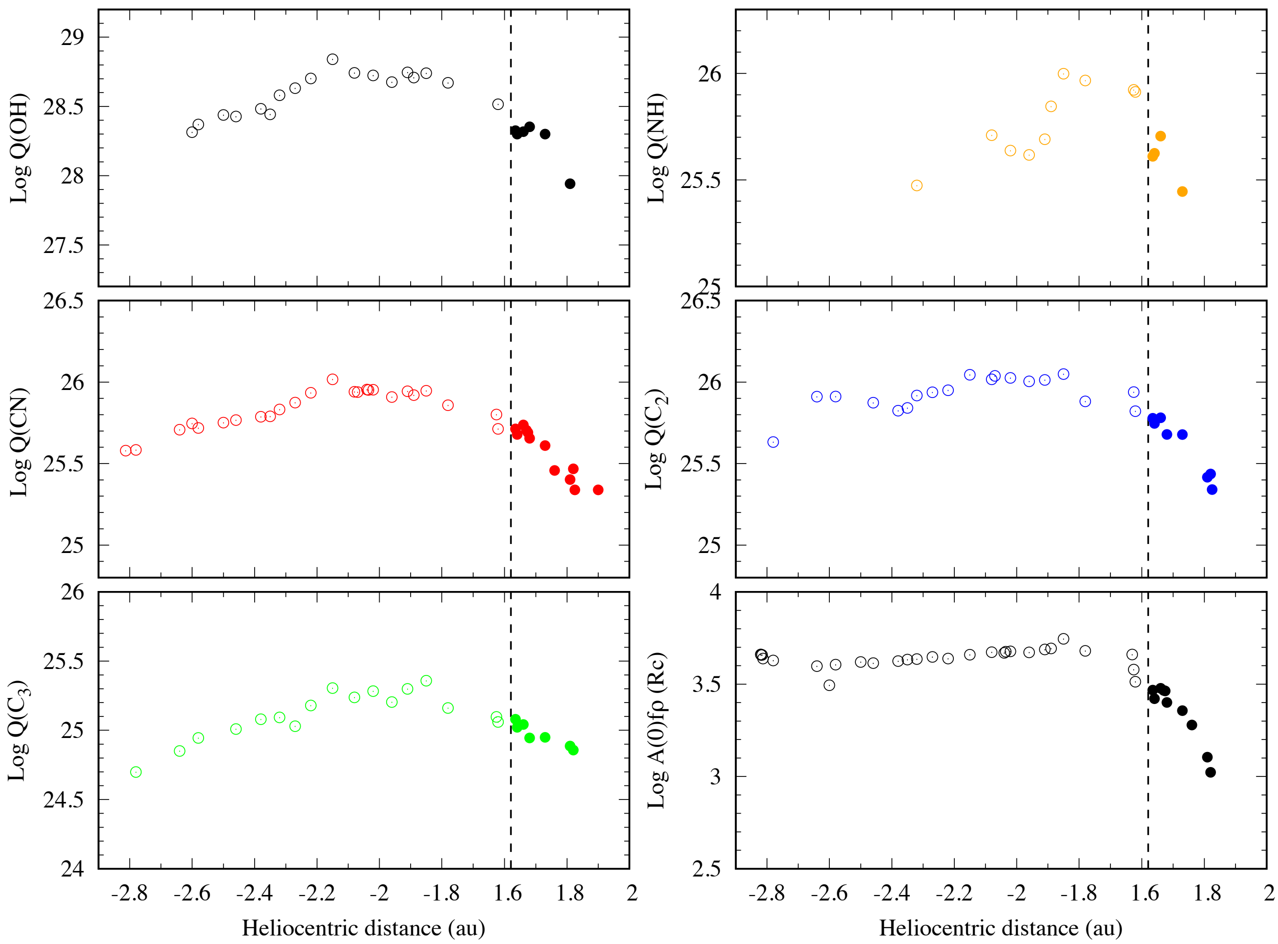

Figure 3.31: Logarithmic evolution of the production rates for each molecular species and A(0)fρ dust parameter with Rc filter of comet C/2017 T2 as a function of the heliocentric distance. The vertical dashed line indicates the perihelion at 1.61 au. The values and their uncertainties are given in Table A.9.

3.10 Comet C/2018 W2 (Africano)

Comet C/2018 W2 (Africano), hereafter Africano, was discovered on November 27, 2018 by Brian Africano at the Mount Lemmon Survey telescope when the comet was at a magnitude of 20 (Africano et al., 2018). The comet reached its perihelion (r_h=1.45 au) on September 6, 2019. We started our observations of comet Africano with TN from July 17, 2019 (r_h= 1.62 au, Δ=2.05 au) until January 9, 2020 (r_h= 2.24 au, Δ=2.87 au). OH and C_3 were detected in our images from the beginning until the end of November 2019, while C_2 and CN were still detected one month later. Only one NH image was taken for comet Africano on September 25, 2019. We followed the activity evolution of the comet over more than six months on both sides of the perihelion. The derived production rates for each gas species and A(0)fρ parameter and their uncertainties are given in Table A.10, their logarithmic evolution as function of heliocentric distance are shown in Figure 3.32. The activity of the comet was quite stable on both sides of perihelion.

Relative abundances of different molecules as well as the dust/gas ratio with respect to CN and to OH were derived and summarized in Table 3.17. We obtained Log[Q(C_2)/Q(CN)]=-0.05±0.04 which is above the limit defined in A'Hearn et al. (1995) for the carbon-chain depleted comets. This classifies comet Africano as a typical comet with a dust/gas ratio a bit higher

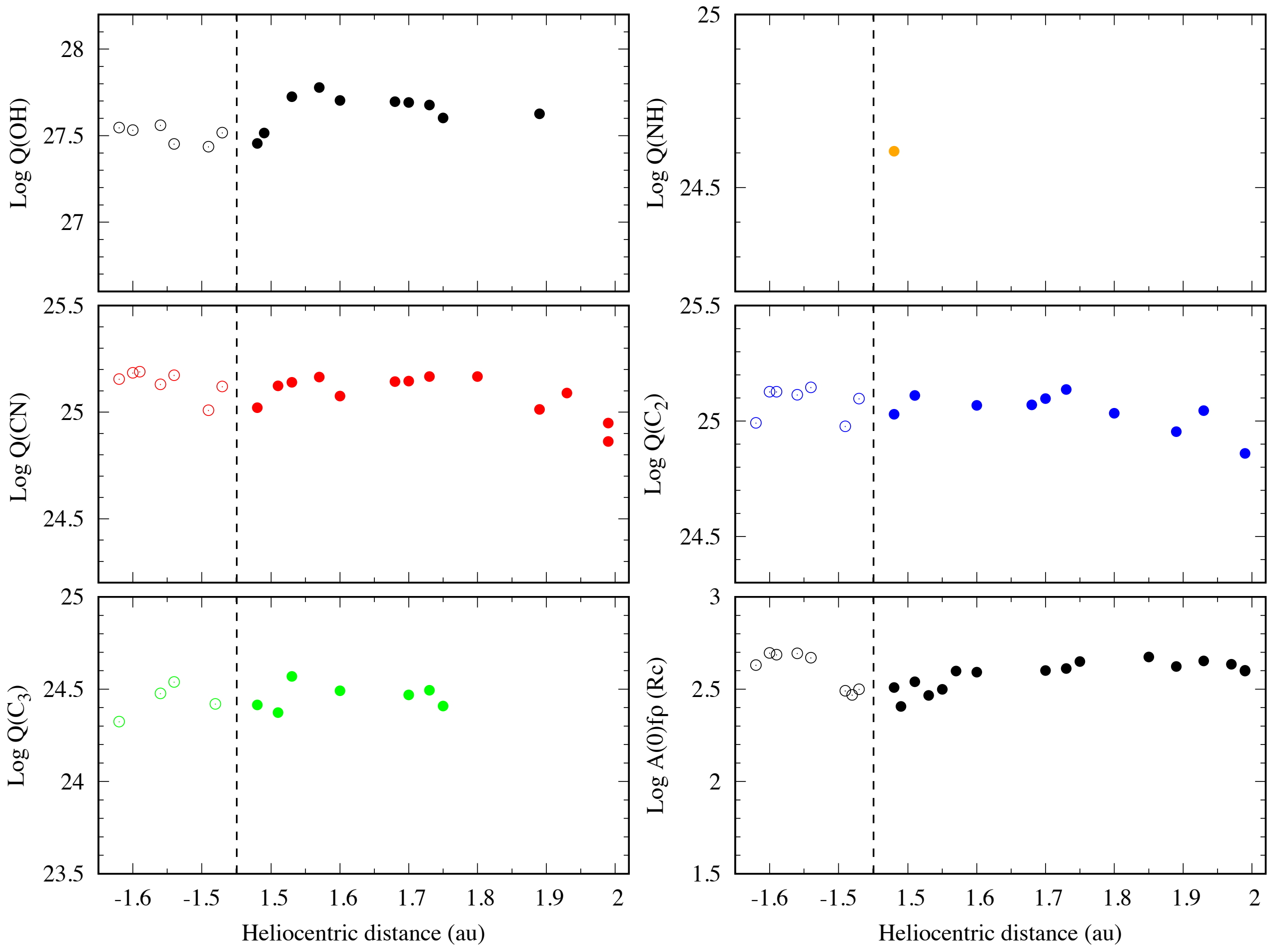

Figure 3.32: Logarithmic evolution of the production rates for each molecular species and A(0)fρ dust parameter with Rc filter of comet C/2018 W2 as a function of the heliocentric distance. The vertical dashed line indicates the perihelion of the comet at 1.45 au. The values and their uncertainties are given in Table A.10.

than the mean value of typical comets.

Table 3.17: Mean relative molecular abundances of comet C/2018 W2 compared to those of typical and depleted comets.

	Log production rate ratio		
	C/2018 W2	Typical comets	Depleted comets
	This work	A'Hearn et al. (1995)	
C_2/CN	-0.05±0.04	0.06±0.10	-0.61±0.35
C_3/CN	-0.66±0.08	-1.09±0.11	-1.49±0.14
CN/OH	-2.48±0.11	-2.55±0.65	-2.69±0.14
C_2/OH	-2.51±0.11	-2.46±0.39	-3.30±0.35
C_3/OH	-3.14±0.10	-3.12±0.68	-4.18±0.28
NH/OH	-2.84±0.10	-2.23±0.22	-2.48±0.34
A(0)fρ/CN	-22.73±0.10	-23.30±0.32	-22.61±0.15
A(0)fρ/OH	-25.23±0.15	-25.82±0.40	-25.30±0.29

3.11 Comet C/2019 Y4 (ATLAS)

Comet C/2019 Y4 (ATLAS), hereafter ATLAS, is a near-parabolic comet discovered on December 28, 2019 by the ATLAS robotic survey[8]. At the discovery time, the comet showed a diffuse coma of diameter about 2″ with magnitude of 19.6, and no tail was observed. Comet ATLAS was one of the brightest comet in 2020, its brightness changed from magnitude 17 to 7 in just two months (February and March 2020). It was expected that the comet would reach a magnitude of 3 in early May 2020. But the comet started disintegrating in many fragments around March 22 (-70 days pre-perihelion), as reported by some public survey programs (Ye and Zhang, 2020; Steele et al., 2020). Images taken later with the HST on April 20 and 23 provide the sharpest views of the fragments breaking apart into more than 30 pieces with four main fragments, two of them clearly seen in TRAPPIST images (see Figure 3.33). The European Space Agency's Solar Orbiter spacecraft passed approximately downstream of the position of the comet ATLAS after its fragmentation. It flew through the ion tail between May 31 and June 1 and the dust tail on June 6 (Jones et al., 2020). It was expected that the spacecraft made some *in situ* measurements of the solar wind features and dust grain collisions in the tails of the comet. Generally, comets have very low tensile strength as they can be pulled apart very easily by tidal force or any other substantial force. Several comets have been observed to split in the past. A few of these cases have been obviously attributable to the tidal forces of Jupiter such as comet 16P/Brooks (Sekanina and Yeomans, 1985) and comet Shoemaker-Levy 9 (Hammel et al., 1995; Weaver et al., 1995) or the Sun (the Kreutz comet family), while other splittings have to be attributed to less obvious causes like 73P/Schwassmann–Wachmann 3 (Dello Russo et al., 2007; Reach et al., 2009). The similarity between the orbits of C/1844 Y1 (Great Comet) and comet ATLAS hints to a possible relationship between the two comets that splitted from a common progenitor. Dynamical evolution study suggests that the split between comets occurred around the previous perihelion passage of the progenitor ∼5 kyr ago, with the in-plane component of their separation velocity ≥ 1 m s^{-1} (Hui and Ye, 2020).

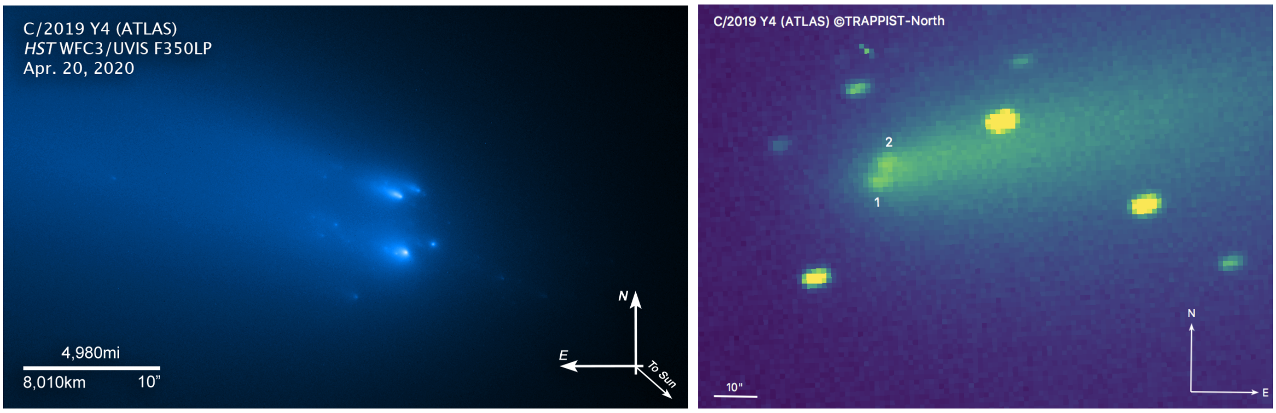

Figure 3.33: Left: Fragments of comet ATLAS as observed by the Hubble Space Telescope on April 20, 2020 (Ye and Hui, 2020). Right: Rc image of comet ATLAS taken with TN on April 20, 2020 where we can see the two bright fragments labeled (1) and (2). The scale and orientation are given at the bottom for each image.

We observed ATLAS with TN from February 21 until May 03, 2020. We started detecting CN, C_3, and C_2 since the beginning of our monitoring -100 days pre-perihelion (r_h=2.13 au), while we got the NH and OH at the beginning of March (r_h=1.86 au). Over two months of observations, OH, NH, CN, C_3, and C_2 production rates and A(0)fρ parameter were derived and summarized in Table A.11. Their logarithmic evolution as a function of heliocentric distance

[8] https://minorplanetcenter.net/mpec/K20/K20AB2.html

are shown in Figure 3.34. The comet reached its maximum activity on March 22 (-70 days pre-perihelion), time of its fragmentation, with a water-production rate peak of (1.52±0.04)10^{28} molec/s. The comet's activity show a symmetric behaviour before and after the disintegration. We used the A(0)fρ values obtained with the narrow-band filters, which are not contaminated by the gas emissions, to derive the dust colours of the comet. We found that the RC-GC, RC-BC and GC-BC colours are redder than the Sun with mean values of (12.7±2.6), (14.7±2.9) and (19.2±6.0)%/1000 respectively (see Figure 3.35). Given the error bars, we did not detect any significant variation of the colour of the dust in the coma before and after the disintegration of the nucleus, this is in agreement with results found by Hui and Ye (2020) using Sloan *gri* system.

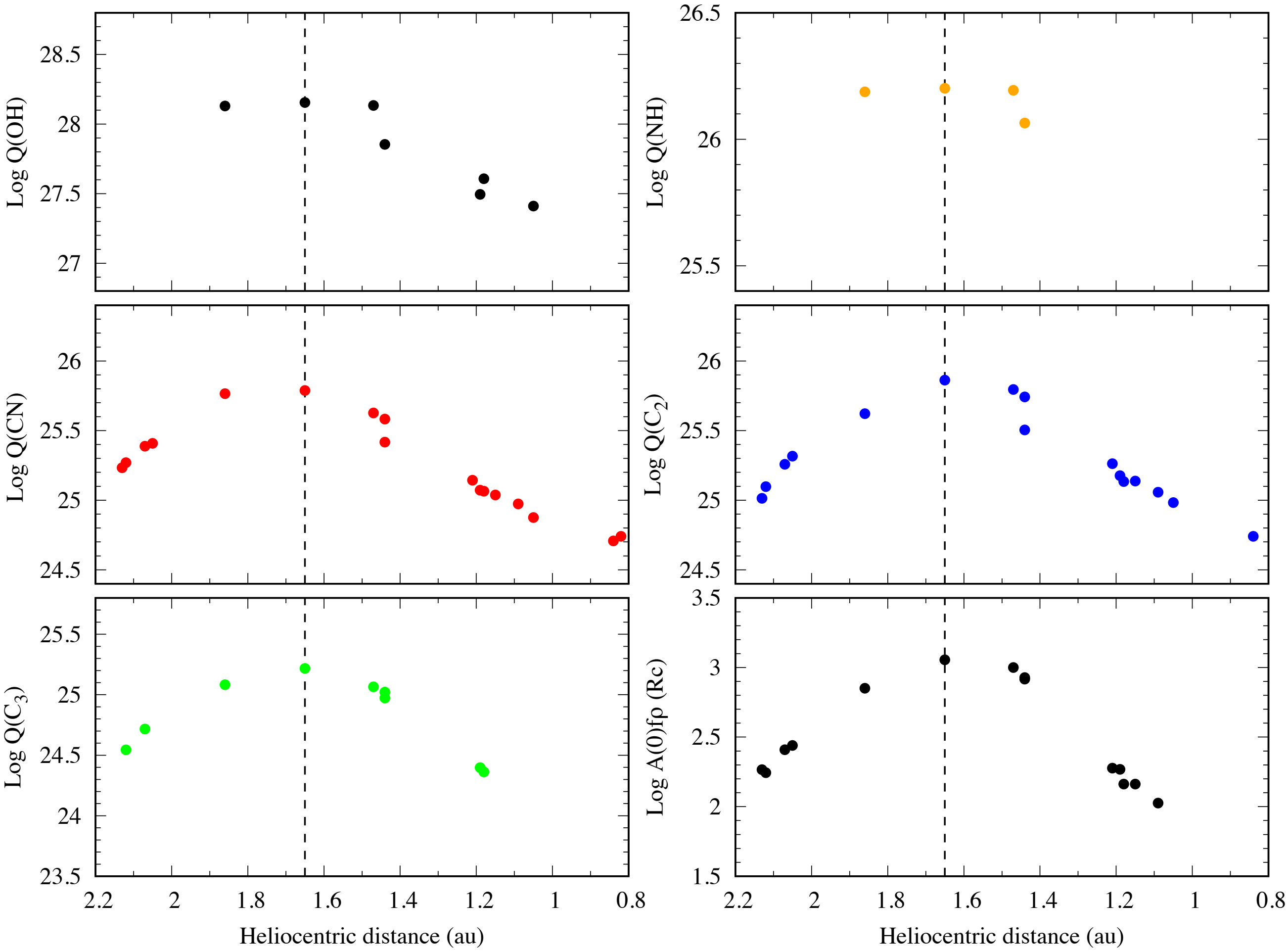

Figure 3.34: Logarithmic evolution of the production rates for each molecular species and A(0)fρ dust parameter with Rc filter of comet C/2019 Y4 as a function of the heliocentric distance. The values and their uncertainties are given in Table A.11. The comet expected to reach its perihelion 0.25 au on May 31, 2020, but it was disintegrated on March 22, 2020 at r_{h}=1.65 au. The vertical dashed line indicates the time when the split occurred.

The relative abundances of different gas species as well as the dust/gas ratios of comet ATLAS before and after its disintegration were derived and summarized in Table 3.18. We found a significant change in the C_2/CN ratio before and after disintegration of the comet, while a moderate variation has been found for other ratios regarding the error-bars. Before the disintegration, we found Log[Q(C_2)/Q(CN)]=-0.15±0.05 which is close to the limit of the carbon-chain depleted comets -0.18 defined in A'Hearn et al. (1995). But this ratio changes to 0.10±0.09 after the fragmentation of the nucleus, which is in an agreement with mean value of typical comets.

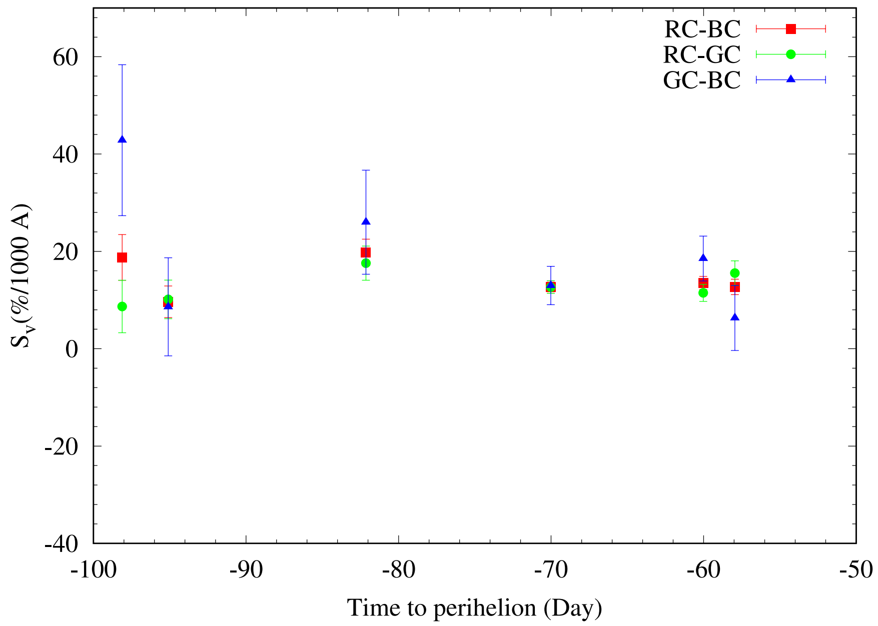

Figure 3.35: Normalized reflectivity gradients S_v(% per 1000 Å) of comet ATLAS for different colour indices as a function of days to perihelion.

Zubko et al. (2020) made polarimetric measurements of comet ATLAS, over a wide range of phase angles, before and after the fragmentation. They obtained a dramatic growth of the positive polarization branch up to (96.5±3.4) % after the disintegration of the nucleus, which might be due to a significant increase of the relative abundance of carbonaceous particles in the coma after disintegration. This indicates that the interiors of comets are richer in carbonaceous material than the surfaces, which have been processed and weathered by the solar radiation (Zubko et al., 2020). Similar polarimetric responses have been found in comets C/1995 O1 (Hale-Bopp) and C/1996 B2 (Hyakutake) (Kikuchi, 2006).

Table 3.18: Mean relative molecular abundances of comet C/2019 Y4 before and after its fragmentation compared to those of typical and depleted comets.

	Log production rate ratio			
	C/2019 Y4		Typical comets	Depleted comets
	Before	After	A'Hearn et al. (1995)	
C_2/CN	-0.15±0.05	0.10±0.09	0.06±0.10	-0.61±0.35
C_3/CN	-0.69±0.03	-0.59±0.10	-1.09±0.11	-1.49±0.14
CN/OH	-2.37±0.02	-2.46±0.11	-2.55±0.65	-2.69±0.14
C_2/OH	-2.51±0.03	-2.37±0.07	-2.46±0.39	-3.30±0.35
C_3/OH	-3.05±0.05	-3.09±0.12	-3.12±0.68	-4.18±0.28
NH/OH	-1.95±0.02	-1.79±0.05	-2.23±0.22	-2.48±0.34
A(0)fρ/CN	-23.18±0.09	-23.06±0.28	-23.30±0.32	-22.61±0.15
A(0)fρ/OH	-25.54±0.18	-25.30±0.17	-25.82±0.40	-25.30±0.29

3.12 Comet C/2020 F3 (NEOWISE)

Comet C/2020 F3 (NEOWISE), hereafter NEOWISE, is a LPC with a near-parabolic orbit discovered on March 27, 2020 by the NEOWISE space telescope[9] at magnitude 18 when it was at 2.00 au from the Sun. NEOWISE was the brightest comet in the northern hemisphere since comet Hale–Bopp in 1997. The comet reached a maximum brightness early July 2020 with a magnitude 1, making it bright enough to be visible to the naked eye. The comet reached its perihelion on July 3, 2020 at 0.29 au and its closest approach to Earth occurred on July 23, 2020 at a distance of 0.69 au. A strong sodium doublet emission at 5890 Å was detected at different epochs in July (Lin et al., 2020; Cochran et al., 2020). The sodium emission is rare in cometary spectra, it was detected only in a few comets like comet C/1996 B2 (Hyakutake) and C/1995 O1 (Hale-Bopp) (Zhang et al., 2001). Several H_2O^+ lines were detected at the visible-red wavelength (5800 to 7400 Å), though they are much weaker than the sodium line, suggesting that the red straight tail reported by numerous observers in mid-July was likely dominated by sodium atoms rather than H_2O^+ ions (Ye et al., 2020). Drahus et al. (2020) derived a rotation period of the nucleus of (7.58±0.03) hr from the coma morphological features, with no obvious temporal changes or deviations from a simple rotation state over the period of July 28 and August 10, 2020.

Figure 3.36: Colour image of NEOWISE as seen by TRAPPIST.

We began the observation of NEOWISE a bit after perihelion on July 22, 2020 (r_{h}=0.63) as it was getting higher in the northern sky, 20 degree above the horizon. We followed its activity with TN until September 10, 2020 (r_{h}=1.61), we tried to follow it as long as possible. All the species were detected since the first day of observation. As the comet was very bright around perihelion, short exposures were used to avoid the saturation in our images. Figure 3.36 shows an Rc image of the comet taken on July 23. NEOWISE displayed typical cometary features,

[9] http://www.nasa.gov/wise

with a condensed coma which was somewhat diffuse and slightly elongated. The coma did not show any sign of increasing elongation, which is often associated with disruption of the nucleus at small heliocentric distances. The derived production rates for each gas species, A(0)fρ dust parameter and their uncertainties are given in Table A.12 and their logarithmic evolution are shown in Figure 3.37. The comet reached its maximum activity at perihelion, with a water-production rate of $(1.68\pm0.05)\times10^{29}$ molec/s, and then decreased slowly as the comet was going away from the Sun. Combi et al. (2020a) derived a water-production rate of 4.45×10^{30} molec/s from the SWAN/SOHO hydrogen Lyman-α brightness and its spatial distribution. This result is higher than our measurement, which is consistent with the systematic offset trend that we have detected for other comets because of different approaches used to derive the water-production rate as widely discussed for comet 21P in section 3.1.1.1.

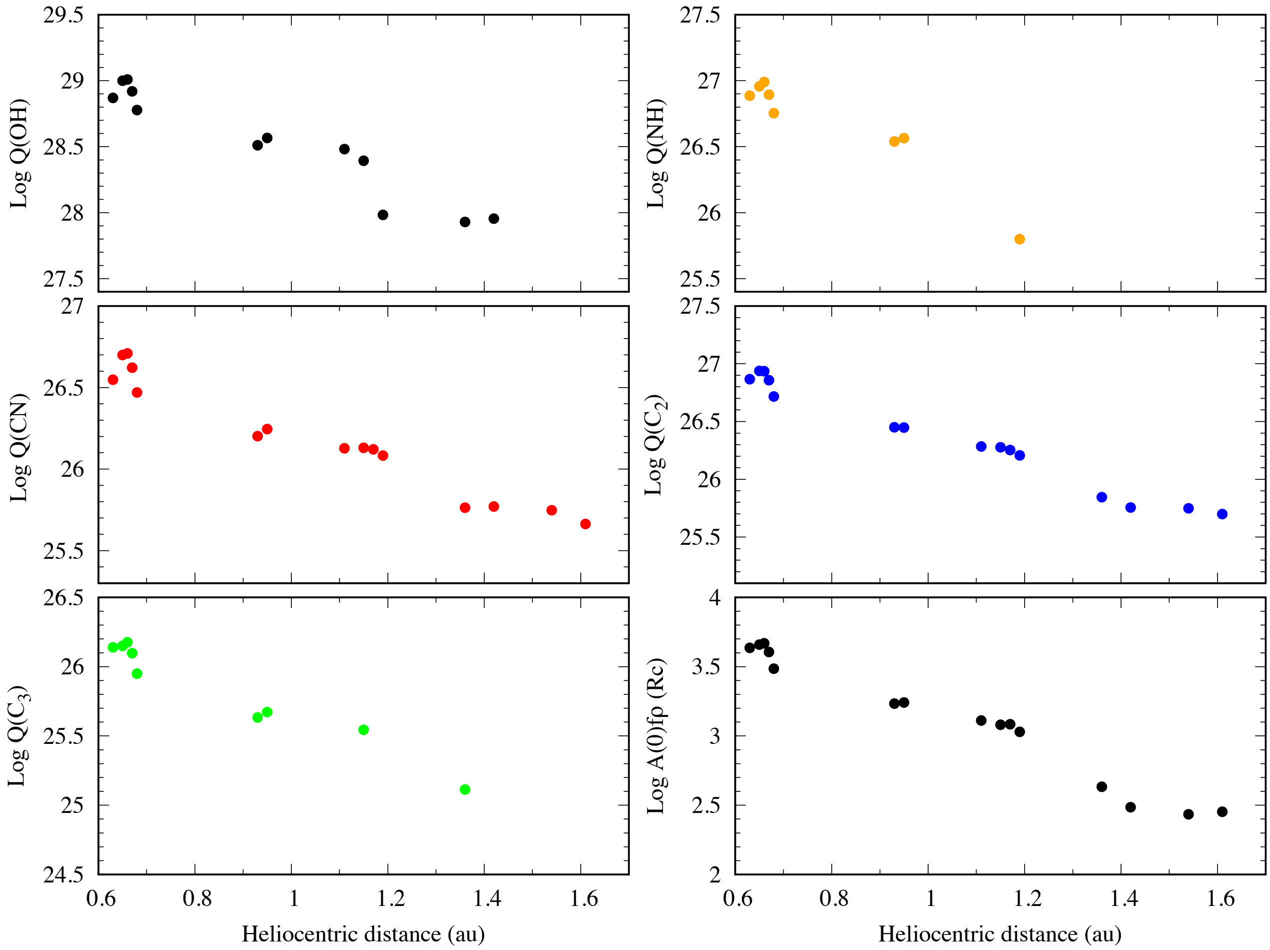

Figure 3.37: Logarithmic evolution of the production rates for each molecular species and A(0)fρ dust parameter with Rc filter of comet C/2020 F3 as a function of the heliocentric distance. The comet reached its perihelion on July 3, 2020 at 0.29 au from the Sun. The values and their uncertainties are given in Table A.12.

Table 3.19 summarizes the relative abundances of the various daughter species as well as dust/gas ratios with respect to CN and to OH. These ratios indicates that NEOWISE has a typical coma composition with also a dust/gas ratio similar to typical comets (A'Hearn et al., 1995). Over the heliocentric distance range of 0.63-1.61 au, we did not detect any significant variation in the relative abundances. Faggi et al. (2020) obtained high-resolution infrared spectra of comet NEOWISE over July 2020. They were able to detect CO, OCS, HCN, C_2H_2, NH_3, NH_2, H_2CO, CH_4, C_2H_6 and CH_3OH. But no production rates were communicated yet.

We monitored the gas morphology of NEOWISE, especially in the CN filter, even if the

Table 3.19: Relative molecular abundances of comet C/2020 F3 compared to the mean values for typical comets.

	Log production rate ratio		
	C/2020 F3	Typical comets	Depleted comets
	This work	A'Hearn et al. (1995)	
C_2/CN	0.15±0.09	0.06±0.10	-0.61±0.35
C_3/CN	-0.54±0.07	-1.09±0.11	-1.49±0.14
CN/OH	-2.25±0.12	-2.55±0.65	-2.69±0.14
C_2/OH	-2.08±0.10	-2.46±0.39	-3.30±0.35
C_3/OH	-2.83±0.05	-3.12±0.68	-4.18±0.28
NH/OH	-2.03±0.06	-2.23±0.22	-2.48±0.34
A(0)fρ/CN	-23.33±0.15	-23.30±0.32	-22.61±0.15
A(0)fρ/OH	-25.60±0.10	-25.82±0.40	-25.30±0.29

window of observation was short due to the visibility of the comet at that time. We acquired several CN images every night in order to distinguish the coma features and their evolution with time to estimate the rotation period of the nucleus. A simple rotational filter applied to the CN images revealed a large spiral jet and a second bright jet close to the nucleus. The same features were observed in the coma of NEOWISE over the two months of observations. On the night of July 26, we made a CN series images over 1.5 hr. Figure 3.38 shows the CN coma feature evolution over that night. It was difficult to estimate any rotation period of the nucleus as the jets remain in the same position over 1.5 hr.

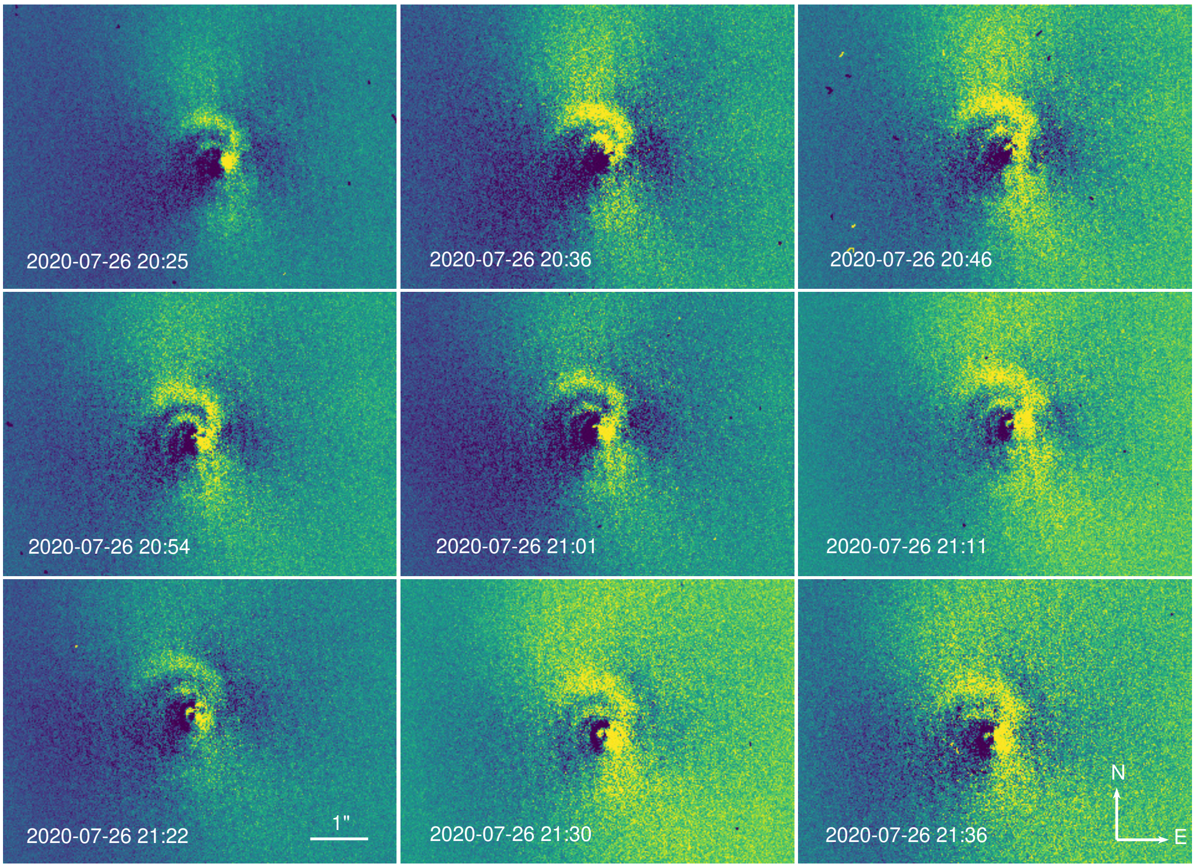

Figure 3.38: CN features in the coma of comet NEOWISE over the night of July 26, 2020.

3.13 Monitoring of outbursting comets

The outbursts of comets, sudden large increases in their luminosity, are very interesting and mysterious signs of activity of bodies. Cometary outbursts are short-lived stochastic events that increase the total mass-loss rate of their progenitor nuclei by a large amount. They are seemingly sporadic events, that can occur throughout the inner Solar System, and beyond the orbit of Jupiter. Most of the outbursts are taking place at heliocentric distances where sublimation of water ice plays an important role in the activity of comets. However, the phenomenon is also observed far away from the Sun (5–20 au) where the sublimation of water ice is negligible and the activity of comets is dominated by more volatile species. A variety of mechanical and chemical processes can drive these events including tidal breakup, rotational spin up, thermal stresses, and internal gas pressure due to heat reaching volatiles (Gronkowski and Wesołowski, 2016). Studying the dust and volatiles ejected by an outburst gives us an opportunity to examine material from a specific area on the nucleus surface, and allows us to distinguish between these causes. We label outbursts based on the observed change in apparent magnitude: small ($\Delta m < 2$ mag), medium (2–5 mag), and large (>5 mag). In this section, we present a follow up of comets that show outbursts in the period of 2017-2020. These comets include 29P/Schwassmann-Wachmann 1, 123P/West-Hartley, 155P/Shoemaker, 243P/NEAT, and 260P/McNaught. We describe here the observations and photometry measurements of the outbursts observed in these comets. Investigating the mechanisms that cause these outbursts for each comet needs simultaneous observations at infrared wavelengths and modeling of the material ejected, which is not presented in this work.

3.13.1 29P/Schwassmann-Wachmann 1

Comet 29P/Schwassmann-Wachmann 1 (hereafter 29P) was discovered by A. Schwassmann and A. Wachmann at Hamburg Observatory (Germany) on November 15, 1927. 29P is classified as a Centaur, it has circular orbit with an eccentricity e=0.044, semi-major axis a=5.99 au, orbital period P=14.6 yr, and a slight inclination with respect to the ecliptic of 9.4°. New dynamical studies suggest that 29P probably transferred recently to its current location, a newly discovered "Gateway" transitional orbit to the JFC population (Sarid et al., 2019). 29P is known for its episodic large outbursts, which tend to occur at an average rate of ~7 outbursts per year (Trigo-Rodríguez et al., 2008). It has been reported that its brightness can increase up to about 6 mag during an outburst. The nucleus size radius of 29P has been estimated between 15 and 27 km assuming a geometric albedo of ρ=0.04 (Stansberry et al., 2004). 29P has a higher dust mass loss rate compared to most of the JFCs, LPCs or Centaurs. The first direct millimeter-wavelength detection of CO emission in any cometary object was made in 29P by Senay and Jewitt (1994), which led to the suggestion that this gas is the primary driver of its activity.

We have been monitoring the outbursts of comet 29P since the installation of TS at La Silla in 2010. In this section, we present only a follow up of the outbursts detected in the last two years 2019-2020. We observed the comet from October 04, 2019 until February 26, 2020. During this period, we detected and followed three small outbursts. The first outburst occurred on October 8 with Δm~0.50 mag, second was detected on October 22 with Δm ~0.80 mag, while the third outburst happened on February 10 with Δm ~1.40 mag and is the largest outburst detected in our data. Table 3.20 summarizes TN and TS measurements of Rc magnitude within 5″ aperture and A(0)fρ parameter computed at 10 000 km from the nucleus. The magnitude evolution of multiple outbursts detected in comet 29P is shown in Figure 3.40 The optical dust colours compared to those of JFCs and LPCs are given in Table 3.25.

Table 3.20: Magnitude and A(0)fρ of comet 29P. T_0 is the time when we start observing the comet on October 4, 2018.

UT Date	r_h (au)	Δ (au)	T-T_0 (Days)	PA (°)	Exp (s)	R_{mag} (5″)	A(0)fρ(Rc) (cm)	Tel. TN/TS
2019 Oct 04	5.77	4.79	+1	1.9	240	15.92±0.05	2757.9±12.5	TS
2019 Oct 05	5.77	4.79	+2	1.8	240	15.82±0.05	3230.9±24.5	TN
2019 Oct 06	5.77	4.79	+3	1.8	240	15.89±0.07	3005.5±15.1	TN
2019 Oct 07	5.77	4.79	+4	1.7	180	15.76±0.08	3412.1±22.9	TN
2019 Oct 08	5.77	4.79	+5	1.7	180	15.50±0.08	4675.5±21.0	TS
2019 Oct 10	5.77	4.79	+7	1.7	180	15.83±0.09	3200.0±36.5	TS
2019 Oct 14	5.77	4.80	+11	2.1	120	15.75±0.08	3216.6±39.5	TN
2019 Oct 18	5.77	4.80	+15	2.4	180	15.19±0.08	4006.3±23.7	TS
2019 Oct 21	5.77	4.81	+18	2.9	240	15.25±0.06	5941.4±23.0	TN
2019 Oct 22	5.77	4.81	+19	3.0	240	15.20±0.08	5705.5±22.0	TS
2019 Oct 24	5.77	4.82	+21	3.3	240	15.40±0.08	4747.7±23.8	TN
2019 Oct 25	5.77	4.83	+22	3.5	240	15.48±0.07	4394.7±14.3	TN
2019 Oct 29	5.77	4.86	+26	4.1	240	15.75±0.05	3616.5±18.8	TN
2019 Oct 31	5.77	4.86	+28	4.4	240	15.89±0.07	3440.5±17.7	TN
2019 Nov 01	5.77	4.88	+29	4.5	240	15.97±0.05	3048.3±13.5	TN
2019 Nov 03	5.77	4.89	+31	4.8	240	15.83±0.06	3697.6±23.2	TN
2019 Nov 04	5.77	4.90	+32	5.0	180	15.96±0.06	3234.3±26.1	TS
2019 Nov 07	5.77	4.92	+35	5.5	180	15.80±0.07	4007.2±34.0	TS
2019 Nov 25	5.77	5.12	+53	7.7	180	16.01±0.06	3562.9±16.2	TN
2020 Feb 09	5.78	6.27	+129	8.1	60	14.61±0.06	11039.9±80.1	TN
2020 Feb 10	5.78	6.28	+130	8.0	180	14.80±0.04	9029.6±36.2	TN
2020 Feb 21	5.79	6.42	+141	7.1	240	15.77±0.07	4184.7±29.6	TN
2020 Feb 23	5.79	6.45	+143	6.9	240	15.84±0.07	4224.9±32.0	TN
2020 Feb 26	5.79	6.48	+146	6.6	240	15.94±0.06	3659.1±27.8	TN

3.13.2 123P/West-Hartley

Comet 123P/West-Hartley, hereafter 123P, was discovered on May 11, 1989 by Richard West at ESO in Chile. 123P is a JFC with an orbital period of 7.59 yr. A radius of 2.2 km has been estimated for its nucleus (Tancredi et al., 2000; Fernández et al., 2013). On January 10, 2019, a small apparent outburst has been reported by the ZTF team (Kelley et al., 2019b). 123P had been steadily brightening at a rate of about -0.05 mag/day since the end of November 2018. ZTF photometry shows a sudden increase in brightness, from R_{mag} = 14.42 to 14.02 mag over a 24 hr period between January 09 and 10, 2019. We observed 123P with TS from January 17 to June 1, 2019. We also collected data with TN on 3 nights, February 23, March 15 and May 28. Both TN and TS measurements show good agreement at closest dates. The Rc magnitude within 5″ aperture and A(0)fρ dust parameter are summarized in Table 3.21. Since January 17, we followed the decrease of the first outburst detected by ZTF with Δm ~0.20 mag until the second outburst that occurred on February 23 with Δm ~0.30 mag. Then, the activity of the comet decreased slightly down to R_{mag}=16 on June 1, 2019. The magnitude evolution of the outburst is given in Figure 3.40. Figure 3.39 shows the r magnitude evolution of comet 123P with different telescopes, TRAPPIST measurements are in agreement with other facilities.

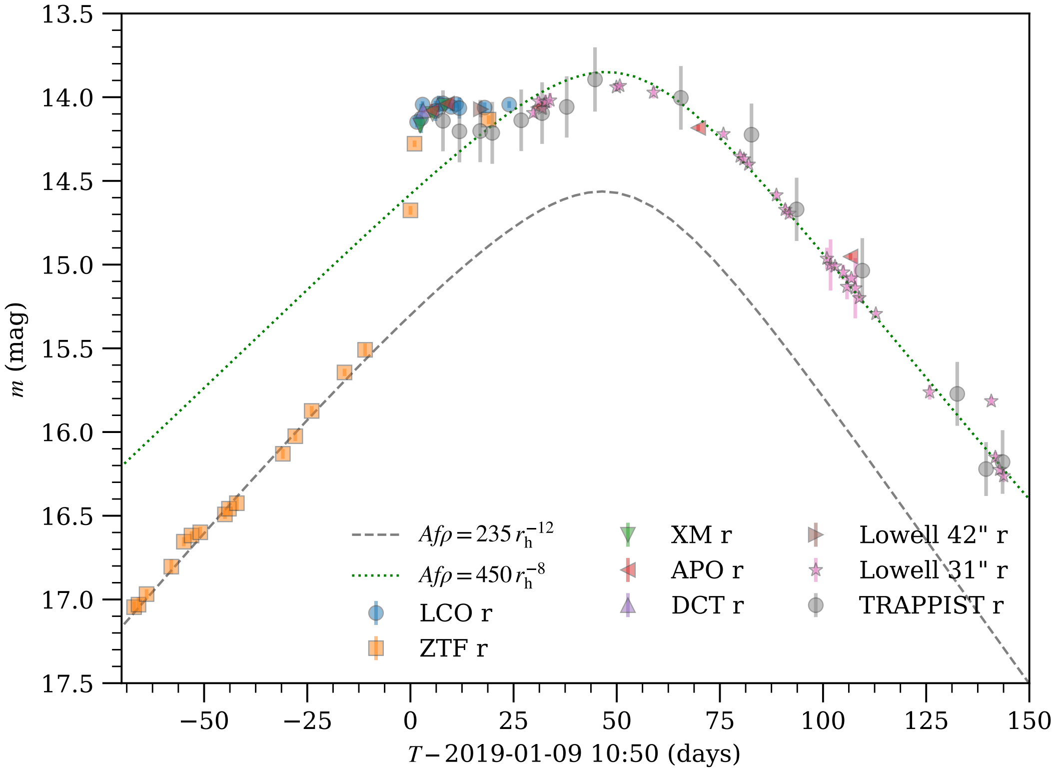

Figure 3.39: Evolution of the r magnitude of comet 123P as a function of days since January 9, 2019 (Kelley et al. in preparation). Rc TRAPPIST magnitudes were converted to r magnitudes using the correlation given in (Tonry et al., 2012). T=0 is the time of the outburst.

Table 3.21: Magnitude and A(0)fρ of comet 123P. T_0 is the time when we start observing the comet on January 17, 2019.

UT Date	r_h (au)	Δ (au)	T-T_0 (Days)	PA (°)	Exp (s)	R_{mag} (5″)	A(0)fρ(Rc) (cm)	Tel TN/TS
2019 Jan 17	2.13	1.36	+1	20.9	180	13.95±0.09	240.7±2.9	TS
2019 Jan 21	2.13	1.34	+5	19.9	180	14.02±0.08	201.2±6.7	TS
2019 Jan 26	2.12	1.30	+10	18.6	180	14.01±0.06	199.8±4.2	TS
2019 Jan 29	2.12	1.28	+13	17.8	180	14.02±0.07	185.3±3.6	TS
2019 Feb 05	2.12	1.25	+19	15.9	180	13.94±0.09	201.3±3.2	TS
2019 Feb 10	2.12	1.23	+24	14.6	180	13.90±0.06	202.9±2.9	TS
2019 Feb 16	2.13	1.21	+30	13.2	180	13.86±0.09	204.4±2.8	TS
2019 Feb 23	2.13	1.20	+37	12.1	240	13.70±0.05	237.8±3.7	TN
2019 Mar 15	2.15	1.22	+57	13.2	180	13.81±0.08	204.8±4.5	TN
2019 Apr 02	2.17	1.32	+74	17.7	180	14.03±0.05	203.9±3.3	TS
2019 Apr 13	2.19	1.40	+85	20.4	180	14.48±0.07	173.6±3.5	TS
2019 Apr 28	2.22	1.55	+100	23.3	180	14.84±0.07	138.9±2.9	TS
2019 May 21	2.27	1.82	+123	25.6	180	15.58±0.08	100.1±3.5	TS
2019 May 28	2.30	1.92	+130	25.8	180	16.03±0.06	85.4±3.4	TN
2019 Jun 01	2.31	1.97	+132	25.8	180	15.99±0.09	94.5±2.7	TS

3.13.3 155P/Shoemaker 3

Comet 155P/Shoemaker 3, hereafter 155P, was discovered by Caroline and Eugene Shoemaker at Palomar Observatory (USA) on January 10, 1986 at a magnitude of 10 using the 0.46-m Schmidt telescope. 155P is a JFC with an orbital period of 16.94 yr. The comet was independently recovered on September 9, 2002 at magnitude of 18 [10]. Between October 10.46 UT, 2019 and October 12.46, ZTF observed a sudden increase from r_{mag} = 16.62±0.06 mag to 15.52±0.05 mag. This brightness increase persisted in ZTF observations acquired on subsequent nights. With TN, we followed the activity of the comet from October 16 until November 6, 2019. The Rc magnitudes and A(0)fρ parameter of the comet are summarized in Table 3.22. We started monitoring the comet with TN three days after ZTF observations, at that time the activity of the comet was increasing rapidly. The outburst reached its maximum brightness on October 19 with R_{mag}=14.40±0.10 and Δm ~2 mag compared to the first observation reported in ZTF data. Then, the activity of the comet decreased rapidly down to R_{mag}=16.10±0.10 in two weeks. The magnitude evolution of the outburst is shown in Figure 3.40. The comet did not show any variation in its dust colour during this outburst. The average BVRI colours of comet 155P compared to those of LPC and JFC are given in Table 3.25.

Table 3.22: Magnitude and A(0)fρ of comet 155P. T_0 is the time when started observing the comet on October 16, 2019.

UT Date	r_h (au)	Δ (au)	T-T_0 (Days)	PA (°)	Exp (s)	R_{mag} (5″)	A(0)fρ(Rc) (cm)	Tel TN/TS
2019 Oct 16	1.83	1.82	+1	31.6	120	15.22±0.05	232.4±10.1	TN
2019 Oct 17	1.82	1.81	+2	31.7	120	14.79±0.08	221.8±7.8	TN
2019 Oct 18	1.82	1.80	+3	31.8	120	14.51±0.09	220.9±8.0	TN
2019 Oct 19	1.82	1.79	+6	31.9	180	14.40±0.10	186.8±6.5	TN
2019 Oct 20	1.82	1.78	+7	32.0	180	15.04±0.08	162.8±7.5	TN
2019 Oct 26	1.81	1.72	+13	32.4	120	15.93±0.04	112.4±6.7	TN
2019 Oct 30	1.80	1.69	+17	32.7	120	16.00±0.05	93.4±6.5	TN
2019 Nov 04	1.80	1.64	+22	32.9	180	16.08±0.07	88.4±6.2	TN
2019 Nov 06	1.80	1.63	+24	33.0	180	16.10±0.08	86.5±6.2	TN

3.13.4 243P/NEAT

Comet 243P/NEAT, hereafter 243P, was discovered by the Near-Earth Asteroid Tracking (NEAT) survey in September 2003 (Hicks et al., 2003). It is a member of the JFC with a 7.5 yr orbital period. It reached its perihelion at distance of 2.45 au on August 26, 2018. Mazzotta Epifani et al. (2008) detected the comet as a point source at r_h=3.97 au in *R*-band images, and estimated a nucleus radius of 0.8–1.55 km, assuming a geometric albedo of 0.04. An outburst of comet 243P was discovered by the Asteroid Terrestrial-Impact Last Alert System (ATLAS) as a brightening of at least 2.5 mag between December 10.38, 2018 and 12.34 UT (Heinze and Kadota, 2018). After receiving notice of the outburst, we observed the comet with both TRAPPIST telescopes to follow its evolution. We started observing the comet from December 15, 2018 (3 days after the outburst) until February 26, 2019. Table 3.23 summarizes the Rc magnitude and A(0)fρ parameter of comet 243P during our monitoring. The activity of the comet was decreasing slightly after the outburst from Rc magnitude of 16.43±0.06 down to

[10] https://cometography.com/pcomets/155p.html

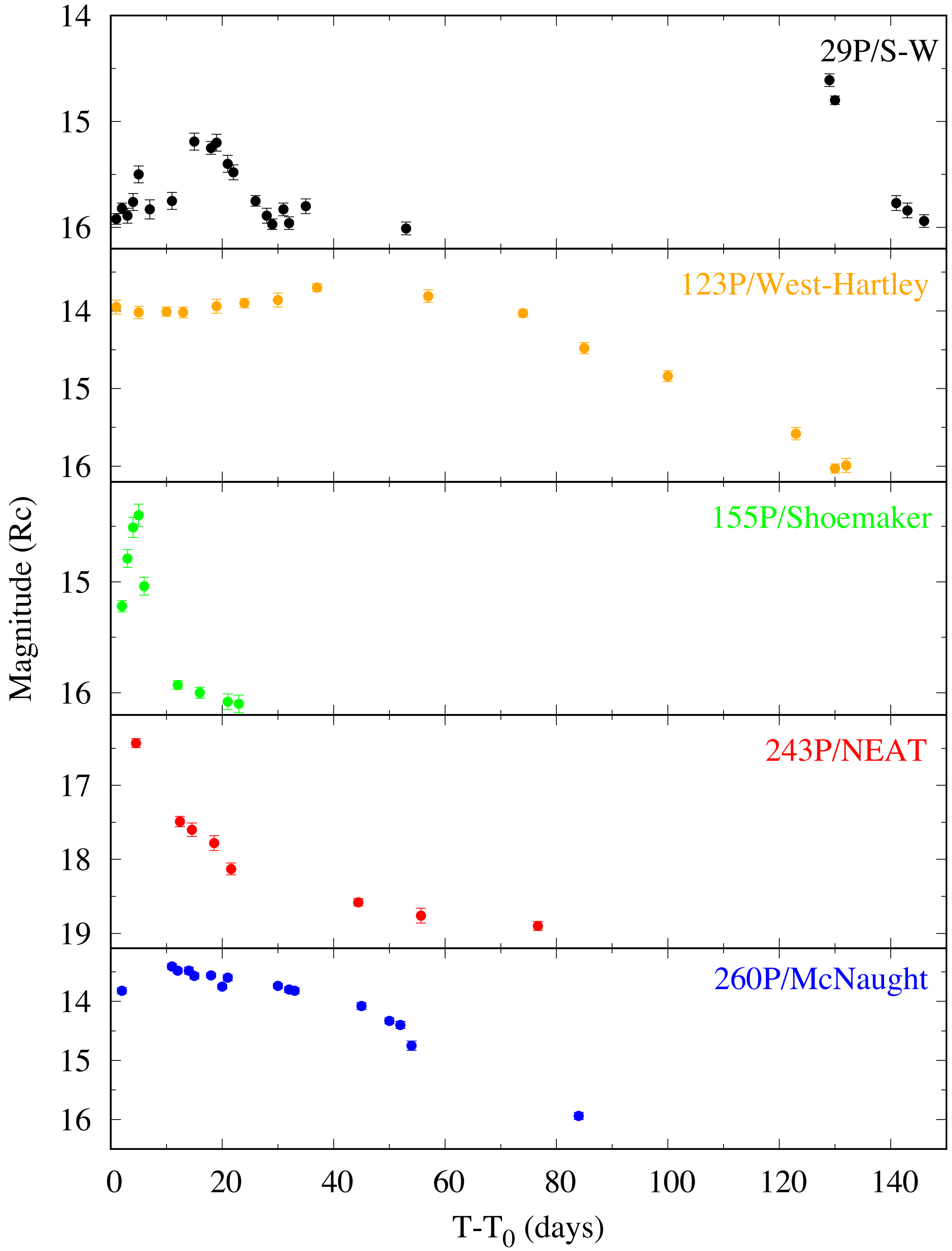

Figure 3.40: Magnitude evolution of comets in outburst as observed with TRAPPIST telescopes. T_0 is the first day when we start observing the comet.

18.90±0.06 in two months (see Figure 3.40). The dust colours of comet 243P compared to those of the Solar System comets are given in Table 3.25. Figure 3.41 shows the evolution of r-band magnitude measurements of 243P with different telescopes. TRAPPIST measurements are in agreement with data from other telescopes. Photometry, imaging, and spectroscopy analysis combined with dynamical and thermophysical models of this large outburst will be published in a separate work (Kelley et al. in preparation) which focuses on the water ice properties of the outburst.

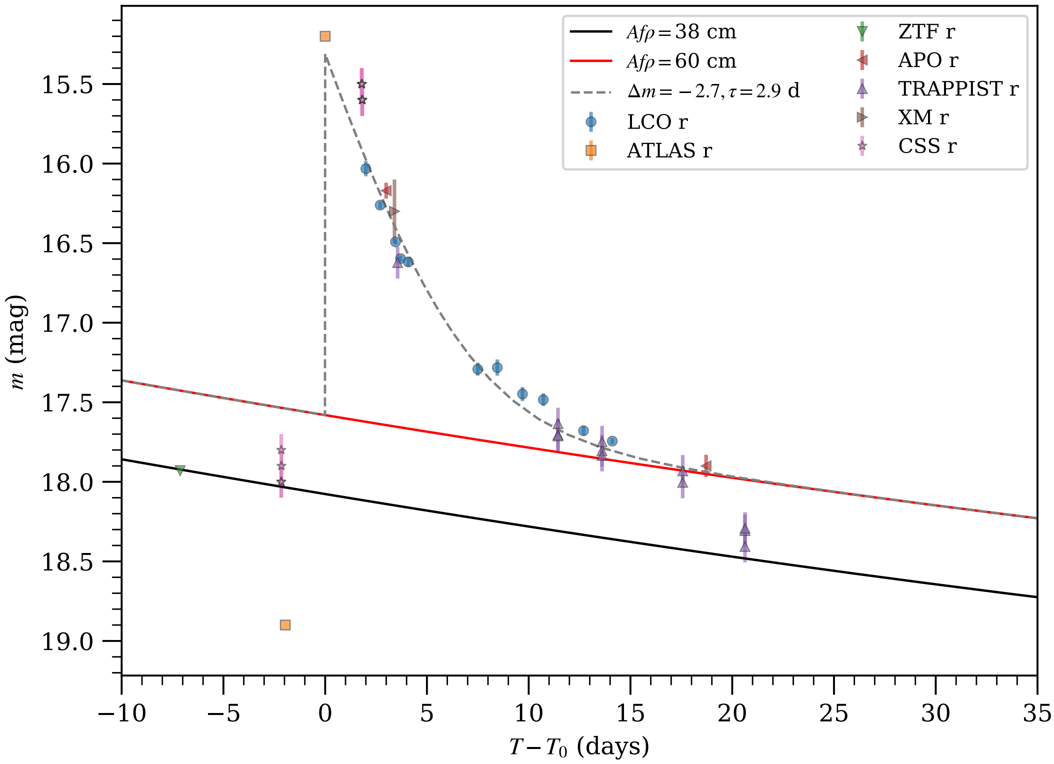

Figure 3.41: Evolution of r magnitude of comet 243P as a function of time (Kelley et al. in preparation). T_0 is the time time from nominal outburst date on December 11, 2018. Rc TRAPPIST magnitudes were converted to r-band magnitudes using the correlation give in (Tonry et al., 2012).

Table 3.23: Magnitude and A(0)fρ of comet 243P. T_0 is the time time from nominal outburst date on December 11, 2018.

UT Date	r_h (au)	Δ (au)	T-T_0 (Days)	PA (°)	Exp (s)	R_{mag} (5″)	A(0)fρ(Rc) (cm)	Tel TN/TS
2018 Dec 15	2.56	1.91	+4	19.3	120	16.43±0.06	184.8±7.9	TN
2018 Dec 23	2.57	2.01	+12	20.5	120	17.49±0.07	76.1±9.5	TN
2018 Dec 25	2.58	2.04	+14	20.7	240	17.60±0.09	67.3±6.8	TN
2018 Dec 29	2.58	2.10	+18	21.1	240	17.78±0.10	59.0±5.8	TN
2019 Jan 01	2.60	2.14	+21	21.4	240	18.13±0.08	43.8±6.5	TN
2019 Jan 24	2.64	2.48	+44	21.9	240	18.58±0.05	39.4±6.7	TN
2019 Feb 05	2.67	2.65	+55	21.4	180	18.76±0.10	29.2±6.0	TS
2019 Feb 26	2.72	2.96	+76	19.4	240	18.90±0.06	25.5±8.5	TS

3.13.5 260P/McNaught

Comet 260P/McNaught, hereafter 260P, is a JFC with an orbital period of 7.05 yr. It reached its last perihelion (r_h=1.49 au) on October 1, 2019. 260P was discovered by Rob McNaught on May 20, 2005 with the 0.5-m Uppsala Schmidt telescope at Siding Spring Observatory[11]. Between 2019 October 04.48 and 05.35 UTC, ZTF data show that the brightness of 260P changed from r=13.78±0.02 to 13.59±0.02 mag, and remained bright until October 08.43 UTC. After receiving this notification, we monitored the comet with TN from October 7 until December 25, 2019. The comet reached its maximum brightness post-perihelion (r_h=1.48 au) on October 19 with R_{mag}= 13.4 and it decreased slightly as the comet was getting away from the Sun. The Rc magnitude within 5″ and A(0)fρ parameter of comet 260P are summarized in Table 3.24. The BVRI colours of 260P compared to those of JFCs and LPCs are given in Table 3.25. We also collected OH, CN, C_2, and C_3 images of comet 260P with TN on October 8 and 23, 2019. We derived the CN production rate of $(3.00\pm0.51)\times10^{24}$ molec/s and upper limits of 9.11×10^{23} molec/s for C_2, 1.62×10^{23} molec/s for C_3 and 1.73×10^{27} molec/s for OH. This provides a maximum C_2 and C_3 ratios with respect to CN of Log[Q(C_2)/Q(CN)] $<$ -0.51 and Log[Q(C_3)/Q(CN)]$<$ -1.26, respectively. These ratios are below the carbon-chain depleted comets limit defined by A'Hearn et al. (1995) which makes 260P a carbon-chain depleted comet. Comet 260P has a dust/gas ratio of Log[A(0)fρ(RC)/Q(CN)]=-22.20±0.25 is in agreement with the average value for depleted comets and larger than for typical comets (A'Hearn et al., 1995).

Table 3.24: Magnitude and A(0)fρ of comet 260P. T_0 is the time time from nominal outburst date reported by ZTF on October 5, 2019.

UT Date	r_h (au)	Δ (au)	T-T_0 (Days)	PA (°)	Exp (s)	R_{mag} (5″)	A(0)fρ (Rc) (cm)	Tel TN/TS
2019 Oct 07	1.45	0.56	+2	29.6	180	13.82±0.05	203.7±6.3	TN
2019 Oct 16	1.47	0.57	+11	26.7	60	13.41±0.05	162.8±7.3	TN
2019 Oct 17	1.47	0.57	+12	26.4	60	13.48±0.04	162.8±8.1	TN
2019 Oct 19	1.48	0.57	+14	25.7	60	13.48±0.06	168.3±7.1	TN
2019 Oct 20	1.48	0.57	+15	25.4	60	13.57±0.05	173.8±7.1	TN
2019 Oct 23	1.49	0.58	+18	24.5	60	13.56±0.04	171.5±8.5	TN
2019 Oct 25	1.50	0.59	+20	23.9	60	13.75±0.04	189.9±6.3	TN
2019 Oct 26	1.50	0.59	+21	23.6	60	13.60±0.05	181.8±6.2	TN
2019 Nov 04	1.50	0.59	+30	23.6	180	13.74±0.04	202.4±5.5	TN
2019 Nov 06	1.50	0.59	+32	23.6	180	13.80±0.05	208.3±6.8	TN
2019 Nov 07	1.50	0.59	+33	23.6	180	13.82±0.05	192.7±6.2	TN
2019 Nov 18	1.61	0.69	+45	19.8	180	14.08±0.06	177.6±5.7	TN
2019 Nov 23	1.64	0.72	+50	19.8	180	14.33±0.05	145.9±6.1	TN
2019 Nov 25	1.65	0.74	+52	19.9	180	14.40±0.06	133.7±6.6	TN
2019 Nov 27	1.66	0.75	+54	20.0	180	14.75±0.08	86.5±6.0	TN
2019 Dec 25	1.82	1.02	+84	23.6	180	15.94±0.06	72.5±6.2	TN

[11] https://people.ast.cam.ac.uk/~jds/per2030.htm#260P

Table 3.25: Optical dust colours of different comets compared to those of active JFCs and LPCs.

Object	Colours				Reference
	B - V	V - Rc	Rc - Ic	B - Rc	
29P/S-W	0.88±0.07	0.46±0.04	0.48±0.04	1.35±0.08	This Work
123P/West-Hartley	0.75±0.08	0.54±0.03	0.50±0.05	1.31±0.06	This Work
155P/Shoemaker	0.86±0.08	0.47±0.07	0.46±0.04	1.37±0.08	This Work
243P/NEAT	0.91±0.06	0.48±0.07	0.49±0.06	1.42±0.07	This Work
260P/McNaught	0.84±0.04	0.41±0.08	0.53±0.09	1.25±0.07	This Work
Active LPC	0.78±0.02	0.47±0.02	0.42±0.03	1.24±0.02	Jewitt et al. (2015)
Active JFC	0.75±0.02	0.47±0.02	0.44±0.02	1.22±0.02	Solontoi et al. (2012)
Sun	0.64±0.02	0.35±0.01	0.33±0.01	0.99±0.02	Holmberg et al. (2006)

3.14 2I/Borisov: The first interstellar Comet

2I/Borisov is the first active interstellar comet observed in the Solar System, providing a unique opportunity to study comets that are formed around other stars. The comet was discovered by an Ukrainian amateur astronomer G. Borisov on August 30, 2019 when the comet was ∼3 au from the Sun. Its orbit was very quickly found to be hyperbolic with an eccentricity > 3. Contrary to the first interstellar object 1I/Oumuamua discovered in 2017, 2I/Borisov has a distinct comet-like appearance with a diffuse coma at ∼3 au from the Sun which provides a way to probe the composition and the properties of the nucleus (de León et al., 2019; Jewitt and Luu, 2019). de León et al. (2019) made early spectroscopic observations of 2I/Borisov with the 2.5-m Nordic Optical Telescope (NOT) on September 17, 2020. Their data did not reveal any emission lines between 4000–9000 Å, but they were able to put an upper limit on the flux of the C_2 emission line, suggesting modest cometary activities at early epochs. Fitzsimmons et al. (2019) used the WHT telescope in La Palma to make the first detection of the CN[388nm] gas emission in the first interstellar comet 2I/Borisov on September 20 (r_h=2.66 au), see Figure 3.42. They derived a CN production rate of 3.7×10^{24} molec/s. A pre-discovery study shows that 2I/Borisov was already active at 6-8 au with R magnitude of 22, which indicates that the activity of the comet is driven by volatiles like CO and CO_2 as for Solar System comets at large heliocentric distances (Bolin et al., 2019; Ye et al., 2019). After the detection of CN and later C_2, 2I/Borisov was found to be depleted in C_2 with respect to CN (Opitom et al., 2019; Kareta et al., 2019; Lin et al., 2019) similar to the Solar System comets carbon-depleted group (A'Hearn et al., 1995; Cochran et al., 2012). Several independent studies have shown that the carbon-chain abundance of 2I/Borisov evolved with heliocentric distance. Early observations show that this object is strongly carbon-chain depleted (Opitom et al., 2019; Kareta et al., 2019). 2I/Borisov became far less depleted as it moved closer to the Sun, and by December 2020 exhibited only moderate carbon-chain depletion (Lin et al., 2019; Bannister et al., 2020). Initial characterization of the comet has been carried out by many studies (Jewitt et al., 2019; Guzik et al., 2019). The radius of the nucleus was estimated to be <1 km based on measurements of the surface brightness profile and modelling of the observed gas and dust production rates. The dust optical colours of 2I/Borisov are basically identical to those of Solar System comets and no significant change of its colours has been reported (Jewitt et al., 2019; Guzik et al., 2019; Fitzsimmons et al., 2019). Cordiner et al. (2020) observed 2I/Borisov with the Atacama Large Millimeter/ submillimeter Array (ALMA) in mid-December 2019. Their observations reveal emissions of HCN and CO, with production rates Q(HCN)=$(7.0\pm1.1)\times10^{23}$

molec/s and Q(CO)=(4.4±0.7)×10^{26} molec/s. They found that HCN abundance relative to water of (0.06–0.16%) is similar to that of comets in our Solar System, while the abundance of CO/H_2O (35–105%) is among the highest observed in any comet within 2 au of the Sun. Bodewits et al. (2020) obtained a similar result with a ratio of CO/H_2O=173% using the HST telescope, this abundance is higher three times than the previously measured for any comet in the inner (<2.5 au) Solar System. The authors suggest that 2I/Borisov must have formed in a relatively CO-rich environment, probably beyond the CO ice-line in the very cold outer regions of a distant protoplanetary accretion disk.

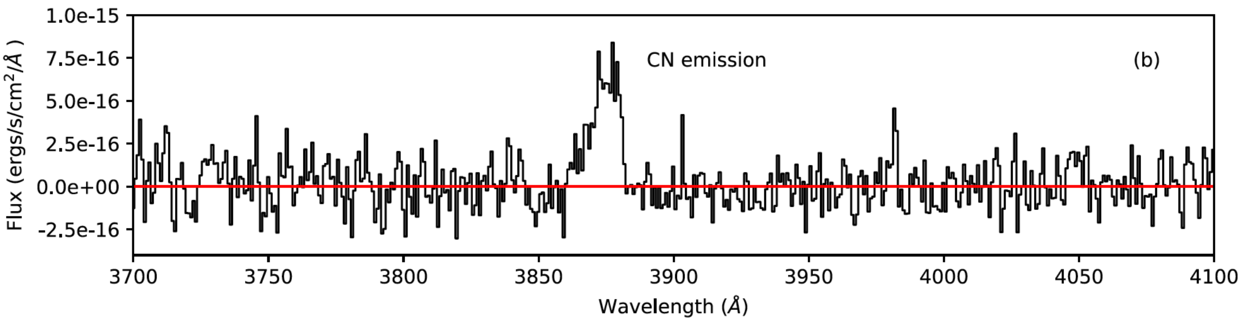

Figure 3.42: Spectral region of comet 2I/Borisov around the CN (0–0) emission band with the background dust continuum subtracted (Fitzsimmons et al., 2019).

We started observing 2I/Boriosv with TN on September 11, 2019, a week after its discovery when the comet was at 2.80 au from the Sun. During the first weeks of our observations, the comet was low in the northern sky with a high air-mass and a small observing window of about 30 minutes. We started acquiring data with the Johnson-Cousin filters B, V, Rc and Ic. On October 2020, the comet was higher in the sky with a good condition of visibility which allows us to observe the comet with narrow-band filters such as CN and C_2 with long exposure times. At the beginning of November, we started observing the comet with TS as it was rising in the southern sky. 2I/Borisov reached its perihelion on December 9, 2019 at 2.00 au from the Sun. The Rc magnitudes within 5″ aperture and A(0)fρ parameter are summarized in Table A.14 and shown in Figure 3.43. The activity of the comet was increasing slightly as the comet was approaching the Sun, while it reached its maximum activity 20 days before perihelion. Its activity was then fading as the comet was getting further a way from the sun.

We started detecting CN in 2I/Borisov with TRAPPIST telescopes from October 18, 2019 (r_{h}=2.65 au) pre-perihelion until January 31, 2020 at heliocentric distance of 2.33 au (post-perihelion). No signal of C_2 was detected during the whole period with TRAPPIST. Table A.13 summarizes the CN production rates and the upper limit for C_2. Figure 3.44 shows the evolution of CN production rates as function of time to perihelion. We derived C_2/CN ratio of Log[Q(C_2)/Q(CN)]<-0.54 which confirms the first interstellar comet 2I/Borisov is a carbon-chain depleted comet. This result is in agreement with the finding of Opitom et al. (2019) using the WHT. The comet has a dust/gas ratio of Log[A(0)fρ(Rc)/Q(CN)]=-22.58±0.04 which is in agreement with the mean value of depleted comets. Later observations of 2I/Borisov with MUSE/VLT instrument in November 2019 show a strong NH_2 emission providing a production rate of Q(NH_2)=4.8 × 10^{24} molec/s, which made the first interstellar comet 2I/Borisov enriched in NH_2 with a ratio of Q(NH_2)/Q(CN)=2.7 compared to the known Solar System comets (Bannister et al., 2020). The optical dust colours, B-V=0.82±0.05, V-Rc=0.46 ±0.03 and Rc-Ic=0.44 ±0.05, are similar to those of Solar System comets (see Table 3.26). This result is in agreement with other studies (Jewitt et al., 2019; Guzik et al., 2019).

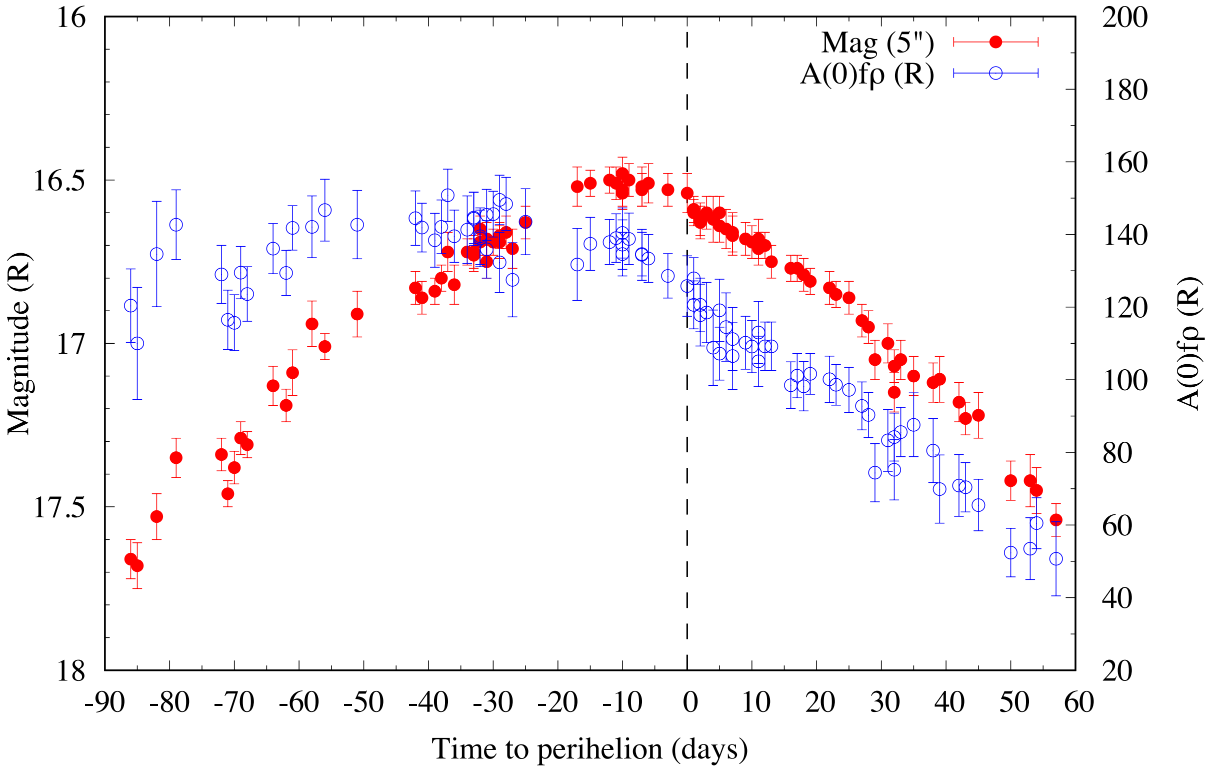

Figure 3.43: Evolution of Rc magnitude and A(0)fρ parameter of 2I/Borisov as a function of days to perihelion. The comet reached its perihelion on December 9, 2019 at 2.00 au from the Sun. The A(0)fρ values were computed at 1000 km from the nucleus and corrected for the phase angle effect.

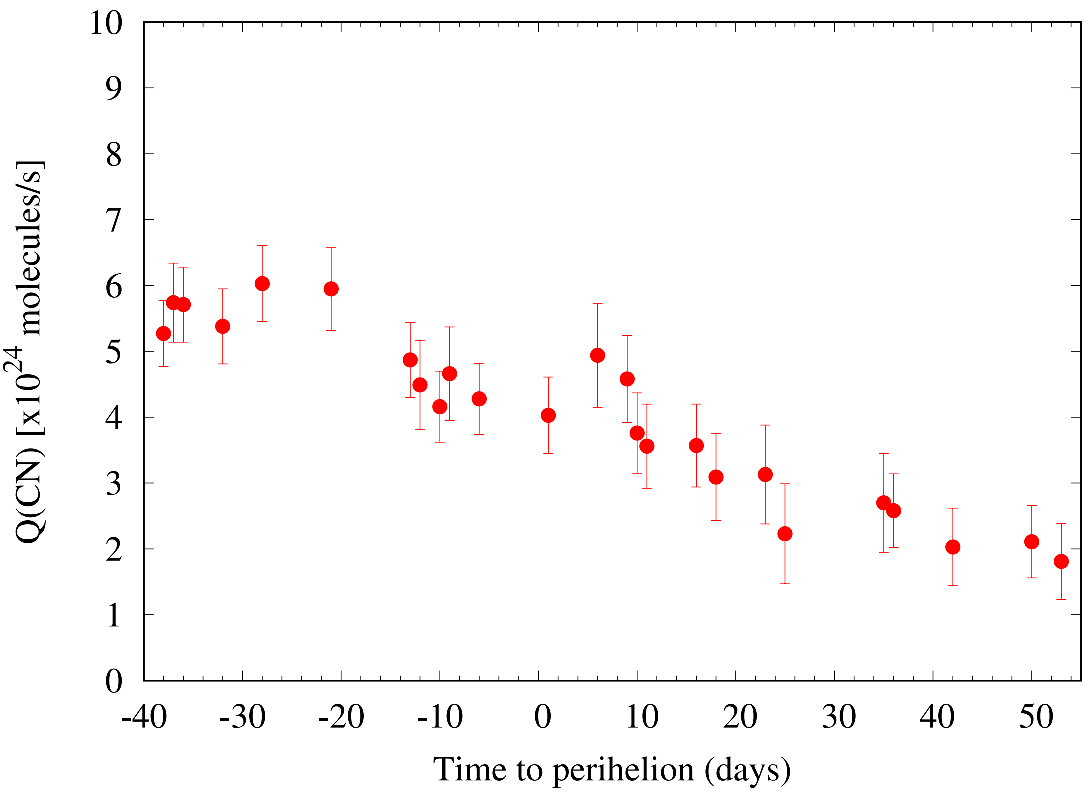

Figure 3.44: Evolution of CN production rates of 2I/Borisov as a function as time to perihelion.

We detected an outburst between March 7.4 and 10.4 UT, 2020. Series of 10 images of 240 s with Rc filter were taken routinely about every two nights in the course of our dense monitoring of the comet. A small circular aperture radius of only 2 pixels (5" diameter) was used to mitigate star contamination as the comet was crossing very crowded fields in early 2020. A constant R magnitude of 18.0±0.1 was measured between Feb 26.4 UT and March 07.4 UT on six different nights in carefully selected images (only few images are not contaminated on each night). On March 10.4 UT the magnitude was 17.1±0.1 showing an increase of 0.8±0.1 mag with respect to March 7 and previous nights. Three nights later, on March 13.4 UT, the comet had faded by 0.3 mag at 17.4±0.1. We confirm the comet had an outburst reported by Drahus et al. (2020) but there is no indication of an other outburst on March 4 or 5 or before as reported by the same team. No peculiar feature (no fragment) was observed with TRAPPIST.

Table 3.26: Colours of 2I/Borisov compared to those of JFCs and LPCs nuclei and coma.

Object	Colours				Reference
	B - V	V - R	Rc - Ic	B - Rc	
2I/Borisov	0.82±0.02	0.46±0.03	0.44±0.03	1.28±0.03	This Work
	0.80±0.05	0.47±0.03	0.49±0.05	1.27±0.04	Jewitt et al. (2019)
1I/Oumuamua	0.70±0.06	0.45±0.05	-	1.15±0.05	Jewitt et al. (2017)
Active LPC	0.78±0.02	0.47±0.02	0.42±0.03	1.24±0.02	Jewitt et al. (2015)
Active JFC	0.75±0.02	0.47±0.02	0.44±0.02	1.22±0.02	Solontoi et al. (2012)
Sun	0.64±0.02	0.35±0.01	0.33±0.01	0.99±0.02	Holmberg et al. (2006)

Chapter 4

Chemical composition of comets with TRAPPIST

In this chapter, we summarize and discuss the composition and activity of 29 comets with different dynamical types collected with both TRAPPIST telescopes in the period of 2017-2020. Here we consider only comets observed with both broad- and narrow-band filters and for which the gas emission was detected in the coma, in order to determine the molecular abundances. We observed 18 JFCs and a Halley type comet (38P/Stephan-Oterma) with both telescopes. We detected the gas emission (at least CN and C_2) in 14 JFCs, while four comets (29P, 123P, 243P and 155P) were observed only with broad-band filters as they show an outburst and no gas emission was detected in our images (see section 3.13 in chapter 3). We also observed 16 LPCs in addition to the first interstellar comet 2I/Borisov. We detected the gas emission in all of them, except for comet C/2017 T2 which was discovered to be active at 16 au from the Sun (Wainscoat et al., 2017) and no gas emission was detected in our images for this comet. From these observations, we derived the production rates of the various gas species. We computed the A(0)fρ parameter from narrow-band (as well as broad-band) aperture photometry to characterize the relative amount of dust present in each comet coma. We followed the evolution of these quantities with the heliocentric distances. We derived relative molecular abundances, dust/gas ratios, and other properties, including the dependence of these properties with the heliocentric distances. We investigated the correlation among all these properties. In order to ensure a homogeneous reduction and to compare our results with other similar studies, we used the same parent and daughter scalelengths, daughter lifetimes with a constant radial velocity of 1 km/s and g-factors given in A'Hearn et al. (1995) and in Schleicher (2008) to compute gas production rates (see chapter 2 for more details). The same parameters were used in the previous analysis of TRAPPIST data covering the period 2011-2016 (Opitom, 2016). We note that other spectroscopic studies used different Haser parameters to derive the production rates of different molecules (Fink, 2009; Langland-Shula and Smith, 2011; Cochran et al., 2012). For this reason, we decided to compare our results with similar photometric studies which uses the same parameters (A'Hearn et al., 1995; Schleicher, 2008).

4.1 Gas production rates and dust

In this section, we investigate the coma composition through the correlation between production rates of different species as well as the dust proxy A(0)fρ parameter. In order to make a coherent comparison between the composition of comets in our database and to distinguish individual comets in our figures, we choose to present the production rates around the perihelion or at the closet heliocentric distance where we acquired the data for all the species at the same night and under similar conditions. Table 4.1 summarizes the production rates of the various species as well as the A(0)fρ parameter for each comet in our database. The error-bars represent the error for the individual measurement of a comet at given heliocentric distance. We were able to derive the gas production rates and A(0)fρ parameter for most of the comets included in our study, or an upper limit for some species. We detected OH in most comets except for some faint comets like 398P, C/2018 N2 and 2I/Borisov, but we were able to derive an upper limit of Q(OH) for comet 260P. NH was detected for most comets except for 45P, 66P, 260P, 398P, C/2018 N2 and 2I/Borisov as they were very faint for TRAPPIST at the time of the observation. CN, C_2 and C_3 were detected in all the comets included in our database, except comets 260P and 398P where we derive upper limit for C_2 and C_3. CN and C_2 were detected in comet 2I/Borisov while C_3 was not detected. C_3 was detected in comet C/2017 T1, but it was contaminated by a star and it was the only image taken for this comet with C_3 filter.

Table 4.1: Summary of production rates at or close to perihelion of the 29 comets observed with TRAPPIST in the period 2017-2021.

Comets	r_h	$\triangle$	Production rates (molec/s)					A(0)fρ(BC)
	(au)	(au)	Q(OH)$\times 10^{27}$	Q(NH)$\times 10^{25}$	Q(CN)$\times 10^{24}$	Q(C_2)$\times 10^{24}$	Q(C_3)$\times 10^{24}$	($\times 10^2$ cm)
21P/Giacobini-Zinner	1.01	0.39	23.60±0.83	5.66±0.38	43.90±1.08	16.70±0.84	2.26±0.17	7.23±0.12
24P/Schaumasse	1.23	1.49	3.63±0.12	2.22±0.06	8.41±0.15	9.19±0.53	2.13±0.14	1.23±0.06
38P/Stephan-Oterma	1.59	0.92	7.56±0.16	4.71±0.21	14.40±0.11	14.40±0.08	4.17±0.03	6.31±0.10
41P/Tuttle-Giacobini-Kresak	1.05	0.15	2.61±0.15	2.17±0.08	4.07±0.52	5.02±0.54	1.23±0.08	0.35±0.03
45P/Honda-Mrkos-Pajdusakova	0.97	0.08	1.42±0.51	-	3.13±0.13	3.50±0.12	0.82± 0.04	0.15±0.02
46P/Wirtanen	1.05	0.08	5.44±0.18	3.33±0.19	13.70±0.32	15.80±0.47	4.00±0.08	1.71±0.17
62P/Tsuchinshan 1	1.38	1.34	4.26±0.19	2.50±0.18	16.30±0.24	16.80±0.17	4.21±0.12	1.44±0.08
64P/Swift-Gehrels	1.39	0.45	6.05±0.23	3.40±0.12	14.30±0.09	13.60±0.10	3.74±0.06	1.59±0.16
66P/du Toit	1.28	0.90	2.53±0.30	-	8.00±0.53	8.22±0.64	2.43±0.22	0.75±0.06
88P/Howell	1.37	1.48	29.60±0.88	13.40±0.45	64.40±1.53	75.50±1.66	16.9±2.34	7.50±0.25
156P/Russell-LINEAR	1.33	1.52	3.87±0.24	3.37±0.41	6.31±0.52	7.83±0.62	2.27±0.17	2.76±0.07
252P/LINEAR	1.00	0.05	2.63±0.12	0.45±0.03	4.75±0.13	4.30±0.19	1.24±0.07	0.10±0.01
260P/McNaught	1.45	0.56	<1.73	-	3.00±0.51	<0.91	<0.16	2.03±0.06
398P/Boattini	1.31	0.38	-	-	1.23±0.50	<0.66	<0.05	0.44±0.04
C/2015 V2 (Johnson)	1.64	0.81	22.10±1.00	5.78±0.72	34.2±0.61	44.80±0.80	8.98±0.26	12.06±0.34
C/2016 M1 (PANSTARRS)	2.29	1.30	63.80±1.36	31.00±1.02	182.00±6.77	175.00±8.91	46.50±4.85	65.93±0.34
C/2017 E4 (Lovejoy)	0.66	0.64	13.70±0.65	16.30±0.38	78.70±5.10	109.00±6.23	13.6±0.28	1.49±0.11
C/2017 O1 (ASASSN)	1.50	0.72	1.05±0.31	0.37±0.04	18.80±0.34	16.90±0.25	4.58±0.17	1.64±0.13
C/2017 T1 (Heinze)	0.90	0.51	1.12±0.25	0.97±0.25	3.16±0.09	3.72±0.11	-	0.23±0.04
C/2017 T2 (PANSTARRS)	2.08	1.60	55.20±1.05	5.13±0.64	87.20±6.00	104.00±8.00	17.3±0.80	36.28±0.44
C/2018 N2 (ASASSN)	3.19	2.59	-	-	24.1±0.90	27.7±0.89	3.24±0.28	31.62±0.37
C/2018 Y1 (Iwamoto)	1.29	0.31	15.70±1.42	7.13±0.77	30.4±1.19	35.8±1.90	8.96±1.65	1.52±0.05
C/2018 W2 (Africano)	1.48	0.50	2.85±0.22	0.40±0.05	10.50±0.55	10.70±0.65	2.60±0.18	1.80±0.15
C/2019 Y4 (ATLAS)	1.86	1.15	13.50±0.45	15.40±1.40	58.20±1.20	41.80±1.10	12.10±0.40	3.92±0.19
C/2020 A2 (Iwamoto)	1.06	1.16	1.77±0.22	3.36±0.38	7.35±0.68	9.91±0.63	1.32±0.18	0.31±0.06
C/2020 F3 (NEOWISE)	0.95	0.94	36.80±3.00	36.70±1.40	176.00±6.20	280.00±7.40	47.00±2.00	9.80±0.19
C/2020 M3 (ATLAS)	1.27	0.41	9.24±0.42	5.20±0.47	15.20±0.59	20.40±0.69	5.40±0.17	1.75±0.08
C/2020 S3 (Erasmus)	0.85	1.06	45.4±3.65	73.70±4.61	246.00±5.27	482.00±6.67	39.30±2.64	13.11±0.19
2I/Borisov	2.18	2.44	-	-	5.27±0.60	<3.65±0.64	-	1.51±0.07

Figure 4.1 represents OH, NH, C_3, and C_2 logarithmic production rates as a function of CN logarithmic production rate for all comets in our database. Generally, we see that the production rates of all the molecules correlate well with the CN production rates. For C_2 over CN plot, we clearly see a strong correlation between C_2 and CN where most comets lie on a diagonal except for the carbon-chain depleted comets (21P, 260P, 398P and 2I/Borisov). The same behavior is observed between C_3 and CN, indicating that these two carbon-chain species are strongly linked to each other. For the correlation between OH and CN, most comets lie on a diagonal band except for comet C/2017 O1 which shows a lower OH with respect to CN.

This could be due to the strong outburst detected in this comet, which could be responsible for bringing more carbon material from the interior of the nucleus. We also found a correlation between NH and CN for most comets, except for comets 252P, C/2017 O1, C/2017 T2 and C/2018 W2 which show a depletion of NH with respect to CN. In the four panels of the plot, most JFCs lie on the lower left end of the diagonal band and the most active LPCs lie on the upper right. This means that JFCs are generally less active than other LPCs, which could be explained by the fact that JFCs have made many passages around the Sun making them to build-up a crust on the surface of their nuclei, thereby reducing the active surface and activity of the comet. This conclusion was already noticed by (A'Hearn et al., 1995) who found that JFCs tend to have smaller active areas than other types of comets. This could also explain the asymmetric activity about perihelion found for some JFCs. The diagonal band in which most comets lie is narrow for C_2 and C_3 with respect to CN, which imply that most comets have a very similar composition except for those that show a depletion in the carbon-chain elements. While the correlation between OH and NH with respect to CN is not so good, which could be due to the fact that those species are in the blue with very strong atmospheric extinction and the uncertainties are larger. In the case of NH, the scale-lengths are also very uncertain and that might bring and extra scatter in the data. But for some comets that located below the trend, it is clearly shown that they are depleted in OH and NH with respect to the CN.

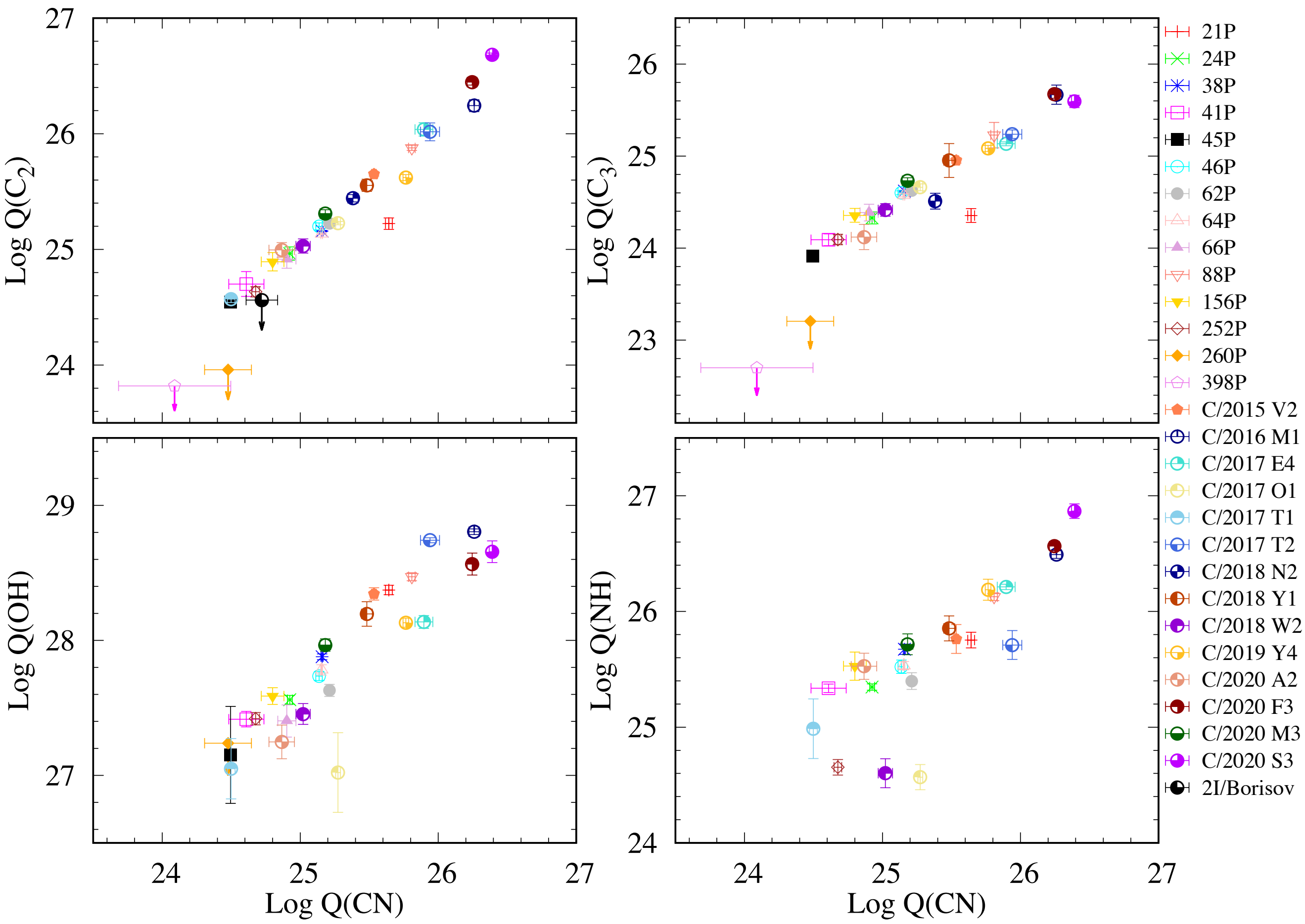

Figure 4.1: OH, NH, C_3, and C_2 logarithmic production rates as a function of CN logarithmic production rate for all comets in our database.

Figure 4.2 represents CN, NH, C_3, and C_2 logarithmic production rates as a function of OH logarithmic production rate for all comets in our database. As for the CN, most comets lie on the diagonal band except of those depleted in carbon-chain elements and in NH with respect to OH or show an enrichment in C_2 and CN. The C_3, C_2 and CN over OH plots look extremely similar. The two carbon-chain depleted comets 21P and 260P are located below the diagonal band for C_3 and C_2 over OH, while the other two depleted comets 2I/Borisov and 398P are not shown in these plots as we did not detect OH in their coma. Unlike what is shown in Figure 4.1 with respect to CN, the diagonal for OH is much wider than for CN as some comets show an enrichment in carbon-chain species with respect to OH. This dispersion might be due to large errors on OH. In the four sub-plots, most comets show a correlation between the production rates of the five radicals. But we have noticed some comets that appear outside of the diagonal band. Comet C/2017 O1 seems to be the richest in C_2, C_3 and CN with respect to OH which is certainly due to the strong outburst detected in this comet. That comet has the lowest NH/OH ratio compared to the rest of comets included in our database. Comets C/2017 E4, C/2020 F3, C/2018 W2 show higher C_2, CN, NH production rates with respect to OH but they show a normal ratio of C_3 to OH. As for the CN, comets 252P, C/2017 O1, C/2017 T2 and C/2018 W2 found to be depleted in NH with respect to OH.

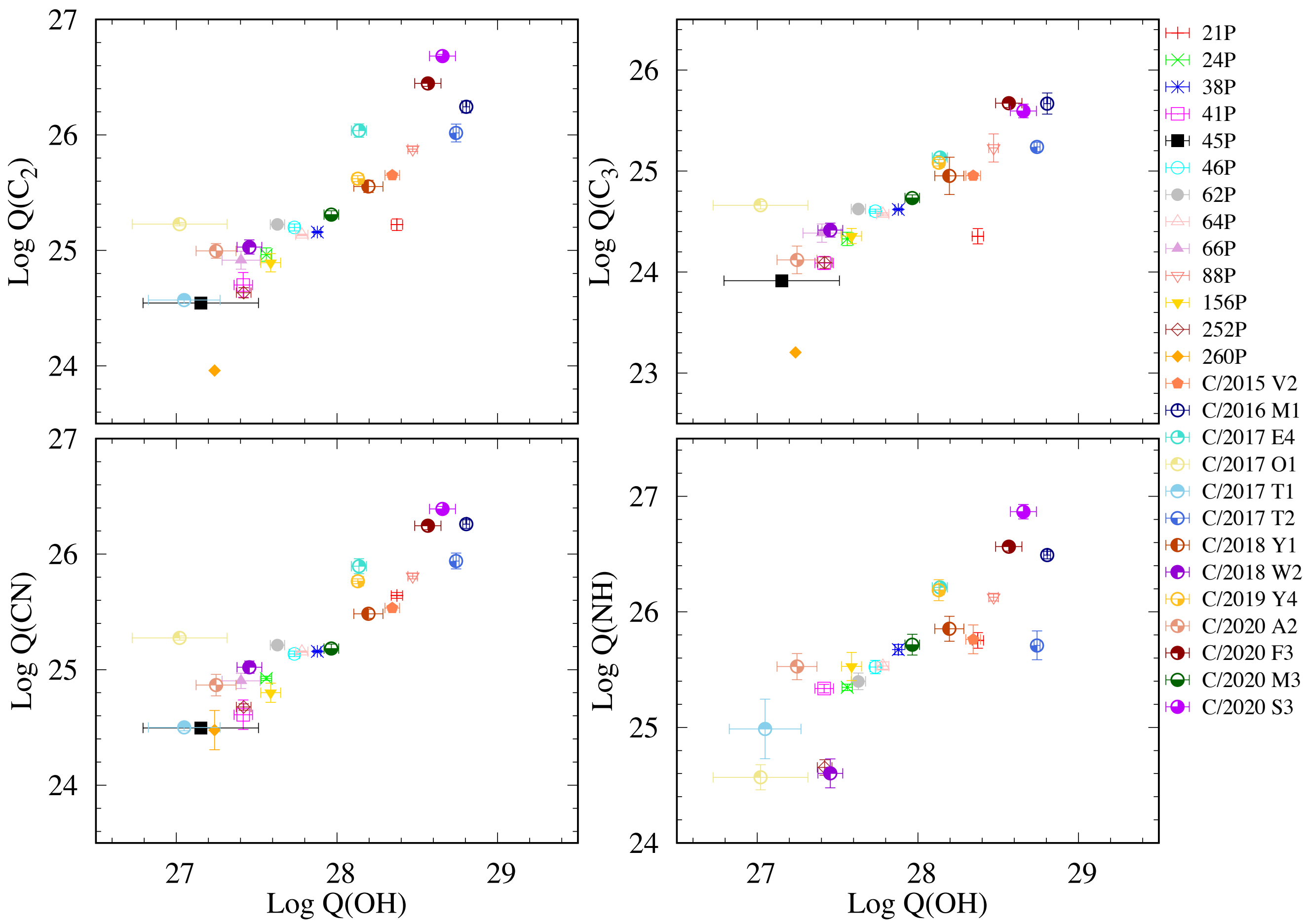

Figure 4.2: CN, NH, C_3, and C_2 logarithmic production rates as a function of OH logarithmic production rate for all comets in our database.

Figure 4.3 represents OH, NH, CN, C_3, and C_2 logarithmic production rates as a function of logarithm of A(0)fρ for all comets included in our database. As for the CN and OH, most comets lie on a diagonal, indicating that the gas and dust releases are correlated. But the dispersion is higher than for the gas species (Figures 4.1 and 4.2). Comets located at the top-right of the plot have higher dust/gas ratio while those located at the bottom-left of the diagonal band have lower dust/gas ratio. C_2, C_3, and CN over A(0)fρ show a similar trend, while the two carbon-chain depleted comets 398P and 260P are located below the correlation (more clearly in C_2 and C_3 plot than in the CN plot), indicating that they have a high dust/gas ratio compared to the comets. But this do not reflect real composition of both comets as we were only able to derive upper limits of C_2 and C_3 production rates for these comets. The same for 2I/Borisov for C_2 over A(0)fρ. In the four sub-plots, comets C/2017 E4, C/2020 F3 and C/2020 S3 are located above the diagonal band with different order from plot to plot (much higher in C_2, CN and NH than in OH and C_3), indicating that they have a higher gas/dust ratio compared to the reset of comets in our database. For OH over A(0)fρ, only comet C/2017 O1 is out of the main trend but it fits very well with other species. This might be due to the outburst of this comet resulting in less OH compared to other comets. For NH over A(0)fρ, the correlation is not good as for the other species. Comets C/2018 W2 and C/2017 T2 are located below the diagonal band with a lower gas/dust ratio, which could be due to their lower NH production rates. The correlation between dust and different gas species was already investigated in the TRAPPIST data (Opitom, 2016) with the exception of some comets that were out of the trend. The same behavior was found in the sample of 85 comets analysed by (A'Hearn et al., 1995), but with a larger dispersion. This trend includes both taxonomy classes, carbon-chain depleted comets and typical comets. The evolution of the dust/gas ratio with the heliocentric distance for the ensemble of comets in our database will be discussed in the next section.

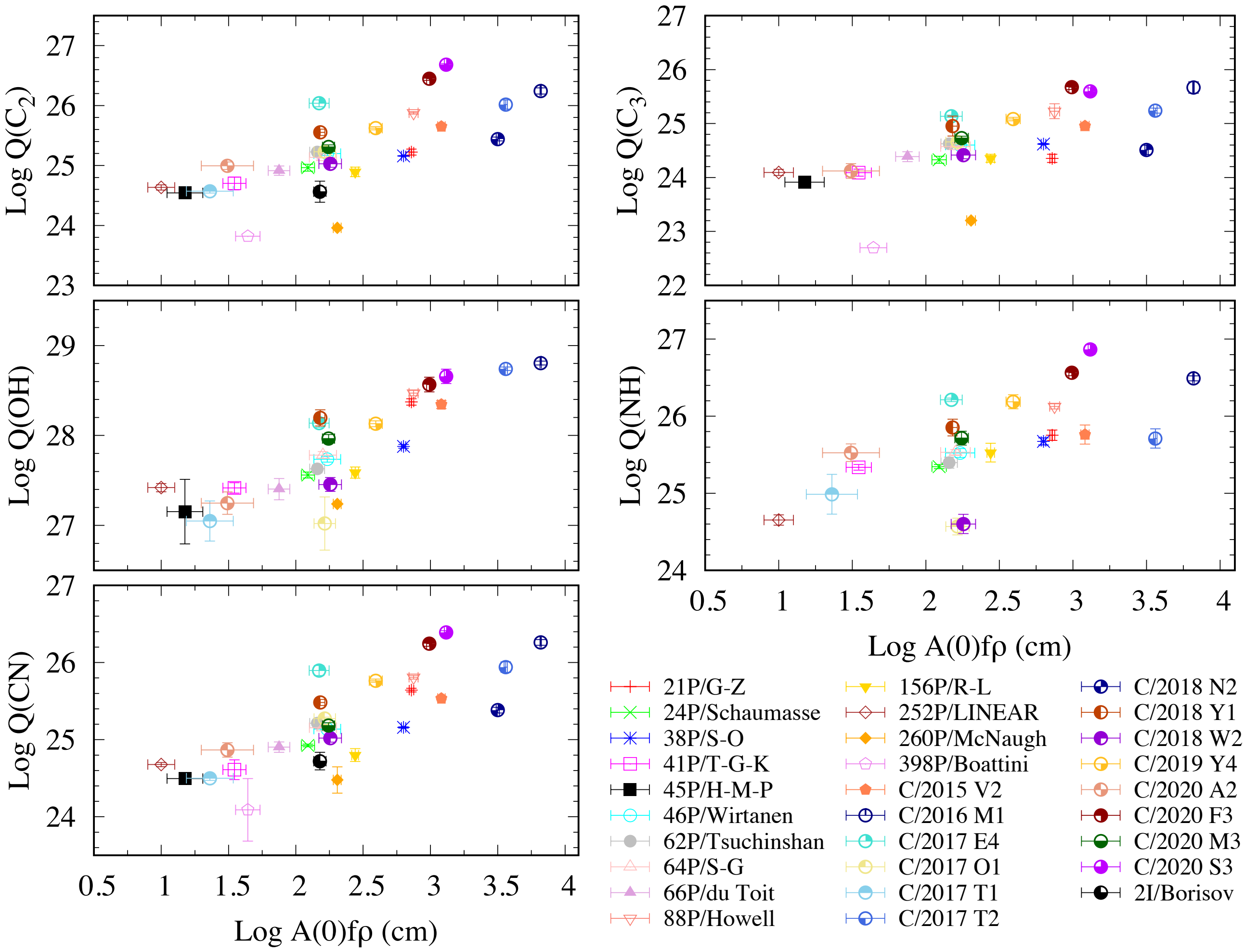

Figure 4.3: Logarithmic production rate of each minor species as a function of the logarithm of A(0)fρ, a dust proxy, for all comets in our database.

Our conclusion from these Figures 4.1 and 4.2 is that most comets in our database show a strong correlation between different species production rates. The CN, C_2, and C_3 are all related to each other much more strongly to either NH or OH. This indicates that these comets have homogeneous composition, except for a few a peculiar chemical composition (depletion in C_2 and C_3 or in NH). The correlation observed between different species and dust (A(0)fρ), as shown in Figure 4.3, indicates that the gas and dust released homogeneously from the surface of the nucleus.

4.2 Relative molecular abundances

A primary goal of compositional studies of comets is to link relative molecular abundances to conditions in comet-forming regions of the early solar nebula. To understand this relationship it is critical to determine to what degree formation conditions and evolutionary processing affect the current chemistry of comets. Several studies have been carried out in a systematic manner on a large number of comets by various groups. These studies focused on the coma composition based on the production rates of several radicals. A'Hearn et al. (1995) used narrow-band photometry of 85 comets to investigate their chemical composition. They found two main classes of comets based on the relative abundance of radicals: typical comets which have a normal C_2/CN ratio and carbon-chain depleted comets which show a lower ratios of C_2 and C_3 with respect to CN. Other spectroscopic and photometric studies confirmed the existence of these classes of comets using larger database (Fink, 2009; Langland-Shula and Smith, 2011; Cochran et al., 2012; Schleicher, 2008). Among all the carbon-chain depleted comets found, 2/3 of them are JFCs originating from the Kuiper Belt and 1/3 are LPCs from the Oort cloud (A'Hearn et al., 1995; Cochran et al., 2012). The definition of carbon-chain depleted comets varies among studies. Some consider they have to be depleted in both C_2 and C_3 (Cochran et al., 2012) while other consider only the C_2/CN abundance (A'Hearn et al., 1995; Fink, 2009). Recent analysis has further identified at least seven compositional groupings (Schleicher and Bair, 2014). Consequently, the proportion of depleted comets varies among studies, even though they are similar if only C_2 is considered. A'Hearn et al. (1995) analysed 85 comets to determine abundance patterns; 41 of those comets formed their restricted data set over which they drew conclusions. They found (12/41) 29% of the comets were in the depleted group. Fink (2009) did not observe C_3 in their bandpass and so their definition of depleted comets was based entirely on on the C_2/H_2O ratio and not C_2/CN, they obtained 30% depleted comets over 50 comets. Langland-Shula and Smith (2011) found (13/26) 50% of their sample are depleted comets based on the definition given in A'Hearn et al. (1995), including several comets with no C_2 detection that they take to indicate a comet is depleted. Cochran et al. (2012) found (5/59) 9% comets belong to the carbon-chain depleted group based on both C_2/CN and C_3/CN ratios, while (15/59) 25% are depleted only in C_2 which consistent with the quantity found by A'Hearn et al. (1995). Thus dichotomy in chemistry reveals that about one-third of sampled comets are classified as carbon-chain depleted comets, a majority of them being JFCs.

The origin of the carbon-chain depletion in Solar System comets is still debated, either if that carbon-chain depletion reflects the primordial composition or it is associated with evolution processes. One of the best constraints on this question is comet 73P/Schwassmann-Wachmann 3 (hereafter SW3). Comet SW3 splitted into several pieces in 1995. SW3 is a strongly C_2 and C_3 depleted comet and thus has a distinctive "fingerprint". If the depletion were just an evolutionary effect, from multiple perihelion passages, we would expect it to be confined mostly to the surface and the interior would appear typical. However, observations of the distinct pieces during the 2006 apparition showed that all the pieces had identical depletion both in the parents observed in the IR and the daughters observed in the optical and IR (Kobayashi et al., 2007; Schleicher and Bair, 2011; Jehin et al., 2008). In addition, there was no change from measurements of SW3 obtained before the splitting in 1995 (Schleicher and Bair, 2011). This has been interpreted as strong evidence that carbon-chain depletion is primarily from the formation of the comets, not from their subsequent evolution.

In this section, we compare the composition of 29 comets included in our database and try to define their taxonomical classes. Table 4.2 summarizes the mean production rates ratios of different species for each comet. As most comets did not show any variation of relative molecular abundances as function of heliocentric distance, we decide to present here the mean value for each comet. The exception in our database was the disintegrated comet C/2019 Y4 which shows a significant variation of C_2 to CN ratio before and after fragmentation, we decided to present the mean value of different ratios before (labeled C/2019 Y4-1) and after (labeled C/2019 Y4-2) fragmentation. The error bars for the production rates ratios are statistical errors based on the standard deviation corresponding to several measurements which were used to compute the average. Most comets show a typical and remarkable similarity in their composition with some exceptions that we discussed below. In our 10 years of data (2010-2020) collected with TRAPPIST, we observed four carbon-chain depleted comets 21P/G-Z, 168/Hergenrother, 260P/McNaught, and 398P/Boattini in addition to the first interstellar comet 2I/Borisov. Comet 168/Hergenrother was found to be depleted in C_2 and C_3 for the first time in TS data (2010-2016), more details and analysis about this comet are given in Opitom (2016). The other three comets were found in both TN and TS data (2017-2020). 21P was already known to be depleted for 50 years (Mianes et al., 1960; Herbig, 1976; Schleicher et al., 1987), while comets 260P/McNaught and 398P/Boattini were found to be depleted in C_2 and C_3 for the first time with TRAPPIST. A detailed study of 21P was published in (Moulane et al., 2020) and given in section 3.1 in chapter 3. Discussion about the composition and activity of comet 260P/McNaught and 2I/Borisov are given in section 3.13.5 and 3.14 in chapter 3, respectively. We will discuss the composition and properties of comet 398P/Boattini with the ensemble of comets in our database in the next section. Figure 4.4 shows the logarithm of C_2/CN ratio of 150 comets (90 comets from Schleicher (2008) and 60 comets from TRAPPIST database (Opitom, 2016, plus this work)) as a function of the Tisserand invariant parameter with respect to Jupiter (T_J).

Taking into account all the data collected with TRAPPIST until now, we found four carbon-chain depleted comets over 57 comets (20 JFCs, 1 HTC and 36 LPCs) in addition to the first interstellar comet 2I/Borisov. This provides about 7% of comets in our database are carbon-chain depleted comets, all of them are JFCs. We note that there is no LPC found to be strongly depleted in carbon-chain elements in the whole TRAPPIST data set. A few comets are located at the edge of the C_2/CN limit for depleted comets, like comets C/2009 P1, C/2013 E2 and C/2013 US10 in the 2011-2016 TS database (Opitom, 2016) and comet C/2019 Y4 before its fragmentation in our sample. If we consider only the 29 comets observed in the period of 2017-2020, we found 10% of comets are depleted in C_2 and C_3 in addition to 2I/Borisov and no LPC was found to be depleted. These percentages are different from what have been found in the previous spectroscopic and photometric studies (A'Hearn et al., 1995; Fink, 2009; Langland-Shula and Smith, 2011; Cochran et al., 2012; Schleicher, 2008). The main reason of the differences between different studies, including ours, is still unclear. As we mentioned previously, we used a completely homogeneous data set in order to avoid biases introduced by the use of different instruments and data reduction procedures. It is important to note that we used the same parameters of Haser Model (scale-lengths, outflow velocity, g-factors, etc) as used in A'Hearn et al. (1995) and in Schleicher (2008) to compute the gas production rates. In section 4.1, we discussed the correlation between production rates of different species

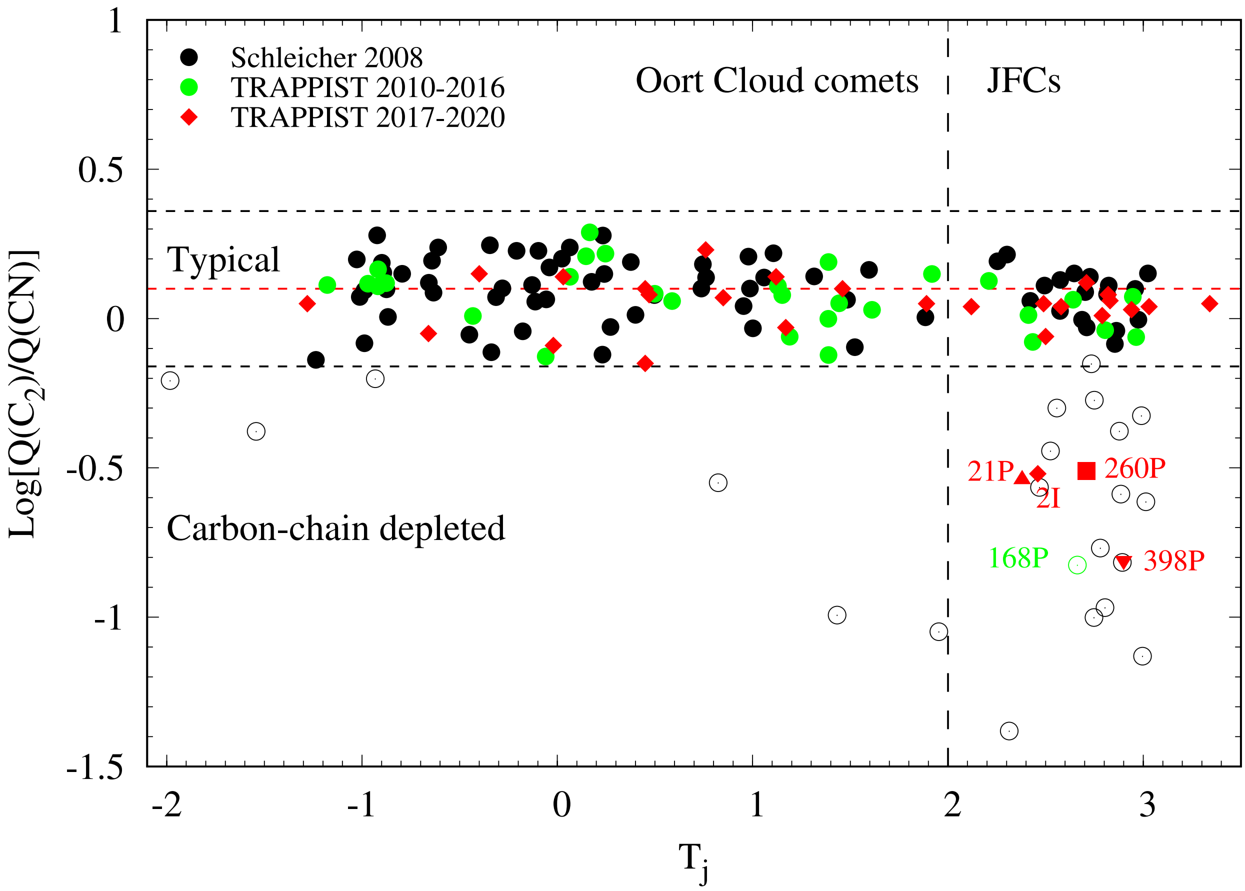

Figure 4.4: The logarithm of C_2-to-CN ratio of 150 comets (90 comets from Schleicher (2008) and 60 comets from TRAPPIST database (Opitom, 2016, and This work)) as a function of the Tisserand invariant parameter with respect to Jupiter (T_J). Filled symbol present typical comets while the opened symbol present the carbon-chain depleted comets. Comets found depleted in TRAPPIST database are labeled with their names. The vertical dashed line at T_j=2 separates the families of JFCs and Oort cloud comets.

as well as the dust proxy A(0)fρ parameter. Classification of our sample of comets and the comparison with the previous studies are given in section 4.2. We also study the correlation between production rates ratios of the ensemble of comets as well as their evolution with the heliocentric distance.

The study of the composition of 29 comets (13 JFCs, 1 HTC, 14 LPCs and 1 ISO) observed with TRAPPIST shows that most comets in our database have a similar composition. Except for those found to be depleted in carbon-chain elements, the rest JFCs and LPCs included in our database have typical composition consistent with their classification in the previous studies. Some JFCs included in our database have been observed and classified previously by different authors. Most JFCs that we have in common with previous studies did not show any change in their classification after several returns. We discus only their classification among sample of comets analysed in each study. As mentioned above, comet 21P has been found depleted in carbon-chain elements for along time ago (Schleicher et al., 1987) and we confirmed its coma composition in 2018 passage (Moulane et al., 2020). Comet 24P has been already classified as a typical comet by Cochran et al. (2012) and by Fink (2009). Comet 38P was classified as a typical comet by A'Hearn et al. (1995) while Cochran et al. (2012) found that it has higher CH/CN ratio compared to reset of comets in their database. Cochran et al. (2012) found that comet 41P has a typical composition with higher C_3/CN ratio. Comet 45P was classified as

Table 4.2: Summary of the relative molecular abundances and dust/gas ratios of 29 comets observed with TRAPPIST.

Comets	r_h	△	Log production rate ratios						Log dust-to-gas ratios	
	(au)	(au)	NH/OH	CN/OH	C_2/OH	C_3/OH	C_2/CN	C_3/CN	A(0)fρ(BC)/OH	A(0)fρ(BC)/CN
21P/Giacobini-Zinner	1.01	0.39	-2.68±0.06	-2.62±0.08	-3.16±0.10	-4.03±0.11	-0.52±0.10	-1.39±0.12	–25.32±0.12	-22.70±0.10
24P/Schaumasse	1.23	1.49	-2.08±0.06	-2.54±0.07	-2.54±0.10	-3.04±0.08	-0.06±0.10	-0.45±0.08	-25.60±0.13	-22.96±0.19
38P/Stephan-Oterma	1.59	0.92	-2.24±0.06	-2.73±0.05	-2.68±0.06	-2.68±0.06	0.05±0.02	-0.59±0.09	-24.98±0.07	-22.28±0.12
41P/Tuttle-Giacobini-Kresak	1.05	0.15	-2.03±0.02	-2.70±0.04	-2.64±0.04	-3.25±0.03	0.06±0.03	-0.55±0.05	-25.70±0.10	-23.00±0.12
45P/Honda-Mrkos-Pajdusakova	0.97	0.08	-	-2.78±0.02	-2.75±0.02	-3.21±0.03	0.04±0.03	-0.45±0.04	-25.71±0.34	-23.01±0.28
46P/Wirtanen	1.05	0.08	-2.10±0.06	-2.57±0.06	-2.49±0.06	-3.10±0.08	0.08±0.04	-0.54±0.08	-25.62±0.25	-23.05±0.20
62P/Tsuchinshan 1	1.38	1.34	-2.14±0.06	-2.43±0.05	-2.42±0.04	-3.04±0.04	0.01±0.02	-0.61±0.03	-25.50±0.04	-23.06±0.03
64P/Swift-Gehrels	1.39	0.45	-2.07±0.06	-2.47±0.11	-2.46±0.09	-3.06±0.07	0.05±0.04	-0.65±0.15	-25.36±0.12	-22.91±0.27
66P/du Toit	1.28	0.90	-	-2.51±0.04	-2.50±0.03	-3.02±0.02	0.04±0.02	-0.56±0.09	-25.53±0.03	-23.02±0.03
88P/Howell	1.35	1.40	-2.31±0.02	-2.64±0.07	-2.61±0.09	-3.20±0.03	0.03±0.07	-0.60±0.02	-25.64±0.16	-22.99±0.11
156P/Russell-LINEAR	1.33	1.52	-1.96±0.14	-2.60±0.10	-2.45±0.12	-3.00±0.15	0.12±0.05	-0.39±0.05	-25.16±0.13	-22.50±0.17
252P/LINEAR	1.00	0.06	-2.14±0.05	2.64±0.09	-2.56±0.06	-3.23±0.03	0.08±0.03	-0.59±0.07	-25.90±0.12	-23.26±0.10
260P/McNaught	1.45	0.56	-	-	-	-	<-0.51	<-1.26	-	-22.20±0.25
398P/Boattini	1.30	0.37	-	-	-	-	<-0.81	<-1.20	-	-22.59±0.28
C/2015 V2 (Johnson)	1.64	0.81	-2.53±0.07	-2.74±0.06	-2.69±0.06	-3.37±0.06	0.05±0.04	-0.62±0.05	-25.17±0.07	-22.42±0.06
C/2016 M1 (PANSTARRS)	2.29	1.30	-2.31±0.04	-2.46±0.07	-2.56±0.06	3.04±0.10	-0.09±0.08	-0.58±0.05	-25.01±0.04	-22.58±0.08
C/2017 E4 (Lovejoy)	0.66	0.64	-1.92±0.02	-2.24±0.04	-2.09±0.02	-2.98±0.05	0.14±0.03	-0.73±0.03	-25.94±0.07	-23.69±0.08
C/2017 O1 (ASASSN)	1.50	0.72	-2.44±0.03	-1.57±0.10	-1.58±0.12	-2.21±0.10	-0.03±0.05	-0.66±0.06	-24.50±0.22	-22.94±0.10
C/2017 T1 (Heinze)	0.90	0.51	-	-2.66±0.16	-2.61±0.18	-	0.04±0.02	-	-25.58±0.15	-22.88±0.20
C/2017 T2 (PANSTARRS)	2.08	1.60	-2.85±0.19	-2.71±0.09	-2.64±0.09	-3.41±0.12	0.07±0.05	-0.70±0.08	-25.06±0.12	-22.31±0.11
C/2018 N2 (ASASSN)	3.12	2.99	-	-	-	-	0.08±0.06	-0.87±0.07	-	-22.01±0.13
C/2018 Y1 (Iwamoto)	1.29	0.39	-2.29±0.06	-2.61±0.10	-2.56±0.07	-3.18±0.06	0.05±0.04	-0.58±0.06	-25.92±0.13	-23.31±0.14
C/2018 W2 (Africano)	1.46	1.10	-2.84±0.10	-2.48±0.11	-2.51±0.11	-3.14±0.10	-0.05±0.04	-0.66±0.08	-25.23±0.15	-22.73±0.10
C/2019 Y4 (ATLAS)∓	0.82	0.90	-1.95±0.02	-2.37±0.02	-2.51±0.03	-3.05±0.05	-0.15±0.05	-0.69±0.03	-25.54±0.18	-23.18±0.09
C/2019 Y4 (ATLAS)	0.82	0.90	-1.79±0.05	-2.46±0.11	-2.37±0.07	-3.09±0.12	0.10±0.09	-0.59±0.10	-25.30±0.17	-23.06±0.28
C/2020 A2 (Iwamoto)	1.05	1.16	-	-2.35±0.09	-2.20±0.10	-2.93±0.16	0.14±0.05	-0.57±0.13	-25.56±0.17	-23.21±0.13
C/2020 F3 (NEOWISE)	1.05	1.16	-2.03±0.06	-2.25±0.12	-2.08±0.10	-2.83±0.05	0.15±0.09	-0.54±0.07	-25.60±0.10	-23.33±0.15
C/2020 M3 (ATLAS)	1.05	1.16	-2.28±0.04	-2.76±0.08	-2.66±0.09	-3.21±0.06	0.10±0.04	-0.47±0.03	-25.80±0.11	-23.03±0.11
C/2020 S3 (Erasmus)	1.05	1.16	-1.84±0.14	-2.35±0.10	-2.09±0.11	-3.05±0.18	0.23±0.03	-0.70±0.09	-25.48±0.08	-23.22±0.15
2I/Borisov	2.00	2.00	-	-	-	-	<-0.54	-	-	-22.58±0.04
Typical comets	-	-	-2.23±0.22	-2.55±0.65	-2.46±0.39	-3.12±0.68	0.06±0.10	-1.09±0.11	-25.82±0.40	-23.30±0.32
Depleted comets	-	-	-2.48±0.34	-2.69±0.14	-3.30±0.35	-4.18±0.28	-0.61±0.35	-1.49±0.14	-25.30±0.29	-22.61±0.15

Note: r_h is the perihelion distance, otherwise the closet distance to the Sun is given. △ is the corespondent geocentric distance at the perihelion. ∓ before the fragmentation of comet C/2019 Y4. The mean values of the typical and depleted comets are from A'Hearn et al. (1995)

typical comet by A'Hearn et al. (1995) but Cochran et al. (2012) found that it has lower C_3 and Fink (2009) found that it has lower C_2. Comet 46P was classified as typical comet by (A'Hearn et al., 1995; Fink, 2009; Langland-Shula and Smith, 2011). Comet 62P was classified as a depleted comet in C_2 with respect to CN with the criteria defined by Cochran et al. (2012), while A'Hearn et al. (1995) and Fink (2009) classified it as typical comet in agreement with our classification. Comet 64P was classified as a typical comet by Cochran et al. (2012), while comet 66P is the first time included in a such taxonomic study. Comet 88P/Howell was observed in its previous passage with TRAPPIST in 2015 and it has a typical composition. The comet was classified previously as a typical comet by A'Hearn et al. (1995) and Cochran et al. (2012). Based on the C_2/CN and C_3/CN ratios, comet 156P has a typical composition and it is the first time that is considered in classification study. As mentioned in the chapter 3, comet 252P has a typical composition and it was the first time included in a such taxonomic study. All the LPCs included in our database were observed and classified for the first time with TRAPPIST.

Figure 4.5 shows the evolution of the logarithm of the OH, NH, C_3, and C_2 to CN ratio as a function of the heliocentric distance for all comets in our database. The horizontal black dash line represents the limit to distinguish between typical and carbon-chain depleted comets as mainly defined by A'Hearn et al. (1995) and updated later by Schleicher (2008) covering a large sample of comets observed at Lowell observatory. Beside the comets depleted in carbon-chain elements with respect to CN, both C_2/CN and C_3/CN ratios for the ensemble of comets did not show a significant changes with heliocentric distance and in agreement with the mean limit for typical comets. The same behavior seen for OH/CN except for comet C/2017 O1 that shows a depletion of OH with respect to CN. The ratio NH/CN may behave similarly, expect for comets that depleted in NH with respect to CN (21P, C/2017 O1, C/2017 T2, and C/2018 W2).

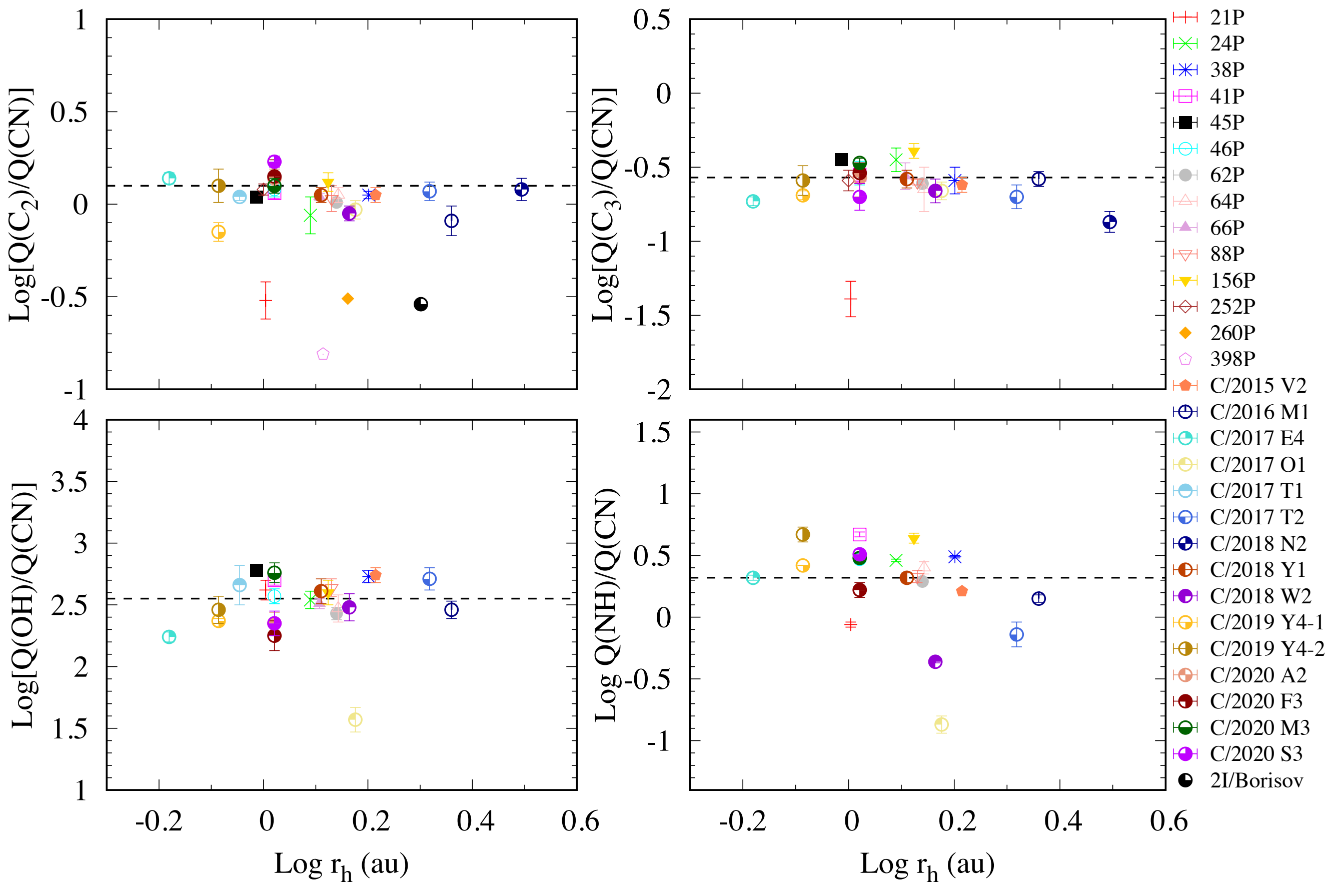

Figure 4.5: Logarithmic production rate ratios of each species to CN as a function of heliocentric distance.

Figure 4.6 shows the evolution of the logarithm of the CN, NH, C_3, and C_2 to OH ratio as a function of the heliocentric distance for all comets in our database. As for the CN, the production rates ratios to OH for most comets are consistent with the mean value of typical comets. It is clearly shown in the plots that comet 21P has lower ratios of C_2, C_3 and NH to OH, while CN/OH ratio is in agreement with the typical value for most comets. Comet 38P surprisingly shows a higher C_3/OH ratio compared to other JFCs, more discussion about this comet is given below. As previously mentioned, comet C/2017 E4 has a higher C_2/OH, CN/OH and NH/OH ratios compared to other comets and to the mean value of typical comets but it has a typical value of C_3/OH. Comet C/2017 O1 has the highest C_2/OH, C_3/OH, CN/OH ratios in our sample of comets and it has a normal NH/OH ratio. Comets C/2017 T2 and C/2018 W2 show the lowest NH/OH ratio compared to comet observed at the same heliocentric distances in our sample of comets. Excluding strongly depleted comets (either in carbon elements or in NH) in our database, there is a dispersion of the ratios with respect to OH around the typical value at both larger and smaller heliocentric distances.

The main conclusion from both Figures 4.5 and 4.6 is that the ensemble of comets exhibits only weak systematic trends in the production rates ratios with heliocentric distance. Previous studies used different and large sample of comets reached the same conclusion (A'Hearn et al., 1995; Fink, 2009; Langland-Shula and Smith, 2011; Cochran et al., 2012; Opitom, 2016). This does not imply that the relative abundances in the coma are sensitive to change in photochemical rates, but could be due to the Haser Model parameters (scale-lengths and outflow velocity) that we assumed to compute the gas production rates. We note that the variation of the production rate of any species with heliocentric distance is sensitive to the assumed scale-lengths in the Haser Model, where the scale-lengths of different species were chosen primarily on the basis of independent data (A'Hearn et al., 1995). We assumed that the outflow velocity is constant, whereas it is more likely to vary as a function of heliocentric distance. Some authors have adjusted the scale-lengths for each observation and outflow velocity with the heliocentric distance in their sample of data in order to eliminate apparent chemical variations (Rauer et al., 2003; Cochran et al., 2012; Langland-Shula and Smith, 2011). In this work, we decided to use the same Haser parameters as in (A'Hearn et al., 1995) to facilitate the comparison between our sample and their data sets and other similar works.

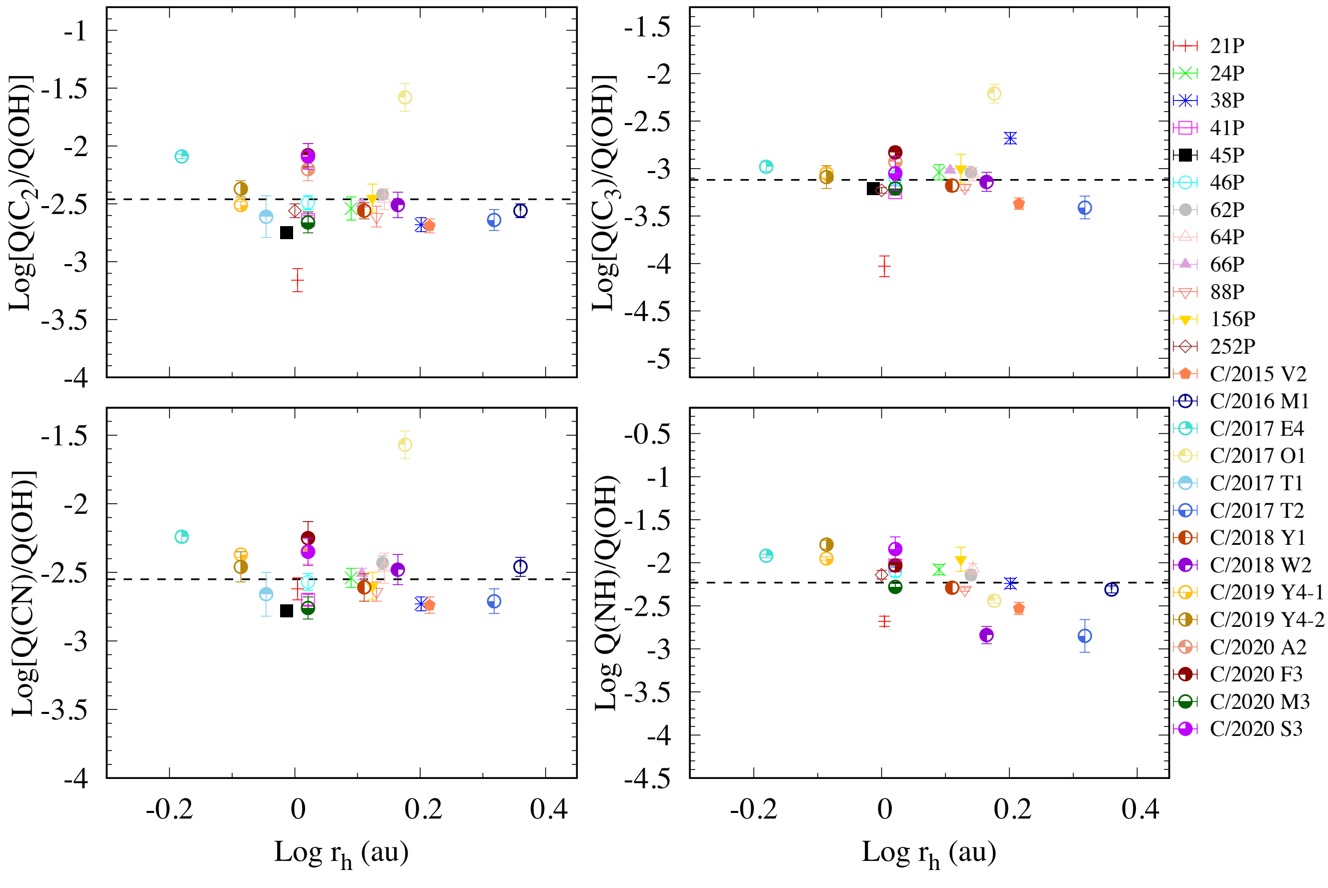

Figure 4.6: Logarithmic production rate ratios of each species to OH as a function of heliocentric distance.

Figure 4.7 shows the ratio of C_2, C_3, and NH to OH as a function the ratio of CN to OH for all comets in our sample. This plot is similar to Figure 10 given in A'Hearn et al. (1995) where they choose to normalize production rates ratios to OH as it is the primary dissociation product of H_2O, which is the dominant volatile in comets coma and could provide a good proxy of the total out-gassing of a comet. As mentioned above, typical comets lie on the diagonal band for C_2 and C_3 over OH while the carbon-chain depleted comets are located above the trend. Within typical comets, C_2/OH and C_3/OH are strongly correlated to CN/OH while NH/OH exhibits no clear correlation pattern with respect to CN/OH. The same behavior has been observed in the previous TRAPPIST data (Opitom, 2016) and in other previous similar studies (A'Hearn et al., 1995; Schleicher, 2008). Comet 21P appears in the bottom of the plot in both C_2/OH and C_3/OH vs CN/OH as a prototype carbon-chain depleted comet. As we normalize different ratios to OH in this plot, we include only the depleted comet 21P where OH was detected unlike the other carbon-chain depleted comets (398P, 260P and 2I/Borisov) for which OH was unfortunately not detected with TRAPPIST. In the plot of C_3/OH vs CN/OH, one comet is located far above the trend, while it lies within trend for C_2 over OH. This comet is the Halley-type comet 38P/Stephan–Oterma (blue star), which is found to be enriched in C_3 with respect to OH with a ratio of log[Q(C_3)/Q(OH)]=-2.68±0.06 but it has a typical ratios of log[Q(C_2)/Q(CN)]=0.05±0.02 and log[Q(C_3)/Q(CN)]=-0.59±0.09. Comet 38P was classified as a typical comet in (A'Hearn et al., 1995) with a ratio of log[Q(C_2)/Q(CN)]=0.02 in agreement with our finding but log[Q(C_3)/Q(OH)]=-3.86 which is 70% smaller than our ratio. Cochran et al. (2012) classified comet 38P as a typical comet with ratios of log[Q(C_2)/Q(CN)]=0.03±0.07 and log[Q(C_3)/Q(CN)]=-0.69±0.13, in agreement with our results. But they found that it has a higher ratio of log[Q(CH)/Q(CN)]=0.56±0.23 compared to comets in their database, while they did not derive the C_3/OH ratio unfortunately. For the plot of NH/OH vs CN/OH, no clear trend is observed among comets in our database. Four comets show lower NH with respect to OH compared to the rest of the data set. These comets are C/2015 V2, 21P, C/2017 T2 and C/2018 W2 which we already discussed above as they are depleted in NH.

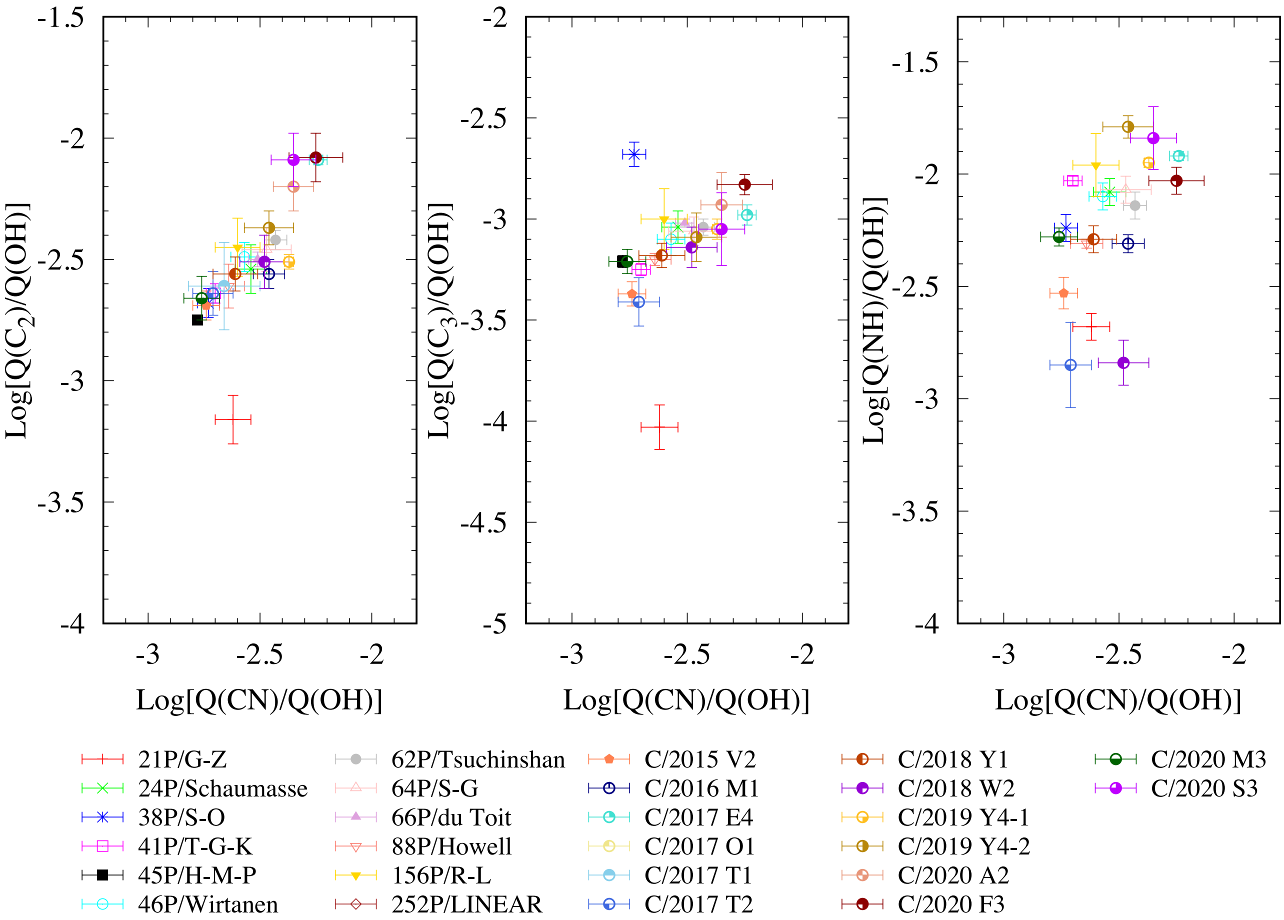

Figure 4.7: Logarithm of the ratio of C_2, C_3, and NH to OH as a function of logarithm of the ratio of CN to OH. These plots are analogs to the composition plots shown in Figure 10 in A'Hearn et al. (1995).

Figure 4.8 shows the evolution of the dust/gas ratios, given by Afρ/OH and Afρ/CN, as function of the heliocentric distance for all comets in our database compared to the typical

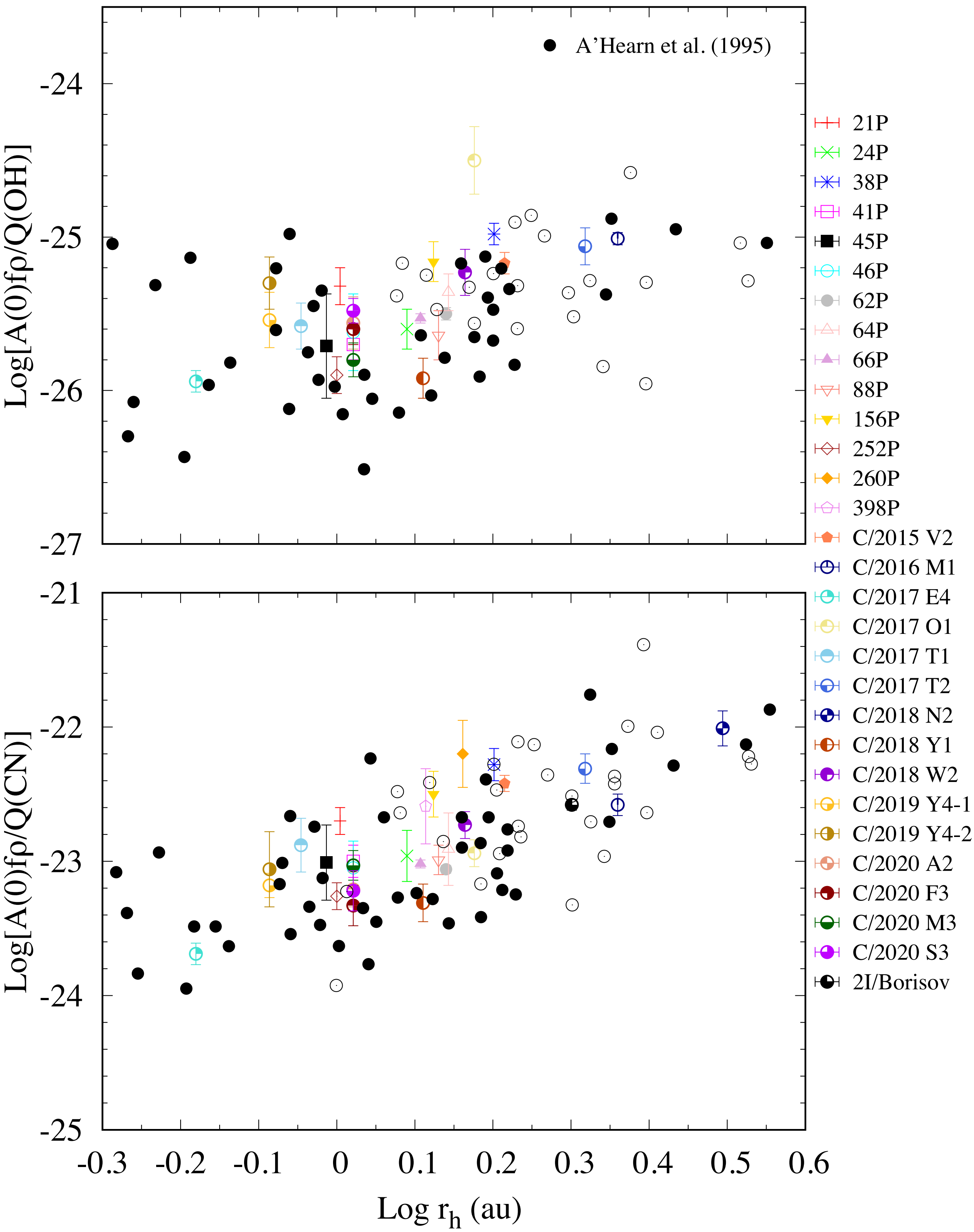

Figure 4.8: Logarithm of dust/gas ratio as a function of logarithm of heliocentric distance for all comets in our sample of comets compared to typical (filled circles) and carbon-chain depleted comets (open circles) published in A'Hearn et al. (1995).

(filled circles) and depleted (open circles) comets given in A'Hearn et al. (1995). First, our sample of comets overlaps well with comets presented in A'Hearn et al. (1995). The behavior of the dust/gas ratios with heliocentric distance is very different from the behaviors of ratios of the gaseous species. The dust/gas ratios are higher at large heliocentric distances and lower at small heliocentric distances, which could be due the ejection of large dust grains at large heliocentric distances. Our data set does not exhibit any difference in the dust/gas ratios regarding the dynamical type of comets. The comets in our database show a clear trend, showing an increase of dust/gas ratio with heliocentric distance. Some comets have higher or lower dust/gas of an order of magnitude with the respect to the average. Comet C/2017 O1 shows a higher dust/gas ratio, especially for Afρ/OH, which could be explained by ejection of large grains at larger distances from the nucleus caused by the outburst that has been detected in this comet. In addition, the reported CO_2 production rate is 2-3 higher than the water production rate (Brinkman, 2020). The high Afρ/OH ratio may be due to that the main driving force for the dust coma is CO/CO_2 or the parent molecule of CN (although unlikely) rather than water. As such, the Afρ/CN ratio is normal but Afρ/OH ratio is high. For most comets, sublimation of water ice is the main mechanism that drive cometary activity within 3 au, so Afρ/OH can be used as a proxy for dust/gas ratio for comets that are close to the Sun. At large heliocentric distances or for special cases, where comets are powered by super volatiles (CO, CO_2 etc), the Afρ/OH ratio can no longer be used as an indicator for the dust/gas ratio. Comet C/2018 Y1 shows a lower dust/gas ratio, in both Afρ/OH and Afρ/CN, with respect to most comets. Comets with low dust/gas ratios are much fainter visually than comets with a higher ratio, which is expected as there is less sunlight scattered by the dust which is a big part of a comet brightness.

This correlation between the dust/gas ratio and the heliocentric distance has been observed in the previous TRAPPIST database (Opitom, 2016) and in other studies (A'Hearn et al., 1995; Langland-Shula and Smith, 2011). Several hypothesis have been proposed to explain this trend. A'Hearn et al. (1995) suggested that the presence of large grains which are less volatile than water ice might explain this trend. A'Hearn et al. (1995); Fink (2009); Langland-Shula and Smith (2011) suggested that this trend could be explained by a possible effect of build-up of a dust crust on the surface of nucleus, where the gas would be released through pores rather than directly from the surface of the nucleus and it would be more difficult to drive away the dust.

Despite these fundamental insights for the taxonomy classification of comets in the optical, a complete understanding of comet chemistry cannot be inferred from the optical database alone owing to the small number of species observed and the difficulty in directly linking mixing ratios of daughter and/or parent species to nucleus ice abundances. It is also necessary to quantify parent species molecules which are more likely released directly from ices in the nucleus into the coma, in order to interpret the chemical composition of comets more fully. Here we try to compare between the taxonomic classes at the optical and at the IR, in order to investigate if there is any correlation or analogy between comets classes observed at different wavelength range. This allows us to explore the parent/daughter molecules identification through the depletion of different species in the coma.

Observations of comets at infrared wavelengths region (2.8 - 5 μm) is highly favorable for targeting parent volatiles molecules of fundamental importance for determining the chemical inventory of comets. In this spectral region, several primary volatiles have been detected in the coma of comets including H_2O, CO, H_2CO, CH_3OH, CH_4, C_2H_2, C_2H_6, HCN, NH_3, and OCS (Mumma et al., 2003; Bockelée-Morvan et al., 2004; Dello Russo et al., 2016). Some of these volatiles are most likely parent species of daughter molecules that we observe at the Optical. For example, C_2H_2 is most favorable parent of C_2 (e.g. Helbert et al. (2005); Weiler (2012)), so it can be compared to C_2 mixing ratios obtained at optical wavelengths. The same for HCN with CN (Rauer et al., 2003; Opitom et al., 2015) and NH_3 with both NH_2 and NH (Kawakita and Watanabe, 1998; Kawakita and Mumma, 2011; Dorman et al., 2013). In the last two decades, several authors analyzed the mixing ratios of these molecules with respect to H_2O, the dominant primary volatile, for more than 30 comets with different dynamical types (JFCs, HTCs and LPCs). They found remarkable overall diversity in the composition of the coma. Dello Russo et al. (2016) found that the mean mixing ratios of measured parent volatiles in 30 comets (11 JFCs and 19 LPCs) show an overall depletion in JFCs compared to the LPCs from the Oort cloud. This depletion is most pronounced for the four symmetric hydrocarbons species (C_2H_2, C_2H_6, CH_4 , and CO). This finding is in agreement what we found at the optical, the 2/3 of depleted comets are JFCs while 1/3 are LPCs. This confirms the correlation between different carbon-chain elements (at least C_2) as daughter molecule of C_2H_2 and C_2H_6, NH and NH_2 as daughter molecules of NH_3.

Chapter 5

Reactive collision of electrons with molecular cations in cometary comae

5.1 Introduction

In order to improve our understanding of the kinetics and chemistry of the cometary coma, theoretical studies of the major reactive collisions in these environments are needed. These processes include:

Dissociative Recombination(DR):

$$AB^+ + e^- \rightarrow AB^*, AB^{**} \rightarrow A + B \tag{5.1}$$

Vibrational/Rotational Excitation (VE/RE), de-Excitation (VdE/RdE):

$$AB^+(N^+, v^+) + e^- \rightarrow AB^*, AB^{**} \rightarrow AB + (N^{+'}, v^{+'}) + e^- \tag{5.2}$$

Dissociative Excitation (DE):

$$AB^+ + e^- \rightarrow AB^{**} \rightarrow A + B^+ + e^- \tag{5.3}$$

where N^+/v^+ stand for the rotational/vibrational quantum numbers of the cation, AB^* for a bound excited (mostly Rydberg) state of the neutral, and AB^{**} for a dissociative (mostly doubly- or multiply-excited) state of the neutral.

The rates of these processes could be particularly elevated due to the high charged particle densities in the inner coma region (Beth et al., 2020). In section 5.2, we addressed the formalism of the Multichannel Quantum Defect Theory (MQDT) used to compute the cross-sections. In section 5.3, we discussed the dissociative recombination, vibrational excitation, and vibrational de-excitation of electrons with CO^+ molecular cations in the cometary coma. The competition between dissociative recombination, vibrational excitation, and dissociative excitation of H_2^+ molecular cations in electron-impact collisions is discussed in section 5.4.

5.2 Multichannel Quantum Defect Theory approach

The cross-section calculations were based on Multichannel Quantum Defect Theory (hereafter MQDT). The MQDT can be considered as an extended diffusion theory in the study of bound states. The study of molecules in this theory poses particular problems associated with long-range diffusion potentials with respect to that of atoms. This theory, originally developed by Seaton (Seaton, 1966) for atoms, was extended to the coupling between electron and rotation movements of the nucleus in a molecule by Fano (Fano, 1970) by introducing the frame transformation. It was generalized by Jungen and Atabek (1977) and Greene and Jungene (1985) to treat rovibronic couplings in diatomic molecules. Giusti (1980) retaining the interference of the two mechanisms of dissociative recombination, improved Lee's work (Lee and Lu, 1973) by neglecting molecular rotation. Eventually, it was applied with a great success to several diatomic systems like H_2^+ and its isotopologues (Giusti-Suzor et al., 1983; Schneider et al., 1991; Takagi, 1993; Tanabe et al., 1995; Schneider et al., 1997; Amitay et al., 1999) and recently to N_2^+ (Little et al., 2014). It is also applied to triatomic systems such as H_3^+ (Schneider et al., 2000; Kokoouline and Greene, 2005; Orel et al., 2000).

In this work, we calculated cross sections that represent the probability that the reaction will occur for a given energy. This is accomplished through several steps, briefly described below. The calculations presented here take into account only the vibrational levels of the ions (Vâlcu et al., 1998) and don't involve its rotational levels. The dissociation and ionization channels are coupled together by a short-range Rydberg-valence interaction. This coupling is given by:

$$V(R) = \langle \phi_d | H_{el} | \phi^{el/ion} \rangle \tag{5.4}$$

The H_{el} is electronic Hamiltonian, ϕ_d the electron wave function describes the dissociative state of the neutral molecule and $\phi^{el/ion}$ the wave function describing the ion/electron scattering.

The elements of the interaction matrix $\mathcal{V}_{d_j,lv}$ are obtained by integration on the inter-nuclear movement given by:

$$\mathcal{V}^{\Lambda}_{d_j,lv}(E',E) = \langle \chi^{\Lambda}_{d_j}(R) | V^{\Lambda}_{d_j,l}(R) | \chi^{\Lambda}_{v}(R) \rangle \tag{5.5}$$

$\chi^{\Lambda}_{d_j}(R)$ represent the dissociative wave function, $\chi^{\Lambda}_{v}(R)$ is the wave function of the vibrational energy level v_i^+. $V^{\Lambda}_{d_j,l}(R)$ is the electronic coupling between the dissociative channel d_j and the ionization continuum lv which were constructed using the autoionization widths of Chakrabarti and Tennyson (2006, 2007) namely

$$V^{\Lambda}_{d_j,l}(R) = \sqrt{\frac{\Gamma^{\Lambda}_{d_j,l}(R)}{2\pi}} \tag{5.6}$$

where R is the internuclear distance and Λ the projection of the total angular momentum on the molecular axis.

Once the interaction matrix $\mathcal{V}_{d_j,lv}$ is constructed, it is used to determine the reaction matrix $\mathcal{K}$ from the Lippmann-Schwinger equation.

$$\mathcal{K} = \mathcal{V} + \mathcal{V}\frac{1}{E - \boldsymbol{H_0}}\mathcal{K} \tag{5.7}$$

Here $\boldsymbol{H_0}$ is the zero-order Hamiltonian associated with the molecular system neglecting the interaction potential $\mathcal{V}$.

The diagonalization of the reaction matrix is given by:

$$\mathcal{K}U = -\frac{1}{\pi}\tan(\eta)U \tag{5.8}$$

where the eigenvalues of that matrix are $-\frac{1}{\pi}\tan(\eta)$, expressed the behavior of the channel functions in the asymptotic zone in the form of a simple phase shift η.

The Born-Oppenheimer representation is appropriate for the interaction zone, in the short-range. In the region of large distances ion/electron, the representation type "close-coupled" is used. The frame transformation coefficients involve angular coupling coefficients, electronic and ro-vibronic factors are given by :

$$\mathcal{C}_{lv^+,\Lambda\alpha} = \sum_v U^\Lambda_{lv,\alpha} \langle \chi_{v^+} | \cos(\pi\mu^\Lambda_l(R) + \eta^\Lambda_\alpha) | \chi^\Lambda_v \rangle, \tag{5.9}$$

$$\mathcal{S}_{lv^+,\Lambda\alpha} = \sum_v U^\Lambda_{lv,\alpha} \langle \chi_{v^+} | \sin(\pi\mu^\Lambda_l(R) + \eta^\Lambda_\alpha) | \chi^\Lambda_v \rangle, \tag{5.10}$$

with

$$\mathcal{S}_{d_j,\Lambda\alpha} = U^\Lambda_{d_j\alpha} \sin \eta^\Lambda_\alpha \qquad , \qquad \mathcal{C}_{d_j,\Lambda\alpha} = U^\Lambda_{d_j\alpha} \cos \eta^\Lambda_\alpha \tag{5.11}$$

The matrices $\boldsymbol{\mathcal{C}}$ and $\boldsymbol{\mathcal{S}}$ make possible to write the generalized diffusion matrix $\boldsymbol{X}$:

$$\boldsymbol{X} = \frac{\boldsymbol{\mathcal{C}} + i\boldsymbol{\mathcal{S}}}{\boldsymbol{\mathcal{C}} - i\boldsymbol{\mathcal{S}}} \tag{5.12}$$

The physical diffusion matrix $\boldsymbol{\mathcal{S}}$ is obtained by the operation called elimination of the closed channels (Seaton, 1983) :

$$\boldsymbol{\mathcal{S}} = \boldsymbol{X}_{oo} - \boldsymbol{X}_{oc} \frac{1}{\boldsymbol{X}_{cc} - exp(-i2\pi\nu)} \boldsymbol{X}_{co} \tag{5.13}$$

Where ν is the matrix containing the effective quantum numbers associated with each closed channel, of threshold energy E_ν, defined like $\nu = 1/\sqrt{2(E_\nu - E)}$, E is the total energy of the system.

Finally, the elements of matrix S allows us to compute the cross sections of dissociative recombination (DR):

$$\sigma^{sym,\Lambda}_{diss \leftarrow v_i^+} = \frac{\pi}{4\varepsilon} \rho^{sym,\Lambda} \sum_j |S_{d_j,v_i^+}|^2 \tag{5.14}$$

or for vibrational excitation (VE) :

$$\sigma^{sym,\Lambda}_{v_f^+ \leftarrow v_i^+} = \frac{\pi}{4\varepsilon} \rho^{sym,\Lambda} \sum |S_{v_f^+,v_i^+}|^2 \tag{5.15}$$

where $\rho^{sym,\Lambda}$ is the ratio of the multiplicities of the neutral system and the ion for a defined symmetry and ε is the incident energy of the electron.

So, the total cross section for dissociative recombination is

$$\sigma_{diss \leftarrow v_i^+} = \sum_\Lambda \sigma^\Lambda_{diss \leftarrow v_i^+} \tag{5.16}$$

and the total cross section for the vibrational excitation given by:

$$\sigma_{v_f^+ \leftarrow v_i^+} = \sum_\Lambda \sigma^\Lambda_{v_f^+ \leftarrow v_i^+} \tag{5.17}$$

5.3 Reactive collision of electrons with CO^+ in cometary coma

The results presented here have been already published in Moulane et al. (2018b). In this section, we addresses the dissociative recombination, vibrational excitation, and vibrational de-excitation of electrons with CO^+ molecular cations. The aim of this study is to understand the importance of these reactive collisions in producing carbon and oxygen atoms in cometary activity. The cross sections for the dissociative recombination, vibrational excitation, and vibrational de-excitation processes, for the six lowest vibrational levels of CO^+ - relevant for the electronic temperatures observed in comets - are computed, as well as their corresponding Maxwell rate coefficients. Moreover, final state distributions for different dissociation pathways are presented. Among all reactive collisions taking place between low-energy electrons and CO^+, the dissociative recombination is the most important process at electronic temperatures characterizing the comets. We have shown that this process can be a major source of $O(^3P)$, $O(^1D)$, $O(^1S)$, $C(^3P)$ and $C(^1D)$ produced in the cometary coma at small cometocentric distances.

The carbon monoxide ion CO^+ is one of the most abundant ions detected in the interstellar medium (Erickson et al., 1981; Latter et al., 1993; Stoerzer et al., 1995; Fuente and Martín-Pintado, 1997) and in the coma and tail region of comets, and it is of key relevance for the Martian atmosphere (Fox and Hac, 1999).

The cometary coma is the gaseous envelope around the comet nucleus, and consists of released molecules and dust grains created and dragged from the nucleus by solar heating and sublimation. Its shape can varies from one comet to another, while its formation depends on the comet's distance to the Sun and the relative amount of dust and produced gases. Due to the intense solar radiation and heavier ionising particles, it is the playground of physical and chemical processes involving various carbon-, oxygen-, hydrogen-, and nitrogen-based, neutral and/or charged, atomic and/or molecular species.

Table 5.1: Relevant reactive processes producing CO^+ ions in the cometary coma.

Reaction	Reference
$h\nu + CO \longrightarrow CO^+ + e^-$	Ip and Mendis (1976)
$h\nu + CO_2 \longrightarrow CO^+ + O + e^-$	Huebner and Giguere (1980)
$e^- + CO \longrightarrow CO^+ + 2e^-$	Vojnovic et al. (2013)
$e^- + CO_2 \longrightarrow CO^+ + O + 2e^-$	Itikawa (2002); Huebner et al. (1991)
$H_2O^+ + CO \longrightarrow CO^+ + H_2O$	Haider and Bhardwaj (2005)
$H_2CO^+ + CO \longrightarrow CO^+ + H_2CO$	Haider and Bhardwaj (2005)
$H_2^+ + CO \longrightarrow CO^+ + H_2$	Kim and Huntress (1975)
$H^+ + CO \longrightarrow CO^+ + H$	López-Patiño et al. (2017); Tinck and Bogaerts (2016)

The CO^+ is the first cation detected in the atmosphere of comet Morehouse 1908c (Fowler, 1909). It has been detected by several spacecraft missions to different comets, such as Giotto mission bond to the comet Halley, which detected it by ion mass spectroscopy, at a distance from approximately 1300 km to about 7.5×10^6 km measured from the nucleus of the comet (Balsiger et al., 1986; Huebner et al., 1991). Moreover, the distribution of CO^+ on the surface and in the cometary coma of comet 29P/Schwassmann-Wachmann 1 was measured using spectroscopic observations (Cochran and Cochran, 1991).

Carbon species can have different origins in cometary coma. Carbon monoxide is thought to originate from direct sublimation from the nucleus and from photo destruction of carbon dioxide, and in some cases from "extended sources", that is, involving production throughout the coma and not only at or near the surface of the nucleus, chemical reactions in the inner coma, or degradation of high molecular weight organic compounds present in cometary grains (Bockelée-Morvan et al., 2010).

The CO^+ ion temperature in cometary coma also varies from one comet to another, depending on the variation of heliocentric distance and on the solar wind, which is responsible for the comet's activity. For example, in coma of comet Halley, where the CO^+ ion was detected, the temperature of ions varies between 10^3 K and 10^4 K at distances of 5×10^3 to 2.5×10^4 km from the nucleus of the comet (Balsiger et al., 1986). The High Intensity Spectrometer (HIS) instrument of the ion mass spectrometer on board the Giotto spacecraft identified the contact surface at 4800 km distance from the comet's nucleus. This boundary is clearly marked by a drastic drop in the temperatures of different ion species from about 2000 K outside to values as low as 300 K inside (Schwenn et al., 1989). Eberhardt and Krankowsky (1995) derived the electronic temperature profile using the H_3O^+/H_2O^+ ratios measured by the Giotto Neutral Mass Spectrometer in the inner coma of the comet P/Halley (Krankowsky et al., 1986). They also show increasing electronic temperature as a function of cometocentric distance.

The different chemical processes that can produce CO^+ molecular ions in the inner coma are summarized in Table 5.1. All these processes contribute to cometary activity, which has its origin in the interaction of the solar wind with the comet nucleus (Mendis et al., 1985; Broiles et al., 2015), where the mother molecules can be found. The solar wind interacts very strongly with the extensive cometary coma, and the various interaction processes are initiated by the ionization of cometary neutrals (Cravens et al., 1987). The CO^+ ion is mainly produced by photoionization and electron impact ionization of CO and CO_2 molecules (Ip and Mendis, 1976; Huebner and Giguere, 1980; Itikawa, 2002; Vojnovic et al., 2013). The photoionization of these neutrals by the solar extreme ultraviolet radiation (EUV) has been assumed to be the main source of ionization near comets (Mendis et al., 1985), although both charge exchange with the solar wind protons and electron impact ionization have also been suggested (Wallis, 1973; Kim and Huntress, 1975; Kimura et al., 2000; Tinck and Bogaerts, 2016; López-Patiño et al., 2017). The charge exchange between CO and H_2O^+ at small distances and the reaction between CO and H_2CO^+ at large distance from the cometary nucleus can contribute to CO^+ production (Haider and Bhardwaj, 2005; Cessateur et al., 2016). The high density of electrons and molecular ions in the inner cometary coma facilitates the reactive processes among them, such as the dissociative recombination (DR). This process plays an important role in producing numerous carbon and oxygen atoms in metastable states (Raghuram et al., 2016; Decock et al., 2013; Bhardwaj and Raghuram, 2012). Moreover, Feldman (1978) showed that the DR of CO^+ by low-energy electron impact is the dominant source of carbon atoms rather than the photodissociation of CO in comets Kohoutek (1973 XII) and West (1976 VI).

We extended our previous study on the reactive collisions between electrons and carbon monoxide cations (Mezei et al., 2015) to more excited states. The major one is the dissociative recombination, which takes place *via* two mechanisms: (i) the *direct* process, consisting in the capture into a dissociative state of the neutral system, CO^{**}:

$$CO^+(v_i^+) + e^- \to CO^{**} \to C + O\,; \tag{5.18}$$

and (ii) the *indirect* process, where the capture occurs into a Rydberg state of the neutral molecule CO^*, subsequently predissociated by the CO^{**} state,

$$CO^+(v_i^+) + e^- \to CO^* \to CO^{**} \to C + O\,. \tag{5.19}$$

We note here that we follow the standard nomenclature in this work, namely that CO^{**} and CO^* represent the doubly excited and singly excited states of CO, respectively, (Mezei et al., 2015).

Table 5.2: Dissociative recombination branching ratios as a function of the electron temperature, for the six lowest vibrational levels of CO$^+$.

Dissociation Path	Electron temperature (K)																	
	300						1000						5000					
	v_i^+=0	v_i^+=1	v_i^+=2	v_i^+=3	v_i^+=4	v_i^+=5	v_i^+=0	v_i^+=1	v_i^+=2	v_i^+=3	v_i^+=4	v_i^+=5	v_i^+=0	v_i^+=1	v_i^+=2	v_i^+=3	v_i^+=4	v_i^+=5
C(^{3}P)+O(^{3}P)	88.4%	97%	61%	50.1%	66.77%	79.97%	87.6%	87.7%	60.5%	47.67%	57.88%	74.84%	76.8%	79.2%	67.45%	60.31%	57.44%	59.12%
C(^{1}D)+O(^{3}P)	11.6%	0.5%	15%	16.9%	4.08%	1.53%	12.1%	0.7%	12.5%	15.74%	4.70%	2.14%	12.5%	3.1%	5.7%	9.88%	6.94%	4.16%
C(^{1}D)+O(^{1}D)		2.5%	24%	33%	29.15%	18.50%	0.1%	11.6%	27%	36.58%	37.40%	22.76%	10%	16.2%	24.45%	25.60%	28.82%	24.68%
C(^{1}S)+O(^{1}D)											0.01%	0.16%	0.4%	1%	1.6%	2.82%	4.54%	8.18%
C(^{1}S)+O(^{3}P)	–	–	–	–	–	–	–	–	–	–	–	0.09%	0.2%	0.4%	0.7%	1.21%	0.25%	2.85%
C(^{3}P)+O(^{1}S)													0.02%	0.1%	0.04%	0.08%	1.85%	0.76%
C(^{1}D)+O(^{1}S)															0.04%	0.08%	0.15%	0.23%

Meanwhile, the competitive processes with respect to DR are:

$$\mathrm{CO}^+(v_i^+) + e^- \longrightarrow \mathrm{CO}^+(v_f^+) + e^- \,, \tag{5.20}$$

that is, the elastic collisions (EC: $v_i^+ = v_f^+$), the vibrational excitation (VE: $v_i^+ < v_f^+$), and the vibrational de-excitation (VdE: $v_i^+ > v_f^+$), where v_i^+ and v_f^+ stand for the initial and final vibrational quantum numbers of the target ion, respectively, and rotational structure is neglected.

In order to understand the role of this molecular ion in the coma and in the tail regions of comets, considerable effort has been directed towards modeling its chemistry (Huebner and Giguere, 1980). In this context, the DR with electrons is a major destruction mechanism of CO$^+$, and it is also believed to be responsible for the C(^{1}D) emissions observed in comet spectra (Feldman, 1978) through the reactions:

$$\mathrm{CO}^+ + e^- \longrightarrow \mathrm{C}(^3\mathrm{P}) + \mathrm{O}(^3\mathrm{P})\,, \tag{5.21}$$

$$\longrightarrow \mathrm{C}(^1\mathrm{D}) + \mathrm{O}(^3\mathrm{P})\,, \tag{5.22}$$

$$\longrightarrow \mathrm{C}(^3\mathrm{P}) + \mathrm{O}(^1\mathrm{D})\,. \tag{5.23}$$

The main goal of our work on CO$^+$ was to evaluate all the DR, VE, and VdE cross sections and rate coefficients of CO$^+$ relevant for cometary comae. This was performed by extending our previous nuclear dynamics computations to high vibrational levels of the target. The Multichannel Quantum Defect Theory (MQDT) is applied to these computations starting from molecular data sets provided in Mezei et al. (2015) based on R-matrix calculations of Chakrabarti and Tennyson (2006, 2007).

5.3.1 Results and Discussion

In order to explore the reactive collisions of electrons with ^{12}C^{16}O$^+$ - the most abundant isotopolog of carbon monoxide - in plasmas characterized by temperatures up to 5000 K, we have extended the previous calculations of Mezei et al. (2015) up to the fifth vibrational level of the target, $v_i^+ = 5$. We have relied on the same molecular structure data, corresponding to the three most important symmetries contributing to these processes, namely $^1\Sigma^+$, $^1\Pi$ and $^3\Pi$, considering four dissociative states for each symmetry. For each available dissociative channel, we have considered its interaction with the most relevant series of Rydberg states, that is, s, p, d and f, for the $^1\Sigma^+$ symmetry, and s, p and d for the $^1\Pi$ and $^3\Pi$ symmetries.

5.3.1.1 Cross sections

We have performed calculations for incident electron energy in the range 0.01 meV - 3 eV. The DR cross sections are displayed in Figure 5.1. They are characterized by resonance

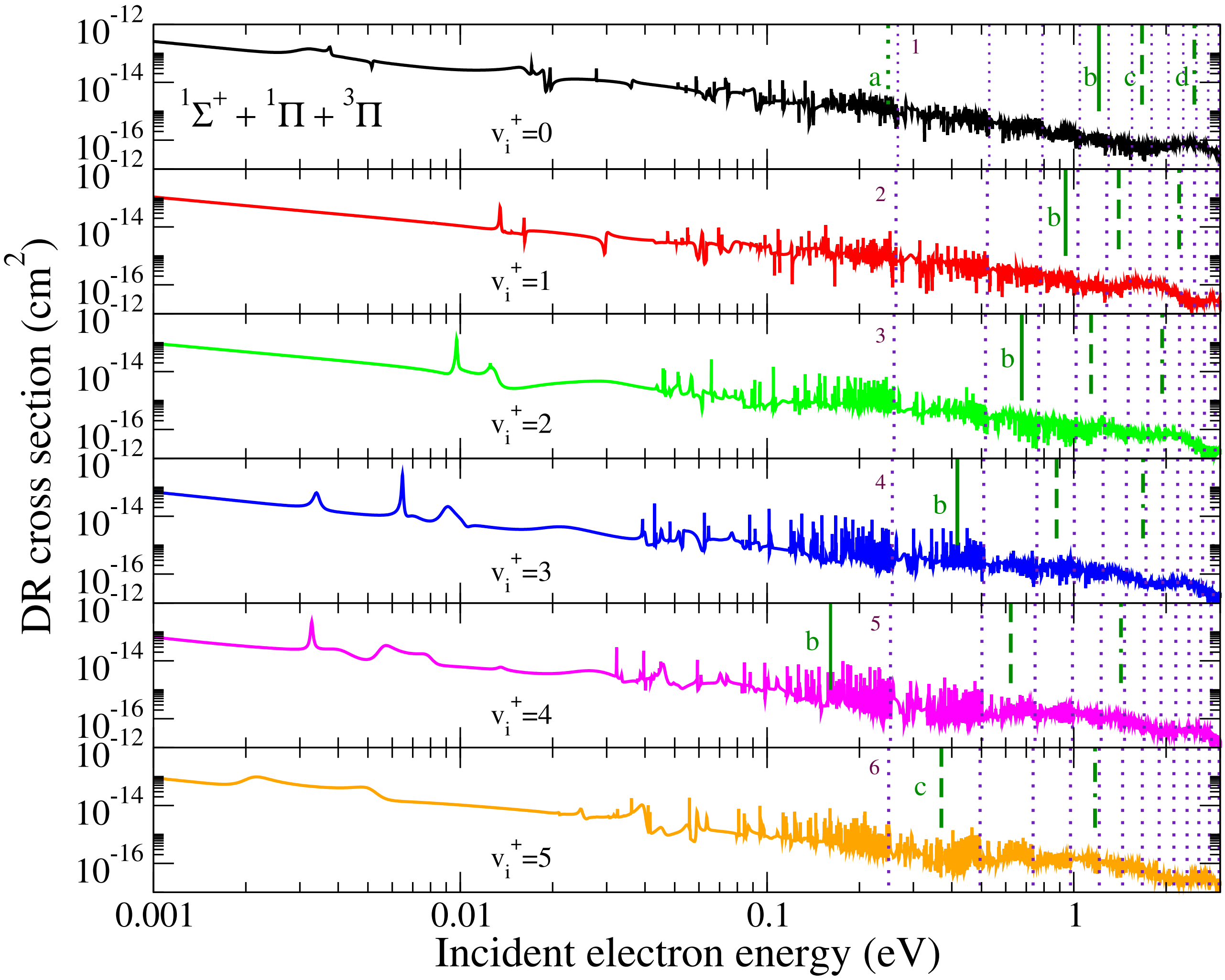

Figure 5.1: Dissociative recombination of CO^+ on its six lowest vibrational levels (v_i^+=0, 1, 2, 3, 4 and 5): cross sections summed-up over all the relevant symmetries - see Mezei et al. (2015). The dotted vertical indigo lines are the different ionization thresholds given by the vibrational levels of the molecular ion. The first ionization thresholds are indicated on the figures. The dark-green shorter vertical lines stand for the different dissociation limits measured from the initial vibrational levels of the ion, as follows: the dotted line (a) stand for the C(^{1}D)+O(^{1}D) limit, the solid lines (b) for the C(^{3}P)+O(^{1}S) one, the dashed lines (c) for C(^{1}S)+O(^{1}D) , and the dashed-dotted lines (d) for C(^{1}D)+O(^{1}S).

structures due to the temporary captures into vibrational levels of Rydberg states embedded in the ionization continuum (*closed* channels, *indirect* process), superimposed on a smooth background originating in the *direct* process (Mezei et al., 2015).

The ionization thresholds (vibrational levels of the molecular ion: Table 5.2) shown as dotted vertical lines in Fig. 5.1 act as accumulation points for these Rydberg resonances. Moreover, the asymptotic limits of the dissociation channels opening progressively are shown with shorter dark-green vertical lines in Fig. 5.1, corresponding to the atomic pairs of states C(^{1}D)+O(^{1}D), C(^{3}P)+O(^{1}S) C(^{1}S)+O(^{1}D) and C(^{1}D)+O(^{1}S). We notice that the C(^{3}P)+O(^{3}P) and C(^{1}D)+O(^{3}P) limits are open at zero collision energy. The role of each dissociation channel in the total cross section depends on the strength of the valence-Rydberg electronic couplings and on the position of the point of crossing between the PEC of the dissociative valence state and that of the target ion. Figure 5.1 shows that the cross section for the ground vibrational level has the largest cross section: about four times larger below 700 meV and above 2 eV, while in-between, the maximum deviation among all the cross sections is smaller than a factor of two. At low-energy collision range, as the vibrational quantum of the initial ionic target is increased, one can observe a systematic decrease of the total cross section, except for $v_i^+ = 5$. In this latter case, the PECs of the open valance states of $^1\Sigma^+$ symmetry correlating to the C(^{3}P)+O(^{3}P) and C(^{1}D)+O(^{3}P) atomic limits both have favorable crossings with the ion PEC, this symmetry displaying the largest valence-Rydberg electronic couplings (see Fig. 2 from Mezei et al. (2015)), leading to an increase in the cross section.

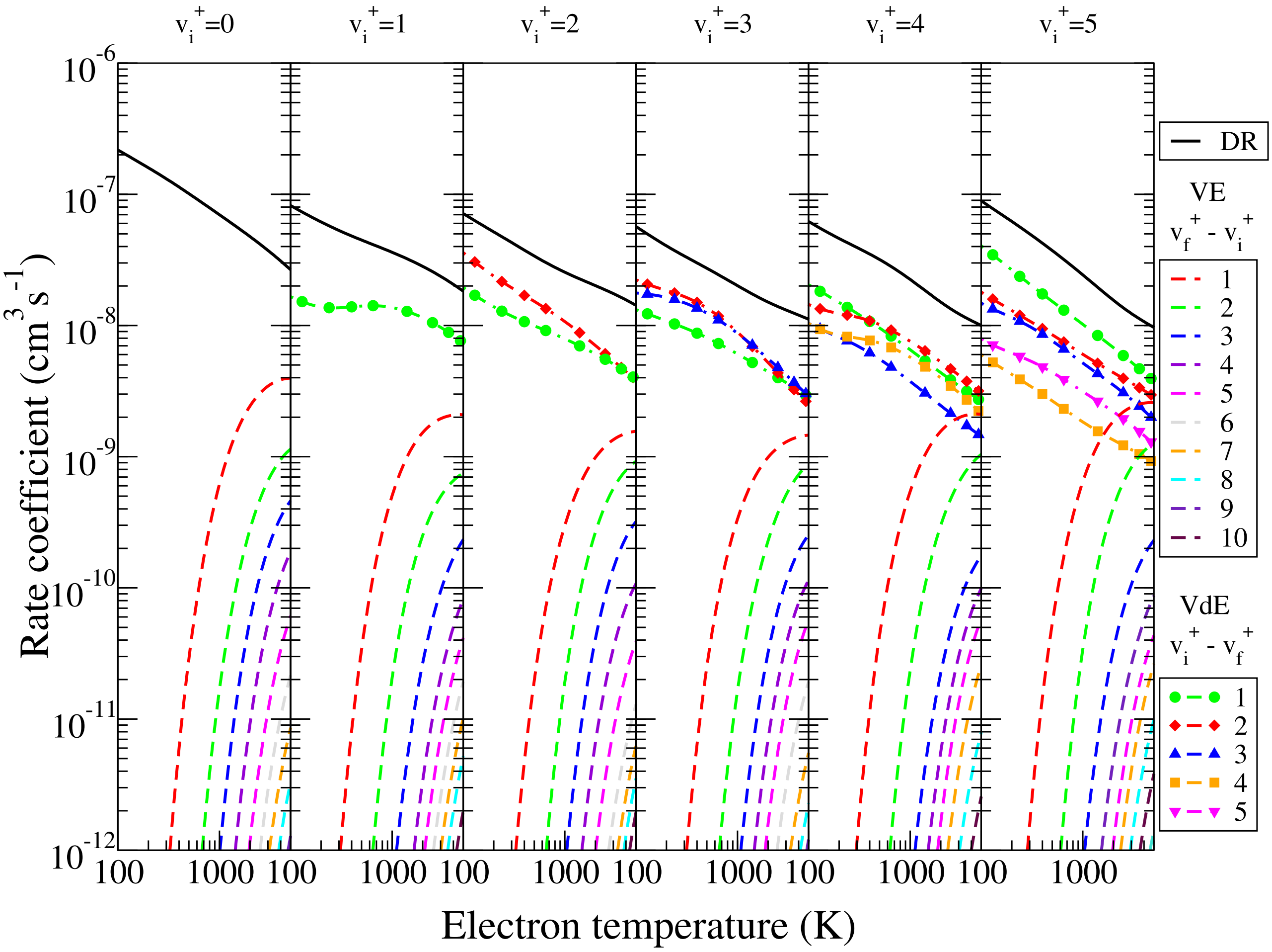

Figure 5.2: Dissociative recombination (DR), vibrational excitation (VE) and vibrational de-excitation (VdE) of CO$^+$ on its lowest six vibrational levels (v_i^+=0, 1, 2, 3, 4 and 5): rate coefficients as a function of the electron temperature.

Another interesting feature can be observed in the high-energy range. One can observe a revival in the cross section, which is due to the opening of the dissociation states correlating to the C(^{1}S)+O(^{1}D) and C(^{1}D)+O(^{1}S) atomic limits represented by dashed and dotted-dashed vertical dark-green lines in Fig. 5.1. The maximum in the cross section can be observed at the collision energies where the crossings of these newly open dissociative states with the ion's ground electronic state become favorable. Besides the total cross sections, an important characteristic of the collision is the branching ratios; Table 5.2 shows them, the results being obtained after summing the three relevant symmetries $^1\Pi$, $^1\Sigma^+$ and $^3\Pi$. This gives an estimation of the atomic neutral species that are formed in the DR of CO$^+$($v_i^+ = 0 \rightarrow 5$). At low collision energy and/or electron temperature, the dominant dissociation pathway for the DR is the one that correlates with the C(^{3}P)+O(^{3}P) atomic limit. In this energy range we have obtained good agreement with experimental measurements of Rosen et al. (1998).

The main channels for producing various atomic/neutral species such as O(^{3}P), O(^{1}D), O(^{1}S), C(^{3}P), and C(^{1}D) in the inner cometary coma (Raghuram et al., 2016) are the dissociative excitation of the neutral molecular species by photons and supra-thermal electrons such as photoelectrons, as well as the DR of the molecular ions. For example, the oxygen atoms (O(^{1}D) and O(^{1}S)) are produced by the photodissociation of CO, CO_2 and H_2O molecules coming from the sublimation of the cometary ices (Bhardwaj and Raghuram, 2012; Decock et al., 2013; Raghuram and Bhardwaj, 2014; Decock et al., 2015). Meanwhile, using a coupled-chemistry-emission model, Raghuram et al. (2016) showed that the DR of the CO^+ ion is an important source of C(^{1}D). Table 5.2 also shows that the DR of the CO^+ ion is one of the main sources of various metastable species, excited states that could not be formed by optical transitions in the inner coma at low energy. For example, the DR of $CO^+(v_i^+ = 1)$ is the major source of C(^{3}P) and O(^{3}P).

One can conclude that the DR process plays an important role in producing the carbon and oxygen atoms in metastable excited states at small cometocentric distances, where the electronic temperature is very low (Krankowsky et al., 1986; Eberhardt and Krankowsky, 1995). Generally speaking, the DR tends to be more important on the tail-ward sides of comets, since ions are channeled on the tail axis by the low magnetic pressure in the magnetic neutral sheet (Gombosi et al., 1996), which leads to high electron and ion density there. Furthermore, the DR is enhanced in cometary tails by the low temperature prevailing there, which elevates the rate constants of this process (Häberli et al., 1997).

5.3.1.2 Rate Coefficients

In order to contribute to the modeling of the cometary coma, we have computed the rate coefficients for DR, VE, and VdE, starting from the previously produced cross sections, and assuming that the velocity/kinetic energy distribution of the electrons is Maxwellian:

$$\alpha(T) = \int \frac{8\pi m_e \varepsilon}{(2\pi m_e kT)^{3/2}} \sigma(\varepsilon) e^{-\frac{\varepsilon}{kT}} d\varepsilon, \tag{5.24}$$

where m_e is the mass of the electron, k is the Boltzmann constant and T stands for the electron's temperature.

Figure 5.2 shows the DR (solid black curve), VE (colored dashed curves), and VdE (colored dashed-dotted curves with symbols) rate coefficients for the six lowest vibrational levels of the CO^+ molecular cation as a function of the electronic temperature. The highest rates for DR and VE correspond to a vibrationally relaxed target, a decrease from the first to the fourth excited state, and an increase for the fifth one, whereas the VdE becomes progressively more important when the excitation of the target increases. In the inner coma of a comet, the molecules tend to be in thermodynamic equilibrium, rather than in a fluorescence one. When they drift outwards, one can find regions where these species will be alternatively in one type of these equilibria. Considering the cometary coma in a thermal equilibrium condition, the DR rate coefficients of CO^+ decreases when the temperature increases. Figure 5.3 (left) shows the average DR rate coefficient of all vibrational levels considered in our calculation at thermodynamical equilibrium, when the vibrational temperature is equal to the electronic one ($T_e = T_{\text{vib}}$). In addition to this, Figure 5.3 (right) shows the same DR rate coefficients with the vibrational levels considered according to a Maxwell distribution, for a wide range of vibrational temperatures, from 100 to 5000 K.

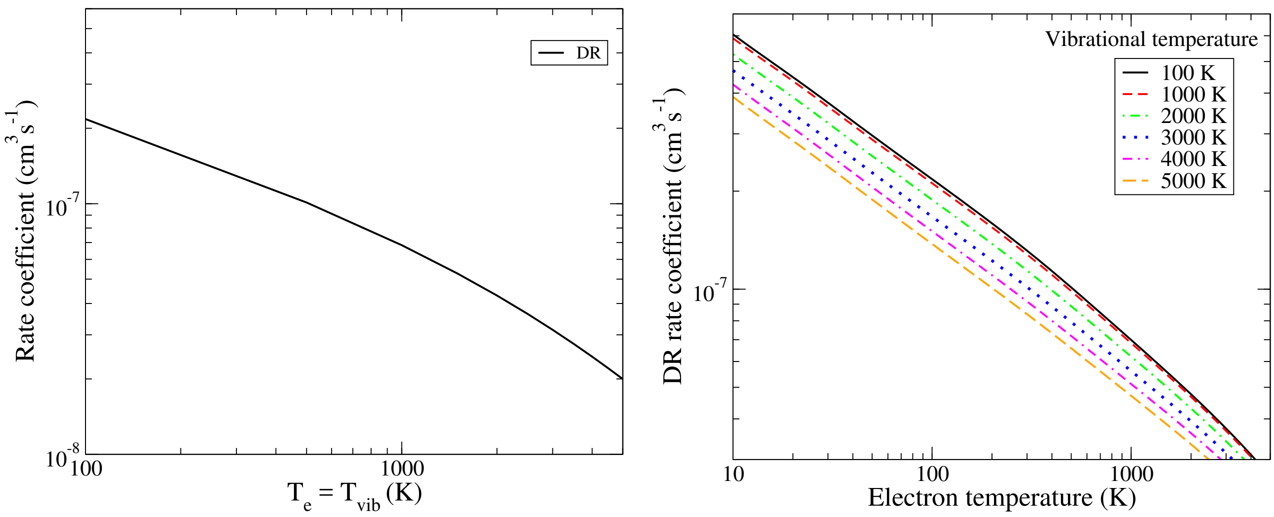

Figure 5.3: Boltzmann vibrational average dissociative recombination of CO^+. *Left*: Rate coefficients as functions of the electron temperature, considered equal to the vibrational temperature. *Right*: Rate coefficients as functions of the electron temperature and of the vibrational temperature.

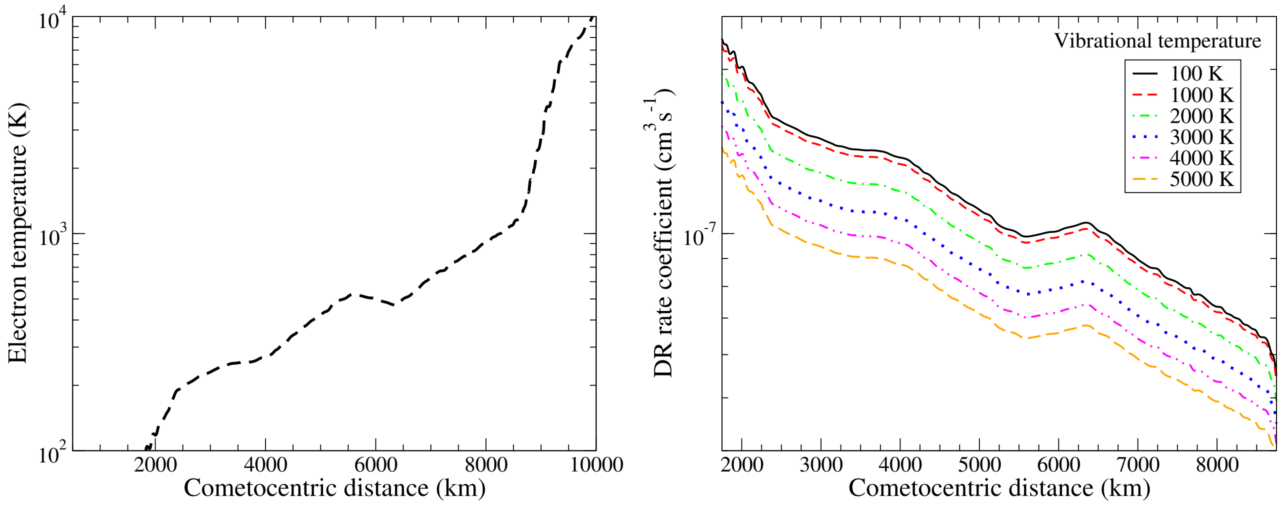

Figure 5.4: *Left*: Electron temperature profile as a function of the cometocentric distance (Eberhardt and Krankowsky, 1995; Gombosi et al., 1996).*Right*: Boltzmann vibrational average dissociative recombination of CO^+: rate coefficients as functions of the cometocentric distance and of the vibrational temperature.

5.3.1.3 Rate coefficients as a function of cometocentric distance

In order to express our rate coefficients as functions of the cometocentric distance, rather than of the electronic temperature, we used the temperature profile resulting from the observations of the Giotto Neutral Mass Spectrometer at Halley's coma (Eberhardt and Krankowsky, 1995; Gombosi et al., 1996) - Figure 5.4. The steep increase of the electron temperature as a function of the cometocentric distance is consistent with earlier theoretical calculations (Ip, 1985; Korosmezey et al., 1987; Marconi and Mendis, 1988; Gan and Cravens, 1990; Huebner et al., 1991), and with the more comprehensive treatment of the electron temperature given by (Häberli et al., 1996).

Corroborating the data of Figs. 5.3 (right) and 5.4 (left) results in Fig. 5.4 (right), which shows the variation of the average DR rate coefficient as a function of the cometocentric distance for different vibrational temperatures (from 100 K to 5000 K). These results suggest that the DR rate coefficients are very important at small distances from the nucleus of the comet and at low vibrational temperatures (up to $\sim$ 1000 K) (Eberhardt and Krankowsky, 1995; Gombosi et al., 1996). Furthermore, one can conclude that the DR is among the most important collision processes in cometary coma at small cometocentric distances. At large distances, where the electronic temperature is much higher in absolute value, the DR is less important, but also in comparison with increasingly fast competitive processes like VE or dissociative excitation.

5.3.2 Conclusion and summary

The present theoretical results (Figs. 5.1 and 5.2) provide the most extensive low-energy collisional data on electron-induced dissociative recombination, vibrational excitation, and de-excitation of the CO^+ molecular cation based on potential energy curves and electronic couplings calculated, derived, and calibrated from *ab initio* R-matrix calculations and spectroscopical data. Cross-sections between 0.01 meV and 3 eV, and Maxwell rate coefficients between 100 and 5000 K were calculated for DR, VE, and VdE of electrons with $CO^+(X^2\Sigma^+)$ ions in their six lowest vibrational levels.

We have focused on the important role of dissociative recombination in producing various atomic species in metastable excited states at small cometocentric distances (Table 5.2). According to our calculations, the DR of CO^+ may be the major source of metastable $O(^1S)$ and $O(^1D)$ oxygen atoms responsible for the green (5577 Å) and red doublet (6300, 6364 Å) emission lines observed in the cometary coma (Bhardwaj and Raghuram, 2012; Raghuram and Bhardwaj, 2014). Moreover, the dissociative recombination process can be considered as a source of excited $C(^1D)$ and $C(^3P)$ atoms, whose emission has been detected in the Hale-Bopp comet (Feldman, 1978; Raghuram et al., 2016). Using different vibrational temperatures of the molecular cation target, we have calculated the DR rate coefficients as a function of cometocentric distance (Figure 5.4), pointing out the importance of the DR process in the nucleus of the comet. The electron temperature profile used in our calculation is based on the measurements of Giotto with the neutral mass spectrometer at Halley's coma (Eberhardt and Krankowsky, 1995; Gombosi et al., 1996).

The next step in our study of the relevance of collisional processes in comets consists in performing calculations on polyatomic systems such as H_3O^+ and H_2O^+, because of their significant abundance in the cometary coma (Haider and Bhardwaj, 2005; Bockelée-Morvan, 2010; Vigren and Galand, 2013; Fuselier et al., 2016; Vigren et al., 2016; Beth et al., 2020).

5.4 Reactive collision of electrons with H_2^+

The collision of an electron with a diatomic molecular hydrogen cation, we will understand by this either H_2^+, or one of its isotopologues, i.e. HD^+, D_2^+, is one of the most simple reactive collisions. It results in products whose identity critically depends on the energy of the neutral molecular complex formed, either H_2, or HD, D_2, etc.. so, consequently, on the couple consisting in the energy of the incident electron and the initial ro-vibrational level of the ionic molecular target.

The presence of H_2 is vital during the collapse of primordial molecular clouds leading to the first generation of stars, since this species provides cooling at temperatures lower (Larsson et al., 2012). Dark clouds consist mainly of molecular hydrogen, which is why the term 'molecular clouds' is often used for them. They are very productive chemical factories and a large share of the hitherto identified interstellar molecules has been detected in dark clouds (Wakelam et al., 2006; Galli et al., 2002). In dark clouds, ionization by cosmic rays mainly leads to the formation of H_2^+. This ion is also detected in cometray coma of several comets, it is produced primarily by dissociation and ionization of cometary H_2O (Fuselier et al., 1988; Balsiger et al., 1986), but it is possible that could be produced by charge exchange with solar wind particles. In the inner coma of a comet, dissociative recombination is the main destruction route of the ions present (Häberli et al., 1996). Dissociative recombination was already of some importance in the early Universe, where it could destroy H_2^+. The role of dissociative recombination in the primeval cosmos is further complicated by the fact that its temperature dependence (unlike that of the dissociative recombination of many larger ions) does not exhibit simple exponential behaviour, but exhibits many resonances even at comparatively low collision energies of the reactants (Zhaunerchyk et al., 2007).

In this section, we addressed some of these processes starting from the simplest mechanisms and advancing towards the complex ones, illustrating our approach with concrete results on the H_2^+/H_2 and systems. In order to obtain the cross sections, we used MQDT approach described above in section in 5.2. Figures 5.5, 5.6 and 5.7 contain the input data for the theoretical model. In particular, they are the potential anergy curves, the couplings and the quantum defects for the rydberg states, respectively. Table 5.3 shows the list of vibrational levels of H_2^+ in its ground electronic states. In the next subsections we will specialise the theoretical model for different scale of energies and the corresponding results will be showed.

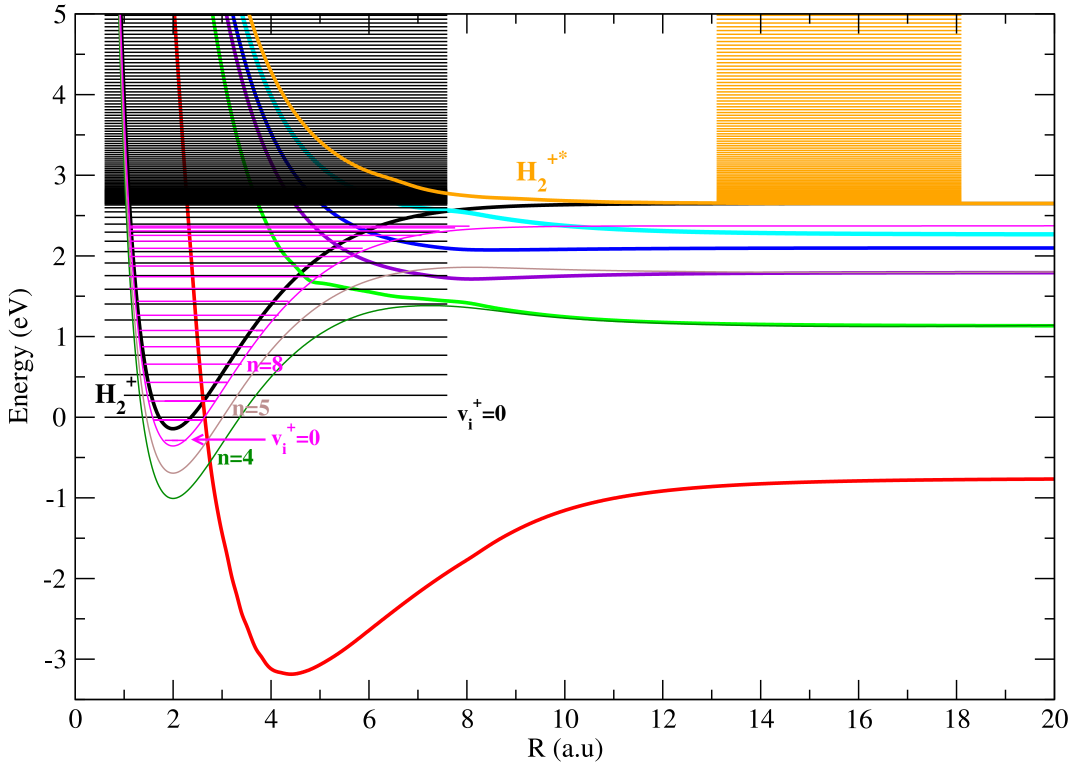

Figure 5.5: Summary on potential energy curves and vibrational levels relevant for the electron–H_2^+ reactive collisions.

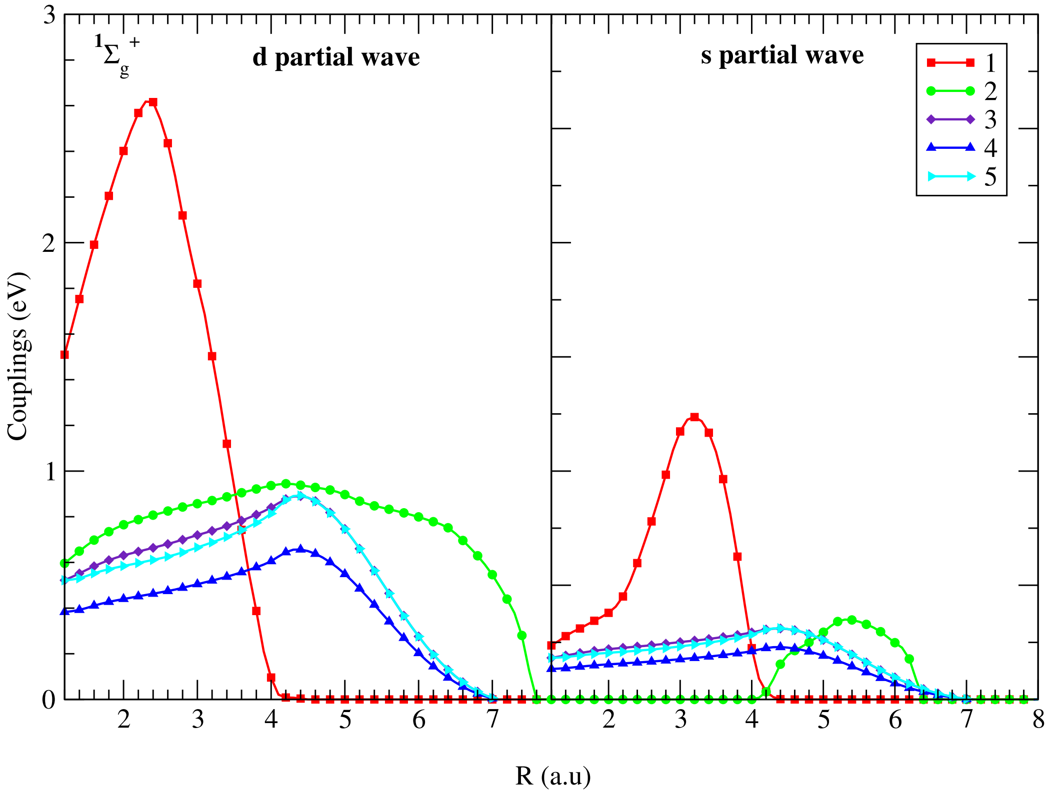

Figure 5.6: Couplings between the valence dissociative states (d and s partials waves) and the ionization continua relevant for H_2^+ with $^1\Sigma_g^+$ symetry.

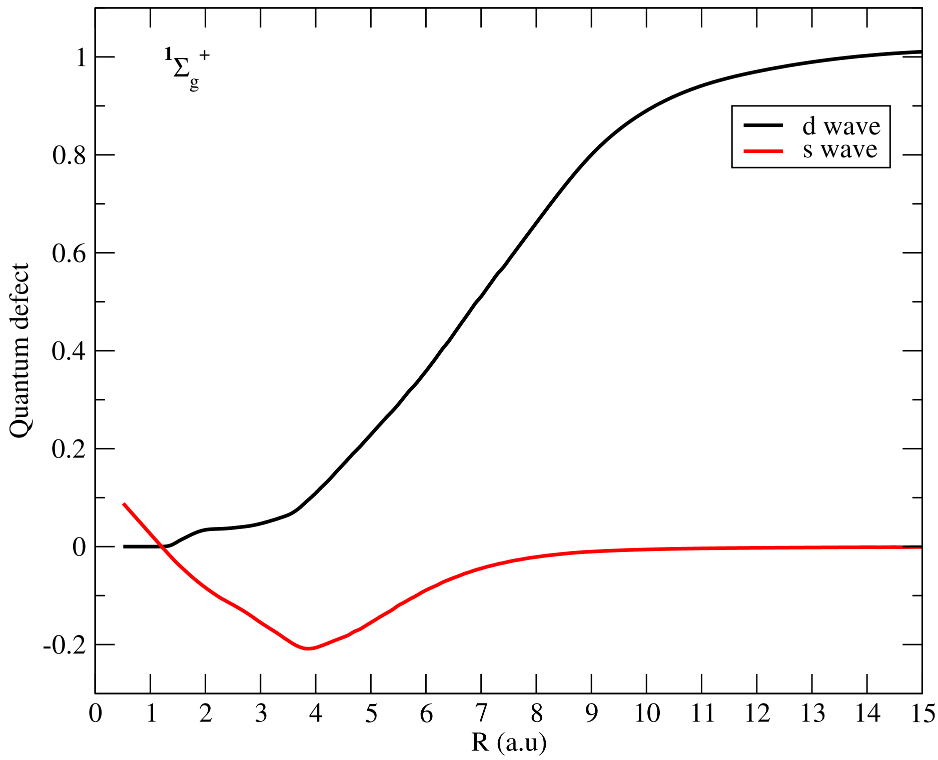

Figure 5.7: Quantum defect

Vibrational level v^+	Energy ϵ_{v^+}(eV)	Vibrational level v^+	Energy ϵ_{v^+}(eV)
0	0.0000	10	2.0533
1	0.2717	11	2.1811
2	0.5277	12	2.2947
3	0.7684	13	2.3937
4	0.9943	14	2.4776
5	1.2057	15	2.5457
6	1.4030	16	2.5973
7	1.5863	17	2.6315
8	1.7558	18	2.6477
9	1.9115	-	-

Table 5.3: Vibrational levels of H_2^+ respect to the first vibrational level.

5.4.1 Middle-range energy

The first energy range we will take into account is less than 3 eV. We will restrict ourselves to the non-rotational case (rotational excitation and rotational couplings are neglected). In this case, one has to perform separate calculation within each symmetry block Λ and eventually sum over this quantum number the resulting cross sections. For a given Λ, the Eqs. (5.5), (5.9), and (5.14) become, respectively:

$$\mathcal{V}^{\Lambda}_{d_j,lv^+}(E,E) = \langle \chi^{\Lambda}_{d_j} | V^{(e)\Lambda}_{d_j,l} | \chi_{v^+} \rangle \, , \tag{5.25}$$

$$\mathcal{C}_{lv^+,\Lambda\alpha} = \sum_v U^{\Lambda}_{lv,\alpha} \langle \chi_{v^+}(R) | \cos(\pi \mu^{\Lambda}_l(R) + \eta^{\Lambda}_{\alpha}) | \chi_v(R) \rangle \, , \tag{5.26}$$

$$\mathcal{C}_{d,\Lambda\alpha} = U^{\Lambda}_{d\alpha} \cos \eta^{\Lambda}_{\alpha} \, , \tag{5.27}$$

$$\sigma^{sym,\Lambda}_{diss \leftarrow v_i^+}(\varepsilon) = \frac{\pi}{4\varepsilon} \rho^{sym,\Lambda} \sum_{l,j} |S^{\Lambda}_{d_j,lv_i^+}|^2 \, . \tag{5.28}$$

In order to illustrate the concept of open and closed channels, and to be more specific, we address the case of the H_2^+/H_2 system, for which a relevant energy diagram - restricted to the $^1\Sigma_g^+$ symmetry of the neutral - is given in Figure 5.5. For simplicity, we will assume that a single partial wave of the electron is dominant in the ionization channels. The thick, violet, horizontal lines stand for possible values of the *total* energy of the system. E_1 corresponds to the case where the only *open* ionization channel is that associated to the ion ground vibrational state (v^+=0). This channel, gathering together states of the type $H_2^{*(c)}$ (according to section 2), and the dissociative channel, consisting on the state H_2^{**}, are always open; all the other channels, which are of ionization type, associated to v^+=1, 2, etc, are *closed*, and correspond to families of states of the type H_2^*. A Born-Oppenheimer - and therefore, *approximate* - picture of some of these states, i.e. those labelled by $^1\Sigma_g^+(1s\sigma_g 5s\sigma_g)$, v=0, 1, 2, etc., is shown in green in Figure 1. E_2 represents a total energy for which ionization channels associated to v^+=0 − 7 are open, and those associated to $v^+ \geq 8$ are closed.

Figure 5.8 reports the DR, EC, VE and VdE cross section for H_2^+ initially in one of its inital vibrational levels, $v_i^+ = 0 - 5$, for the incident electron energy 0.01 meV to 3 eV. Color codes are used to indicate the process in the graph.

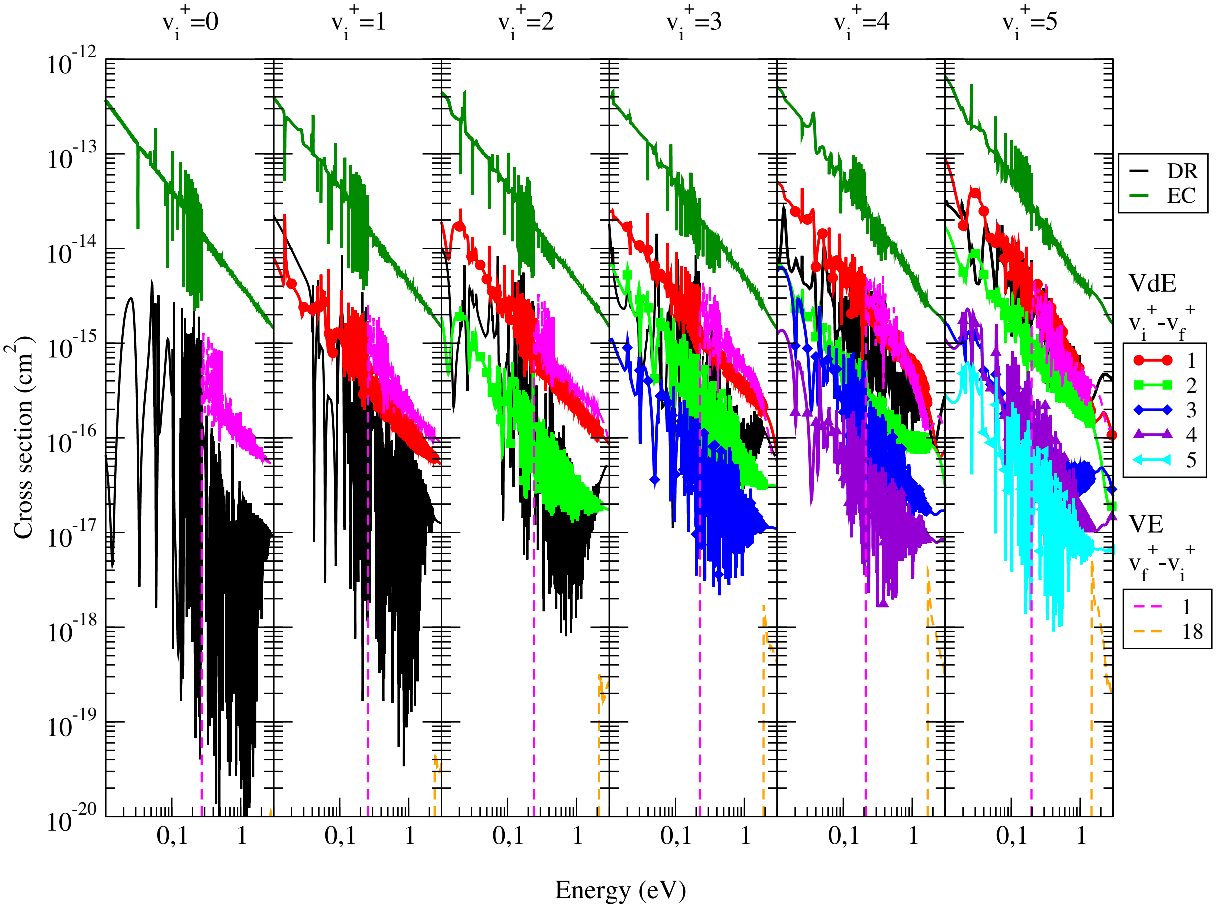

Figure 5.8: DR and related processes cross section for H_2^+ initially in one of its inital vibrational levels, $v_i^+ = 0 - 5$, for the incident electron energy 0.01 meV to 3 eV. Color codes are used to indicate the process in the graph. DR stands for dissociative recombination, EC for elastic collisions, VE for vibrational excitation or inelastic collision, and VdE for vibrational de-excitation or superelastic collision.

5.4.2 The direct process at high energy: recombination versus dissociative excitation

At energies higher than the dissociation threshold of the ion - *e.g.* E_3 in Figure 5.5 - we have to allow for the autoionization with respect to ion states from the continuum part of the vibrational spectrum, *i.e. dissociative excitation* (DE). For the two available electronic states of the ionic core, $^2\Sigma_g^+(1s\sigma_g)$ and $^2\Sigma_u^+(2p\sigma_u)$, we have discretized their vibrational continua by adding a 15 eV high potential energy step at R=25 a_0. This corresponds, for every partial wave of the incident electron, to 334 further ionization channels for the ground core (responsible for what we call DE of the first kind, DE1, relying on states of $AB^{*(c)}$ type), and to 382 ionization channels for the excited core (responsible for what we call DE of the second kind, DE2, relying on states of $AB^{**(c)}$ type). The red curve in Figure 5.9 represents the cross section of DR assisted by DE1 only, and shows that this process decreases it with respect to that affected by vibrational excitation (blue curve) by a factor up to 2. We have performed extensive calculations of DE-assisted DR cross section for capture into all the dissociative states within all the relevant symmetries, $^1\Sigma_g^+$, $^{1,3}\Sigma_u^+$, $^{1,3}\Pi_{u,g}$, and for a broad range of energy, 0 – 12 eV. The computations have been carried out in the first and second order of the K-matrix, and relied on molecular data previously used (Motapon et al., 2008; Tennyson, 1996; Ngassam, V. et al., 2003).

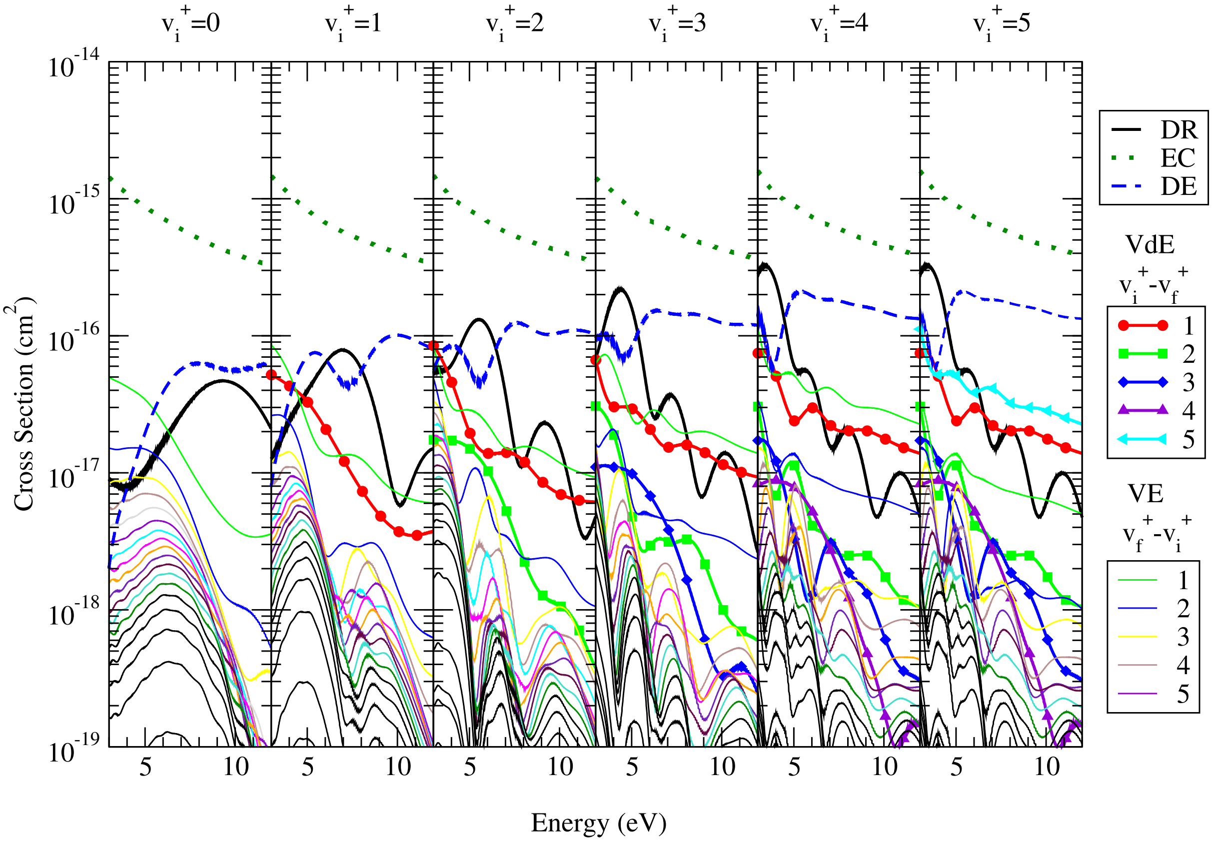

Figure 5.9: DR and related processes cross section for H_2^+ initially in one of its inital vibrational levels, $v_i^+ = 0 - 5$, for the incident electron energy 3 to 12 eV. Color codes are used to indicate the process in the graph. DR stands for dissociative recombination, EC for elastic collisions, VE for vibrational excitation or inelastic collision, and VdE for vibrational de-excitation or superelastic collision.

5.4.3 The indirect process: quantum interference between direct dissociation and temporary capture into bound Rydberg states

Allowing for closed channels means taking into account the temporary capture into bound electron-ion states, which induce local resonances in the shape of the cross section, according to Eq. (5.13). In a Born-Oppenheimer picture, this corresponds to the capture into a Rydberg bound state. One may notice that the levels v=3 and v=12 of the Rydberg state having as potential the green curve appearing in Figure 5.5 are situated at the energies E_1 and E_2 respectively, which suggests the occurrence of resonant features in the cross section close to these total energies. Since numerous computations of the total - i.e. direct and indirect - process are nowadays available (Motapon et al., 2008).

5.4.4 The direct process at low energy: recombination vs vibrational (de-)excitation

When the closed channels are either not available or neglected, the $\boldsymbol{X}$-matrix from eq. 5.12 reduces to its $\boldsymbol{X}_{oo}$ component and all the resonant part from the second term of the $\boldsymbol{\mathcal{S}}$-matrix (eq. (5.13)) is missing.

In the case when (i) one single dissociation channel 'd' is open only, (ii) the first order

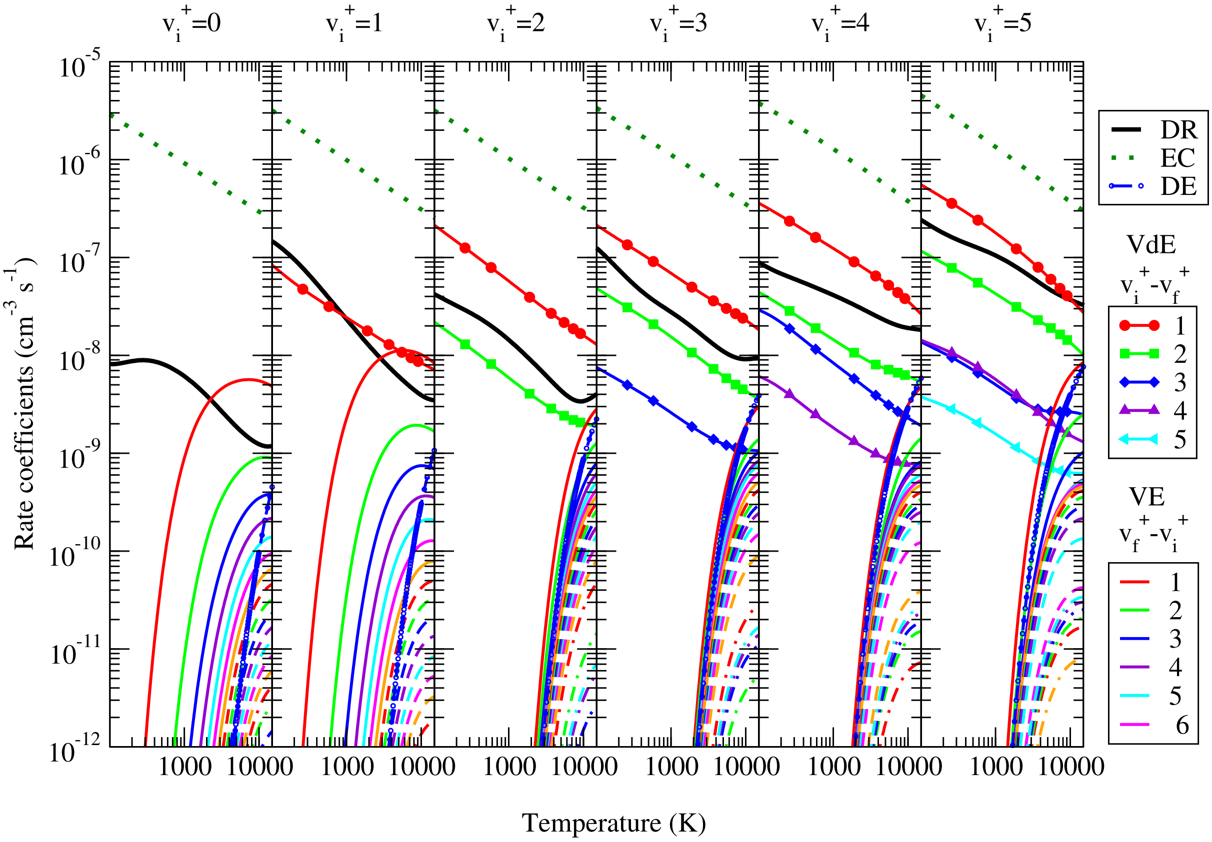

Figure 5.10: Rate coefficients of DR and related processes for H_2^+ initially in one of its inital vibrational levels, $v_i^+ = 0-5$, for electronic temperatures 100 to 11000 K. Color codes are used to indicate the process in the graph. DR stands for dissociative recombination, EC for elastic collisions, VE for vibrational excitation or inelastic collision, and VdE for vibrational de-excitation or superelastic collision.

solution of the Lippman-Schwinger equation (5.7) is adopted, and (iii) the R-dependence of the quantum defects is neglected, the direct DR cross section can be written as a product of a capture cross section $\sigma^{(cap)}_{dv_i^+}$ and a 'survival' factor $f^{(surv)}_{dv_i^+}$ (Giusti, 1980):

$$\sigma_{dv_i^+} = \sigma^{(cap)}_{dv_i^+} \cdot f^{(surv)}_{dv_i^+} \qquad \sigma^{(cap)}_{dv_i^+} = \frac{\pi}{\varepsilon}\rho^{sym,\Lambda}\widetilde{\xi}^2_{v_i^+} \qquad f^{(surv)}_{dv_i^+} = \frac{1}{[1+\sum\limits_{v^+}\widetilde{\xi}^2_{v^+}]^2} \tag{5.29}$$

These quantities rely all on the strength of the Rydberg-valence interaction:

$$\widetilde{\xi}^2_{v^+} = \sum_l \xi^2_{v^+l} \qquad \xi_{v^+l} = \pi \cdot \mathcal{V}^{\Lambda}_{d,lv^+} \tag{5.30}$$

Note that even if we do not use approximations (ii) and (iii) invoked above, the computed direct cross section is very close to that modeled by the simple formulas (5.29). Figure 5.9 displays the cross section for DR of a ground state H_2^+ ion into H_2** $^1\Sigma_g^+(2p\sigma_u^2)$ dissociative state in three cases. The simplest one comes from the account of only a single ionization channel, the entrance one, i.e. v^+=0. DR here is in competition with elastic scattering only and, according to the preceding equations, one finds the cross section given by the smooth black curve in Fig. 5.9. In a second case, we involve further ionization channels, which means that we allow for more autoionization through *vibrational excitation*. At very low energy the cross section – the blue curve in Fig. 2 – evolves smoothly, and is identical to that from the first case invoked.

However, it drops suddenly as each new vibrational threshold opens, in agreement with the simple predictive formulas (5.29). When the last vibrational (bound) level is reached ($v^+=19$), the cross section continues to decrease without displaying any further step-like structure. Note that autoionization through vibrational excitation results in the decrease of the DR cross section by a factor of up to 5 with respect to the first case discussed.

5.4.5 Summary & Conclusion

Using the Multichannel Quantum Defect Theory, we have illustrated the competition between different processes, subject to quantum interference: dissociative recombination, vibrational excitation, dissociative excitation and resonant capture into super-excited bound states. Dissociative excitation has been included in our approach after extending our collision formalism to the case of two active electronic states of the cation. The computed cross sections for H_2^+/H_2 system is in good agreement with the measurements. A huge amount of cross sections and rate coefficients (Waffeu Tamo et al., 2011) will complete those already displayed in the present article, corresponding to a broad range of energy and coming from careful state-to-state analysis.

Conclusions and perspectives

The study of activity and composition of comets is important from several points of view. Cometary activity arises basically from the solar heating of the nucleus, releasing the gas and dust forming a coma where several chemical reactions and physical processes are taking place. As the comet gets closer to the Sun, only a thin layer of the material of the nucleus is ablated and nothing much would have happened in the inner regions of the nucleus of a comet, except if it is disintegrated. The inner core of the comet may thus represents the composition of the original material at the time of its formation. Therefore, a systematic study of the material of the nuclei of comets can give information with regard to the nature of the material present at the early phase of the solar nebula 4.6 billion years ago. It is also believed that comets were the building blocks of the cores of the giant planets and that they delivered water and organics to the terrestrial planets, although it is still argued whether the comets dominated that delivery. So, comets present an opportunity to us to study the history of the Solar System formation and maybe have played a role in the apparition of life on earth.

As we know today, comets reside in two primary reservoirs the Oort cloud and the Kuiper Belt. Recently, the main belt of asteroids has been recognized as a possible third reservoir of comets as several objects show an activity from time to time. Oort cloud comets include nearly isotropic comets, and it includes subclass of dynamically new, LPCs, and HTCs while Kuiper Belt comets includes ecliptic comets and JFCs. The comets from the Oort cloud are generally thought to have formed in the region of the giant planets and been ejected from that region as part of the process that resulted in the accumulation of comets into the cores of the giant planets. It is believed that the comets from the Kuiper Belt and scattered disk contributed relatively little to the cores of the giant planets, although the details of how comets get into the scattered disk are still unclear. This leads us to study comets from both reservoirs and explore their chemical composition in order to see if there are any differences between the two groups, which will help to understand under which conditions these objects were formed.

In this work, we observed and analyzed more than 15 000 broad- and narrow-band images of 17 JFCs, 1 HTC and 18 LPCs collected with the 60-cm robotic TRAPPIST telescopes in the period 2017-2020. From this unique data set, we were able to derive the production rates of five radicals, OH, NH, CN, C_3, and C_2 with the Haser Model, and we computed the dust production in the coma through the A$f\rho$ parameter. From these quantities, we derived the relative molecular abundances and dust/gas ratios with respect to the CN and to OH for all the comets where the gas emission was detected in their coma. Based on these ratios, we were able to classify the composition of all comets included in our database. In addition, we also applied enhancement techniques on narrow band images to identify features in the coma and derive the rotation period of the nucleus through these features. The rotation period for some comets was also derived from flux variation in a series of images that we collected for several hours at the same night.

The first chapter of this work was dedicated to a general consideration about comets, including their history, dynamical type and their coma activity and composition. We also presented a brief summary about the previous and future spacecraft missions to comets.

In chapter 3, we presented in more detail the analysis and discussion of 17 comets including 12 JFCs and 5 LPCs in addition to the first interstellar comet 2I/Borisov. These comets were chosen because they were observed over a wide range of heliocentric distances with a large number of observations, and they were particularly interesting because they made a very close approach to us, observed simultaneously with large telescopes, or because they show outbursts. For the JFCs, we studied the composition and activity of comet 21P as it is the protype of depleted comets. Comet 21P shows an asymmetric activity with respect to perihelion which might be due to the nucleus shape, the spin axis orientation, and the distribution of activity on the comet's surface. The maximum of the gas and dust activity was about 24 days pre-perihelion similar to the previous apparitions. We confirm that comet 21P is depleted in C_2, C_3 and NH during its recent return in 2018 with high quality data on a large heliocentric distance range. We also obtained a high resolution UVES spectrum of 21P, where we measured the isotopic ratios that show an agreement with those found for several comets of different dynamical types and origins (Moulane et al., 2020). We presented a study of comets 41P, 45P, 46P, and 64P that made a very close approach to the Earth. We found that these four comets have a typical composition in terms of carbon-bearing species. We found that the rotation period of comet 41P was surprisingly changed by 26 hr in just two months (Moulane et al., 2018a), while the rotation period of comet 46P did not change significantly on both sides of perihelion with an average of 9.10$\pm$0.05 hr (Moulane et al. in preparation). We presented comet 66P as it was observed simultaneously with high- and medium resolution spectroscopy at VLT. Comet 66P has been suggested to have a high probabilities of coming from the main belt of asteroids. Our observations demonstrate that the measured physical properties of 66P are consistent with typical short-period comets and differ significantly from other main belt comets. Therefore, 66P is unlikely to have a main belt origin (Yang et al., 2019). We also include comet 252P as it made a very close approach to the Earth of 0.04 au during its passage in 2016. We found that comet 252P has a typical composition. Given the similarity between their orbits, it was suggested that comet 252P is a pair with comet P/2016 BA14 that fragmented from one common parent body. A dynamical study of the past of their orbits is still ongoing (Moulane et al. in preparation). We made rapid follow-up observations of five JFCs that had outbursts. These comets includes 29P, 123P, 155P, 243P and 260P. Comet 29P, as usual, shows multiple outbursts with various amplitudes while other comets show unique outburst. We discussed the evolution of the outbursts for each comet, by measuring the magnitude, Afρ parameter, and dust colours.

For the LPCs, we highlighted comets C/2017 O1, C/2017 T2, C/2018 W2, C/2019 Y4, and C/2020 F3. Comet C/2017 O1 was observed after its large outburst, the comet shows a different composition compared to the rest of comets in our data set. Comets C/2017 T2 and C/2018 W2 were monitored extensively given their brightness and visibility in both hemispheres. Both comets found to be depleted in NH and they have lower dust/gas ratios compared to the rest of comets included in our sample. Comet C/2019 Y4 was disintegrated to several pieces as it approaches to the Sun on March 22, 2020. The coma composition of the comet shows a significant change in the C_2/CN ratio before and after its fragmentation. Comet C/2020 F3 was presented as it was the brightest comet we observed, and even the brightest comet in the last two decades. The comet has a typical coma composition with a dust/gas ratio similar to that for typical comets. We made an extensive monitoring of the activity of the first interstellar comet 2I/Borisov. We presented an initial characterization of its activity including magnitude, Afρ dust parameter and dust colours during our observation period. 2I/Borisov found to be depleted in C_2 with respect to CN similar to the Solar System comets carbon-depleted group.

In chapter 4, we performed a global analysis of the ensemble properties of 29 comets including the correlation between the production rates of different species and their corresponding ratios. This allowed us to classify all the comets in our data set. Among 29 comets studied in this work, we identified three depleted comets (21P, 260P, 398P) in carbon-chain elements in addition to 2I/Borisov. 21P was found to be depleted a long time ago, but we confirm it depletion in 2018 passage. While the other three comets were found to be depleted in C_2 and C_3 for the first time with TRAPPIST. The three comets depleted are JFCs, beside the first interstellar comet 2I/Borisov no LPC was found to be depleted, except for comet C/2019 Y4 which was at the limit of depleted comets before its fragmentation when we see a significant change in its coma composition. We also found four comets (21P, C/2015 V2, C/2017 T2 and C/2018 W2) depleted in NH with respect to OH and CN. In term of dust activity, most comets show a normal dust/gas activity with respect to the heliocentric distance, except for comet C/2017 O1 which shows a higher dust/gas ratio (especially for Afρ/OH) and comet C/2018 Y1 that shows a lower dust/gas ratio (in both Afρ/OH and Afρ/CN) with respect to trend of most comets.

The last chapter was dedicated to a theoretical study of the reactive collision of electrons with molecular cations in cometary coma. We presented the study of reactive collisions of electrons with CO^+ and H_2^+ molecular cations. The results show that among all reactive collisions taking place between low energy electrons and CO^+/H_2^+, the dissociative recombination is the most important process at electronic temperatures characteristic of comets, which can be a major source of atoms in the cometary coma at small distances from the nucleus (Moulane et al., 2018b).

We summarize the main conclusions of this work as follows:

- No temporal variation is observed in the chemical compositions as well as the mixing ratios of most comets over the monitoring period of TRAPPIST, typically for a few month around perihelion and the range of heliocentric distance below 2.0 au. This result is consistent with the study by A'Hearn et al. (1995). This indicates that cometary nuclei are not differentiated and have a homogeneous composition, and they were relatively uniform through the region where they formed.

- The dust/gas ratio is strongly correlated with perihelion distance. The origin of this trend is still unclear, but it does not seem related to the perihelion distance of the comets, as suggested by previous studies. A possible explanation could be due to the fact that at larger distance this is not anymore CN and H_2O (usually used to measure the gas component in the ratio) that are responsible for main outgassing but CO and CO_2 that would continue to sublimate and lift the dust.

- We found three JFCs depleted in carbon-chain elements or 10% of our sample of 29 comets, in addition to the first interstellar comet 2I/Borisov. This fraction is significantly lower than that of other surveys estimated between 25 and 30% (A'Hearn et al., 1995; Schleicher, 2008; Fink, 2009; Langland-Shula and Smith, 2011; Cochran et al., 2012). This could be explained by an observational bias effect to the most active comets (for which CN and C_2 are well visible as easier to measure) but we believe this is a limited effect. Moreover, our database is self consistent we use always the same techniques and the same parameters. More JFCs needs to be observed in order to confirm the origin of the discrepancy between our study and previous ones.

- We did not find any LPC depleted in carbon-chain elements in TRAPPIST database, while previous studies found that about 10% of observed comets are LPCs depleted in carbon-chain elements. This could be due to an observational effect, these comets might have been observed at larger distance when C_2 is often depleted. In this work, we studied the case of comet C/2019 Y4 which was disintegrated and show a significant variation in its coma composition (especially in C_2/CN ratio) after its fragmentation, which could play some role.

The next step of this work is to investigate deeply the composition of all the comets that show peculiar chemical composition and try to identify the origin of this difference, whether it is a primordial, due to the evolution process, or any other possible reason. Investigating this topic will allow us to understand if the solar nebula was more or less homogeneous when the comets formed and the cometary compositions therefore were also homogeneous, or if some species that show much lower abundances might be due to the loss of the parent volatile ice by sublimation from the nucleus for comets that have been near the Sun over longer periods of time. This will allow us to study the observational evidence whether JFCs are likely to be depleted and whether LPCs are unlikely to be depleted is real or simply due to the selection effect.

Appendix

Appendix A

Gas production rates and A(0)fρ

A.1 Comet 21P/Giacobini-Zinner

Table A.1: OH, NH, CN, C_2, and C_3 production rates and A(0)fρ measurements for comet 21P/Giacobini-Zinner. The A(0)fρ values are computed at 10 000 km form the nucleus and corrected for the phase angle effect.

UT Date	r_h	Production rates ($\times10^{24}$ molec/s)					A(0)fρ (cm)					Tel
	(au)	OH	NH	CN	C_2	C_3	BC	RC	GC	Rc	Ic	
2018 Jun 09	1.61	-	-	-	-	-	-	-	-	236.5±14.0	265.5±18.7	TN
2018 Jun 19	1.52	-	-	25.20±0.52	4.30±0.65	-	234.8±13.6	351.1±17.5	-	-	326.9±15.6	TN
2018 Jun 22	1.49	6200±253	-	28.00±0.53	-	1.50±0.20	-	-	-	333.6±16.8	367.5±18.4	TN
2018 Jun 28	1.44	9560±365	-	32.00±0.64	-	-	-	673.7±21.4	-	411.0±13.7	475.7±12.9	TN
2018 Jul 26	1.21	15200±322	31.30±4.90	37.80±0.54	8.40±0.66	1.08±0.20	618.6±36.4	801.5±12.9	-	687.8±11.5	758.2±15.9	TN
2018 Jul 30	1.18	18100±278	-	45.50±0.63	12.60±0.65	-	-	-	-	959.8±15.8	-	TN
2018 Aug 17	1.07	28300±558	54.10±4.59	52.00±0.65	17.90±0.64	2.52±0.19	1087.6±13.7	1646.1±12.7	-	1502.7±12.1	1609.3±12.7	TN
2018 Aug 18	1.07	25600±276	-	50.80±0.64	18.00±0.62	2.47±0.17	-	-	-	1522.1±11.6	1648.9±10.3	TN
2018 Aug 23	1.04	27300±304	50.20±3.60	55.20±0.67	19.20±0.64	2.55±0.17	1028.9±12.5	1570.7±11.8	-	1463.7±11.7	1570.2±10.0	TN
2018 Aug 29	1.03	23000±286	43.50±4.07	42.50±0.62	13.70±0.62	1.66±0.18	887.6±29.6	1229.9±12.5	-	1100.0±12.7	1176.3±16.1	TN
2018 Sep 05	1.01	20800±312	-	38.20±0.64	14.00±0.63	1.95±0.17	651.2±12.4	-	-	933.1±10.5	984.0±14.8	TN
2018 Sep 09	1.01	23600±328	56.60±3.86	43.90±0.68	16.70±0.64	2.26±0.17	723.3±12.4	1103.1±15.7	815.5±12.4	1062.9±12.7	1123.3±12.1	TN
2018 Sep 17	1.01	17100±300	39.80±3.77	37.10±0.66	11.60±0.64	1.91±0.18	574.6±14.1	861.6±12.4	642.0±10.7	799.0±15.1	833.7±14.0	TN
2018 Sep 17	1.01	14700±326	38.30±3.84	37.60±0.53	12.30±0.63	2.02±0.22	571.6±19.6	851.4±17.2	599.9±19.2	767.0±16.2	832.1±14.8	TS
2018 Sep 18	1.01	-	-	30.00±0.52	11.00±0.65	2.07±0.28	459.5±34.2	872.2±22.2	595.9±14.8	733.3±14.8	849.6±20.4	TS
2018 Sep 21	1.02	-	-	-	-	-	-	-	-	604.7±16.6	652.2±14.9	TN
2018 Sep 21	1.02	12800±212	28.50±3.79	33.00±0.52	10.90±0.63	1.72±0.22	542.3±17.4	808.3±12.5	606.4±19.9	658.3±14.9	779.5±21.4	TS
2018 Sep 22	1.02	13600±216	29.40±3.84	32.80±0.51	10.80±0.65	1.64±0.23	510.9±17.4	744.0±15.0	569.2±12.5	649.8±12.5	740.3±14.7	TS
2018 Sep 23	1.02	12800±249	-	28.60±0.61	9.48±0.62	-	394.5±12.5	596.1±12.5	-	-	629.3±15.2	TN
2018 Sep 25	1.03	10880±216	29.00±4.15	27.30±0.54	9.62±0.76	1.24±0.31	406.8±22.4	611.7±19.9	460.0±20.1	540.5±14.8	611.6±15.3	TS
2018 Sep 29	1.04	11300±254	23.80±4.11	24.50±0.58	7.21±0.67	0.79±0.19	368.1±20.4	517.1±15.1		530.7±17.8	535.4±15.2	TN
2018 Oct 01	1.05	10220±217	18.40±3.68	22.40±0.52	7.84±0.64	1.13±0.23	381.4±23.2	490.7±20.6	368.1±21.9	418.3±15.3	478.8±15.7	TS
2018 Oct 02	1.06	9860±182	19.50±3.27	21.70±0.52	6.55±0.71	1.04±0.21	350.8±15.3	-	-	-	-	TS
2018 Oct 04	1.07	9460±268		20.20±0.55	5.95±0.63	0.70±0.18	282.6±14.0	412.3±12.2	-	411.2±12.2	437.4±15.4	TN
2018 Oct 08	1.08	8340±248	10.70±3.53	16.80±0.53	4.03±0.61	0.36±0.17	-	318.5±19.9	-	350.5±12.2	350.5±18.3	TN
2018 Oct 12	1.10	5950±248	-	15.80±0.52	4.24±0.63	-	199.7±12.3	280.1±19.1	-	294.6±12.8	296.5±20.4	TN
2018 Oct 14	1.12	4730±247	11.00±4.16	13.30±0.52	3.90±0.67	-	190.9±25.7	-	-	234.0±17.3	269.8±20.5	TS
2018 Oct 15	1.12	-	-	-	-	-	166.9±18.3	257.9±18.6	192.1±21.2	226.1±13.3	-	TS
2018 Oct 18	1.14	-	-	-	-	-	151.0±17.2	-	-	208.2±12.4	230.8±11.7	TS
2018 Oct 18	1.14	-	-	10.80±0.54	-	-	-	-	-	229.7±14.3	-	TN
2018 Oct 21	1.16	-	-	9.87±0.51	3.02±0.65	-	-	-	-	198.2±19.4	-	TN
2018 Oct 22	1.17	3500±188		9.04±0.50	2.30±0.65	0.34±0.21	137.6±21.1	149.0±26.1	-	114.4±13.3	127.9±14.4	TS
2018 Oct 25	1.19	-	-	-	-	-	-	-	-	111.5±20.0	-	TS
2018 Oct 28	1.21	-	-	6.00±0.55	-	-	-	151.2±13.8	117.2±16.5	137.6±12.1	144.7±14.1	TS
2018 Nov 01	1.24	2320±234	-	6.88±0.56	-	-	-	108.1±18.6	85.7±23.6	109.6±15.7	123.2±12.4	TS
2018 Nov 05	1.27	2010±191	-	5.62±0.52	1.16±0.66	-	95.7±20.4	120.5±21.8	50.1±16.2	121.1±15.4	139.0±15.0	TS
2018 Nov 09	1.31	-	-	-	-	-	-	-	-	88.8±13.4	129.3±15.6	TS
2018 Nov 14	1.35	-	-	4.39±0.55	1.27±0.69	-	85.5±13.2	88.7±18.7	87.2±14.6	86.9±13.6	91.3±12.0	TS
2018 Dec 07	1.55	-	-	3.30±0.52	-	-	-	-	-	42.9±10.5	71.7±13.2	TS
2018 Dec 10	1.58	-	-	3.00±0.56	-	-	-	75.9±14.2		28.1±13.9	-	TS
2018 Dec 19	1.66	-	-	3.30±0.54	-	-	-	80.6±12.5		27.2±11.5	172.3±18.2	TS
2018 Dec 29	1.75	-	-	-	-	-	-	-	-	-	57.9±18.1	TS
2019 Jan 14	1.90	-	-	-	-	-	-	-	-	60.7±11.1	-	TS
2019 Jan 15	1.91	-	-	-	-	-	-	-	-	57.2±11.0	60.4±11.6	TS
2019 Jan 29	2.04	-	-	-	-	-	-	-	-	85.5±11.4	93.5±11.5	TS
2019 Feb 02	2.08	-	-	-	-	-	-	-	-	83.7±12.5	91.6±11.3	TS
2019 Feb 04	2.10	-	-	-	-	-	-	-	-	71.5±22.0	96.3±17.1	TS

A.2 Comet 41P/Tuttle–Giacobini–Kresak

Table A.2: OH, NH, CN, C_2 and C_3 production rates and A(0)fρ parameter for comet 41P/Tuttle–Giacobini–Kresak. The A(0)fρ values are computed at 5000 km from the nucleus and corrected for the phase angle effect. (†) present the TRAPPIST-South measurements.

UT Date	r_h	$\triangle$		Production rates (10^{24}molecules/s)					A(0)fρ (cm)			Tel.
	(au)	(au)	Q(OH)	Q(CN)	Q(NH)	Q(C_2)	Q(C_3)	BC	RC	GC	Rc	
2017 Feb 16.88	1.27	0.29		2.20±0.04		2.26±0.03	0.61±0.02	31.0±1.4	39.5±0.7	29.7±1.6	36.0±0.2	TN
2017 Feb 19.08	1.26	0.27		2.55±0.04		2.66±0.03	0.73±0.02	31.9±1.8	43.7±1.3	37.0±0.7	42.8±0.2	TN
2017 Feb 25.04	1.22	0.24				2.51±0.03	0.67±0.01	29.8±1.2	39.9±1.2		41.3±0.1	TN
2017 Feb 25.10	1.22	0.24		2.67±0.02		3.04±0.03	0.76±0.03	25.1±1.1	37.9±0.5		46.2±0.3	TS
2017 Mar 01.92	1.19	0.22		2.63±0.05		3.14±0.05	0.74±0.02	45.3±2.3			55.3±0.2	TN
2017 Mar 03.12	1.18	0.21		2.69±0.03		3.16±0.02	0.87±0.02	36.4±2.1	49.3±1.2		55.8±0.6	TN
2017 Mar 03.84	1.18	0.21		3.35±0.05		3.94±0.05						TN
2017 Mar 04.16	1.17	0.20		3.02±0.05		3.78±0.05						TN
2017 Mar 07.84	1.15	0.19		3.55±0.08		4.36±0.05	0.88±0.05	50.6±5.1	66.8±3.6		74.0±2.6	TN
2017 Mar 08.12	1.15	0.19		3.35±0.05		3.24±0.04					79.1±2.0	TN
2017 Mar 08.12	1.15	0.19		3.16±0.03		4.29±0.06	0.84±0.07		50.9±1.9		70.6±1.7	TS
2017 Mar 11.84	1.13	0.18	2190±127	3.11±0.06		3.83±0.05	0.87±0.04	56.1±3.9	64.5±8.3		69.0±5.3	TN
2017 Mar 14.84	1.12	0.17	2270±155	4.34±0.06		5.10±0.06	1.38±0.02	54.7±1.4			87.3±1.1	TN
2017 Mar 26.04	1.07	0.15	2530±140	5.07±0.09	21.10±0.64	6.07±0.09	1.56±0.02	54.8±1.2	73.7±2.9	63.4±1.5	93.0±1.8	TN
2017 Mar 26.96	1.07	0.14	2570±128			6.21±0.10	1.67±0.02	56.2±2.4	71.7±2.7		89.5±1.2	TN
2017 Mar 28.08	1.07	0.14		5.17±0.07		6.03±0.08	1.53±0.01	53.5±1.8	71.4±2.6		89.5±1.4	TN
2017 Mar 29.92	1.06	0.14		4.54±0.09		5.21±0.07		48.1±1.7				TN
2017 Mar 29.96	1.06	0.14	2150±146	4.93±0.08		5.50±0.07					81.1±1.1	TN
2017 Mar 30.00	1.06	0.14		4.88±0.09		4.92±0.08		49.5±2.0				TN
2017 Mar 30.96	1.06	0.14	2010±131	4.21±0.10		5.00±0.09		46.9±1.7			71.1±1.4	TN
2017 Mar 31.00	1.06	0.14		4.41±0.09		4.52±0.09						TN
2017 Mar 31.04	1.06	0.14	2180±144	4.08±0.07		4.29±0.08						TN
2017 Mar 31.12	1.06	0.14		3.94±0.07		4.66±0.08						TN
2017 Mar 31.16	1.06	0.14	2470±199	3.91±0.07		4.28±0.07		41.4±2.3			71.3±1.2	TN
2017 Mar 31.88	1.06	0.14	2010±173	3.80±0.06		4.69±0.06		34.0±3.1			67.3±0.9	TN
2017 Mar 31.96	1.06	0.14		3.67±0.09		4.44±0.09			50.6±1.4		63.7±1.1	TN
2017 Apr 01.00	1.06	0.14		3.83±0.09		4.52±0.09				43.7±2.0	65.7±1.5	TN
2017 Apr 01.04	1.06	0.14		3.58±0.07	15.10±0.63	4.55±0.10					64.8±1.7	TN
2017 Apr 01.08	1.06	0.14		3.75±0.08		4.49±0.08			54.2±1.1		68.5±1.0	TN
2017 Apr 01.16	1.06	0.14		3.91±0.07		4.54±0.08	1.33±0.01	41.9±1.1				TN
2017 Apr 01.88	1.06	0.14	2250±173	3.77±0.06		4.43±0.06		33.2±2.3			59.7±1.2	TN
2017 Apr 01.92	1.06	0.14		4.05±0.06		4.77±0.06		33.5±1.4			64.5±1.6	TN
2017 Apr 02.88	1.05	0.14		4.07±0.07	21.70±0.80	5.02±0.07	1.23±0.02	34.7±2.5	49.6±0.8	41.1±1.1	60.5±1.0	TN
2017 Apr 03.88	1.05	0.14	2610±149	4.24±0.05		5.15±0.06	1.38±0.02	40.8±2.0	53.7±2.8		68.9±0.6	TN
2017 Apr 07.96	1.05	0.15				5.42±0.08	1.36±0.02	31.6±3.8	52.9±2.5		66.3±2.8	TN
2017 Apr 08.00	1.05	0.15	2350±178	4.42±0.09								TN
2017 Apr 13.00	1.05	0.15	2590±157	4.84±0.10		5.41±0.07	1.42±0.03	34.3±4.5	56.1±1.9		66.1±1.9	TN
2017 Apr 20.00	1.05	0.17	1840±131	4.81±0.07	17.00±0.78	5.24±0.07	1.37±0.01	36.7±1.1		40.4±1.3	60.6±1.2	TN
2017 Apr 26.08	1.06	0.18				6.05±0.08	1.50±0.02	45.8±2.2			74.2±1.3	TN
2017 Apr 26.12	1.06	0.18	2260±54	5.34±0.08	20.20±0.84							TN
2017 Apr 26.21	1.06	0.18		5.12±0.06							72.5±1.4	TN
2017 Apr 27.96	1.07	0.18		5.02±0.08	19.10±1.02	5.81±0.07	1.38±0.02	45.4±1.9			72.9±1.4	TN
2017 Apr 28.00	1.07	0.18	2080±134	5.13±0.07								TN
2017 Apr 28.21	1.07	0.19		5.15±0.06								TN
2017 May 03.00	1.08	0.20		4.04±0.05		4.55±0.06	1.18±0.02	37.7±1.7			56.2±1.0	TN
2017 May 15.16	1.13	0.23	2070±115	4.08±0.06		5.02±0.06	1.08±0.03	41.7±7.1				TN
2017 May 24.12	1.18	0.26	1570±83	3.39±0.03		3.94±0.03	1.00±0.03	42.3±2.3				TN
2017 May 26.12	1.20	0.27		4.23±0.05		5.19±0.04	1.13±0.02	55.0±3.1				TN
2017 Jun 07.12	1.28	0.32				2.68±0.07		33.2±2.9			54.6±1.2	TN
2017 Jun 09.12	1.29	0.33				2.10±0.11					48.3±5.1	TN
2017 Jun 10.04	1.30	0.33		1.15±0.10			0.94±0.03				44.6±6.7	TN
2017 Jun 11.12	1.31	0.34		1.81±0.04			0.23±0.08				38.5±5.2	TN
2017 Jun 22.04	1.39	0.40		1.69±0.03		1.81±0.04	0.44±0.02	21.9±1.5			34.1±0.8	TN
2017 Jun 29.12	1.45	0.46		2.03±0.04		2.00±0.04					36.2±0.5	TN
2017 July 20.88	1.63	0.67		1.32±0.04		1.33±0.05					20.5±2.3	TN

A.3 Comet 45P/Honda-Mrkos-Pajdusakova

Table A.3: OH, CN, C_2 and C_3 production rates and the A(0)fρ parameter for comet 45P/Honda-Mrkos-Pajdusakova. The A(0)fρ values are computed at 5000 km from the nucleus and corrected for the phase angle effect.

UT Date	r_h	$\triangle$	Production rates (10^{24} molecules/s)				A(0)fρ (cm)				Tel
	(au)	(au)	Q(OH)	Q(CN)	Q(C_2)	Q(C_3)	BC	RC	GC	Rc	
2017 Feb 10.25	0.97	0.08	1420±51	3.13±0.13	3.50±0.12	0.82± 0.04					TN
2017 Feb 13.12	1.01	0.09		2.85±0.07	2.42±0.10			13.8±2.2			TN
2017 Feb 13.16	1.01	0.09	1210±55	2.85±0.06		0.67±0.04					TN
2017 Feb 13.20	1.01	0.09		2.89±0.04	1.92±0.08			18.5±1.6	14.9±2.0	20.0±2.0	TN
2017 Feb 16.20	1.05	0.11	1060±43	2.23±0.06	2.85±0.10	0.76±0.02	14.0±2.5	25.7±1.9	23.3±2.2	32.2±1.8	TN
2017 Feb 19.16	1.09	0.13		1.97±0.05	2.62±0.08			28.8±1.6		32.7±1.4	TN
2017 Feb 19.20	1.09	0.13		1.98±0.05		0.67±0.02	28.7±2.0		24.3±1.5		TN
2017 Feb 19.25	1.09	0.13	953±52	2.04±0.07							TN
2017 Feb 25.20	1.18	0.20		1.64±0.04	1.77±0.05			23.5±1.0	25.5±1.6	26.9±0.8	TN
2017 Feb 25.25	1.18	0.20			2.38±0.02	0.43±0.04		17.9±1.7		25.0±0.9	TS
2017 Feb 25.84	1.19	0.21		1.58±0.03	2.04±0.04		26.3±2.3		22.2±1.5		TN
2017 Feb 25.92	1.19	0.21		1.61±0.03	1.90±0.05				22.2±1.1		TN
2017 Feb 25.96	1.19	0.21	744±32	1.66±0.03	1.91±0.04		20.3±1.3		22.5±1.3		TN
2017 Feb 26.12	1.19	0.22		1.66±0.03	2.10±0.05		21.2±1.5		22.1±1.3		TN
2017 Feb 26.16	1.19	0.22		1.65±0.03	1.93±0.05		20.2±1.1		25.9±1.5		TN
2017 Feb 26.25	1.19	0.22		1.56±0.16	2.02±0.07				26.4±1.9	27.5±0.8	TN
2017 Mar 02.16	1.25	0.27		1.33±0.03	1.37±0.04					21.0±0.6	TN
2017 Mar 02.20	1.25	0.27		1.16±0.04			19.3±1.5	22.3±1.0	19.6±1.5		TN
2017 Mar 03.16	1.26	0.28		1.19±0.04	1.20±0.04	0.36±0.03	22.8±2.7	23.3±0.7		21.6±0.6	TN
2017 Mar 04.20	1.28	0.30		1.29±0.04						22.8±0.6	TN
2017 Mar 08.16	1.33	0.35		1.28±0.03	1.04±0.04	0.35±0.03	18.2±2.0	21.1±2.0		21.2±0.7	TN
2017 Mar 08.16	1.33	0.35		1.12±0.05				15.3±1.3		18.0±1.2	TS
2017 Mar 08.25	1.33	0.36		1.21±0.06	1.58±0.07	0.44±0.13				18.8±1.2	TS
2017 Mar 20.16	1.49	0.54		1.01±0.03	1.09±0.06					10.3±1.0	TS
2017 Mar 21.16	1.50	0.56			1.10±0.10		10.7±1.9	12.5±1.7		13.0±0.9	TS
2017 Mar 25.94	1.56	0.36								15.7±0.3	TN

A.4 Comet 46P/Wirtanen

Table A.4: Gas production rates and A(0)fρ parameter of comet 46P/Wirtanen. The A(0)fρ values are computed at 10 000 km from the nucleus and corrected for the phase angle effect.

UT Date	r_h	Δ	ΔT	Production rates ($\times 10^{24}$ molecules/s)					A(0)fρ (cm)				Tel
	(au)	(au)	(Days)	OH	NH	CN	C_2	C_3	BC	RC	GC	Rc	
2018 Sep 14	1.55	0.63	-89.52			2.28±0.29	2.79±0.14					29.8±10.4	TS
2018 Sep 15	1.54	0.62	-88.60			2.80±0.15	2.95±0.16					29.7±10.4	TS
2018 Sep 17	1.53	0.60	-86.61			3.21±0.08	3.42±0.12		28.7±14.6	33.3±11.5		35.2±10.6	TS
2018 Sep 18	1.52	0.59	-85.60	1050±371		3.38±0.09	3.60±0.15	1.05±0.05	26.6±13.0			32.0±10.4	TS
2018 Sep 23	1.48	0.55	-80.59	1080±248		3.63±0.08	4.03±0.20	1.00±0.06				35.8±10.8	TS
2018 Oct 01	1.42	0.48	-72.65	1690±271		4.70±0.10	5.43±0.22	1.39±0.08	55.8±12.8			59.4±11.1	TS
2018 Oct 05	1.38	0.45	-68.58	1590±100		4.49±0.07	4.68±0.10	1.40±0.12				54.7±10.4	TS
2018 Oct 12	1.33	0.39	-61.54	1780±328		4.79±0.06						71.8±10.5	TS
2018 Oct 15	1.30	0.38	-58.63	1930±164		6.11±0.11	6.98±0.14	1.71±0.13	62.9±13.1	75.5±12.1		74.0±11.0	TS
2018 Oct 21	1.26	0.34	-52.62	2860±180		8.73±0.09	10.50±0.13	2.63±0.11	85.4±15.0	93.4±13.5		84.1±12.2	TS
2018 Oct 24	1.24	0.32	-49.60	3240±120	27.60±1.03	7.87±0.12	9.32±0.21	2.14±0.20	69.5±17.9	90.0±13.1		68.2±12.6	TS
2018 Nov 01	1.19	0.27	-41.71	3830±110	28.30±0.84	8.91±0.08	10.10±0.10	2.13±0.07	83.4±15.9	101.5±13.0	93.6±14.9	119.7±11.6	TS
2018 Nov 04	1.18	0.26	-38.61	4050±176	31.80±1.61	9.55±0.06	11.40±0.09	2.72±0.09	103.5±16.3	118.5±12.7	109.8±12.2	129.2±10.8	TS
2018 Nov 08	1.15	0.23	-34.61	4970±119	37.00±1.03	10.60±0.10	12.70±0.11	3.22±0.07	108.1±16.4	126.5±13.6	116.7±13.1	147.7±10.8	TS
2018 Nov 13	1.13	0.21	-29.61	5220±310	35.20±1.60	10.90±0.06	12.80±0.13	3.24±0.11	115.8±18.0	137.5±14.0		155.4±11.4	TS
2018 Nov 14	1.13	0.20	-28.90	5050±140		11.20±0.15						156.1±11.7	TS
2018 Nov 15	1.12	0.20	-27.67	5260±177		11.30±0.08	13.50±0.13					159.6±12.9	TS
2018 Nov 17	1.11	0.19	-25.57	5280±133		12.30±0.16	13.90±0.18		114.2±16.6	135.0±12.6	128.6±14.6	169.3±11.7	TS
2018 Nov 20	1.10	0.17	-22.62	5650±122	34.70±1.03	12.10±0.18	14.20±0.20	3.32±0.05	99.7±17.5	155.1±12.6		171.0±12.9	TS
2018 Nov 21	1.10	0.17	-21.58	5510±130		13.00±0.20						165.3±13.8	TS
2018 Nov 23	1.09	0.16	-19.70	5050±191	40.20±1.10	14.20±0.19		4.18±0.16	99.7±20.4	147.0±16.4	131.6±18.7	178.1±13.8	TS
2018 Nov 26	1.08	0.14	-16.89	5770±101	44.30±0.90	14.10±0.18	17.40±0.22	4.13±0.05	123.4±17.8	160.3±11.7	154.2 ±11.5	200.8±13.2	TS
2018 Nov 27	1.08	0.14	-15.90			13.70±0.21						205.0±12.6	TS
2018 Nov 27	1.08	0.13	-14.99	5340±155		13.20±0.23	15.40±0.26	4.10±0.06	112.9±17.5	165.6±14.1	149.1±14.6	201.6±13.8	TN
2018 Nov 28	1.07	0.13	-14.66	5140±102	39.30±0.80	14.00±0.20	17.00±0.22	4.16±0.06	135.5±11.7	175.0±13.2	153.5±13.8	205.3±12.9	TS
2018 Nov 30	1.07	0.13	-12.90	5700±265	43.80±1.50	13.60±0.30	17.00±0.32	4.21±0.09	157.5±14.0	180.0±12.0	167.6±13.5	210.7±13.5	TS
2018 Dec 01	1.07	0.12	-11.73	5250±117	39.40±0.75	12.90±0.26	16.80±0.21	4.45±0.10	146.8±18.9	178.6±15.2	150.0±15.4	207.8±10.6	TS
2018 Dec 02	1.06	0.11	-10.01	6040±219	42.90±1.46	12.80±0.25	16.60±0.35	4.04±0.12	127.4±12.3	182.7±13.4	143.6±13.7	207.7±14.5	TN
2018 Dec 03	1.06	0.11	-09.74	5730±110	36.90±1.00	13.90±0.28		4.72±0.08	135.7±21.9	186.9±15.4	153.2±17.1	216.9±14.0	TS
2018 Dec 04	1.06	0.11	-08.68		39.30±0.62	13.80±0.32	16.60±0.25		143.9±14.5	169.6±17.0	149.9±15.3	213.6±12.8	TS
2018 Dec 04	1.06	0.10	-08.01	4830±135	36.90±1.20	12.40±0.26	14.90±0.40	3.95±0.10	146.0±12.8	174.4±13.3	148.2±13.6	211.1±15.3	TN
2018 Dec 07	1.06	0.10	-05.71			13.90±0.33	18.50±0.22			202.4±17.3		225.7±15.7	TS
2018 Dec 07	1.06	0.10	-05.90	4950±131	42.50±1.12	12.50±0.27	18.40±0.28	4.32±0.11	149.5±13.3	193.1±13.2	166.2±14.3	222.1±16.5	TN
2018 Dec 08	1.06	0.19	-04.93	5380±130	41.40±1.14	14.20±0.28	17.70±0.45	4.20±0.08	153.6±13.2	198.2±14.2	171.0±15.3	238.5±16.9	TN
2018 Dec 09	1.06	0.09	-04.00			13.60±0.30	17.50±0.43	4.10±0.11				234.3±17.1	TN
2018 Dec 09	1.06	0.09	-03.69	5050±152	38.90±1.21	14.50±0.40	17.50±0.40	4.30±0.09	176.6±19.4	204.2±17.3	144.2±13.1	234.3±16.5	TS
2018 Dec 10	1.06	0.09	-02.98	5030±166	34.50±1.34	13.70±0.28	18.40±0.41						TN
2018 Dec 10	1.06	0.09	-02.65	5410±144		14.40±0.42	19.90±0.50	4.04±0.09	162.2±15.0	207.0±16.0	207.0±16.0	236.9±17.2	TS
2018 Dec 12	1.06	0.08	-01.00	5260±173	41.80±1.63	13.00±0.34	15.40±0.62	4.07±0.12					TN
2018 Dec 14	1.06	0.08	+01.01	5440±180	33.30±1.89	13.70±0.32	15.80±0.47	4.00±0.08	170.6±16.8	217.8±17.7	186.7±17.0	249.1±19.2	TN
2018 Dec 15	1.06	0.08	+02.17	5260±237		14.90±0.41		4.12±0.05	196.1±16.4	180.7±12.9	216.2±14.2	219.0±16.3	TS
2018 Dec 16	1.06	0.08	+03.10	5600±154	40.30±1.58	13.70±0.34	17.20±0.50	3.93±0.06	160.7±17.2	213.6±16.0	181.9±16.6	242.6±18.0	TN
2018 Dec 17	1.06	0.08	+04.02			13.10±0.34							TN
2018 Dec 17	1.06	0.08	+04.02			14.60±0.40							TS
2018 Dec 18	1.06	0.08	+05.95			12.30±0.26	15.00±0.38		172.2±17.6	200.7±15.6	162.4±19.1	227.1±19.7	TN
2018 Dec 21	1.06	0.08	+08.01						236.6 ±20.4	152.9±20.1	116.2±20.1	221.6±28.8	TN
2018 Dec 23	1.07	0.09	+10.88	4120±183	30.50±1.88	11.40±0.21	13.70±0.48	2.95±0.16	180.5±20.1	172.2±14.3	125.5±19.8	170.5±25.6	TN
2018 Dec 25	1.07	0.10	+12.95	3620±110	29.20±1.28	11.20±0.23	14.10±0.46	3.25±0.12	127.7±14.9	143.3±17.7	121.3±12.1	169.8±13.4	TN
2018 Dec 29	1.08	0.11	+16.91	3500±100	31.00±0.89	10.80±0.18	14.60±0.26	3.39±0.08	87.0±14.9	137.2±13.4	99.2±13.2	143.9±14.7	TN
2019 Jan 02	1.09	0.13	+20.98		27.00±0.95	10.50±0.25	13.40±0.40	3.14±0.05	73.3±14.3	118.4±15.4	101.1±13.4	140.2±13.4	TN
2019 Jan 05	1.10	0.14	+23.21			10.30±0.17	14.00±0.44	3.00±0.06	88.0±11.5	116.9±12.1	99.0±11.9	125.9±11.9	TN
2019 Jan 10	1.12	0.17	+28.32	2940±115	25.50±0.90	9.89±0.14	12.70±0.32	2.64±0.07	75.4±12.8	109.4±10.8	87.4±11.1	115.2±11.5	TN
2019 Jan 13	1.14	0.19	+31.22			9.36±0.11	12.00±0.26	2.46±0.07				106.4±11.5	TN
2019 Jan 15	1.15	0.21	+34.01			8.58±0.09	10.30±0.22						TN
2019 Jan 19	1.17	0.23	+37.29	3000±120	23.20±0.85	8.75±0.10	11.00±0.23	2.44±0.05	80.7±11.3	100.1±11.3	82.8±11.7	102.3±11.7	TN
2019 Jan 23	1.19	0.25	+41.27	2690±105	22.90±1.67	8.05±0.21	9.27±0.20	2.04±0.06	61.1±14.7	95.8±12.1	96.3±15.8	101.0±13.2	TN
2019 Jan 25	1.20	0.27	+43.26	2150±110	24.40±0.95	7.56±0.09	9.10±0.10	1.94±0.07	82.6±13.8	94.8±11.0	66.6±12.8	91.1±15.1	TN
2019 Jan 28	1.22	0.28	+46.15			8.37±0.08						106.7±11.3	TN
2019 Jan 31	1.24	0.31	+49.31	1920±100	17.30±1.15	6.80±0.07	7.33±0.13	1.75±0.04	27.9±13.6	56.3±10.2	37.5±15.5	56.3±11.9	TN
2019 Feb 05	1.28	0.35	+55.04			6.01±0.05						52.3±14.3	TN
2019 Feb 08	1.30	0.37	+57.26		14.70±0.90	5.67±0.06	5.89±0.08	1.26±0.03	25.4±12.3	62.3±11.5	40.9±10.6	62.9±11.3	TN
2019 Feb 11	1.32	0.39	+60.15	1730±95	16.30±0.95	6.18±0.07	5.53±0.12	1.34±0.05				64.2±13.0	TN
2019 Feb 14	1.34	0.41	+63.25			5.02±0.07						58.8±11.5	TN
2019 Feb 22	1.40	0.49	+71.30			5.69±0.10	4.00±0.16	0.90±0.10					TN
2019 Feb 28	1.45	0.55	+77.45			4.33±0.04	4.13±0.08					48.1±12.1	TN
2019 Mar 10	1.53	0.65	+87.10			3.16±0.05	2.81±0.10	0.60±0.03	17.2±10.9		19.4±11.4	33.4±12.5	TN
2019 Mar 20	1.62	0.77	+97.35			3.05±0.13	2.00±0.13						TN

A.5 Comet 64P/Swift-Gehrels

Table A.5: Gas production rates and A(0)fρ parameter of comet 64P/Swift-Gehrels. The A(0)fρ values are computed at 10 000 km from the nucleus and corrected for the phase angle effect.

UT Date	r_h	Δ	Production rates ($\times 10^{24}$ molec/s)					A(0)fρ (cm)				Tel.
	(au)	(au)	OH	NH	CN	C_2	C_3	BC	RC	GC	Rc	
2018 Aug 15	1.69	0.82			2.12±0.06	2.13±0.05		131.1±12.9	173.5±15.6		57.8±5.4	TN
2018 Aug 17	1.67	0.80			2.00±0.06	2.05±0.07					58.7±6.5	TN
2018 Aug 20	1.66	0.77			2.13±0.18	2.10±0.08					54.9±4.8	TN
2018 Oct 21	1.40	0.45	5330±530		9.98±0.07						130.2±13.9	TN
2018 Nov 02	1.39	0.45	5250±207		12.90±0.10	12.30±0.07	3.50±0.05	152.2±18.2	192.4±14.5		188.7±13.6	TN
2018 Nov 07	1.39	0.45	6050±236	34.00±1.24	14.30±0.09	13.60±0.10	3.74±0.06	159.4±15.8	207.9±16.2	163.9±13.7	203.9±17.3	TN
2018 Nov 11	1.40	0.46	5890±156	45.60±1.91	15.40±0.09	15.00±0.11	4.16±0.05	171.5±16.3	229.0±16.5	178.0±19.0	227.1±15.2	TN
2018 Nov 29	1.43	0.51	5860±182	45.10±1.80	19.60±0.11	20.40±0.12	5.04±0.06	231.3±15.3	316.7±16.8	258.3±14.6	312.1±17.7	TN
2018 Dec 03	1.44	0.53	5710±196	49.90±1.78	20.10±0.10	21.50±0.10	5.19±0.05	242.0±16.0	323.8±14.6	264.1±14.6	326.0±17.0	TN
2018 Dec 05	1.44	0.54	5920±120	47.70±1.05	19.10±0.09	21.10±0.11	4.77±0.07	253.3±14.7	331.2±14.7	266.6±15.1	326.7±15.1	TN
2018 Dec 12	1.47	0.58	5940±185	56.60±1.99	20.60±0.10	20.60±0.13	5.02±0.05	263.3±11.6	336.3±15.7	260.7±11.6	333.6±15.2	TN
2018 Dec 14	1.47	0.59	6900±253		21.20±0.10	21.10±0.12		262.5±18.9	337.1±19.8		335.2±15.2	TN
2018 Dec 19	1.49	0.62	7000±216	69.20±3.14	24.00±0.09	21.00±0.11	5.41±0.05		335.1±13.6	270.0±22.0	330.2±12.4	TN
2018 Dec 22	1.51	0.65	6230±110		19.40±0.13			249.0±28.2	347.1±34.2	261.8±28.2	330.8±21.2	TN
2018 Dec 23	1.51	0.66			21.90±0.22							TN
2018 Dec 26	1.53	0.68	6060±134		22.40±0.12	21.50±0.14	5.19±0.08	281.4±16.7	336.9±13.6	268.7±18.3	335.6±17.4	TN
2018 Dec 27	1.53	0.69			20.00±0.09							TN
2018 Dec 30	1.54	0.71	5050±112	46.00±1.55		21.60±0.12	5.07±0.04	268.1±10.5	407.6±16.9	298.5±15.0		TN
2019 Jan 04	1.57	0.76			20.60±0.07						371.4±16.3	TN
2019 Jan 05	1.58	0.78	4690±113	39.00±1.02	19.50±0.09	20.80±0.09	4.63±0.05	282.9±15.8	372.6±11.5	280.5±19.8	374.4±16.6	TN
2019 Jan 05	1.58	0.78	5400±500	43.00±4.74	21.30±0.12	19.75±0.13	4.87±0.26	283.1±17.0	350.3±17.4	275.9±21.8	339.2±17.2	TS
2019 Jan 06	1.59	0.79			19.70±0.10						333.6±17.4	TN
2019 Jan 07	1.59	0.80			19.90±0.08						313.9±15.1	TN
2019 Jan 08	1.60	0.80			19.60±0.09						324.8±18.4	TN
2019 Jan 09	1.60	0.81			19.90±0.10						306.6±15.8	TN
2019 Jan 10	1.60	0.82	4260±104	38.10±1.69	18.60±0.11	18.70±0.10	4.00±0.06	223.2±10.9	319.2±19.2	249.1±17.5	317.4±14.7	TN
2019 Jan 11	1.61	0.83			19.40±0.12						298.6±16.1	TN
2019 Jan 12	1.62	0.84			19.60±0.13						289.5±16.6	TN
2019 Jan 14	1.63	0.87			18.40±0.12						281.4±18.5	TN
2019 Jan 14	1.63	0.87			17.85±0.15							TS
2019 Jan 15	1.64	0.88			19.00±0.13						257.8±11.0	TN
2019 Jan 15	1.64	0.88			15.30±0.14	10.90±0.11						TS
2019 Jan 29	1.73	1.06	2570±685	23.90±7.80	12.80±0.17	11.60±0.15	3.06±0.08	153.4±45.7	191.8±18.1	173.1±16.7	201.8±19.3	TS
2019 Feb 04	1.76	1.13	2260±65	21.60±1.05	11.50±0.09	9.62±0.05	2.33±0.04	148.3±17.1	180.5±10.9			TN
2019 Feb 22	1.89	1.42			8.16±0.07						122.1±6.8	TN
2019 Mar 09	2.00	1.67			14.30±0.05	3.21±0.11	0.89±0.04	26.1±6.2	71.4±17.9	55.6±9.6	67.4±8.4	TN

A.6 Comet 66P/du Toit

Table A.6: OH, CN, C_2 and C_3 production rates and A(0)fρ parameter of comet 66P. The A(0)fρ values are computed at 5000 km from the nucleus and corrected for the phase angle effect. The perihelion of 66P was on May 20, 2018 (r_{h}= 1.28 au Δ=0.90 au au).

UT Date	r_h	$\triangle$	Production rates ($\times10^{24}$ molec/s)				A(0)fρ (cm)				Tel
	(au)	(au)	Q(OH)	Q(CN)	Q(C_2)	Q(C_3)	BC	RC	Rc	Ic	
2018 May 06	1.30	0.90		5.67±0.55	4.65±0.68						TS
2018 May 16	1.29	0.90	2880±297	8.59±0.53	8.63±0.70	2.67±0.20	82.6±6.3	108.0±7.7	102.4±6.3	98.6±8.6	TS
2018 May 23	1.29	0.90	2530±298	8.00±0.53	8.22±0.64	2.43±0.22	75.6±5.7				TS
2018 May 26	1.29	0.90		7.60±0.52	7.78±0.64	2.20±0.21	70.8±6.0	97.7±6.1	76.7±6.9	88.0±8.6	TS
2018 Jun 17	1.34	0.91		6.23±0.56	3.40±0.67	1.26±0.23			46.9±6.8	55.2±7.4	TS
2018 Jun 28	1.39	0.92		3.60±0.56	3.85±0.68						TS
2018 Jul 08	1.45	0.92	891±280	2.15±0.20	2.07±0.20	1.92±0.20					XSH
2018 Jul 13	1.48	0.92		1.65±0.51	1.40±0.62						TS
2018 Jul 14	1.49	0.92	541±230	1.53±0.20	1.78±0.20	1.26±0.20					XSH

A.7 Comet 252P/LINEAR

Table A.7: OH, NH, CN, C_2 and C_3 production rate and A(0)fρ parameter for comet 252P/LINEAR. The A(0)fρ values are computed at 1000 km from the nucleus and corrected for the phase angle effect.

UT Date	r_h	$\triangle$	Production rates ($\times$ 10^{24}molecules/s)					A(0)fρ (cm)				Tel
	(au)	(au)	Q(OH)	Q(NH)	Q(CN)	Q(C_2)	Q(C_3)	BC	RC	GC	Rc	
2016 Mar 04	1.01	0.11	-	-	0.78±0.04	0.85±0.03	0.28±0.04	2.1±0.1	3.2±0.1	2.3±0.1	9.2±0.1	TS
2016 Mar 06	1.01	0.10	859±500	-	1.31±0.04	1.52±0.05	0.42±0.04			3.0±0.1	5.8±0.1	TS
2016 Mar 14	1.00	0.06	2360±159	-	4.31±0.10	-	-	8.5±0.1			14.0±0.1	TS
2016 Mar 17	1.00	0.05	2630±121	4.56±0.31	4.75±0.13	4.30±0.19	1.24±0.07	9.6±0.1	14.6±0.1	11.0±0.2	14.6±0.2	TS
2016 Mar 19	1.00	0.04	2840±155	-	7.54±0.09	7.23±0.11	1.51±0.05		14.1±0.2	15.1±0.2	20.5±0.2	TS
2016 Mar 21	1.00	0.04	-	-	8.33±0.25	6.17±0.34	1.71±0.09	15.4±0.3	17.7±0.1	17.9±0.3	26.9±0.3	TS
2016 Mar 23	1.00	0.04	3670±172	6.63±0.21	8.73±0.29	7.45±0.35	2.01±0.08	16.2±0.8	22.1±0.6		32.2±0.3	TS
2016 Mar 24	1.00	0.04	3600±131	7.41±0.30	8.84±0.20	8.75±0.24	2.08±0.05	16.1±0.9	25.6±0.4	21.0±0.8	34.0±0.9	TS
2016 Mar 25	1.01	0.04	3700±100	-	9.43±0.27	6.74±0.34	2.10±0.08	18.5±0.4	42.0±1.5	30.0±0.4	34.4±1.4	TS
2016 Mar 27	1.01	0.05	4150±111	-	10.30±0.23	10.00±0.36	2.55±0.07	23.7±0.7	26.6±1.1	28.5±0.8	43.8±0.7	TS
2016 Mar 28	1.01	0.05	4360±134	10.70±0.27	10.70±0.24	12.00±0.39	2.60±0.10	29.2±1.3		31.5±0.7	45.0±1.4	TS
2016 Apr 01	1.02	0.07	4780±110	15.10±0.29	10.40±0.20	12.90±0.31	2.87±0.05	32.0±1.7		55.0±0.5	58.5±0.4	TS
2016 Apr 08	1.05	0.11	5740±70	-	-	-	-				40.1±0.2	TS
2016 Apr 10	1.06	0.12	6370±56	20.90±0.27	13.30±0.12	18.90±0.14	3.67±0.03	44.7±0.3	57.5±0.3		77.9±0.4	TS
2016 Apr 11	1.07	0.13	-	-	13.30±0.14	-	-		35.3±0.3	54.4±0.3	58.1±0.2	TS
2016 Apr 15	1.09	0.15	6160±75	21.90±0.28	12.90±0.13	18.30±0.22	3.73±0.05		55.3±0.2	48.5±0.3	56.0±0.3	TS
2016 Apr 16	1.09	0.16	5770±66	-	12.60±0.12	17.20±0.20	3.51±0.02	39.4±0.3		55.8±0.3	74.1±0.3	TS
2016 Apr 20	1.12	0.18	5240±65	20.00±0.30	12.60±0.11	17.50±0.16	-			52.3±0.3	76.3±0.3	TS
2016 Apr 21	1.12	0.19	5690±90	20.20±0.35	13.00±0.11	17.50±0.15	3.32±0.04		19.4±0.1	51.4±0.3	74.4±0.3	TS
2016 Apr 26	1.15	0.22	5020±114	-	13.90±0.13	17.10±0.17	3.60±0.10			66.0±3.3	83.2±0.2	TS
2016 Apr 27	1.16	0.22	-	-	10.80±0.12	13.80±0.13	-	22.5±1.5	21.4±1.1			TS
2016 May 04	1.21	0.26	2150±46	-	8.20±0.05	11.20±0.08	2.16±0.03				23.1±0.1	TS
2016 May 14	1.29	0.33	2220±63	-	7.18±0.04	-	1.95±0.03	18.9±0.3		34.0±0.4	28.0±0.8	TS
2016 June 08	1.50	0.53	-	-	-	-	-				5.6±0.2	TS

A.8 Comet C/2017 O1 (ASASSN)

Table A.8: Gas production rates and A(0)fρ parameter of comet C/2017 O1 (ASASSN). The A(0)fρ values are computed at 10 000 km from the nucleus and corrected for the phase angle effect.

UT Date	r_h	Δ	Production rates ($\times 10^{24}$ molec/s)					A(0)fρ (cm)				Tel
	(au)	(au)	OH	NH	CN	C_2	C_3	BC	RC	GC	Rc	
2017 Jul 31	1.83	1.53	1080±47		37.10±0.20	40.40±0.18	7.66±0.24	535.5±16.5	563.8±12.6		610.8±10.0	TN
2017 Aug 01	1.82	1.52	1070±36		32.90±0.18	34.00±0.22	7.84±0.20	441.7±15.6	521.1±13.5		510.5±11.8	TN
2017 Aug 01	1.82	1.52	900±25		32.50±0.20	31.50±0.19	6.60±0.27	457.6±15.0			764.3±11.8	TS
2017 Aug 05	1.79	1.44	1250±50		37.50±0.24							TS
2017 Aug 25	1.66	1.15			29.00±0.20			400.9±14.5			516.9±12.7	TN
2017 Aug 31	1.62	1.07	1060±35		31.20±0.22	31.00±0.19	7.78±0.18	383.9±16.7			511.3±11.3	TN
2017 Sep 04	1.60	1.02	1100±45		26.60±0.28	27.50±0.20			320.2±18.4		346.2±27.9	TS
2017 Sep 16	1.55	0.88	1110±40		25.70±0.24	25.30±0.18	6.49±0.25	158.3±16.5	283.9±15.9		295.5±27.2	TS
2017 Oct 21	1.50	0.72	1050±31	3.68±0.34	18.80±0.34	16.90±0.25	4.58±0.17	164.5±13.6	242.4±13.4	195.8±14.7		TN
2017 Oct 26	1.51	0.73	889±28	3.27±0.20	16.70±0.16	16.20±0.21	4.12±0.20		221.1±13.6	195.8±14.7	244.3±13.3	TN
2017 Oct 31	1.52	0.75			15.60±0.18		3.60±0.16	173.8±12.8	233.2±11.8	150.3±11.5	202.1±11.9	TN
2017 Nov 09	1.54	0.79				14.80±0.18					177.7±12.8	TN
2017 Nov 17	1.57	0.85	500±14		14.40±0.20	13.30±0.15	3.47±0.17	163.1±12.3	196.0±13.1	176.0±12.3	169.8±11.0	TN
2017 Nov 21	1.59	0.88			11.80±0.18	12.00±0.18	2.70±0.22	156.5±12.3			154.2±11.6	TN
2017 Nov 23	1.60	0.89			13.50±0.19	12.30±0.22	2.95±0.28	149.4±12.8	185.7±11.3		157.1±11.8	TN
2017 Dec 02	1.64	0.96			10.90±0.22	7.69±0.23	1.80±0.19	116.2±20.6	185.4±23.7		143.9±14.1	TN
2017 Dec 18	1.74	1.10			8.43±0.26		1.42±0.25		115.2±14.2		92.6±11.7	TN
2017 Dec 27	1.81	1.19			8.11±0.20	6.17±0.14					91.8±12.0	TN
2018 Jan 12	1.93	1.34			5.49±0.22	4.20±0.12			84.6±11.6		77.1±11.2	TN

A.9 Comet C/2017 T2 (PANSTARRS)

Table A.9: Gas production rates and A(0)fρ parameter of comet C/2017 T2 (PANSTARRS). The A(0)fρ values are computed at 10 000 km from the nucleus and corrected for the phase angle effect.

UT Date	r_h	Δ	Production rates ($\times 10^{25}$ molec/s)					A(0)fρ ($\times 10^2$cm)				Tel
	(au)	(au)	OH	NH	CN	C_2	C_3	BC	RC	GC	Rc	
2019 Sep 05	2.81	2.00									45.80±0.21	TN
2019 Sep 19	2.81	2.00									45.50±0.27	TN
2019 Sep 25	2.81	2.00									45.56±0.40	TN
2019 Nov 06	2.81	2.00			3.80±0.07			35.80±0.18			43.46±0.36	TN
2019 Nov 08	2.78	1.95			3.84±0.08	4.29±0.10	0.50±0.04	34.19±0.35	46.87±0.35	36.76±0.34	42.47±0.26	TN
2019 Nov 23	2.64	1.73			5.11±0.07	8.13±0.08	0.71±0.05	32.28±0.27	42.58±0.34	36.21±0.31	39.56±0.34	TN
2019 Nov 27	2.60	1.68	2060±125		5.57±0.07						31.19±0.22	TN
2019 Nov 30	2.58	1.65	2340±150		5.23±0.07	8.16±0.09	0.88±0.06	32.75±0.31	41.53±0.39		40.36±0.21	TN
2019 Dec 08	2.50	1.59	2740±138		5.64±0.10			33.13±0.60	44.49±0.31		41.71±0.27	TN
2019 Dec 13	2.46	1.56	2670±128		5.85±0.07	7.47±0.12	1.02±0.08	35.72±0.28			41.14±0.25	TN
2019 Dec 22	2.38	1.53	3040±100		6.13±0.06	6.68±0.08	1.20±0.07	34.24±0.19	47.79±0.20		42.14±0.18	TN
2019 Dec 25	2.35	1.52	2770±105		6.16±0.06	6.94±0.09		33.93±0.20	45.32±0.38		42.98±0.16	TN
2019 Dec 29	2.32	1.52	3810±127	2.98±0.82	6.79±0.06	8.27±0.09	1.24±0.07	34.13±0.20	45.55±0.21		43.21±0.19	TN
2020 Jan 04	2.30	1.52	4280±100		7.48±0.07	8.65±0.09	1.07±0.08	34.51±0.25	46.67±0.44		44.41±0.22	TN
2020 Jan 10	2.30	1.52	5030±111		8.60±0.08	8.90±0.13	1.51±0.09	33.52±0.44	47.60±0.44		43.54±0.25	TN
2020 Jan 18	2.31	1.52	6940±100		10.4±0.07	11.10±0.08	2.02±0.07	34.17±0.45	51.10±0.25		45.61±0.37	TN
2020 Jan 26	2.08	1.60	5520±105	5.13±0.64	8.72±0.06	10.40±0.08	1.73±0.08	36.28±0.44	48.37±0.95		47.16±0.15	TN
2020 Jan 27	2.07	1.61			8.69±0.06	10.90±0.09		33.74±0.26			46.00±0.35	TN
2020 Jan 31	2.04	1.63			9.00±0.07						46.71±0.68	TN
2020 Feb 01	2.04	1.63			8.95±0.07						47.46±0.25	TN
2020 Feb 03	2.02	1.64	5300±112	4.34±0.87	8.97±0.12	10.60±0.16	1.92±0.07	35.73±0.50	49.27±0.65		47.65±0.38	TN
2020 Feb 10	1.96	1.67	4730±78	4.14±0.73	8.10±0.07	10.10±0.10	1.60±0.08	34.71±0.64	50.84±0.52	40.04±0.51	46.98±0.25	TN
2020 Feb 17	1.91	1.70	5570±95	4.91±0.51	8.78±0.06	10.30±0.09	1.99±0.10	38.66±0.42	51.33±0.70	42.86±0.28	48.74±0.45	TN
2020 Feb 21	1.89	1.72	5110±75	7.00±0.58	8.32±0.06			39.08±0.28			49.37±0.20	TN
2020 Feb 26	1.85	1.73	5500±120	9.97±0.60	8.85±0.06	11.20±0.09	2.28±0.09	38.37±0.27	52.58±0.78	39.27±0.15	55.64±0.18	TN
2020 Mar 10	1.78	1.76	4680±85	9.27±0.76	7.21±0.06	7.62±0.08	1.45±0.08	35.86±0.28	49.60±0.33	37.88±0.28	47.90±0.45	TN
2020 Apr 01	1.63	1.73						28.92±0.29	48.04±0.29	38.43±0.29	45.77±0.27	TN
2020 Apr 20	1.63	1.73		8.36±0.52	6.32±0.05	8.69±0.07	1.25±0.07	28.91±0.30			37.93±0.20	TN
2020 May 03	1.62	1.70	3280±80	8.19±0.85	5.16±0.06	6.63±0.16	1.15±0.06				32.60±0.23	TN
2020 May 19	1.63	1.66	2110±65	4.08±0.46	5.16±0.05	6.00±0.07	1.20±0.08	21.67±0.33	32.35±0.16		29.35±0.15	TN
2020 May 25	1.64	1.66	2000±55	4.22±0.45	4.78±0.05	5.57±0.07	1.05±0.07	20.22±0.18	27.35±0.13		26.40±0.17	TN
2020 May 31	1.66	1.66	2080±60	5.08±0.58	5.45±0.06	6.05±0.07	1.10±0.07	21.63±0.26	32.53±0.16		30.05±0.20	TN
2020 Jun 03	1.67	1.66			5.07±0.06						29.26±0.24	TN
2020 Jun 05	1.67	1.66			4.90±0.06						29.05±0.22	TN
2020 Jun 12	1.68	1.67	2250±70		4.52±0.05	4.78±0.07	0.88±0.04	19.56±0.28	28.02±0.13		25.20±0.17	TN
2020 Jun 19	1.73	1.72	2000±55	2.79±0.46	4.08±0.05	4.76±0.07	0.89±0.03	14.05±0.28	23.20±0.20		22.72±0.15	TN
2020 Jul 04	1.81	1.83	873±65		2.52±0.07	2.61±0.12	0.77±0.04		14.69±0.20		12.71±0.19	TN
2020 Jul 08	1.82	1.85			2.94±0.05	2.73±0.08	0.72±0.05				10.53±0.15	TN
2020 Jul 09	1.82	1.85			2.18±0.05	2.19±0.10					13.10±0.13	TN
2020 Jul 18	1.90	1.98			2.18±0.05				14.03±0.15		13.18±0.11	TN
2020 Aug 15	2.11	2.42			2.03±0.05	2.46±0.09			13.89±0.12		12.88±0.12	TN

A.10 Comet C/2018 W2 (Africano)

Table A.10: Gas production rates and A(0)fρ parameter of comet C/2018 W2 (Africano). The A(0)fρ values are computed at 10 000 km from the nucleus and corrected for the phase angle effect.

UT Date	r_h	Δ	Production rates ($\times 10^{24}$ molec/s)					Af$\rho(\theta=0°)$fρ (cm)				Tel
	(au)	(au)	OH	NH	CN	C_2	C_3	BC	RC	GC	Rc	
2019 Jul 17	1.62	2.05	3520±314		14.30±0.68	9.82±0.65	2.11±0.26				427.1±17.9	TN
2019 Jul 20	1.60	1.99	3400±311		15.30±0.55	13.40±0.72		317.2±15.6	460.6±17.3		496.5±19.5	TN
2019 Jul 22	1.59	1.95			15.50±0.53	13.40±0.68		319.7±16.3	531.3±10.1		486.0±19.9	TN
2019 Jul 27	1.56	1.85	3630±315		13.50±0.52	13.00±0.64	3.00±0.19				494.2±18.9	TN
2019 Aug 02	1.54	1.72	2830±286		14.90±0.51	14.00±0.63	3.46±0.18	304.0±11.0	472.6±18.1		468.2±19.2	TN
2019 Aug 13	1.49	1.46	2730±273		10.20±0.51	9.50±0.63		153.4±18.5	284.1±14.5		309.8±18.5	TN
2019 Sep 19	1.48	0.52					2.63±0.28	169.2±17.7	250.5±19.1		294.0±12.0	TN
2019 Sep 21	1.47	0.54	3290±201		13.20±0.56	12.50±0.65		177.3±18.1	289.3±19.3	241.0±16.8	316.0±11.5	TN
2019 Sep 25	1.48	0.50	2850±220	4.03±0.48	10.50±0.55	10.70±0.65	2.60±0.18	180.4±15.6	266.5±16.8	225.3±15.6	322.9±15.8	TN
2019 Sep 28	1.49	0.50	3280±324							169.5±14.9	255.1±15.5	TN
2019 Oct 03	1.51	0.53			13.30±0.55	12.90±0.66	2.36±0.20	198.9±16.7		234.4±15.9	346.9±16.1	TN
2019 Oct 14	1.55	0.76									315.4±11.2	TN
2019 Oct 08	1.53	0.61	5310±348		13.80±0.55		3.71±0.26				292.3±18.9	TS
2019 Oct 17	1.57	0.84	6000±350		14.60±0.55			204.5±12.1	332.9±10.	271.5±8.2	396.5±10.3	TS
2019 Oct 22	1.60	0.94	5050±224		11.90±0.58	11.70±0.68	3.10±0.22		282.9±11.0	224.4±10.8	390.9±17.2	TS
2019 Nov 04	1.68	1.31	4970±339		13.90±0.62	11.75±0.93		239.0±14.3	362.1±10.8	281.5±10.0		TS
2019 Nov 07	1.70	1.40	4920±210		14.00±0.58	12.50±0.71	2.94±0.21	230.4±17.3	378.3±10.8	289.0±10.8	399.1±19.2	TS
2019 Nov 11	1.73	1.51	4750±282		14.70±0.75	13.70±0.95	3.12±0.29	262.3±28.0	379.9±13.2	310.9±13.2	408.9±18.8	TS
2019 Nov 15	1.75	1.63	4000±637				2.56±0.61				445.8±20.0	TS
2019 Nov 21	1.80	1.79			14.70±0.57	10.80±0.80		280.8±26.7	429.3±15.2			TS
2019 Nov 28	1.85	1.95									472.5±17.3	TS
2019 Dec 01	1.89	2.05	4230±306		10.30±0.57	9.00±0.82		299.2±21.5	413.1±19.7		419.8±18.1	TS
2019 Dec 06	1.93	2.17			12.30±0.74	11.10±1.13		269.4±34.7			449.8±20.6	TS
2019 Dec 11	1.97	2.29						262.0±30.0	388.5±15.9		431.4±15.1	TS
2019 Dec 21	1.99	2.33			8.89±0.58	7.24±0.70		263.0±20.0			400.1±17.5	TS
2019 Dec 27	1.99	2.33			7.29±0.61						396.8±16.2	TS
2020 Jan 03	2.18	2.77									346.3±18.6	TS
2020 Jan 09	2.24	2.87									323.2±19.1	TS

A.11 Comet C/2019 Y4 (ATLAS)

Table A.11: Gas production rates and A(0)fρ parameter of comet C/2019 Y4 (ATLAS). The A(0)fρ values are computed at 10 000 km from the nucleus and corrected for the phase angle effect.

UT Date	r_h	Δ	Production rates ($\times 10^{25}$ molec/s)						Af$\rho(\theta=0°)$fρ (cm)				Tel
	(au)	(au)	Q(OH)	Q(H_2O)	Q(NH)	Q(CN)	Q(C_2)	Q(C_3)	BC	RC	GC	Rc	
2020 Feb 21	2.13	1.32				1.71±0.06	1.03±0.07					184.3±5.2	TN
2020 Feb 22	2.12	1.30				1.86±0.06	1.25±0.07	0.35±0.03	105.5±8.3	176.2±8.9	149.8±7.5	175.2±9.7	TN
2020 Feb 25	2.07	1.27				2.44±0.06	1.81±0.07	0.52±0.02	187.0±9.0	242.4±9.5	200.5±6.8	256.3±7.0	TN
2020 Feb 26	2.05	1.26				2.56±0.06	2.07±0.07					275.5±6.0	TN
2020 Mar 09	1.86	1.15	1350±45	1347±45	15.40±1.40	5.82±0.12	4.18±0.11	1.21±0.04	391.8±19.0	674.2±18.7	484.0±18.7	709.5±15.0	TN
2020 Mar 22	1.65	1.08	1430±33	1515±35	15.90±0.48	6.14±0.06	7.28±0.07	1.65±0.02	763.3±13.4	1075.5±10.8	848.0±12.3	1137.2±8.4	TN
2020 Mar 31	1.47	1.05	1360±39	1527±44	15.60±0.47	4.23±0.06	6.25±0.07	1.16±0.02	694.1±14.4	1000.6±16.0	806.7±13.5	1000.0±13.3	TN
2020 Apr 02	1.44	1.04				2.61±0.07	5.52±0.07	1.05±0.02		802.5±14.5		826.9±14.1	TN
2020 Apr 03	1.44	1.04	715±32	811±37	11.60±0.50	3.82±0.06	3.20±0.08	0.94±0.02	555.0±13.4	782.3±14.5	584.1±17.4	848.0±14.7	TN
2020 Apr 14	1.21	1.00				1.39±0.05	1.83±0.06		96.1±8.9			189.3±8.0	TN
2020 Apr 15	1.19	1.00	313±31	332±38		1.18±0.05	1.50±0.06	0.25±0.02	91.3±9.5	157.8±9.2		185.4±7.4	TN
2020 Apr 16	1.18	0.99	405±30	390±39		1.16±0.05	1.36±0.06	0.23±0.02		132.3±7.1		145.3±8.0	TN
2020 Apr 18	1.15	0.99				1.09±0.05	1.37±0.06					145.1±7.4	TN
2020 Apr 20	1.09	0.97				0.94±0.06	1.14±0.06					106.0±7.3	TN
2020 Apr 22	1.05	0.97	258±22	342±30		0.75±0.04	0.96±0.06		26.4±5.2	38.0±5.5			TN
2020 May 02	0.84	0.91				0.51±0.05	0.55±0.06					26.7±5.3	TN
2020 May 03	0.82	0.90				0.55±0.05	-						TN

A.12 Comet C/2020 F3 (NEOWISE)

Table A.12: Gas production rates and A(0)fρ parameter of comet C/2020 F3 (NEOWISE). The A(0)fρ values are computed at 10 000 km from the nucleus and corrected for the phase angle effect.

UT Date	r_h	Δ	Production rates ($\times 10^{26}$ molec/s)					A(0)fρ ($\times 10^2$ cm)				Tel
	(au)	(au)	OH	NH	CN	C_2	C_3	BC	RC	GC	Rc	
2020 Jul 22	0.63	0.69	741±18	7.69±0.04	3.53±0.06	7.35±0.07	1.38±0.03	22.92±0.20	36.29±0.16	32.66±0.16	43.21±0.12	TN
2020 Jul 23	0.65	0.69	1000±28	9.04±0.03	5.00±0.06	8.66±0.06	1.41±0.03	26.40±0.17	36.11±0.17	31.21±0.17	45.60±0.17	TN
2020 Jul 24	0.66	0.70	1020±44	9.78±0.04	5.12±0.07	8.62±0.07	1.50±0.03	26.82±0.18	35.91±0.18	31.58±0.12	46.67±0.19	TN
2020 Jul 25	0.66	0.70	832±42	7.83±0.04	4.18±0.06	7.20±0.07	1.25±0.03	22.09±0.19	30.62±0.27	27.87±0.19	40.30±0.20	TN
2020 Jul 26	0.66	0.70	600±30	5.67±0.04	2.95±0.06	5.20±0.06	0.89±0.02	16.27±0.16	24.32±0.20	21.89±0.14	30.57±0.19	TN
2020 Aug 05	0.93	0.91	324±55	3.46±0.05	1.59±0.05	2.82±0.06	0.43±0.02	8.82±0.22	11.49±0.22	10.07±0.23	17.09±0.20	TN
2020 Aug 06	0.95	0.94	368±30	3.67±0.04	1.76±0.06	2.80±0.07	0.47±0.02	9.80±0.19	11.50±0.22	10.15±0.28	17.45±0.22	TN
2020 Aug 14	1.11	1.17	303±36		1.34±0.05	1.92±0.07		7.66±0.16	9.61±0.18		12.94±0.13	TN
2020 Aug 16	1.15	1.23	247±28		1.35±0.05	1.89±0.06	0.35±0.02	7.24±0.18	9.21±0.21		12.04±0.18	TN
2020 Aug 17	1.17	1.26			1.32±0.05	1.79±0.07		7.25±0.14			12.15±0.20	TN
2020 Aug 18	1.19	1.30	96±7	0.63±0.04	1.21±0.05	1.61±0.06					10.70±0.15	TN
2020 Aug 27	1.36	1.58	85±5		0.58±0.06	0.70±0.05	0.13±0.02	1.12±0.14	2.96±0.19	2.27±0.20	4.30±0.17	TN
2020 Aug 30	1.42	1.68	90±6		0.59±0.06	0.57±0.05					3.06±0.18	TN
2020 Sep 06	1.54	1.90			0.56±0.05	0.56±0.04		1.73±0.16	2.66±0.15		2.72±0.19	TN
2020 Sep 10	1.61	2.02			0.46±0.04	0.50±0.03		1.45±0.14	2.54±0.11		2.84±0.11	TN

A.13 Comet 2I/Borisov

Table A.13: CN and C_2 production rates of comet 2I/Borisov

UT Date	r_h	Δ	ΔT	Exp Time	Production rates (molec/s)		Tel.
	(au)	(au)	(Days)	(s)	Q(CN)	Q(C_2)	TN/TS
2019 Oct 18	2.31	2.67	-50	1500	$(5.87 \pm 0.78) \times 10^{24}$	-	TN
2019 Oct 20	2.29	2.64	-48	1500	$(4.95 \pm 0.52) \times 10^{24}$	-	TN
2019 Oct 27	2.22	2.51	-42	1500	$(6.31 \pm 0.51) \times 10^{24}$	-	TN
2019 Oct 31	2.18	2.44	-38	1500	$(5.27 \pm 0.50) \times 10^{24}$	$< (3.65 \pm 0.64) \times 10^{24}$	TN
2019 Nov 01	2.17	2.43	-37	1500	$(5.74 \pm 0.60) \times 10^{24}$	-	TN
2019 Nov 02	2.16	2.41	-36	1500	$(5.71 \pm 0.57) \times 10^{24}$	-	TN
2019 Nov 04	2.15	2.37	-34	1200	-	$< (3.63 \pm 0.68) \times 10^{24}$	TN
2019 Nov 06	2.13	2.34	-32	1500	$(5.38 \pm 0.57) \times 10^{24}$	-	TN
2019 Nov 10	2.10	2.28	-28	1500	$(6.03 \pm 0.58) \times 10^{24}$	-	TN
2019 Nov 17	2.06	2.19	-21	1500	$(5.95 \pm 0.63) \times 10^{24}$	-	TN
2019 Nov 25	2.03	2.10	-13	1500	$(4.87 \pm 0.57) \times 10^{24}$	$< (4.30 \pm 0.67) \times 10^{24}$	TN
2019 Nov 26	2.02	2.09	-12	1500	$(4.49 \pm 0.68) \times 10^{24}$	$< (3.05 \pm 0.74) \times 10^{24}$	TS
2019 Nov 29	2.01	2.06	-9	1500	$(4.66 \pm 0.71) \times 10^{24}$	-	TS
2019 Dec 01	2.01	2.04	-6	1500	$(4.28 \pm 0.54) \times 10^{24}$	$<(3.98 \pm 0.65) \times 10^{24}$	TN
2019 Dec 14	2.01	1.96	+6	1500	$(4.94 \pm 0.79) \times 10^{24}$	-	TS
2019 Dec 17	2.01	1.95	+9	1500	$(4.58 \pm 0.66) \times 10^{24}$	-	TS
2019 Dec 18	2.01	1.95	+10	1500	$(3.76 \pm 0.61) \times 10^{24}$	-	TS
2019 Dec 19	2.02	1.94	+11	1500	$(3.56 \pm 0.64) \times 10^{24}$	$<(2.33 \pm 0.76) \times 10^{24}$	TN
2019 Dec 24	2.03	1.93	+16	1500	$(3.57 \pm 0.63) \times 10^{24}$	-	TS
2019 Dec 26	2.04	1.93	+18	1500	$(3.09 \pm 0.66) \times 10^{24}$	-	TS
2019 Dec 31	2.07	1.94	+23	1500	$(3.13 \pm 0.75) \times 10^{24}$	-	TS
2020 Jan 02	2.08	1.94	+25	1500	$(2.23 \pm 0.56) \times 10^{24}$	-	TS
2020 Jan 13	2.15	1.97	+35	1500	$(2.70 \pm 0.55) \times 10^{24}$	-	TS
2020 Jan 14	2.15	1.97	+36	1500	$(2.58 \pm 0.56) \times 10^{24}$	-	TS
2020 Jan 20	2.22	2.00	+42	1500	$(2.03 \pm 0.59) \times 10^{24}$	-	TS
2020 Jan 28	2.30	2.05	+50	1500	$(2.11 \pm 0.55) \times 10^{24}$	-	TS
2020 Jan 31	2.33	2.07	+53	1500	$(1.81 \pm 0.58) \times 10^{24}$	-	TS

Table A.14: Magnitude and A(0)fρ of 2I/Borisov. The R magnitudes were performed with an aperture radius of 5″. The A(0)fρ(R) values computed at 10 000 km from the nucleus and corrected for the phase angle effect.

UT Date	r_h (au)	Δ (au)	ΔT Days	Magnitude (R) 5″	A(0)fρ (R) (cm)	Telescope TN/TS
2019 Sep 11	2.80	3.45	-87	17.54±0.06	134.9±15.6	TN
2019 Sep 12	2.78	3.43	-86	17.66±0.07	120.4±10.1	TN
2019 Sep 13	2.76	3.40	-85	17.68±0.07	110.0±15.4	TN
2019 Sep 16	2.72	3.34	-82	17.53±0.06	134.6±14.5	TN
2019 Sep 19	2.68	3.27	-79	17.35±0.06	142.7±9.6	TN
2019 Sep 26	2.58	3.12	-72	17.34±0.05	129.0±8.0	TN
2019 Sep 27	2.56	3.10	-71	17.46±0.04	116.5±8.2	TN
2019 Sep 28	2.54	3.07	-70	17.38±0.05	115.7±7.7	TN
2019 Sep 29	2.53	3.05	-69	17.29±0.05	129.5±7.2	TN
2019 Sep 30	2.52	3.03	-68	17.31±0.03	123.6±7.5	TN
2019 Oct 04	2.48	2.97	-64	17.13±0.06	136.1±6.9	TN
2019 Oct 06	2.44	2.90	-62	17.19±0.05	129.4±6.2	TN
2019 Oct 07	2.43	2.88	-61	17.09±0.07	141.8±6.1	TN
2019 Oct 12	2.37	2.79	-56	17.01±0.04	146.7±8.5	TN
2019 Oct 15	2.33	2.73	-58	16.94±0.07	142.1±8.5	TN
2019 Oct 17	2.31	2.69	-51	16.91±0.07	142.7±9.4	TN
2019 Oct 26	2.22	2.52	-42	16.83±0.05	144.5±7.5	TN
2019 Oct 27	2.22	2.51	-41	16.86±0.05	141.9±6.7	TN
2019 Oct 30	2.18	2.45	-38	16.80±0.04	142.1±7.4	TN
2019 Oct 31	2.18	2.44	-39	16.84±0.04	138.4±7.4	TN
2019 Nov 01	2.17	2.43	-37	16.72±0.06	150.8±7.2	TN
2019 Nov 02	2.16	2.41	-36	16.82±0.06	139.5±7.2	TN
2019 Nov 04	2.15	2.37	-34	16.72±0.06	141.3±9.3	TN
2019 Nov 05	2.14	2.36	-33	16.73±0.05	144.6±7.1	TN
2019 Nov 05	2.14	2.36	-33	16.72±0.05	144.3±7.3	TS
2019 Nov 06	2.13	2.34	-32	16.65±0.04	138.9±7.8	TN
2019 Nov 06	2.13	2.34	-32	16.69±0.04	139.5±7.8	TS
2019 Nov 07	2.12	2.33	-31	16.68±0.05	145.4±7.0	TN
2019 Nov 07	2.12	2.33	-31	16.75±0.05	135.9±7.9	TS
2019 Nov 08	2.11	2.31	-30	16.69±0.04	145.6±6.3	TN
2019 Nov 09	2.11	2.30	-29	16.67±0.04	149.5±6.8	TN
2019 Nov 09	2.11	2.30	-29	16.69±0.05	132.3±8.3	TS
2019 Nov 10	2.10	2.28	-28	16.66±0.05	148.4±7.3	TN
2019 Nov 11	2.09	2.27	-27	16.71±0.07	127.5±10.2	TS
2019 Nov 13	2.08	2.24	-25	16.63±0.06	143.5±9.1	TN
2019 Nov 17	2.06	2.19	-21	16.62±0.06	133.5±8.8	TN
2019 Nov 21	2.04	2.14	-17	16.54±0.07	131.7±9.9	TS
2019 Nov 23	2.03	2.12	-15	16.53±0.04	137.4±7.3	TS
2019 Nov 26	2.02	2.09	-12	16.56±0.04	137.9±6.2	TS
2019 Nov 27	2.02	2.07	-11	16.54±0.05	139.0±6.7	TS
2019 Nov 28	2.02	2.07	-10	16.54±0.04	137.2±6.8	TN
2019 Nov 28	2.02	2.06	-10	16.51±0.05	140.4±6.9	TS
2019 Nov 29	2.01	2.06	-10	16.53±0.05	134.6±6.0	TN
2019 Nov 29	2.01	2.06	-9	16.50±0.05	138.8±7.1	TS

Table A.15: Table A.14 continue.

UT Date	r_h (au)	Δ (au)	ΔT Days	Magnitude (R) 5″	A(0)fρ (R) (cm)	Telescope TN/TS
2019 Dec 01	2.01	2.04	-7	16.52±0.06	134.4±7.0	TS
2019 Dec 01	2.01	2.04	-7	16.53±0.05	134.6±6.0	TN
2019 Dec 02	2.01	2.03	-6	16.51±0.06	133.4±6.6	TS
2019 Dec 05	2.00	2.01	-3	16.53±0.05	128.6±6.1	TS
2019 Dec 08	2.00	1.99	0	16.54±0.06	125.8±8.3	TS
2019 Dec 09	2.00	1.99	+1	16.60±0.04	120.6±6.6	TS
2019 Dec 09	2.00	1.99	+1	16.59±0.04	127.9±5.7	TN
2019 Dec 10	2.00	1.98	+2	16.63±0.05	120.6±7.4	TS
2019 Dec 10	2.00	1.98	+2	16.62±0.05	117.8±8.5	TN
2019 Dec 11	2.00	1.98	+3	16.60±0.05	118.5±8.3	TS
2019 Dec 12	2.01	1.97	+4	16.62±0.07	108.8±10.4	TN
2019 Dec 13	2.01	1.97	+5	16.60±0.05	107.2±7.3	TS
2019 Dec 13	2.01	1.97	+5	16.64±0.05	119.1±8.6	TN
2019 Dec 14	2.01	1.96	+6	16.65±0.06	114.5±9.4	TN
2019 Dec 15	2.01	1.96	+7	16.66±0.06	106.5±9.2	TS
2019 Dec 15	2.01	1.96	+7	16.67±0.06	111.2±8.7	TN
2019 Dec 17	2.01	1.95	+9	16.68±0.05	110.2±7.3	TS
2019 Dec 18	2.01	1.95	+10	16.69±0.05	109.1±7.2	TS
2019 Dec 19	2.02	1.94	+11	16.68±0.06	113.0±8.5	TN
2019 Dec 19	2.02	1.94	+11	16.71±0.05	105.1±6.9	TS
2019 Dec 20	2.02	1.94	+12	16.70±0.04	109.2±6.7	TS
2019 Dec 21	2.02	1.94	+13	16.75±0.05	109.2±6.7	TS
2019 Dec 24	2.03	1.93	+16	16.77±0.04	98.5±6.4	TS
2019 Dec 24	2.03	1.93	+16	16.80±0.05	104.1±6.8	TN
2019 Dec 25	2.04	1.93	+17	16.78±0.04	101.1±6.1	TS
2019 Dec 26	2.04	1.93	+18	16.79±0.05	99.1±6.6	TS
2019 Dec 27	2.05	1.93	+19	16.81±0.04	101.6±5.6	TS
2019 Dec 30	2.06	1.93	+22	16.83±0.05	100.1±6.4	TS
2019 Dec 31	2.07	1.94	+23	16.85±0.04	98.6±5.6	TS
2020 Jan 02	2.08	1.94	+25	16.86±0.05	97.2±6.2	TS
2020 Jan 04	2.09	1.94	+27	16.93±0.05	92.8±6.6	TS
2020 Jan 05	2.10	1.94	+28	16.95±0.05	90.3±6.2	TS
2020 Jan 06	2.10	1.95	+29	17.05±0.06	74.4±8.0	TS
2020 Jan 08	2.12	1.95	+31	17.00±0.06	83.3±8.5	TS
2020 Jan 10	2.13	1.96	+32	17.07±0.05	84.2±6.6	TS
2020 Jan 11	2.14	1.96	+33	17.15±0.06	75.2±8.3	TS
2020 Jan 12	2.15	1.97	+34	17.05±0.06	85.6±6.8	TS
2020 Jan 13	2.15	1.97	+35	17.10±0.06	87.6±8.8	TS
2020 Jan 16	2.18	1.98	+38	17.12±0.06	80.5±8.8	TS
2020 Jan 17	2.19	1.99	+39	17.11±0.07	69.9±9.4	TS
2020 Jan 20	2.22	2.00	+42	17.18±0.06	70.9±8.5	TS
2020 Jan 21	2.23	2.01	+43	17.23±0.05	70.4±6.8	TS
2020 Jan 23	2.25	2.02	+45	17.22±0.07	65.5±7.1	TS
2020 Jan 28	2.30	2.05	+50	17.42±0.06	52.4±6.7	TS
2020 Jan 31	2.33	2.07	+53	17.42±0.08	53.5±8.5	TS
2020 Feb 01	2.34	2.07	+54	17.45±0.07	60.5±7.0	TS
2020 Feb 04	2.37	2.10	+57	17.54±0.05	50.7±10.2	TS

Appendix B

List of publications

Papers in referee journals (14 in total, 3 as first author):

1. **Y. Moulane**, J. Zs. Mezei, V. Laporta, E. Jehin, Z. Benkhaldoun, I. F. Schneider, "Reactive collision of electrons with CO^+ in cometary coma", A&A 615, A53 (2018)

2. **Y. Moulane**, E. Jehin, C. Opitom, F. J. Pozuelos, J. Manfroid, Z. Benkhaldoun, A. Daassou, M. Gillon. "Monitoring of the activity and composition of comets 41P/Tuttle-Giacobini-Kresak and 45P/Honda-Mrkos-Pajdusakova", A&A 619, A156 (2018)

3. F. J. Pozuelos, E. Jehin, **Y. Moulane**, C. Opitom, J. Manfroid, Z. Benkhaldoun, M. Gillon, "Dust modelling and a dynamical study of comet 41P/Tuttle-Giacobini-Kresak during its 2017 perihelion passage", A&A 615, A154 (2018)

4. A. Abdoulanziz, F. Colboc, D. A. Little, **Y. Moulane**, J. Zs. Mezei, E. Roueff, J. Tennyson, I. F. Schneider, V. Laporta, "Theoretical study of ArH^+ dissociative recombination and electron-impact vibrational excitation", MNRAS, 479, 2415-2420 (2018)

5. C. Opitom, D. Hutsemékers, E. Jehin, P. Rousselot, F. J. Pozuelos, J. Manfroid, **Y. Moulane**, M. Gillon, Z. Benkhaldoun, "High resolution optical spectroscopy of the N2-rich comet C/2016 R2 (PanSTARRS)", A&A 624, A64 (2019)

6. E. Mez et al. (**Y. Moulane**), "Pluto's lower atmosphere and pressure evolution from ground-based stellar occultations, 1988-2016", A&A 625, A42 (2019)

7. F. Moreno, E. Jehin, J. Licandro, M. Ferrais, **Y. Moulane**, F. J. Pozuelos, J. Manfroid, M. Devogèle, Z. Benkhaldoun, N. Moskovitz, M. Popescu, M. Serra-Ricart, A. Cabrera-Lavers, M. Monelli, "Dust Properties of Double-Tailed Active Asteroid (6478) Gault", A&A 624, L14 (2019)

8. M. Ferrais, E. Jehin, J. Manfroid, **Y. Moulane**, F. Pozuelos, M. Gillon, Z. Benkhaldoun, "Trappist Lightcurves of Main-Belt Asteroids 31 Euphrosyne, 41 Daphne and 89 Julia", Minor Planet Bulletin Vol. 46, No. 3, pp. 278-279 (2019)

9. M. Ferrais, E. Jehin, **Y. Moulane**, F. Pozuelos, K. Barkaoui, Z. Benkhaldoun, "Trappist-North and -South Combined Lightcurves of Near-Earth Asteroid 3122 Florence", Minor Planet Bulletin Vol. 47, No. 1, pp. 21-22 (2020)

10. A. Fitzsimmons, O. Hainaut, K. Meech, E. Jehin, **Y. Moulane**, C. Opitom, B. Yang, J. V. Keane, J. T. Kleyna, Marco Micheli, Colin Snodgrass, "Detection of CN gas in Interstellar Object 2I/Borisov", APJ 885 L9 (2019)

11. B. Yang, E. Jehin, F. J. Pozuelos, **Y. Moulane**, Y. Shinnaka, C. Opitom, H. H. Hsieh, D. Hutsemékers, J. Manfroid, "Comet 66P/du Toit: not a near Earth main belt comet", A&A 631, A168 (2019)

12. C. Opitom, A. Fitzsimmons, E. Jehin, **Y. Moulane**, O. Hainaut, K. J. Meech, B. Yang, C. Snodgrass, M. Micheli, J. V. Keane, Z. Benkhaldoun, J. T. Kleyna, "2I/Borisov: A C_2 depleted interstellar comet", A&A 631, L8 (2019)

13. M. Bannister, C. Opitom, A. Fitzsimmons, **Y. Moulane**, E. Jehin, D. Seligman, P. Rousselot, M. Knight, M. Marsset, M. Schwamb, A. Guilbert-Lepoutre, L. Jorda, P. Vernazza, Z. Benkhaldoun, "Interstellar comet 2I/Borisov as seen by MUSE: C2, NH2 and red CN detections", Accepted for publication in ApJ (2020)

14. **Y. Moulane**, E. Jehin, P. Rousselot, J. Manfroid, Y. Shinnaka, F. J. Pozuelos, D. Hutsemékers, C. Opitom, B. Yang, and Z. Benkhaldoun, "Photometry and high-resolution spectroscopy of the peculiar comet 21P/Giacobini-Zinner during its 2018 apparition", A&A 640, A54 (2020)

Papers in preparation (5 in total, 2 as first author)

1. B. Hubert, G. Munhoven, **Y. Moulane**, D. Hutsemekers, J. Manfroid, C. Opitom and E. Jehin, "Analytic and numerical methods for the Abel transform of exponential functions for planetary and cometary atmospheres", submitted to Icarus.

2. M. Devogele, ... **Y. Moulane** ... (2021), "(6478) Gault: Physical characterization of an active main-belt asteroid", submitted to MNRAS.

3. Michael S. P. Kelley, ... **Y. Moulane** ... (2021), "Comet 243P/NEAT and the Prospects for Detecting of Water Ice in Cometary Outburst".

4. **Y. Moulane**, E. Jehin, J. Manfroid, D. Hutsemékers, C. Opitom, B. Yang, F. J. Pozuelos, Z. Benkhaldoun (2021), "Photometry, imaging and rotation period of comet 46P/Wirtanen during its 2018 apparition".

5. **Y. Moulane**, E. Jehin, F. J. Pozuelos, B. Novakovic, J. Manfroid, Z. Benkhaldoun (2021), "Photometry, imaging and dynamical evolution of comets 252P/LINEAR and P/2016 B14".

Communications in conferences (as first author)

1. **Y. Moulane**, E. Jehin, C. Opitom, Z. Benkhaldoun, M. Gillon and, I. F. Schneider, "Monitoring of comets activity and composition with the TRAPPIST-North Telescope", Comets: A new vision after Rosetta/Philae, Nov. 14 -18, 2016, Toulouse, France.

2. **Y. Moulane**, Z. Benkhaldoun, E. Jehin, C. Opitom, M. Gillon, and A. Daassou, "Monitoring of comets activity and composition with the TRAPPIST-North Telescope", Frontiers in Theoretical and Applied Physics, Feb. 22 - 25, 2017, AUS, UAE.

3. **Y. Moulane**, E. Jehin, C. Opitom, F. Pozuelos, M. Gillon, Z. Benkhaldoun, and I. F. Schneider, "Study of comets activity with the TRAPPIST-North telescope", Asteroids, Comets, Meteors, Ap. 10-14, 2017, Montevideo, Uruguay

4. **Y. Moulane**, J. Zs. Mezei, V. Laporta, E. Jehin, Z. Benkhaldoun, I. F. Schneider, "The new view of comet coma processes after Rosetta: The importance of electrons", May 24 - 26, 2017, Bratislava, Slovakia

5. **Y. Moulane**, E. Jehin, F. J. Pozuelos, J. Manfroid, C. Opitom, Z. Benkhaldoun, A. Daassou, and M. Gillon, "Monitoring of comets activity and composition with the TRAPPIST-North Telescope", Sep. 19, 2017, Brussels, Belgium.
6. **Y. Moulane**, E. Jehin, F. J. Pozuelos Romero, J. Manfroid, C. Opitom, Z. Benkhaldoun, A. Daassou, and M. Gillon, "TRAPPIST monitoring of the activity and composition of the small near-Earth Jupiter Family Comets : 41P and 252P", EPSC-2018, Sep. 16 – 21, 2018, Berlin, Germany
7. **Y. Moulane**, E. Jehin, P. Rousselot, J. Manfroid, D. Hutsemékers, C. Opitom, F. J. Pozuelos, B. Yang, and Z. Benkhaldoun, "Photometry and high-resolution spectroscopy of the peculiar comet 21P/Giacobini-Zinner during its 2018 apparition", EPSC-DPS Joint Meeting, Sep. 15 – 20, 2019, Geneva, Switzerland
8. **Y. Moulane**, E. Jehin, J. Manfroid, D. Hutsemékers, C. Opitom, B. Yang, and Z. Benkhaldoun, "Photometry, imaging and rotation period of comet 46P/Wirtannen during its 2018 apparition", EPSC-DPS Joint Meeting, Sep. 15 – 20, 2019, Geneva, Switzerland
9. **Y. Moulane**, E. Jehin, J. Manfroid, D. Hutsemékers, C. Opitom, B. Yang, and Z. Benkhaldoun, "Narrow-band photometry of Comets with TRAPPIST telescopes", Planets2020 Workshop, Mar. 2-7, 2020, Santiago, Chile
10. **Y. Moulane**, E. Jehin, F. J. Pozuelos, J. Manfroid, Z. Benkhaldoun, and B. Yang, "Narrow-band photometry of Long Period Comets with TRAPPIST telescopes in 2019-2020", EPSC-2020, Sep. 21 - Oct. 9, 2020, Virtual meeting.

Bibliography

B. Africano, H. Groeller, D. T. Durig, K. Korlevic, R. Haver, R. Gorelli, E. J. Christensen, G. A. Farneth, D. C. Fuls, A. R. Gibbs, A. D. Grauer, J. A. Johnson, R. A. Kowalski, S. M. Larson, G. J. Leonard, R. L. Seaman, F. C. Shelly, A. Ortiz, J. R. Hofstetter, C. B. Smith, B. Lutkenhoner, F. Valentine, G. Ventre, P. Sicoli, S. Urakawa, A. Asami, and G. V. Williams. COMET C/2018 W2 (Africano). *Minor Planet Electronic Circulars*, 2018-X23, December 2018.

M. F. A'Hearn. Spectrophotometry of comets at optical wavelengths. In L. L. Wilkening, editor, *IAU Colloq. 61: Comet Discoveries, Statistics, and Observational Selection*, pages 433–460, 1982.

M. F. A'Hearn, D. G. Schleicher, R. L. Millis, P. D. Feldman, and D. T. Thompson. Comet Bowell 1980b. *The Astronomical Journal*, 89:579–591, April 1984. doi: 10.1086/113552.

M. F. A'Hearn, S. Hoban, P. V. Birch, C. Bowers, R. Martin, and D. A. Klinglesmith, III. Cyanogen jets in comet Halley. *Nature*, 324:649–651, December 1986. doi: 10.1038/324649a0.

M. F. A'Hearn, R. C. Millis, D. O. Schleicher, D. J. Osip, and P. V. Birch. The ensemble properties of comets: Results from narrowband photometry of 85 comets, 1976-1992. *Icarus*, 118:223–270, December 1995. doi: 10.1006/icar.1995.1190.

M. F. A'Hearn, M. J. S. Belton, W. A. Delamere, J. Kissel, K. P. Klaasen, L. A. McFadden, K. J. Meech, H. J. Melosh, P. H. Schultz, J. M. Sunshine, P. C. Thomas, J. Veverka, D. K. Yeomans, M. W. Baca, I. Busko, C. J. Crockett, S. M. Collins, M. Desnoyer, C. A. Eberhardy, C. M. Ernst, T. L. Farnham, L. Feaga, O. Groussin, D. Hampton, S. I. Ipatov, J.-Y. Li, D. Lindler, C. M. Lisse, N. Mastrodemos, W. M. Owen, J. E. Richardson, D. D. Wellnitz, and R. L. White. Deep Impact: Excavating Comet Tempel 1. *Science*, 310:258–264, October 2005. doi: 10.1126/science.1118923.

Michael F. A'Hearn, Humberto Campins, David G. Schleicher, and Robert L. Millis. The Nucleus of Comet P/Tempel 2. *ApJ*, 347:1155, December 1989. doi: 10.1086/168204.

Kathrin Altwegg, Hans Balsiger, and Stephen A. Fuselier. Cometary chemistry and the origin of icy solar system bodies: The view after rosetta. *Annual Review of Astronomy and Astrophysics*, 57(1):113–155, August 2019. doi: 10.1146/annurev-astro-091918-104409. URL https://doi.org/10.1146/annurev-astro-091918-104409.

Z. Amitay, A. Baer, M. Dahan, J. Levin, Z. Vager, D. Zajfman, L. Knoll, M. Lange, D. Schwalm, R. Wester, A. Wolf, I. F. Schneider, and A. Suzor-Weiner. Dissociative recombination of vibrationally excited hd^+: State-selective experimental investigation. *Phys. Rev. A*, 60:3769–3785, Nov 1999. doi: 10.1103/PhysRevA.60.3769. URL https://link.aps.org/doi/10.1103/PhysRevA.60.3769.

C. Arpigny. Anomalous nitrogen isotope ratio in comets. *Science*, 301(5639):1522–1524, September 2003. doi: 10.1126/science.1086711. URL https://doi.org/10.1126/science.1086711.

Michael F A'Hearn, Michael JS Belton, W Alan Delamere, Lori M Feaga, Donald Hampton, Jochen Kissel, Kenneth P Klaasen, Lucy A McFadden, Karen J Meech, H Jay Melosh, et al. Epoxi at comet hartley 2. *Science*, 332(6036):1396–1400, 2011.

H. Balsiger, K. Altwegg, F. Buhler, J. Geiss, A. G. Ghielmetti, B. E. Goldstein, R. Goldstein, W. T. tress, W.-H. Ip, A. J. Lazarus, A. Meier, M. Neugebauer, U. Rettenmund, H. Rosenbauer, R. Schwenn, R. D. Sharp, E. G. Shelly, E. Ungstrup, and D. T. Young. Ion composition and dynamics at comet Halley. *Nature*, 321:330–334, May 1986. doi: 10.1038/321330a0.

Michele T. Bannister, Cyrielle Opitom, Alan Fitzsimmons, Youssef Moulane, Emmanuel Jehin, Darryl Seligman, Philippe Rousselot, Matthew M. Knight, Michael Marsset, Megan E. Schwamb, Aurélie Guilbert-Lepoutre, Laurent Jorda, Pierre Vernazza, and Zouhair Benkhaldoun. Interstellar comet 2I/Borisov as seen by MUSE: C_2, NH_2 and red CN detections. *arXiv e-prints*, art. arXiv:2001.11605, January 2020.

J. E. Beaver, R. M. Wagner, D. G. Schleicher, and B. L. Lutz. Anomalous molecular abundances and the depletion of NH2 in Comet P/Giacobini-Zinner. *ApJ*, 360:696–701, September 1990. doi: 10.1086/169155.

M. Beech. The Draconid meteoroids. *AJ*, 91:159–162, January 1986. doi: 10.1086/113995.

M. J. S. Belton. The Excited Rotation State of 2P/Encke. In *AAS/Division for Planetary Sciences Meeting Abstracts 32*, volume 32 of *Bulletin of the American Astronomical Society*, page 1062, October 2000.

M. J. S. Belton, K. J. Meech, S. Chesley, J. Pittichová, B. Carcich, M. Drahus, A. Harris, S. Gillam, J. Veverka, N. Mastrodemos, W. Owen, M. F. A'Hearn, S. Bagnulo, J. Bai, L. Barrera, F. Bastien, J. M. Bauer, J. Bedient, B. C. Bhatt, H. Boehnhardt, N. Brosch, M. Buie, P. Candia, W.-P. Chen, P. Chiang, Y.-J. Choi, A. Cochran, C. J. Crockett, S. Duddy, T. Farnham, Y. R. Fernández, P. Gutiérrez, O. R. Hainaut, D. Hampton, K. A. Herrmann, H. Hsieh, M. A. Kadooka, H. Kaluna, J. Keane, M.-J. Kim, K. Klaasen, J. Kleyna, K. Krisciunas, L. M. Lara, T. R. Lauer, J.-Y. Li, J. Licandro, C. M. Lisse, S. C. Lowry, L. McFadden, N. Moskovitz, B. Mueller, D. Polishook, N. S. Raja, T. Riesen, D. K. Sahu, N. Samarasinha, G. Sarid, T. Sekiguchi, S. Sonnett, N. B. Suntzeff, B. W. Taylor, P. Thomas, G. P. Tozzi, R. Vasundhara, J.-B. Vincent, L. H. Wasserman, B. Webster-Schultz, B. Yang, T. Zenn, and H. Zhao. Stardust-NExT, Deep Impact, and the accelerating spin of 9P/Tempel 1. *Icarus*, 213:345–368, May 2011. doi: 10.1016/j.icarus.2011.01.006.

M. J. S. Belton, P. Thomas, J.-Y. Li, J. Williams, B. Carcich, M. F. A'Hearn, S. McLaughlin, T. Farnham, L. McFadden, C. M. Lisse, S. Collins, S. Besse, K. Klaasen, J. Sunshine, K. J. Meech, and D. Lindler. The complex spin state of 103P/Hartley 2: Kinematics and orientation in space. *Icarus*, 222:595–609, February 2013. doi: 10.1016/j.icarus.2012.06.037.

Michael JS Belton, William H Julian, A Jay Anderson, and Béatrice EA Mueller. The spin state and homogeneity of comet halley's nucleus. *Icarus*, 93(2):183–193, 1991.

Zouhair Benkhaldoun. Peering into space with the morocco oukaïmeden observatory. *Nature Astronomy*, 2(5):352–354, may 2018. doi: 10.1038/s41550-018-0463-7. URL https://doi.org/10.1038/s41550-018-0463-7.

J. L. Bertaux, J. Costa, T. Mäkinen, E. Quémerais, R. Lallement, E. Kyrölä, and W. Schmidt. Lyman-alpha observations of comet 46P/Wirtanen with swan on SOHO: H2O production rate near 1997 perihelion. 47:725–733, June 1999. doi: 10.1016/S0032-0633(98)00130-5.

F. W. Bessel. Beobachtungen uber die physische Beschaffenheit des Halley's schen Kometen und dadurch veranlasste Bemerkungen. *Astronomische Nachrichten*, 13:185–232, February 1836. doi: 10.1002/asna.18360131302.

M. S. Bessell. UBVRI passbands. *PASP*, 102:1181–1199, October 1990. doi: 10.1086/132749.

A. Beth, K. Altwegg, H. Balsiger, J.-J. Berthelier, M. R. Combi, J. De Keyser, B. Fiethe, S. A. Fuselier, M. Galand, T. I. Gombosi, M. Rubin, and T. Sémon. ROSINA ion zoo at comet 67p. *Astronomy & Astrophysics*, 642:A27, September 2020. doi: 10.1051/0004-6361/201936775. URL https://doi.org/10.1051/0004-6361/201936775.

A. Bhardwaj and S. Raghuram. A Coupled Chemistry-emission Model for Atomic Oxygen Green and Red-doublet Emissions in the Comet C/1996 B2 Hyakutake. *ApJ*, 748:13, March 2012. doi: 10.1088/0004-637X/748/1/13.

L Biermann. Comet tails and solar corpuscular radiation. *Z. Astrophys*, 29:274–286, 1951.

N. Biver. Cometary spectroscopy. In J.-P. Rozelot and C. Neiner, editors, *EAS Publications Series*, volume 47 of *EAS Publications Series*, pages 165–188, April 2011. doi: 10.1051/eas/1147006.

D. Bockelée-Morvan. HCl, HF and H2O+ in comets : probing solar nebula and coma chemistry. Herschel Space Observatory Proposal, id.796, July 2010.

D. Bockelée-Morvan, J. Crovisier, M. J. Mumma, and H. A. Weaver. The composition of cometary volatiles. In M. C. Festou, H. U. Keller, and H. A. Weaver, editors, *Comets II*, pages 391–423. Univ. Arizona Press, Tucson, AZ, 2004.

D. Bockelée-Morvan, N. Biver, E. Jehin, A. L. Cochran, H. Wiesemeyer, J. Manfroid, D. Hutsemékers, C. Arpigny, J. Boissier, W. Cochran, P. Colom, J. Crovisier, N. Milutinovic, R. Moreno, J. X. Prochaska, I. Ramirez, R. Schulz, and J.-M. Zucconi. Large excess of heavy nitrogen in both hydrogen cyanide and cyanogen from comet 17p/holmes. *The Astrophysical Journal*, 679(1):L49–L52, April 2008. doi: 10.1086/588781. URL https://doi.org/10.1086/588781.

Dominique Bockelée-Morvan, Ursina Calmonte, Steven Charnley, Jean Duprat, Cécile Engrand, Adeline Gicquel, Myrtha Hässig, Emmanuël Jehin, Hideyo Kawakita, Bernard Marty, Stefanie Milam, Andrew Morse, Philippe Rousselot, Simon Sheridan, and Eva Wirström. Cometary Isotopic Measurements. , 197(1-4):47–83, Dec 2015. doi: 10.1007/s11214-015-0156-9.

Dominique Bockelée-Morvan, Ursina Calmonte, Steven Charnley, Jean Duprat, Cécile Engrand, Adeline Gicquel, Myrtha Hässig, Emmanuël Jehin, Hideyo Kawakita, Bernard Marty, Stefanie Milam, Andrew Morse, Philippe Rousselot, Simon Sheridan, and Eva Wirström. Cometary isotopic measurements. *Space Science Reviews*, 197(1-4):47–83, May 2015. doi: 10.1007/s11214-015-0156-9. URL https://doi.org/10.1007/s11214-015-0156-9.

Dominique Bockelée-Morvan, Jérémie Boissier, Nicolas Biver, and Jacques Crovisier. No compelling evidence of distributed production of {CO} in comet c/1995 {O1} (hale-bopp) from millimeter interferometric data and a re-analysis of near-ir lines. *Icarus*, 201(2):

898 – 915, 2010. ISSN 0019-1035. doi: http://doi.org/10.1016/j.icarus.2010.07.005. URL http://www.sciencedirect.com/science/article/pii/S0019103510002770.

D. Bodewits, T. L. Farnham, M. F. A'Hearn, L. M. Feaga, A. McKay, D. G. Schleicher, and J. M. Sunshine. The Evolving Activity of the Dynamically Young Comet C/2009 P1 (Garradd). *ApJ*, 786(1):48, May 2014. doi: 10.1088/0004-637X/786/1/48.

D. Bodewits, J. W. Noonan, P. D. Feldman, M. T. Bannister, D. Farnocchia, W. M. Harris, J. Y. Li, K. E. Mandt, J. Wm. Parker, and Z. X. Xing. The carbon monoxide-rich interstellar comet 2I/Borisov. *Nature Astronomy*, 4:867–871, April 2020. doi: 10.1038/s41550-020-1095-2.

Dennis Bodewits, Tony L. Farnham, Michael S. P. Kelley, and Matthew M. Knight. A rapid decrease in the rotation rate of comet 41p/tuttle–giacobini–kresák. *Nature*, 553(7687):186–188, jan 2018. doi: 10.1038/nature25150. URL https://doi.org/10.1038/nature25150.

Hermann Boehnhardt. Split comets. *Comets II*, 745:301–316, 2004.

D. C. Boice, L. A. Soderblom, D. T. Britt, R. H. Brown, B. R. Sandel, R. V. Yelle, B. J. Buratti, Hicks, Nelson, Rayman, J. Oberst, and N. Thomas. *Earth, Moon, and Planets*, 89 (1/4):301–324, 2000. doi: 10.1023/a:1021519124588. URL https://doi.org/10.1023/a:1021519124588.

Bryce T. Bolin, Carey M. Lisse, Mansi M. Kasliwal, Robert Quimby, Hanjie Tan, Chris Copperwheat, Zhong-Yi Lin, Alessandro Morbidelli, James Bauer, Kevin B. Burdge, Michael Coughlin, Christoffer Fremling, Ryosuke Itoh, Michael Koss, Frank J. Masci, Syota Maeno, Eric E. Mamajek, Federico Marocco, Katsuhiro Murata, Michael L. Sitko, Daniel Stern, Richard Walters, Lin Yan, Igor Andreoni, Varun Bhalerao, Dennis Bodewits, Kishalay De, Kunal P. Deshmukh, Eric C. Bellm, Nadejda Blagorodnova, Derek Buzasi, S. Bradley Cenko, Chan-Kao Chang, Drew Chojnowski, Richard Dekany, Dmitry A. Duev, Matthew Graham, Mario Juric, Emily A. Kramer, Shrinivas R. Kulkarni, Thomas Kupfer, Ashish Mahabal, James D. Neill, Chow-Choong Ngeow, Bryan Penprase, Reed Riddle, Hector Rodriguez, Philippe Rosnet, Jesper Sollerman, and Maayane T. Soumagnac. Characterization of the Nucleus, Morphology and Activity of Interstellar Comet 2I/Borisov by Optical and Near-Infrared GROWTH, Apache Point, IRTF, ZTF and Keck Observations. *arXiv e-prints*, art. arXiv:1910.14004, Oct 2019.

Tycho Brahe. *Manuscript (in German)*, volume Codex Vind. 10689. Translated in 1986 by J. Brager and N. Henningsen, E. Eilert- sen Publ., Copenhagen., 1578.

C. L. Brinkman. Comet ASASSN: The Discovery and Outburst of Comet C/2017 O1. In *American Astronomical Society Meeting Abstracts*, volume 52 of *American Astronomical Society Meeting Abstracts*, page 454.02, Jan 2020.

T. W. Broiles, J. L. Burch, G. Clark, C. Koenders, E. Behar, R. Goldstein, S. A. Fuselier, K. E. Mandt, P. Mokashi, and M. Samara. Rosetta observations of solar wind interaction with the comet 67p/churyumov-gerasimenko. *Astronomy & Astrophysics*, 583:A21, oct 2015. doi: 10.1051/0004-6361/201526046. URL https://doi.org/10.1051%2F0004-6361%2F201526046.

D. E. Brownlee, F. Horz, R. L. Newburn, M. Zolensky, T. C. Duxbury, S. Sandford, Z. Sekanina, P. Tsou, M. S. Hanner, B. C. Clark, S. F. Green, and J. Kissel. Surface of Young Jupiter Family Comet 81 P/Wild 2: View from the Stardust Spacecraft. 304:1764–1769, June 2004. doi: 10.1126/science.1097899.

A. Carusi and G. B. Valsecchi. Dynamical evolution of short-period comets. *Publications of the Astronomical Institute of the Czechoslovak Academy of Sciences*, 2:21–28, Jan 1987.

G. Cessateur, J. De Keyser, R. Maggiolo, A. Gibbons, G. Gronoff, H. Gunell, F. Dhooghe, J. Loreau, N. Vaeck, K. Altwegg, A. Bieler, C. Briois, U. Calmonte, M. R. Combi, B. Fiethe, S. A. Fuselier, T. I. Gombosi, M. Hässig, L. Le Roy, E. Neefs, M. Rubin, and T. Sémon. Photochemistry of forbidden oxygen lines in the inner coma of 67p/churyumov-gerasimenko. *Journal of sical Research: Space Physics*, 121(1):804–816, jan 2016. doi: 10.1002/2015ja022013. URL https://doi.org/10.1002%2F2015ja022013.

K. Chakrabarti and J. Tennyson. R -matrix calculation of the potential energy curves for rydberg states of carbon monoxide. *Journal of Physics B: Atomic, Molecular and Optical Physics*, 39(6):1485, 2006. URL http://stacks.iop.org/0953-4075/39/i=6/a=017.

K Chakrabarti and Jonathan Tennyson. R -matrix calculation of the continuum states of carbon monoxide. *Journal of Physics B: Atomic, Molecular and Optical Physics*, 40(11):2135, 2007. URL http://stacks.iop.org/0953-4075/40/i=11/a=015.

J. E. Chambers. A hybrid symplectic integrator that permits close encounters between massive bodies. *MNRAS*, 304:793–799, April 1999. doi: 10.1046/j.1365-8711.1999.02379.x.

A. L. Cochran and E. S. Barker. Comet Giacobini-Zinner - A normal comet? *AJ*, 93:239–243, January 1987. doi: 10.1086/114304.

A. L. Cochran and W. D. Cochran. The first detection of CN and the distribution of CO(+) gas in the coma of Comet P/Schwassmann-Wachmann 1. *Icarus*, 90:172–175, March 1991. doi: 10.1016/0019-1035(91)90077-7.

A. L. Cochran and D. G. Schleicher. Observational Constraints on the Lifetime of Cometary H_2O. *Icarus*, 105:235–253, September 1993. doi: 10.1006/icar.1993.1121.

A. L. Cochran, E. S. Barker, and C. L. Gray. Thirty years of cometary spectroscopy from McDonald Observatory. *Icarus*, 218(1):144–168, Mar 2012. doi: 10.1016/j.icarus.2011.12.010.

A. L. Cochran, A.-C. Levasseur-Regourd, M. Cordiner, E. Hadamcik, J. Lasue, A. Gicquel, D. G. Schleicher, S. B. Charnley, M. J. Mumma, L. Paganini, D. Bockelée-Morvan, N. Biver, and Y.-J. Kuan. The Composition of Comets. July 2015. doi: 10.1007/s11214-015-0183-6.

A. L. Cochran, T. Nelson, A. J. McKay, P. J. MacQueen, W. D. Cochran, and M. Endl. High Spectral Resolution Observations of Comet C/2020 F3 (NEOWISE) From McDonald Observatory. In *AAS/Division for Planetary Sciences Meeting Abstracts*, volume 52 of *AAS/Division for Planetary Sciences Meeting Abstracts*, page 111.03, October 2020.

M Combi. Soho swan derived cometary water production rates collection, urn: nasa: pds: soho: swan_derived: 1.0. *NASA Planetary Data System*, 2017.

M. R. Combi and A. H. Delsemme. Neutral cometary atmospheres. I - an average random walk model for photodissociation in comets. *ApJ*, 237:633–640, April 1980. doi: 10.1086/157909.

M. R. Combi, A. I. F. Stewart, and W. H. Smyth. Pioneer venus lyman-Î observations of comet p/giacobini-zinner and the life expectancy of cometary hydrogen. *Geophysical Research Letters*, 13(4):385–388, 1986. doi: 10.1029/GL013i004p00385. URL https://agupubs.onlinelibrary.wiley.com/doi/abs/10.1029/GL013i004p00385.

M. R. Combi, J. T. Makinen, N. J. Henry, J. L. Bertaux, and E. Quemerais. Water Production Rates from SOHO/SWAN H Lyman-alpha Observations of Active and Moderately Active Comets. In *AAS/Division for Planetary Sciences Meeting Abstracts #38*, volume 38 of *Bulletin of the American Astronomical Society*, page 535, September 2006.

M. R. Combi, J.-L. Bertaux, E. Quémerais, S. Ferron, and J. T. T. Mäkinen. Water Production by Comet 103P/Hartley 2 Observed with the SWAN Instrument on the SOHO Spacecraft. *ApJL*, 734:L6, June 2011. doi: 10.1088/2041-8205/734/1/L6.

M. R. Combi, T. T. Mäkinen, J. L. Bertaux, E. Quémerais, and S. Ferron. A survey of water production in 61 comets from SOHO/SWAN observations of hydrogen Lyman-alpha: Twenty-one years 1996-2016. *Icarus*, 317:610–620, January 2019. doi: 10.1016/j.icarus.2018.08.031.

M. R. Combi, T. Mäkinen, J. Bertaux, E. Quemerais, and S. Ferron. Water Production Rate Activity of C/2020 F3 (NEOWISE) from SOHO/SWAN. In *AAS/Division for Planetary Sciences Meeting Abstracts*, volume 52 of *AAS/Division for Planetary Sciences Meeting Abstracts*, page 111.04, October 2020a.

M. R. Combi, T. Mäkinen, J. L. Bertaux, E. Quémerais, S. Ferron, and R. Coronel. Comet 41P/Tuttle-Giacobini-Kresak, 45P/Honda-Mrkos-Pajdusakova, and 46P/Wirtanen: Water Production Activity over 21 yr with SOHO/SWAN. *The Planetary Science Journal*, 1(3):72, December 2020b. doi: 10.3847/PSJ/abb026.

Michael R. Combi and Paul D. Feldman. Iue observations of h lyman-Î in comet p/giacobini-zinner. *Icarus*, 97(2):260 – 268, 1992. ISSN 0019-1035. doi: https://doi.org/10.1016/0019-1035(92)90132-Q. URL http://www.sciencedirect.com/science/article/pii/001910359290132Q.

Michael R. Combi and Uwe Fink. A critical study of molecular photodissociation and CHON grain sources for cometary c2. *The Astrophysical Journal*, 484(2):879–890, August 1997. doi: 10.1086/304349. URL https://doi.org/10.1086/304349.

M. A. Cordiner, S. N. Milam, N. Biver, D. Bockelée-Morvan, N. X. Roth, E. A. Bergin, E. Jehin, A. J. Remijan, S. B. Charnley, M. J. Mumma, J. Boissier, J. Crovisier, L. Paganini, Y. J. Kuan, and D. C. Lis. Unusually high CO abundance of the first active interstellar comet. *Nature Astronomy*, 4:861–866, April 2020. doi: 10.1038/s41550-020-1087-2.

Iain M. Coulson, Martin A. Cordiner, Yi-Jehng Kuan, Wei-Ling Tseng, Yo-Ling Chuang, Zhong-Yi Lin, Stefanie N. Milam, Steven B. Charnley, and Wing-Huen Ip. Jcmt spectral and continuum imaging of comet 252p/linear. *The Astronomical Journal*, 153(4):169, 2017. URL http://stacks.iop.org/1538-3881/153/i=4/a=169.

J. J. Cowan and M. F. A'Hearn. Vaporization of comet nuclei: Light curves and life times. *Moon and Planets*, 21(2):155–171, October 1979. doi: 10.1007/BF00897085.

S. W. H. Cowley. ICE observations of comet giacobini-zinner. *Philosophical Transactions of the Royal Society of London. Series A, Mathematical and Physical Sciences*, 323(1572):405–420, September 1987. doi: 10.1098/rsta.1987.0095. URL https://doi.org/10.1098/rsta.1987.0095.

T. E. Cravens, J. U. Kozyra, A. F. Nagy, T. I. Gombosi, and M. Kurtz. Electron impact ionization in the vicinity of comets. *jgr*, 92:7341–7353, July 1987. doi: 10.1029/JA092iA07p07341.

G. Cremonese. *Space Science Reviews*, 90(1/2):83–89, 1999. doi: 10.1023/a:1005281611036. URL https://doi.org/10.1023/a:1005281611036.

G. Cremonese, W.F. Huebner, H. Rauer, and D.C. Boice. Neutral sodium tails in comets. *Advances in Space Research*, 29(8):1187–1197, April 2002. doi: 10.1016/s0273-1177(02)00136-9. URL https://doi.org/10.1016/s0273-1177(02)00136-9.

J. Crovisier. The photodissociation of water in cometary atmospheres. *A&A*, 213(1-2):459–464, Apr 1989.

J. Crovisier, K. Leech, D. Bockelee-Morvan, T. Y. Brooke, M. S. Hanner, B. Altieri, H. U. Keller, and E. Lellouch. The spectrum of Comet Hale-Bopp (C/1995 01) observed with the Infrared Space Observatory at 2.9 AU from the Sun. 275:1904–1907, March 1997. doi: 10.1126/science.275.5308.1904.

J. Crovisier, P. Colom, E. Gérard, D. Bockelée-Morvan, and G. Bourgois. Observations at Nançay of the OH 18-cm lines in comets. The data base. Observations made from 1982 to 1999. *A&A*, 393:1053–1064, October 2002. doi: 10.1051/0004-6361:20020673.

Björn JR Davidsson. Tidal splitting and rotational breakup of solid biaxial ellipsoids. *Icarus*, 149(2):375–383, 2001.

Julia de León, Javier Licandro, Miquel Serra-Ricart, Antonio Cabrera-Lavers, Joan Font Serra, Riccardo Scarpa, Carlos de la Fuente Marcos, and Raúl de la Fuente Marcos. Interstellar visitors: A physical characterization of comet c/2019 q4 (borisov) with OSIRIS at the 10.4 m GTC. *Research Notes of the AAS*, 3(9):131, sep 2019. doi: 10.3847/2515-5172/ab449c. URL https://doi.org/10.3847%2F2515-5172%2Fab449c.

M de Val-Borro, L Rezac, P Hartogh, N Biver, D Bockelée-Morvan, J Crovisier, M Küppers, DC Lis, S Szutowicz, GA Blake, et al. An upper limit for the water outgassing rate of the main-belt comet 176p/linear observed with herschel/hifi. *Astronomy & Astrophysics*, 546: L4, 2012.

A. Decock, E. Jehin, D. Hutsemékers, and J. Manfroid. Forbidden oxygen lines in comets at various heliocentric distances. *A&A*, 555:A34, July 2013. doi: 10.1051/0004-6361/201220414.

A. Decock, E. Jehin, P. Rousselot, D. Hutsemékers, J. Manfroid, S. Raghuram, A. Bhardwaj, and B. Hubert. Forbidden oxygen lines at various nucleocentric distances in comets. *A&A*, 573:A1, January 2015. doi: 10.1051/0004-6361/201424403.

H. Dekker, S. D'Odorico, A. Kaufer, B. Delabre, and H. Kotzlowski. Design, construction, and performance of UVES, the echelle spectrograph for the UT2 Kueyen Telescope at the ESO Paranal Observatory. In M. Iye and A. F. Moorwood, editors, *Optical and IR Telescope Instrumentation and Detectors*, volume 4008 of *Procceding of SPIE*, pages 534–545, August 2000. doi: 10.1117/12.395512.

N. Dello Russo, R. J. Vervack, H. A. Weaver, N. Biver, D. Bockelée-Morvan, J. Crovisier, and C. M. Lisse. Compositional homogeneity in the fragmented comet 73P/Schwassmann-Wachmann 3. *Nature*, 448(7150):172–175, July 2007. doi: 10.1038/nature05908.

N. Dello Russo, H. Kawakita, R. J. Vervack, and H. A. Weaver. Emerging trends and a comet taxonomy based on the volatile chemistry measured in thirty comets with high-resolution infrared spectroscopy between 1997 and 2013. 278:301–332, November 2016. doi: 10.1016/j.icarus.2016.05.039.

Emmanuel Desvoivres. Modélisation de la dynamique des fragments cométaires: Application à la comète c/1996 b2 hyakutake, 1999.

M. A. DiSanti, B. P. Bonev, G. L. Villanueva, and M. J. Mumma. HIGHLY DEPLETED ETHANE AND MILDLY DEPLETED METHANOL IN COMET 21p/GIACOBINI-ZINNER: APPLICATION OF a NEW EMPIRICAL 2-BAND MODEL FOR CH3oh NEAR 50 k. *The Astrophysical Journal*, 763(1):1, December 2012. doi: 10.1088/0004-637x/763/1/1. URL https://doi.org/10.1088/0004-637x/763/1/1.

Michael A. DiSanti, Boncho P. Bonev, Neil Dello Russo, Ronald J. Vervack Jr., Erika L. Gibb, Nathan X. Roth, Adam J. McKay, Hideyo Kawakita, Lori M. Feaga, and Harold A. Weaver. Hypervolatiles in a jupiter-family comet: Observations of 45p/honda–mrkos–pajdušáková using ishell at the nasa-irtf. *The Astronomical Journal*, 154(6):246, 2017. URL http://stacks.iop.org/1538-3881/154/i=6/a=246.

N. Divine. A simple radiation model of cometary dust for P/Halley. In B. Battrick and E. Swallow, editors, *The Comet Halley. Dust and Gas Environment*, volume 174 of *ESA Special Publication*, November 1981.

G. B. Donati. Schreiben des Herrn Prof. Donati an den Herausgeber. *Astronomische Nachrichten*, 62:375, August 1864.

Garrett Dorman, Donna M. Pierce, and Anita L. Cochran. THE SPATIAL DISTRIBUTION OF c2, c3, AND NH IN COMET 2p/ENCKE. *The Astrophysical Journal*, 778(2):140, November 2013. doi: 10.1088/0004-637x/778/2/140. URL https://doi.org/10.1088/0004-637x/778/2/140.

M. Drahus and W. Waniak. Non-constant rotation period of Comet C/2001 K5 (LINEAR). *Icarus*, 185:544–557, December 2006. doi: 10.1016/j.icarus.2006.06.010.

Michal Drahus, Piotr Guzik, Andrew Stephens, Steve B. Howell, Stanislaw Zola, Mikolaj Sabat, and Daniel E. Reichart. Rotation of Comet C/2020 F3 (NEOWISE). *The Astronomer's Telegram*, 13945:1, August 2020.

P. Eberhardt and D. Krankowsky. The electron temperature in the inner coma of comet P/Halley. *A&A*, 295:795, March 1995.

A. Egal, P. Wiegert, P. G. Brown, D. E. Moser, M. Campbell-Brown, A. Moorhead, S. Ehlert, and N. Moticska. Meteor shower modeling: Past and future Draconid outbursts. *Icarus*, 330: 123–141, Sep 2019. doi: 10.1016/j.icarus.2019.04.021.

N. R. Erickson, R. L. Snell, R. B. Loren, L. Mundy, and R. L. Plambeck. Detection of interstellar CO/+/ toward OMC-1. *Apj*, 245:L83–L86, April 1981. doi: 10.1086/183528.

S. Faggi, M. J. Mumma, G. L. Villanueva, L. Paganini, and M. Lippi. Quantifying the evolution of molecular production rates of comet 21p/giacobini–zinner with iSHELL/NASA-IRTF. *The Astronomical Journal*, 158(6):254, December 2019. doi: 10.3847/1538-3881/ab4f6e. URL https://doi.org/10.3847/1538-3881/ab4f6e.

S. Faggi, M. Mumma, G. Villanueva, and M. Lippi. The Unique Passage of Comet C/2020 F3 (NEOWISE): Deep Investigations of its Organic and Isotopic Composition as Revealed by iSHELL at NASA/IRTF. In *AAS/Division for Planetary Sciences Meeting Abstracts*, volume 52 of *AAS/Division for Planetary Sciences Meeting Abstracts*, page 111.01, October 2020.

U. Fano. Quantum defect theory of l uncoupling in h_2 as an example of channel-interaction treatment. *Phys. Rev.*, 15:817, 1970.

T Farnham and D Schleicher. Physical and compositional studies of comet 81p/wild 2 at multiple apparitions. *Icarus*, 173(2):533–558, February 2005. doi: 10.1016/j.icarus.2004.08.021. URL https://doi.org/10.1016/j.icarus.2004.08.021.

T. L. Farnham and D. G. Schleicher. Narrowband photometric results for comet 46P/Wirtanen. 335:L50–L55, July 1998.

T. L. Farnham, D. G. Schleicher, and M. F. A'Hearn. The HB Narrowband Comet Filters: Standard Stars and Calibrations. *Icarus*, 147:180–204, September 2000. doi: 10.1006/icar.2000.6420.

T. L. Farnham, N. H. Samarasinha, B. E. A. Mueller, and M. M. Knight. Cyanogen Jets and the Rotation State of Comet Machholz (C/2004 Q2). *AJ*, 133:2001–2007, May 2007. doi: 10.1086/513186.

T. L. Farnham, MM Knight, N Eisner, DG Schleicher, and A Thirouin. Comet 41p/tuttle-giacobini-kresák. *CBET*, 4375, 2017.

Tony L. Farnham, Matthew M. Knight, David G. Schleicher, Lori M. Feaga, Dennis Bodewits, Brian A. Skiff, and Josephine Schindler. Narrowband Observations of Comet 46P/Wirtanen During Its Exceptional Apparition of 2018/19 I: Apparent Rotation Period and Outbursts. *arXiv e-prints*, art. arXiv:2012.01291, December 2020.

R. Farquhar. ISEE-3 - A late entry in the great comet chase. *Astronautics Aeronautics*, 21:50–55, September 1983.

P. D. Feldman. A model of carbon production in a cometary coma. *A&A*, 70:547–553, November 1978.

P. D. Feldman, S. A. Budzien, M. C. Festou, M. F. A'Hearn, and G. P. Tozzi. Ultraviolet and visible variability of the coma of Comet Levy (1990c). *Icarus*, 95:65–72, January 1992. doi: 10.1016/0019-1035(92)90191-9.

J. A. Fernández and A. Sosa. Jupiter family comets in near-Earth orbits: Are some of them interlopers from the asteroid belt? *planss*, 118:14–24, December 2015. doi: 10.1016/j.pss.2015.07.010.

Julio A. Fernández and Andrea Sosa. Jupiter family comets in near-earth orbits: Are some of them interlopers from the asteroid belt? *Planetary and Space Science*, 118:14–24, December 2015. doi: 10.1016/j.pss.2015.07.010. URL https://doi.org/10.1016/j.pss.2015.07.010.

Y. R. Fernandez, C. M. Lisse, M. F. A'Hearn, H. U. Kaufl, E. Grun, and S. B. Peschke. Nucleus and Dust Coma of Comet 2P/Encke. In *AAS/Division for Planetary Sciences Meeting Abstracts 30*, volume 30 of *Bulletin of the American Astronomical Society*, page 1095, September 1998.

Y. R. Fernández, M. S. Kelley, P. L. Lamy, I. Toth, O. Groussin, C. M. Lisse, M. F. A'Hearn, J. M. Bauer, H. Campins, A. Fitzsimmons, J. Licand ro, S. C. Lowry, K. J. Meech, J. Pittichová, W. T. Reach, C. Snodgrass, and H. A. Weaver. Thermal properties, sizes, and size distribution of Jupiter-family cometary nuclei. *Icarus*, 226(1):1138–1170, Sep 2013. doi: 10.1016/j.icarus.2013.07.021.

M. C. Festou. The density distribution of neutral compounds in cometary atmospheres. I - Models and equations. *A&A*, 95:69–79, February 1981a.

M. C. Festou. The density distribution of neutral compounds in cometary atmospheres. II - Production rate and lifetime of OH radicals in Comet Kobayashi-Berger-Milon /1975 IX/. *A&A*, 96:52–57, March 1981b.

M. C. Festou, H. U. Keller, and H. A. Weaver. *A brief conceptual history of cometary science*, pages 3–16. 2004.

U. Fink, M. D. Hicks, R. A. Fevig, and J. Collins. Spectroscopy of 46 P/Wirtanen during its 1997 apparition. *A&A*, 335:L37–L45, July 1998.

Uwe Fink. A taxonomic survey of comet composition 1985-2004 using CCD spectroscopy. *Icarus*, 201(1):311–334, May 2009. doi: 10.1016/j.icarus.2008.12.044.

Fink Uwe and M. D. Hicks. A survey of 39 comets using CCD spectroscopy. *ApJ*, 459:729–743, Mar 1996. doi: 10.1086/176938.

Alan Fitzsimmons, Olivier Hainaut, Karen Meech, Emmanuel Jehin, Youssef Moulane, Cyrielle Opitom, Bin Yang, Jacqueline V. Keane, Jan T. Kleyna, Marco Micheli, and Colin Snodgrass. Detection of CN gas in Interstellar Object 2I/Borisov. *arXiv e-prints*, art. arXiv:1909.12144, Sep 2019.

George J. Flynn. Interplanetary dust particles collected from the stratosphere: physical, chemical, and mineralogical properties and implications for their sources. *Planetary and Space Science*, 42(12):1151–1161, December 1994. doi: 10.1016/0032-0633(94)90014-0. URL https://doi.org/10.1016/0032-0633(94)90014-0.

S. Fornasier, P. H. Hasselmann, M. A. Barucci, C. Feller, S. Besse, C. Leyrat, L. Lara, P. J. Gutierrez, N. Oklay, C. Tubiana, F. Scholten, H. Sierks, C. Barbieri, P. L. Lamy, R. Rodrigo, D. Koschny, H. Rickman, H. U. Keller, J. Agarwal, M. F. A'Hearn, J.-L. Bertaux, I. Bertini, G. Cremonese, V. Da Deppo, B. Davidsson, S. Debei, M. De Cecco, M. Fulle, O. Groussin, C. Güttler, S. F. Hviid, W. Ip, L. Jorda, J. Knollenberg, G. Kovacs, R. Kramm, E. Kührt, M. Küppers, F. La Forgia, M. Lazzarin, J. J. Lopez Moreno, F. Marzari, K.-D. Matz, H. Michalik, F. Moreno, S. Mottola, G. Naletto, M. Pajola, A. Pommerol, F. Preusker, X. Shi, C. Snodgrass, N. Thomas, and J.-B. Vincent. Spectrophotometric properties of the nucleus of comet 67p/churyumov-gerasimenko from the OSIRIS instrument onboard the ROSETTA spacecraft. *Astronomy & Astrophysics*, 583:A30, October 2015. doi: 10.1051/0004-6361/201525901. URL https://doi.org/10.1051/0004-6361/201525901.

A. Fowler. Terrestrial reproduction of the spectra of the tails of recent comets : (plate 8.). *Monthly Notices of the Royal Astronomical Society*, 70(2):176–182, December 1909. doi: 10.1093/mnras/70.2.176. URL https://doi.org/10.1093/mnras/70.2.176.

J. L. Fox and A. Hac. Velocity distributions of c atoms in co+ dissociative recombination: Implications for photochemical escape of c from mars. *J. Geophys. Res.*, 104(37):24729, 1999. URL http://dx.doi.org/10.1029/1999JA900330.

N. Fray, Y. Bénilan, H. Cottin, M.-C. Gazeau, and J. Crovisier. The origin of the CN radical in comets: A review from observations and models. *Planetary and Space Science*, 53(12): 1243–1262, October 2005. doi: 10.1016/j.pss.2005.06.005. URL https://doi.org/10.1016/j.pss.2005.06.005.

W. Freudling, M. Romaniello, D. M. Bramich, P. Ballester, V. Forchi, C. E. García-Dabló, S. Moehler, and M. J. Neeser. Automated data reduction workflows for astronomy. The ESO Reflex environment. *A&A*, 559:A96, November 2013. doi: 10.1051/0004-6361/201322494.

A. Fuente and J. Martín-Pintado. Detection of co+ toward the reflection nebula ngc 7023. *The Astrophysical Journal Letters*, 477(2):L107, 1997. URL http://stacks.iop.org/1538-4357/477/i=2/a=L107.

S. A. Fuselier, E. G. Shelley, H. Balsiger, J. Geiss, B. E. Goldstein, R. Goldstein, and W. H. Ip. Cometary h2+ and solar wind he2+ dynamics across the halley cometopause. *Geophysical Research Letters*, 15(6):549–552, 1988. ISSN 1944-8007. doi: 10.1029/GL015i006p00549. URL http://dx.doi.org/10.1029/GL015i006p00549.

S. A. Fuselier, K. Altwegg, H. Balsiger, J. J. Berthelier, A. Beth, A. Bieler, C. Briois, T. W. Broiles, J. L. Burch, U. Calmonte, G. Cessateur, M. Combi, J. De Keyser, B. Fiethe, M. Galand, S. Gasc, T. I. Gombosi, H. Gunell, K. C. Hansen, M. Hässig, K. L. Heritier, A. Korth, L. Le Roy, A. Luspay-Kuti, U. Mall, K. E. Mandt, S. M. Petrinec, H. Rème, M. Rinaldi, M. Rubin, T. Sémon, K. J. Trattner, C.-Y. Tzou, E. Vigren, J. H. Waite, and P. Wurz. Ion chemistry in the coma of comet 67P near perihelion. *MNRAS*, 462:S67–S77, November 2016. doi: 10.1093/mnras/stw2149.

D. Galli, M. Walm ley, and J. Gonçalves. The structure and stability of molecular cloud cores in external radiation fields. *A&A*, 394(1):275–284, 2002. doi: 10.1051/0004-6361:20021125. URL https://doi.org/10.1051/0004-6361:20021125.

L. Gan and T. E. Cravens. Electron energetics in the inner coma of Comet Halley. *jgr*, 95: 6285–6303, May 1990. doi: 10.1029/JA095iA05p06285.

Neil Gehrels, Guido Chincarini, P Giommi, KO Mason, JA Nousek, AA Wells, NE White, SD Barthelmy, DN Burrows, LR Cominsky, et al. The swift gamma-ray burst mission. *The Astrophysical Journal*, 611(2):1005, 2004.

Michaël Gillon, Amaury H. M. J. Triaud, Brice-Olivier Demory, Emmanuël Jehin, Eric Agol, Katherine M. Deck, Susan M. Lederer, Julien de Wit, Artem Burdanov, James G. Ingalls, Emeline Bolmont, Jeremy Leconte, Sean N. Raymond, Franck Selsis, Martin Turbet, Khalid Barkaoui, Adam Burgasser, Matthew R. Burleigh, Sean J. Carey, Aleksander Chaushev, Chris M. Copperwheat, Laetitia Delrez, Catarina S. Fernandes, Daniel L. Holdsworth, Enrico J. Kotze, Valérie Van Grootel, Yaseen Almleaky, Zouhair Benkhaldoun, Pierre Magain, and Didier Queloz. Seven temperate terrestrial planets around the nearby ultracool dwarf star TRAPPIST-1. *Nature*, 542:456–460, February 2017. doi: 10.1038/nature21360.

A Giusti. A multichannel quantum defect approach to dissociative recombination. *Journal of Physics B: Atomic and Molecular Physics*, 13(19):3867, 1980. URL http://stacks.iop.org/0022-3700/13/i=19/a=025.

A Giusti-Suzor, J. N Bardsley, and Derkits. *Phys. Rev. A*, 28:682–691, 1983.

K.-H. Glassmeier, H. Boehnhardt, D. Koschny, E. Kührt, and I. Richter. The Rosetta Mission: Flying Towards the Origin of the Solar System. 128:1–21, February 2007. doi: 10.1007/s11214-006-9140-8.

T. I. Gombosi, D. L. De Zeeuw, R. M. Häberli, and K. G. Powell. Three-dimensional multiscale MHD model of cometary plasma environments. *jgr*, 101:15233–15252, July 1996. doi: 10.1029/96JA01075.

Rodney Gomes, Harold F Levison, Kleomenis Tsiganis, and Alessandro Morbidelli. Origin of the cataclysmic late heavy bombardment period of the terrestrial planets. *Nature*, 435(7041): 466, 2005.

D. W. E. Green. Comet C/2017 O1 (Asassn). *Central Bureau Electronic Telegrams*, 4426:1, Aug 2017.

Chris H. Greene and Ch. Jungene. Molecular applications of quantum defect theory. *Advances in Atomic and Molecular Physics*, 21:51 – 121, 1985. ISSN 0065-2199. doi: http://dx.doi.org/10.1016/S0065-2199(08)60141-4. URL http://www.sciencedirect.com/science/article/pii/S0065219908601414.

P. Gronkowski and M. Wesołowski. A Review of Cometary Outbursts at Large Heliocentric Distances. *Earth Moon and Planets*, 119(1):23–33, November 2016. doi: 10.1007/s11038-016-9497-y.

Samuel Gulkis, Mark Allen, Paul von Allmen, Gerard Beaudin, Nicolas Biver, Dominique Bockelée-Morvan, Mathieu Choukroun, Jacques Crovisier, Björn J. R. Davidsson, Pierre Encrenaz, Therese Encrenaz, Margaret Frerking, Paul Hartogh, Mark Hofstadter, Wing-Huen Ip, Michael Janssen, Christopher Jarchow, Stephen Keihm, Seungwon Lee, Emmanuel Lellouch, Cedric Leyrat, Ladislav Rezac, F. Peter Schloerb, and Thomas Spilker. Subsurface properties and early activity of comet 67P/Churyumov-Gerasimenko. *Science*, 347(6220): aaa0709, January 2015. doi: 10.1126/science.aaa0709.

Piotr Guzik, Michał Drahus, Krzysztof Rusek, Wacław Waniak, Giacomo Cannizzaro, and Inés Pastor-Marazuela. Interstellar comet C/2019 Q4 (Borisov). *arXiv e-prints*, art. arXiv:1909.05851, Sep 2019.

R. M. Häberli, K. Altwegg, H. Balsiger, and J. Geiss. Heating of the thermal electrons in the coma of comet P/Halley. *jgr*, 101:15579–15590, July 1996. doi: 10.1029/96JA01191.

Roman M. Häberli, Michael R. Combi, Tamas I. Gombosi, Darren L. De Zeeuw, and Kenneth G. Powell. Quantitative analysis of h2o+coma images using a multiscale mhd model with detailed ion chemistry. *Icarus*, 130(2):373 – 386, 1997. ISSN 0019-1035. doi: http://dx.doi.org/10.1006/icar.1997.5835.

S.A. Haider and Anil Bhardwaj. Radial distribution of production rates, loss rates and densities corresponding to ion masses $\leqslant$ 40 amu in the inner coma of comet halley: Composition and chemistry. *Icarus*, 177(1):196 – 216, 2005. ISSN 0019-1035. doi: http://doi.org/10.1016/j.icarus.2005.02.019. URL http://www.sciencedirect.com/science/article/pii/S0019103505000837.

E. Halley. A Proposal of a Method for Finding the Longitude at Sea within a Degree, or Twenty Leagues. By Dr. Edmund Halley, Astr. Reg. Vice-President of the Royal Society. With an Account of the Progress He Hath Made Therein, by a Continued Series of Accurate Observations of the Moon, Taken by Himself at the Royal Observatory at Greenwich. *Philosophical Transactions of the Royal Society of London Series I*, 37:185–195, 1731.

T. Hama and N. Watanabe. Surface processes on interstellar amorphous solid water: Adsorption, diffusion, tunneling reactions, and nuclear-spin conversion. *Chemical Review*, 113: 8783–8839, 2013.

T. Hama, N. Watanabe, A. Kouchi, and Yokoyama M. Spin temperature of water molecules desorbed from the surfaces of amorphous solid water, vapor-deposited and produced from photolysis of a ch4/o2 solid mixture. *The Astrophysical Journal Letters*, 738:L15, 2011.

Tetsuya Hama, Akira Kouchi, and Naoki Watanabe. Statistical ortho-to-para ratio of water desorbed from ice at 10 kelvin. *Science*, 351(6268):65–67, Jan 2016. doi: 10.1126/science.aad4026.

H. B. Hammel, R. F. Beebe, A. P. Ingersoll, G. S. Orton, J. R. Mills, A. A. Simon, P. Chodas, J. T. Clarke, E. de Jong, T. E. Dowling, J. Harrington, L. F. Huber, E. Karkoschka, C. M. Santori, A. Toigo, D. Yeomans, and R. A. West. HST Imaging of Atmospheric Phenomena Created by the Impact of Comet Shoemaker-Levy 9. *Science*, 267(5202):1288–1296, March 1995. doi: 10.1126/science.7871425.

M. S. Hanner and R. L. Newburn. Infrared photometry of comet wilson (1986l) at two epochs. *The Astrophysical Journal*, 97:254–261, January 1989. doi: 10.1086/114977.

MS Hanner, GJ Veeder, and AT Tokunaga. The dust coma of comet p/giacobini-zinner in the infrared. *The Astronomical Journal*, 104:386–393, 1992.

Paul Hartogh, Dariusz C. Lis, Dominique Bockelée-Morvan, Miguel de Val-Borro, Nicolas Biver, Michael Küppers, Martin Emprechtinger, Edwin A. Bergin, Jacques Crovisier, Miriam Rengel, Raphael Moreno, Slawomira Szutowicz, and Geoffrey A. Blake. Ocean-like water in the jupiter-family comet 103p/hartley 2. *Nature*, 478(7368):218–220, October 2011. doi: 10.1038/nature10519. URL https://doi.org/10.1038/nature10519.

L. Haser. Distribution d'intensité dans la tête d'une comète. *Bulletin de la Societe Royale des Sciences de Liege*, 43:740–750, 1957.

M. Hässig, K. Altwegg, H. Balsiger, J. J. Berthelier, A. Bieler, U. Calmonte, F. Dhooghe, B. Fiethe, S. A. Fuselier, S. Gasc, T. I. Gombosi, L. Le Roy, A. Luspay-Kuti, K. Mand t, M. Rubin, C. Y. Tzou, S. F. Wampfler, and P. Wurz. Isotopic composition of CO_2 in the coma of 67P/Churyumov-Gerasimenko measured with ROSINA/DFMS. *A&A*, 605:A50, Sep 2017. doi: 10.1051/0004-6361/201630140.

A. Heinze and A. Kadota. Comet 243P/NEAT. 4587:1, December 2018.

Julia Heisler. Monte carlo simulations of the oort comet cloud. *Icarus*, 88(1):104–121, November 1990. doi: 10.1016/0019-1035(90)90180-h. URL https://doi.org/10.1016/0019-1035(90)90180-h.

J. Helbert, H. Rauer, D. C. Boice, and W. F. Huebner. The chemistry of c2 and c3 in the coma of comet c/1995 o1 (hale-bopp) at heliocentric distances rh $\geq$ 2.9 AU. *Astronomy & Astrophysics*, 442(3):1107–1120, October 2005. doi: 10.1051/0004-6361:20041571. URL https://doi.org/10.1051/0004-6361:20041571.

G. H. Herbig. *Review of cometary spectra.*, volume 393, pages 136–158. 1976.

M. Hicks, R. Apitzsch, P. Birtwhistle, F. Hormuth, S. Gajdos, and A. Galad. Comet P/2003 S2 (NEAT). 8209:2, September 2003.

Y. Hillman and D. Prialnik. A quasi 3-D model of an outburst pattern that explains the behavior of Comet 17P/Holmes. 221:147–159, September 2012. doi: 10.1016/j.icarus.2012.07.014.

K. Hirao and T. Itoh. The planet-a halley encounters. *Nature*, 321(S6067):294–297, May 1986. doi: 10.1038/321294a0. URL https://doi.org/10.1038/321294a0.

P. Y. Ho. Ancient and mediaeval observations of comets and novae in Chinese sources. *Vistas in Astronomy*, 5:127–225, 1962. doi: 10.1016/0083-6656(62)90007-7.

Bryan J. Holler, Stefanie N. Milam, James M. Bauer, Charles Alcock, Michele T. Bannister, Gordon L. Bjoraker, Dennis Bodewits, Amanda S. Bosh, Marc W. Buie, Tony L. Farnham, Nader Haghighipour, Paul S. Hardersen, Alan W. Harris, Christopher M. Hirata, Henry H.

Hsieh, Michael S. P. Kelley, Matthew M. Knight, Emily A. Kramer, Andrea Longobardo, Conor A. Nixon, Ernesto Palomba, Silvia Protopapa, Lynnae C. Quick, Darin Ragozzine, Vishnu Reddy, Jason D. Rhodes, Andy S. Rivkin, Gal Sarid, Amanda A. Sickafoose, Amy A. Simon, Cristina A. Thomas, David E. Trilling, and Robert A. West. Solar system science with the Wide-Field Infrared Survey Telescope. *Journal of Astronomical Telescopes, Instruments, and Systems*, 4:034003, July 2018. doi: 10.1117/1.JATIS.4.3.034003.

Johan Holmberg, Chris Flynn, and Laura Portinari. The colours of the Sun. *MNRAS*, 367(2): 449–453, Apr 2006. doi: 10.1111/j.1365-2966.2005.09832.x.

Alexander Hölscher. *Formation of C3 and C2 in Cometary Comae*. PhD thesis, -, Mar 2015.

Henry H Hsieh, Bin Yang, Nader Haghighipour, Heather M Kaluna, Alan Fitzsimmons, Larry Denneau, Bojan Novaković, Robert Jedicke, Richard J Wainscoat, James D Armstrong, et al. Discovery of main-belt comet p/2006 vw139 by pan-starrs1. *The Astrophysical Journal Letters*, 748(1):L15, 2012a.

Henry H Hsieh, Bin Yang, Nader Haghighipour, Bojan Novaković, Robert Jedicke, Richard J Wainscoat, Larry Denneau, Shinsuke Abe, Wen-Ping Chen, Alan Fitzsimmons, et al. Observational and dynamical characterization of main-belt comet p/2010 r2 (la sagra). *The Astronomical Journal*, 143(5):104, 2012b.

Henry H. Hsieh, Heather M. Kaluna, Bojan Novaković, Bin Yang, Nader Haghighipour, Marco Micheli, Larry Denneau, Alan Fitzsimmons, Robert Jedicke, Jan Kleyna, Peter Vereš, Richard J. Wainscoat, Megan Ansdell, Garrett T. Elliott, Jacqueline V. Keane, Karen J. Meech, Nicholas A. Moskovitz, Timm E. Riesen, Scott S. Sheppard, Sarah Sonnett, David J. Tholen, Laurie Urban, Nick Kaiser, K. C. Chambers, William S. Burgett, Eugene A. Magnier, Jeffrey S. Morgan, and Paul A. Price. MAIN-BELT COMET p/2012 t1 (PANSTARRS). *The Astrophysical Journal*, 771(1):L1, jun 2013. doi: 10.1088/2041-8205/771/1/l1. URL https://doi.org/10.1088/2041-8205/771/1/l1.

W. F. Huebner and P. T. Giguere. A model of comet comae. II - Effects of solar photodissociative ionization. *ApJ*, 238:753–762, June 1980. doi: 10.1086/158033.

W. F. Huebner, D. C. Boice, H. U. Schmidt, and R. Wegmann. Structure of the coma - Chemistry and solar wind interaction. In R. L. Newburn, Jr., M. Neugebauer, and J. Rahe, editors, *IAU Colloq. 116: Comets in the post-Halley era*, volume 167 of *Astrophysics and Space Science Library*, pages 907–936, 1991.

William Huggins. Xxi. further observations on the spectra of some the stars and nebulæ, with an attempt to determine therefrom whether these bodies are moving towards or from the earth, also observations on the spectra of the sun and of comet ii., 1868. *Philosophical Transactions of the Royal Society of London*, 158:529–564, 1868. doi: 10.1098/rstl.1868.0022. URL https://royalsocietypublishing.org/doi/abs/10.1098/rstl.1868.0022.

Man-To Hui and Quan-Zhi Ye. Observations of Disintegrating Long-Period Comet C/2019 Y4 (ATLAS) – A Sibling of C/1844 Y1 (Great Comet). *arXiv e-prints*, art. arXiv:2004.10990, April 2020.

Fujio Hyodo, Soichiro Kusaka, David A. Wardle, and Marie-Charlotte Nilsson. Changes in stable nitrogen and carbon isotope ratios of plants and soil across a boreal forest fire chronosequence. *Plant and Soil*, 364(1):315–323, Mar 2013. ISSN 1573-5036. doi: 10.1007/s11104-012-1339-8. URL https://doi.org/10.1007/s11104-012-1339-8.

W.-H. Ip. An overview of gas phenomena in Comet Halley. *Advances in Space Research*, 5: 233–245, 1985. doi: 10.1016/0273-1177(85)90091-2.

W.-H. Ip and D. A. Mendis. The structure of cometary ionospheres. I - H2O dominated comets. *Icarus*, 28:389–400, July 1976. doi: 10.1016/0019-1035(76)90152-4.

Yukikazu Itikawa. Cross sections for electron collisions with carbon dioxide. *Journal of Physical and Chemical Reference Data*, 31(3):749–767, 2002. doi: 10.1063/1.1481879. URL http://dx.doi.org/10.1063/1.1481879.

E. Jehin, J. Manfroid, H. Kawakita, D. Hutsemékers, M. Weiler, C. Arpigny, A. Cochran, O. Hainaut, H. Rauer, R. Schulz, and J. M. Zucconi. Optical Spectroscopy of the B and C Fragments of Comet 73P/Schwassmann-Wachmann 3 at the ESO VLT. In *Asteroids, Comets, Meteors 2008*, volume 1405, page 8319, January 2008.

E. Jehin, J. Manfroid, D. Hutsemékers, C. Arpigny, and J.-M. Zucconi. Isotopic ratios in comets: Status and perspectives. *Earth, Moon, and Planets*, 105(2-4):167–180, June 2009. doi: 10.1007/s11038-009-9322-y. URL https://doi.org/10.1007/s11038-009-9322-y.

E. Jehin, J. Manfroid, D. Hutsemekers, M. Gillon, and P. Magain. Comet 103P/Hartley. *Central Bureau Electronic Telegrams*, 2589, December 2010.

E. Jehin, M. Gillon, D. Queloz, P. Magain, J. Manfroid, V. Chantry, M. Lendl, D. Hutsemékers, and S. Udry. TRAPPIST: TRAnsiting Planets and PlanetesImals Small Telescope. *The Messenger*, 145:2–6, September 2011.

D. Jewitt. Color Systematics of Comets and Related Bodies. 150:201, December 2015. doi: 10.1088/0004-6256/150/6/201.

D. C. Jewitt and K. J. Meech. Surface brightness profiles of 10 comets. *ApJ*, 317:992–1001, June 1987. doi: 10.1086/165347.

David Jewitt. Cometary rotation: An overview. *Earth, Moon, and Planets*, 79(1-3):35–53, 1997.

David Jewitt. THE ACTIVE ASTEROIDS. *The Astronomical Journal*, 143(3):66, February 2012. doi: 10.1088/0004-6256/143/3/66. URL https://doi.org/10.1088/0004-6256/143/3/66.

David Jewitt and Jane Luu. Discovery of the candidate kuiper belt object 1992 QB1. *Nature*, 362(6422):730–732, April 1993. doi: 10.1038/362730a0. URL https://doi.org/10.1038/362730a0.

David Jewitt and Jane Luu. Initial Characterization of Interstellar Comet 2I/2019 Q4 (Borisov). *arXiv e-prints*, art. arXiv:1910.02547, Oct 2019.

David Jewitt and Karen J. Meech. Cometary Grain Scattering versus Wavelength, or, "What Color Is Comet Dust?". *ApJ*, 310:937, Nov 1986. doi: 10.1086/164745.

David Jewitt, Bin Yang, and Nader Haghighipour. Main-belt comet p/2008 r1 (garradd). *The Astronomical Journal*, 137(5):4313, 2009.

David Jewitt, Jessica Agarwal, Jing Li, Harold Weaver, Max Mutchler, and Stephen Larson. Disintegrating asteroid p/2013 r3. *The astrophysical journal letters*, 784(1):L8, 2014.

David Jewitt, Jessica Agarwal, Nuno Peixinho, Harold Weaver, Max Mutchler, Man-To Hui, Jing Li, and Stephen Larson. NEW ACTIVE ASTEROID 313p/GIBBS. *The Astronomical Journal*, 149(2):81, jan 2015. doi: 10.1088/0004-6256/149/2/81. URL https://doi.org/10.1088/0004-6256/149/2/81.

David Jewitt, Man-To Hui, Max Mutchler, Harold Weaver, Jing Li, and Jessica Agarwal. A comet active beyond the crystallization zone. *The Astrophysical Journal*, 847(2):L19, sep 2017. doi: 10.3847/2041-8213/aa88b4. URL https://doi.org/10.3847%2F2041-8213%2Faa88b4.

David Jewitt, Jessica Agarwal, Man-To Hui, Jing Li, Max Mutchler, and Harold Weaver. Distant comet c/2017 k2 and the cohesion bottleneck. *The Astronomical Journal*, 157(2):65, jan 2019. doi: 10.3847/1538-3881/aaf38c. URL https://doi.org/10.3847%2F1538-3881%2Faaf38c.

Geraint H. Jones, Qasim Afghan, and Oliver Price. Prospects for the In Situ detection of Comet C/2019 Y4 ATLAS by Solar Orbiter. *Research Notes of the American Astronomical Society*, 4(5):62, May 2020. doi: 10.3847/2515-5172/ab8fa6.

L. Jorda, R. Gaskell, C. Capanna, S. Hviid, P. Lamy, J. Ďurech, G. Faury, O. Groussin, P. Gutiérrez, C. Jackman, S.J. Keihm, H.U. Keller, J. Knollenberg, E. Kührt, S. Marchi, S. Mottola, E. Palmer, F.P. Schloerb, H. Sierks, J.-B. Vincent, M.F. A'Hearn, C. Barbieri, R. Rodrigo, D. Koschny, H. Rickman, M.A. Barucci, J.L. Bertaux, I. Bertini, G. Cremonese, V. Da Deppo, B. Davidsson, S. Debei, M. De Cecco, S. Fornasier, M. Fulle, C. Güttler, W.-H. Ip, J.R. Kramm, M. Küppers, L.M. Lara, M. Lazzarin, J.J. Lopez Moreno, F. Marzari, G. Naletto, N. Oklay, N. Thomas, C. Tubiana, and K.-P. Wenzel. The global shape, density and rotation of comet 67p/churyumov-gerasimenko from preperihelion rosetta/OSIRIS observations. *Icarus*, 277:257–278, October 2016. doi: 10.1016/j.icarus.2016.05.002. URL https://doi.org/10.1016/j.icarus.2016.05.002.

L. Jorda, R. Gaskell, C. Capanna, S. Hviid, P. Lamy, J. Ďurech, G. Faury, O. Groussin, P. Gutiérrez, C. Jackman, S. J. Keihm, H. U. Keller, J. Knollenberg, E. Kührt, S. Marchi, S. Mottola, E. Palmer, F. P. Schloerb, H. Sierks, J.-B. Vincent, M. F. A'Hearn, C. Barbieri, R. Rodrigo, D. Koschny, H. Rickman, M. A. Barucci, J. L. Bertaux, I. Bertini, G. Cremonese, V. Da Deppo, B. Davidsson, S. Debei, M. De Cecco, S. Fornasier, M. Fulle, C. Güttler, W.-H. Ip, J. R. Kramm, M. Küppers, L. M. Lara, M. Lazzarin, J. J. Lopez Moreno, F. Marzari, G. Naletto, N. Oklay, N. Thomas, C. Tubiana, and K.-P. Wenzel. The global shape, density and rotation of Comet 67P/Churyumov-Gerasimenko from preperihelion Rosetta/OSIRIS observations. 277:257–278, October 2016. doi: 10.1016/j.icarus.2016.05.002.

Laurent Jorda. Le paramètre afp- traceur de l'activité cométaire. *personnal communication*, 2010.

C Jungen and O Atabek. Dissociative recombination and vibrational excitation of co + : model calculations and comparison with experiment. *J. Chem. Phys.*, 66:5584, 1977.

Theodore Kareta, Jennifer Andrews, John W. Noonan, Walter M. Harris, Nathan Smith, Patrick O'Brien, Benjamin N. L. Sharkey, Vishnu Reddy, Alessondra Springmann, Cassandra Lejoly, Lunar, Planetary Laboratory, :, and Steward Observatory. Carbon Chain Depletion of 2I/Borisov. *arXiv e-prints*, art. arXiv:1910.03222, Oct 2019.

Hideyo Kawakita and Michael J. Mumma. FLUORESCENCE EXCITATION MODELS OF AMMONIA AND AMIDOGEN RADICAL (NH2) IN COMETS: APPLICATION TO

COMET c/2004 q2 (MACHHOLZ). *The Astrophysical Journal*, 727(2):91, January 2011. doi: 10.1088/0004-637x/727/2/91. URL https://doi.org/10.1088/0004-637x/727/2/91.

Hideyo Kawakita and Junchi Watanabe. NH2and its parent molecule in the inner coma of comet hyakutake (c/1996 b2). *The Astrophysical Journal*, 495(2):946–950, March 1998. doi: 10.1086/305318. URL https://doi.org/10.1086/305318.

H. U. Keller, C. Arpigny, C. Barbieri, R. M. Bonnet, S. Cazes, M. Coradini, C. B. Cosmovici, W. A. Delamere, W. F. Huebner, D. W. Hughes, C. Jamar, D. Malaise, H. J. Reitsema, H. U. Schmidt, W. K. H. Schmidt, P. Seige, F. L. Whipple, and K. Wilhelm. First Halley Multicolour Camera imaging results from Giotto. 321:320–326, May 1986. doi: 10.1038/321320a0.

HU Keller, S Mottola, Y Skorov, and L Jorda. The changing rotation period of comet 67p/churyumov-gerasimenko controlled by its activity. *Astronomy & Astrophysics*, 579:L5, 2015.

M. S. P. Kelley, D. Bodewits, and Q. Z. Ye. Comet 64P/Swift-Gehrels. *Central Bureau Electronic Telegrams*, 4544:1, August 2018.

Michael S. P. Kelley, Dennis Bodewits, Quanzhi Ye, Tomás Ahumada, John Cromer, Richard Dekany, George Helou, Russ R. Laher, Frank J. Masci, Chow-Choong Ngeow, Ben Rusholme, and David L. Shupe. Outbursts at Comets 46P/Wirtanen, 64P/Swift-Gehrels, and 78P/Gehrels 2 in 2018. *Research Notes of the American Astronomical Society*, 3(9):126, September 2019a. doi: 10.3847/2515-5172/ab3fb4.

Michael S. P. Kelley, Tim Lister, and Dennis Bodewits. Small Apparent Outburst of Comet 123P/West-Hartley. *The Astronomer's Telegram*, 12380:1, January 2019b.

S. Kikuchi. Linear polarimetry of five comets. *Journal of Quantitative Spectroscopy and Radiative Transfer*, 100(1-3):179–186, July 2006. doi: 10.1016/j.jqsrt.2005.11.036. URL https://doi.org/10.1016/j.jqsrt.2005.11.036.

J. K. Kim and W. T. Huntress. Ion cyclotron resonance studies on the reaction of h2+ and d2+ ions with various simple molecules and hydrocarbons. *The Journal of Chemical Physics*, 62, 1975. URL http://dx.doi.org/10.1063/1.430817.

M. Kimura, J.-P. Gu, G. Hirsch, R. J. Buenker, and P. C. Stancil. Electron capture in collisions of protons with CO molecules in the keV region: The steric effect. *pra*, 61(3):032708, March 2000. doi: 10.1103/PhysRevA.61.032708.

Nikolai N Kiselev, Klaus Jockers, Vera K Rosenbush, Fedor P Velichko, Tanyu Bonev, and Nikolai Karpov. Anomalous wavelength dependence of polarization of comet 21p/giacobini-zinner. *Planetary and Space Science*, 48(10):1005–1009, 2000.

M. M. Knight and D. G. Schleicher. Observations of comet 252P/LINEAR during its historically close approach to Earth in 2016 from Lowell Observatory. In *AAS/Division for Planetary Sciences Meeting Abstracts 48*, volume 48 of *AAS/Division for Planetary Sciences Meeting Abstracts*, page 217.02, October 2016.

M. M. Knight, B. E. A. Mueller, N. H. Samarasinha, and D. G. Schleicher. A Further Investigation of Apparent Periodicities and the Rotational State of Comet 103P/Hartley 2 from Combined Coma Morphology and Light Curve Data Sets. *AJ*, 150:22, July 2015. doi: 10.1088/0004-6256/150/1/22.

Matthew M Knight and David G Schleicher. Cn morphology studies of comet 103p/hartley 2. *The Astronomical Journal*, 141(6):183, 2011.

MM Knight, N Eisner, DG Schleicher, and A Thirouin. Comet 41p/tuttle-giacobini-kresák. *CBET*, 4377, 2017.

H. Kobayashi, H. Kawakita, M. J. Mumma, B. P. Bonev, J.-i. Watanabe, and T. Fuse. Organic Volatiles in Comet 73P-B/Schwassmann-Wachmann 3 Observed during Its Outburst: A Clue to the Formation Region of the Jupiter-Family Comets. 668:L75–L78, October 2007. doi: 10.1086/522586.

Hitomi Kobayashi and Hideyo Kawakita. Water Production Rate of the Jupiter-Family Comet 46P/Wirtanen in the 2008 Apparition with the Subaru Telescope/IRCS. , 62:1025, August 2010. doi: 10.1093/pasj/62.4.1025.

Viatcheslav Kokoouline and Chris H Greene. Theoretical study of the h3+ ion dissociative recombination process. *Journal of Physics: Conference Series*, 4(1):74, 2005. URL http://stacks.iop.org/1742-6596/4/i=1/a=010.

I. Konno and S. Wyckoff. Atomic and molecular abundances in Comet Giacobini-Zinner. *Advances in Space Research*, 9:163–168, 1989. doi: 10.1016/0273-1177(89)90256-1.

A. Korosmezey, T. E. Cravens, A. F. Nagy, T. I. Gombosi, and D. A. Mendis. A new model of cometary ionospheres. *jgr*, 92:7331–7340, July 1987.

D. Krankowsky, P. Lämmerzahl, D. Dörflinger, I. Herrwerth, U. Stubbemann, J. Woweries, P. Eberhardt, U. Dolder, J. Fischer, U. Herrmann, H. Hofstetter, M. Jungck, F. O. Meier, W. Schulte, J. J. Berthelier, J. M. Illiano, M. Godefroy, G. Gogly, P. Thévenet, J. H. Hoffman, R. R. Hodges, and W. W. Wright. The Giotto Neutral Mass Spectrometer. In *ESA Special Publication*, volume 1070 of *ESA Special Publication*, pages 109–128, 1986.

L. Kresak and M. Kresakova. The real dispersion of orbital periods in meteor streams. *Bulletin of the Astronomical Institutes of Czechoslovakia*, 25:336–344, 1974.

M Królikowska, G Sitarski, and S Szutowicz. Forced precession models for six erratic comets. *Astronomy & Astrophysics*, 368(2):676–688, 2001.

G. W. Kronk. 41P/Tuttle–Giacobini–Kresak. *Gary W. Kronk's Cometography*, 2017.

I.-L. Lai, W.-H. Ip, J.-C. Lee, Z.-Y. Lin, J.-B. Vincent, N. Oklay, H. Sierks, C. Barbieri, P. Lamy, R. Rodrigo, D. Koschny, H. Rickman, H. U. Keller, J. Agarwal, M. A. Barucci, J.-L. Bertaux, I. Bertini, D. Bodewits, S. Boudreault, G. Cremonese, V. Da Deppo, B. Davidsson, S. Debei, M. De Cecco, J. Deller, S. Fornasier, M. Fulle, O. Groussin, P. J. Gutiérrez, C. Güttler, M. Hofmann, S. F. Hviid, L. Jorda, J. Knollenberg, G. Kovacs, J.-R. Kramm, E. Kührt, M. Küppers, L. M. Lara, M. Lazzarin, J. J. López-Moreno, F. Marzari, G. Naletto, X. Shi, C. Tubiana, and N. Thomas. Seasonal variations in source regions of the dust jets on comet 67p/churyumov-gerasimenko. *Astronomy & Astrophysics*, 630:A17, September 2019. doi: 10.1051/0004-6361/201732094. URL https://doi.org/10.1051/0004-6361/201732094.

P. L. Lamy, I. Toth, L. Jorda, H. A. Weaver, and M. A'Hearn. The nucleus and inner coma of Comet 46P/Wirtanen. *A&A*, 335:L25–L29, July 1998.

P. L. Lamy, I. Toth, M. F. A'Hearn, and H. A. Weaver. Hubble Space Telescope Observations of the Nucleus of Comet 45P/Honda-Mrkos-Pajdusakova and Its Inner Coma. *Icarus*, 140: 424–438, August 1999. doi: 10.1006/icar.1999.6153.

P. L. Lamy, I. Toth, Y. R. Fernandez, and H. A. Weaver. *The sizes, shapes, albedos, and colors of cometary nuclei*, pages 223–264. 2004a.

P. L. Lamy, I. Toth, Y. R. Fernandez, and H. A. Weaver. The sizes, shapes, albedos, and colors of cometary nuclei. In M. C. Festou, H. U. Keller, and H. A. Weaver, editors, *Comets II*, pages 223–264. Univ. Arizona Press, Tucson, AZ, 2004b.

Laura E. Langland-Shula and Graeme H. Smith. Comet classification with new methods for gas and dust spectroscopy. *Icarus*, 213(1):280–322, May 2011. doi: 10.1016/j.icarus.2011.02.007. URL https://doi.org/10.1016/j.icarus.2011.02.007.

Laura E. Langland-Shula and Graeme H. Smith. Comet classification with new methods for gas and dust spectroscopy. *Icarus*, 213(1):280–322, May 2011. doi: 10.1016/j.icarus.2011.02.007.

L-M Lara, J Licandro, A Oscoz, and V Motta. Behaviour of comet 21p/giacobini-zinner during the 1998 perihelion. *Astronomy & Astrophysics*, 399(2):763–772, 2003.

M. Larsson, W. D. Geppert, and G Nyman. Ion chemistry in space. *Reports on Progress in Physics*, 75(6):066901, 2012. URL http://stacks.iop.org/0034-4885/75/i=6/a=066901.

W. B. Latter, C. K. Walker, and P. R. Maloney. Detection of the Carbon Monoxide Ion (CO +) in the Interstellar Medium and a Planetary Nebula. *ApJL*, 419:L97, December 1993. doi: 10.1086/187146.

C. M. Lee and K. T. Lu. A multichannel quantum defect approach to dissociative recombination. *Phys. Rev.*, 8:1241, 1973.

Elia M Leibowitz and Noah Brosch. Periodic photmmetric variations in the near-nucleus zone of p/giacobini-zinner. *Icarus*, 68(3):430–441, 1986.

MM Lejoly and N Howell. Comet 45p/honda-mrkos-pajdušáková. *CBET*, 4357, 2017.

H. F. Levison. *Comet Taxonomy*, volume 107 of *Astronomical Society of the Pacific Conference Series*, pages 173–191. 1996.

Harold F. Levison and Martin J. Duncan. The Long-Term Dynamical Behavior of Short-Period Comets. *Icarus*, 108(1):18–36, March 1994. doi: 10.1006/icar.1994.1039.

J.-Y. Li, N. H. Samarasinha, M. S. P. Kelley, D. Farnocchia, M. J. Mutchler, Y. Ren, X. Lu, D. J. Tholen, T. Lister, and M. Micheli. The Implications of the Excited Rotation of Comet 252P/2000 G1 (LINEAR). volume 231 of *American Astronomical Society Meeting Abstracts*, page 115.07, January 2018.

Jian-Yang Li, Michael S. P. Kelley, Nalin H. Samarasinha, Davide Farnocchia, Max J. Mutchler, Yanqiong Ren, Xiaoping Lu, David J. Tholen, Tim Lister, and Marco Micheli. The unusual apparition of comet 252p/2000 g1 (linear) and comparison with comet p/2016 ba 14 (panstarrs). *The Astronomical Journal*, 154(4):136, 2017. URL http://stacks.iop.org/1538-3881/154/i=4/a=136.

J Licandro, H Campins, GP Tozzi, J De Léon, N Pinilla-Alonso, H Boehnhardt, and OR Hainaut. Testing the comet nature of main belt comets. the spectra of 133p/elst-pizarro and 176p/linear. *Astronomy & Astrophysics*, 532:A65, 2011.

Hsing Wen Lin, Chien-Hsiu Lee, David W. Gerdes, Fred C. Adams, Juliette Becker, Kevin Napier, and Larissa Markwardt. Low Resolution Optical Spectra and Diatomic Carbon Detections of 2I/Borisov. *arXiv e-prints*, art. arXiv:1912.06161, Dec 2019.

Zhong-Yi Lin, Chiahui Wang, Wing-Huen Ip, Kuo-Pin Huang, Chi-Sheng Lin, Hsiang-Yao Hsiao, Wei-Jir Hou, and Hung-Chin Lin. The Sodium Emission of comet C/2020 F3 (NEOWISE) observed at KenTing and Lulin observatory. *The Astronomer's Telegram*, 13886:1, July 2020.

D. C. Lis, N. Biver, D. Bockelée-Morvan, P. Hartogh, E. A. Bergin, G. A. Blake, J. Crovisier, M. de Val-Borro, E. Jehin, M. Küppers, J. Manfroid, R. Moreno, M. Rengel, and S. Szutowicz. AHERSCHELSTUDY OF d/h IN WATER IN THE JUPITER-FAMILY COMET 45p/HONDA-MRKOS-PAJDUšáKOVá AND PROSPECTS FOR d/h MEASUREMENTS WITH CCAT. *The Astrophysical Journal*, 774(1):L3, August 2013. doi: 10.1088/2041-8205/774/1/l3. URL https://doi.org/10.1088/2041-8205/774/1/l3.

Dariusz C. Lis, Dominique Bockelée-Morvan, Rolf Güsten, Nicolas Biver, Jürgen Stutzki, Yan Delorme, Carlos Durán, Helmut Wiesemeyer, and Yoko Okada. Terrestrial deuterium-to-hydrogen ratio in water in hyperactive comets. *Astronomy & Astrophysics*, 625:L5, May 2019. doi: 10.1051/0004-6361/201935554. URL https://doi.org/10.1051/0004-6361/201935554.

Dariusz C. Lis, Dominique Bockelée-Morvan, Rolf Güsten, Nicolas Biver, Jürgen Stutzki, Yan Delorme, Carlos Durán, Helmut Wiesemeyer, and Yoko Okada. Terrestrial deuterium-to-hydrogen ratio in water in hyperactive comets. *A&A*, 625:L5, May 2019. doi: 10.1051/0004-6361/201935554.

D. A. Little, K. Chakrabarti, J. Zs. Mezei, I. F. Schneider, and J. Tennyson. Dissociative recombination of n_2^+: An ab initio study. *Phys. Rev. A*, 90:052705, Nov 2014. doi: 10.1103/PhysRevA.90.052705. URL https://link.aps.org/doi/10.1103/PhysRevA.90.052705.

J López-Patiño, BE Fuentes, FB Yousif, and H Martínez. Ionization and electron capture for h+ collisions with co at low kev energy. *Physics Procedia*, 90:391–398, 2017.

S. C. Lowry, A. Fitzsimmons, and S. Collander-Brown. CCD photometry of distant comets. III. Ensemble properties of Jupiter-family comets. *A&A*, 397:329–343, January 2003. doi: 10.1051/0004-6361:20021486.

J. Luu and D. Jewitt. The nucleus of Comet P/Encke. *Icarus*, 86:69–81, July 1990. doi: 10.1016/0019-1035(90)90199-J.

A. Mainzer, J. Bauer, T. Grav, J. Masiero, R. M. Cutri, J. Dailey, P. Eisenhardt, R. S. McMillan, E. Wright, R. Walker, R. Jedicke, T. Spahr, D. Tholen, R. Alles, R. Beck, H. Brandenburg, T. Conrow, T. Evans, J. Fowler, T. Jarrett, K. Marsh, F. Masci, H. McCallon, S. Wheelock, M. Wittman, P. Wyatt, E. DeBaun, G. Elliott, D. Elsbury, T. Gautier, IV, S. Gomillion, D. Leisawitz, C. Maleszewski, M. Micheli, and A. Wilkins. Preliminary Results from NEOWISE: An Enhancement to the Wide-field Infrared Survey Explorer for Solar System Science. 731:53, April 2011. doi: 10.1088/0004-637X/731/1/53.

J. Manfroid, E. Jehin, D. Hutsemékers, A. Cochran, J. M. Zucconi, C. Arpigny, R. Schulz, J. A. Stüwe, and I. Ilyin. The CN isotopic ratios in comets. *A&A*, 503(2):613–624, Aug 2009. doi: 10.1051/0004-6361/200911859.

Jean Manfroid, Damien Hutsemékers, Emmanuël Jehin, Anita L. Cochran, Claude Arpigny, William M. Jackson, Karen J. Meech, Rita Schulz, and Jean-Marc Zucconi. The impact and rotational light curves of comet 9p/tempel 1. *Icarus*, 191(2, Supplement):348 – 359, 2007. ISSN 0019-1035. doi: https://doi.org/10.1016/j.icarus.2006.08.033. URL http://www.

sciencedirect.com/science/article/pii/S0019103507004149. Deep Impact at Comet Tempel 1.

M. L. Marconi and D. A. Mendis. On the ammonia abundance in the coma of Halley's Comet. *ApJ*, 330:513–517, July 1988. doi: 10.1086/166488.

J. N. Marcus. Forward-Scattering Enhancement of Comet Brightness. I. Background and Model. *International Comet Quarterly*, 29:39–66, April 2007.

D. Marshall, L. Rezac, P. Hartogh, Y. Zhao, and N. Attree. Interpretation of heliocentric water production rates of comets. *Astronomy & Astrophysics*, 623:A120, March 2019. doi: 10.1051/0004-6361/201833959. URL https://doi.org/10.1051/0004-6361/201833959.

M. Patrick Martin, Nalin Samarasinha, and Stephen Larson. Cometcief: A web-based image enhancement facility to digitally enhance images of cometary comae. *Planetary and Space Science*, 118:181 – 186, 2015. ISSN 0032-0633.

E. Mazzotta Epifani, P. Palumbo, M. T. Capria, G. Cremonese, M. Fulle, and L. Colangeli. The distant activity of Short Period Comets - II. 390:265–280, October 2008. doi: 10.1111/j.1365-2966.2008.13718.x.

L. A. McFadden, M. F. A'Hearn, P. D. Feldman, H. Bohnhardt, J. Rahe, M. C. Festou, J. C. Brandt, S. P. Maran, M. B. Niedner, A. M. Smith, and D. G. Schleicher. Ultraviolet spectrophotometry of comet Giacobini-Zinner during the ICE encounter. *Icarus*, 69:329–337, February 1987. doi: 10.1016/0019-1035(87)90109-6.

A. McKay, M. DiSanti, A. Cochran, N. Dello Russo, B. Bonev, R. Vervack, E. Gibb, N. Roth, and H. Kawakita. Constraining the Volatile Composition and Coma Photochemistry in Jupiter Family Comet 41P/Tuttle-Giacobini-Kresak with High Resolution IR and Optical Spectroscopy. In *American Astronomical Society Meeting Abstracts #231*, volume 231 of *American Astronomical Society Meeting Abstracts*, page 144.13, January 2018.

Adam J. McKay, Michael A. DiSanti, Michael S. P. Kelley, Matthew M. Knight, Maria Womack, Kacper Wierzchos, Olga Harrington Pinto, Boncho Bonev, Geronimo L. Villanueva, Neil Dello Russo, Anita L. Cochran, Nicolas Biver, James Bauer, Jr. Vervack, Ronald J., Erika Gibb, Nathan Roth, and Hideyo Kawakita. The Peculiar Volatile Composition of CO-dominated Comet C/2016 R2 (PanSTARRS). *AJ*, 158(3):128, September 2019. doi: 10.3847/1538-3881/ab32e4.

K. J. Meech, J. M. Bauer, and O. R. Hainaut. Rotation of comet 46P/Wirtanen. 326:1268–1276, October 1997.

K. J. Meech, O. R. Hainaut, and B. G. Marsden. Comet nucleus size distributions from HST and Keck telescopes. 170:463–491, August 2004. doi: 10.1016/j.icarus.2004.03.014.

R. Meier, D. Wellnitz, S. J. Kim, and M. F. A'Hearn. The NH and CH Bands of Comet C/1996 B2 (Hyakutake). *Icarus*, 136:268–279, December 1998. doi: 10.1006/icar.1998.6022.

D. A. Mendis. A postencounter view of comets. *Annual Review of Astronomy and Astrophysics*, 26(1):11–49, September 1988. doi: 10.1146/annurev.aa.26.090188.000303. URL https://doi.org/10.1146/annurev.aa.26.090188.000303.

D. A. Mendis, H. L. F. Houpis, and M. L. Marconi. The physics of comets. *fcp*, 10:2, 1985.

J Zs Mezei, R D Backodissa-Kiminou, D E Tudorache, V Morel, K Chakrabarti, O Motapon, O Dulieu, J Robert, W-Ü L Tchang-Brillet, A Bultel, X Urbain, J Tennyson, K Hassouni, and I F Schneider. Dissociative recombination and vibrational excitation of co + : model calculations and comparison with experiment. *Plasma Sources Science and Technology*, 24 (3):035005, 2015. URL http://stacks.iop.org/0963-0252/24/i=3/a=035005.

Pierre Mianes, Stefania Grudzinska, and Antoni Stawikowski. Observations physiques de la comète périodique giacobini-zinner (1959b). In *Annales d'Astrophysique*, volume 23, page 788, 1960.

A. Morbidelli, H. F. Levison, and R. Gomes. *The Dynamical Structure of the Kuiper Belt and Its Primordial Origin*, page 275. 2008.

Alessandro Morbidelli, Harold F Levison, Kleomenis Tsiganis, and Rodney Gomes. Chaotic capture of jupiter's trojan asteroids in the early solar system. *Nature*, 435(7041):462, 2005.

F. Moreno, F. Pozuelos, F. Aceituno, V. Casanova, A. Sota, J. Castellano, and E. Reina. Comet 22P/Kopff: Dust Environment and Grain Ejection Anisotropy from Visible and Infrared Observations. *ApJ*, 752:136, June 2012. doi: 10.1088/0004-637X/752/2/136.

Ousmanou Motapon, Francois Olivier Waffeu Tamo, Xavier Urbain, and Ioan F. Schneider. Decisive role of rotational couplings in the dissociative recombination and superelastic collisions of ${H_2}^+$ with low-energy electrons. *Phys. Rev. A*, 77:052711, May 2008. doi: 10.1103/PhysRevA.77.052711. URL https://link.aps.org/doi/10.1103/PhysRevA.77.052711.

S Mottola, S Lowry, Colin Snodgrass, PL Lamy, I Toth, A Rożek, H Sierks, MF A'Hearn, F Angrilli, C Barbieri, et al. The rotation state of 67p/churyumov-gerasimenko from approach observations with the osiris cameras on rosetta. *Astronomy & Astrophysics*, 569:L2, 2014.

Y. Moulane, E. Jehin, C. Opitom, F. J. Pozuelos, J. Manfroid, Z. Benkhaldoun, A. Daassou, and M. Gillon. Monitoring of the activity and composition of comets 41p/tuttle–giacobini–kresak and 45p/honda–mrkos–pajdusakova. *Astronomy & Astrophysics*, 619:A156, nov 2018a. doi: 10.1051/0004-6361/201833582. URL https://doi.org/10.1051/0004-6361/201833582.

Y. Moulane, J. Zs. Mezei, V. Laporta, E. Jehin, Z. Benkhaldoun, and I. F. Schneider. Reactive collision of electrons with CO in cometary coma. *Astronomy & Astrophysics*, 615:A53, July 2018b. doi: 10.1051/0004-6361/201832912. URL https://doi.org/10.1051/0004-6361/201832912.

Y. Moulane, E. Jehin, P. Rousselot, J. Manfroid, Y. Shinnaka, F. J. Pozuelos, D. Hutsemékers, C. Opitom, B. Yang, and Z. Benkhaldoun. Photometry and high-resolution spectroscopy of comet 21P/Giacobini-Zinner during its 2018 apparition. *A&A*, 640:A54, August 2020. doi: 10.1051/0004-6361/202037997.

M. J. Mumma, M. A. DiSanti, N. Dello Russo, K. Magee-Sauer, and T. W. Rettig. Detection of CO and ethane in comet 21p/giacobini-zinner: Evidence for variable chemistry in the outer solar nebula. *The Astrophysical Journal*, 531(2):L155–L159, March 2000. doi: 10.1086/312530. URL https://doi.org/10.1086/312530.

M. J. Mumma, M. A. Disanti, N. dello Russo, K. Magee-Sauer, E. Gibb, and R. Novak. Remote infrared observations of parent volatiles in comets: A window on the early solar system. 31: 2563–2575, June 2003. doi: 10.1016/S0273-1177(03)00578-7.

Michael J. Mumma and Steven B. Charnley. The chemical composition of comets—emerging taxonomies and natal heritage. *Annual Review of Astronomy and Astrophysics*, 49(1):471–524, September 2011. doi: 10.1146/annurev-astro-081309-130811. URL https://doi.org/10.1146/annurev-astro-081309-130811.

S. P. Naidu, L. A. M. Benner, M. Brozovic, J. D. Giorgini, J. S. Jao, C. G. Lee, M. A. Slade, L. G. Snedeker, M. W. Busch, and F. D. Ghigo. High-resolution Goldstone radar imaging of comet P/2016 BA14 (Pan-STARRS). In *AAS/Division for Planetary Sciences Meeting Abstracts 48*, volume 48 of *AAS/Division for Planetary Sciences Meeting Abstracts*, page 219.05, October 2016.

L. Neslušan. The fading problem and the population of the oort cloud. *Astronomy & Astrophysics*, 461(2):741–750, October 2006. doi: 10.1051/0004-6361:20065200. URL https://doi.org/10.1051/0004-6361:20065200.

D. Nesvorný, D. Vokrouhlický, L. Dones, H. F. Levison, N. Kaib, and A. Morbidelli. Origin and Evolution of Short-period Comets. 845:27, August 2017. doi: 10.3847/1538-4357/aa7cf6.

I. Newton. *Philosophiae Naturalis Principia Mathematica. Auctore Js. Newton.* 1687. doi: 10.3931/e-rara-440.

E. P. Ney and K. M. Merrill. Comet West and the scattering function of cometary dust. *Science*, 194:1051–1053, December 1976. doi: 10.1126/science.194.4269.1051.

Ngassam, V., Florescu, A., Pichl, L., Schneider, I. F., Motapon, O., and Suzor-Weiner, A. The short-range reaction matrix in mqdt treatment of dissociative recombination and related processes. *Eur. Phys. J. D*, 26(2):165–171, 2003. doi: 10.1140/epjd/e2003-00248-8. URL https://doi.org/10.1140/epjd/e2003-00248-8.

J. H. Oort. The structure of the cloud of comets surrounding the Solar System and a hypothesis concerning its origin. *Bull. Astron. Inst.*, 11:91–110, January 1950.

Takafumi Ootsubo, Hideyo Kawakita, Saki Hamada, Hitomi Kobayashi, Mitsuru Yamaguchi, Fumihiko Usui, Takao Nakagawa, Munetaka Ueno, Masateru Ishiguro, Tomohiko Sekiguchi, Jun ichi Watanabe, Itsuki Sakon, Takashi Shimonishi, and Takashi Onaka. AKARINEAR-INFRARED SPECTROSCOPIC SURVEY FOR CO2in 18 COMETS. *The Astrophysical Journal*, 752(1):15, May 2012. doi: 10.1088/0004-637x/752/1/15. URL https://doi.org/10.1088/0004-637x/752/1/15.

C. Opitom. Monitoring of the chemical composition of comets in the framework of the trappist survey, 2016.

C. Opitom, E. Jehin, J. Manfroid, D. Hutsemékers, M. Gillon, and P. Magain. TRAPPIST photometry and imaging monitoring of comet C/2013 R1 (Lovejoy): Implications for the origin of daughter species. *A&A*, 584:A121, Dec 2015. doi: 10.1051/0004-6361/201526427.

C. Opitom, E. Jehin, J. Manfroid, D. Hutsemékers, M. Gillon, and P. Magain. TRAPPIST monitoring of comet c/2012 f6 (lemmon). *Astronomy & Astrophysics*, 574:A38, jan 2015. doi: 10.1051/0004-6361/201424582. URL https://doi.org/10.1051/0004-6361/201424582.

C. Opitom, C. Snodgrass, A. Fitzsimmons, E. Jehin, J. Manfroid, G. P. Tozzi, S. Faggi, and M. Gillon. Ground-based monitoring of comet 67P/Churyumov-Gerasimenko gas activity throughout the Rosetta mission. *MNRAS*, 469:S222–S229, Jul 2017. doi: 10.1093/mnras/stx1591.

Cyrielle Opitom, Alan Fitzsimmons, Emmanuel Jehin, Youssef Moulane, Olivier Hainaut, Karen J. Meech, Bin Yang, Colin Snodgrass, Marco Micheli, Jacqueline V. Keane, Zouhair Benkhaldoun, and Jan T. Kleyna. 2i/borisov: A c2-depleted interstellar comet. *Astronomy & Astrophysics*, 631:L8, November 2019. doi: 10.1051/0004-6361/201936959. URL https://doi.org/10.1051/0004-6361/201936959.

A. E. Orel, I. F. Schneider, and A. Suzor-Weiner. Dissociative recombination of h3+: progress in theory. *Philosophical Transactions of the Royal Society of London A: Mathematical, Physical and Engineering Sciences*, 358(1774):2445–2456, 2000. ISSN 1364-503X. doi: 10.1098/rsta.2000.0659. URL http://rsta.royalsocietypublishing.org/content/358/1774/2445.

L. O'Rourke, C. Snodgrass, M. de Val-Borro, N. Biver, D. Bockelée-Morvan, H. Hsieh, D. Teyssier, Y. Fernandez, M. Kueppers, M. Micheli, and P. Hartogh. Determination of an Upper Limit for the Water Outgassing Rate of Main-belt Comet P/2012 T1 (PANSTARRS). *ApJL*, 774(1):L13, Sep 2013. doi: 10.1088/2041-8205/774/1/L13.

D. J. Osip, D. G. Schleicher, R. L. Millis, M. F. A. Hearn, and P. V. Birch. 15 years of comet photometry: A comparative analysis of 80 comets. In A. W. Harris and E. Bowell, editors, *Asteroids, Comets, Meteors 1991*, December 1992.

L. Paganini, M. N. Camarca, M. J. Mumma, S. Faggi, M. Lippi, and G. L. Villanueva. Observations of jupiter family comet 252p/LINEAR during a close approach to earth reveal large abundances of methanol and ethane. *The Astronomical Journal*, 158(3):98, August 2019. doi: 10.3847/1538-3881/ab289c. URL https://doi.org/10.3847/1538-3881/ab289c.

Mieczyslaw Leszek Paradowski. A new method of determining brightness and size of cometary nuclei. *MNRAS*, 492(3):4175–4188, March 2020. doi: 10.1093/mnras/stz3597.

Jana Pittichová, Charles E Woodward, Michael S Kelley, and William T Reach. Ground-based optical and spitzer infrared imaging observations of comet 21p/giacobini-zinner. *The Astronomical Journal*, 136(3):1127, 2008.

F. J. Pozuelos, E. Jehin, Y. Moulane, C. Opitom, J. Manfroid, Z. Benkhaldoun, and M. Gillon. Dust modelling and a dynamical study of comet 41p/tuttle–giacobini–kresak during its 2017 perihelion passage. *Astronomy & Astrophysics*, 615:A154, jul 2018. doi: 10.1051/0004-6361/201832851. URL https://doi.org/10.1051/0004-6361/201832851.

Dina Prialnik and Eric D. Rosenberg. Can ice survive in main-belt comets? Long-term evolution models of comet 133P/Elst-Pizarro. *MNRAS*, 399(1):L79–L83, Oct 2009. doi: 10.1111/j.1745-3933.2009.00727.x.

JJ. L. Prieto, B. J. Shappee, J. Brimacombe, K. Z. Stanek, Ping Chen, Subo Dong, T. W. S. Holoien, C. S. Kochanek, J. S. Brown, J. V. Shields, and T. A. Thompson. ASASSN1: Bright Comet Discovered by the All Sky Automated Survey for SuperNovae. *The Astronomer's Telegram*, 10597:1, July 2017.

S. Raghuram and A. Bhardwaj. Photochemistry of atomic oxygen green and red-doublet emissions in comets at larger heliocentric distances. *A&A*, 566:A134, June 2014. doi: 10.1051/0004-6361/201321921.

S. Raghuram, A. Bhardwaj, and M. Galand. Prediction of Forbidden Ultraviolet and Visible Emissions in Comet 67P/Churyumov-Gerasimenko. *ApJ*, 818:102, February 2016. doi: 10.3847/0004-637X/818/2/102.

C. E. Randall, D. G. Schleicher, R. G. Ballou, and D. J. Osip. Observational Constraints on Molecular Scalelengths and Lifetimes in Comets. In *AAS/Division for Planetary Sciences Meeting Abstracts #24*, volume 24 of *Bulletin of the American Astronomical Society*, page 1002, June 1992.

H. Rauer, J. Helbert, C. Arpigny, J. Benkhoff, D. Bockelée-Morvan, H. Boehnhardt, F. Colas, J. Crovisier, O. Hainaut, L. Jorda, M. Kueppers, J. Manfroid, and N. Thomas. Long-term optical spectrophotometric monitoring of comet C/1995 O1 (Hale-Bopp). *A&A*, 397:1109–1122, January 2003. doi: 10.1051/0004-6361:20021550.

William T. Reach, Jeremie Vaubaillon, Michael S. Kelley, Carey M. Lisse, and Mark V. Sykes. Distribution and properties of fragments and debris from the split Comet 73P/Schwassmann-Wachmann 3 as revealed by Spitzer Space Telescope. *Icarus*, 203(2):571–588, October 2009. doi: 10.1016/j.icarus.2009.05.027.

V. Reddy and J. Y. Li. Dark object investigated while making one of the closest ever comet flybys of earth, 2016. URL http://www.psi.edu/news/darkcomet2.

R. Reinhard. The giotto encounter with comet halley. *Nature*, 321(S6067):313–318, May 1986. doi: 10.1038/321313a0. URL https://doi.org/10.1038/321313a0.

H. Rickman and L. Jorda. Comet 46p/wirtanen, the target of the rosetta mission. *Advances in Space Research*, 21(11):1491–1504, January 1998. doi: 10.1016/s0273-1177(97)00942-3. URL https://doi.org/10.1016/s0273-1177(97)00942-3.

Frans JM Rietmeijer. Sodium tails of comets: Na/o and na/si abundances in interplanetary dust particles. *The Astrophysical Journal Letters*, 514(2):L125, 1999.

S. Rosen, R. Peverall, M. Larsson1, A. Le Padellec, J. Semaniak, A. Larson, C. Stromholm, W. J. van der Zande, H. Danared, and G. H. Dunn. Absolute cross sections and final-state distributions for dissociative recombination and excitation of co+(v=0) using an ion storage ring. *Physical Review A*, 57:4462, 1998. URL https://doi.org/10.1103/PhysRevA.57.4462.

Nathan Roth, Erika Gibb, Neil Dello Russo, Michael DiSanti, Boncho Bonev, Ron J. Vervack, Mohammad Saki, Adam McKay, and Hideyo Kawakita. Probing the Evolutionary History of Comets: An Investigation of the Hypervolatiles CO and CH_4 and Parent Volatile Abundances in the Jupiter-family Comet 21P/Giacobini-Zinner. In *AAS/Division for Planetary Sciences Meeting Abstracts #50*, AAS/Division for Planetary Sciences Meeting Abstracts, page 210.11, Oct 2018.

Nathan X. Roth, Erika L. Gibb, Boncho P. Bonev, Michael A. DiSanti, Neil Dello Russo, Adam J. McKay, Ronald J. Vervack, Hideyo Kawakita, Mohammad Saki, Nicolas Biver, Dominique Bockelée-Morvan, Lori M. Feaga, Nicolas Fougere, Anita L. Cochran, Michael Combi, and Yinsi Shou. Probing the evolutionary history of comets: An investigation of the hypervolatiles CO, CH4, and c2h6 in the jupiter-family comet 21p/giacobini–zinner. *The Astronomical Journal*, 159(2):42, January 2020. doi: 10.3847/1538-3881/ab536b. URL https://doi.org/10.3847/1538-3881/ab536b.

P. Rousselot, A. Decock, P. P. Korsun, E. Jehin, I. Kulyk, J. Manfroid, and D. Hutsemékers. High-resolution spectra of comet C/2013 R1 (Lovejoy). *A&A*, 580:A3, Aug 2015. doi: 10.1051/0004-6361/201526173.

P. Rousselot, C. Opitom, E. Jehin, D. Hutsemékers, J. Manfroid, M. N. Villarreal, J. Y. Li, J. Castillo-Rogez, C. T. Russell, P. Vernazza, M. Marsset, L. Roth, C. Dumas, B. Yang, T. H. Prettyman, and O. Mousis. Search for water outgassing of (1) Ceres near perihelion. *A&A*, 628:A22, Aug 2019. doi: 10.1051/0004-6361/201935738.

Philippe Rousselot, Olivier Pirali, Emmanuël Jehin, Michel Vervloet, Damien Hutsemékers, Jean Manfroid, Daniel Cordier, Marie-Aline Martin-Drumel, Sébastien Gruet, Claude Arpigny, Alice Decock, and Olivier Mousis. Toward a Unique Nitrogen Isotopic Ratio in Cometary Ices. *ApJL*, 780(2):L17, Jan 2014. doi: 10.1088/2041-8205/780/2/L17.

M. Rubin, K. Altwegg, H. Balsiger, J. J. Berthelier, A. Bieler, U. Calmonte, M. Combi, J. De Keyser, C. Engrand, B. Fiethe, S. A. Fuselier, S. Gasc, T. I. Gombosi, K. C. Hansen, M. Hässig, L. Le Roy, K. Mezger, C. Y. Tzou, S. F. Wampfler, and P. Wurz. Evidence for depletion of heavy silicon isotopes at comet 67P/Churyumov-Gerasimenko. *A&A*, 601:A123, May 2017. doi: 10.1051/0004-6361/201730584.

R. Rudawska, J. Vaubaillon, J. Tóth, and S. Raetz. What do comets 252P/LINEAR and P2016 BA14 have in common? In *AAS/Division for Planetary Sciences Meeting Abstracts 48*, volume 48 of *AAS/Division for Planetary Sciences Meeting Abstracts*, page 218.01, October 2016.

R. Z. Sagdeev, J. Blamont, A. A. Galeev, V. I. Moroz, V. D. Shapiro, V. I. Shevchenko, and K. Szegő. Vega spacecraft encounters with comet halley. *Nature*, 321(S6067):259–262, May 1986. doi: 10.1038/321259a0. URL https://doi.org/10.1038/321259a0.

N. H. Samarasinha, B. E. A. Mueller, M. J. S. Belton, A. Henrici, and J. Barrera. Determination of the rotational state of comet 103P/Hartley 2. In *AAS/Division for Planetary Sciences Meeting Abstracts 49*, volume 49 of *AAS/Division for Planetary Sciences Meeting Abstracts*, page 414.25, October 2017.

Nalin H. Samarasinha and Stephen M. Larson. Image enhancement techniques for quantitative investigations of morphological features in cometary comae: A comparative study. *Icarus*, 239(Supplement C):168 – 185, 2014. ISSN 0019-1035. doi: https://doi.org/10.1016/j.icarus.2014.05.028. URL http://www.sciencedirect.com/science/article/pii/S0019103514002814.

Nalin H Samarasinha and Béatrice EA Mueller. Relating changes in cometary rotation to activity: current status and applications to comet c/2012 s1 (ison). *The Astrophysical Journal Letters*, 775(1):L10, 2013.

Nalin H. Samarasinha, Beatrice E.A. Mueller, and Michael J.S. Belton. Comments on the rotational state and non-gravitational forces of comet 46p/wirtanen. *Planetary and Space Science*, 44(3):275–281, March 1996. doi: 10.1016/0032-0633(95)00145-x. URL https://doi.org/10.1016/0032-0633(95)00145-x.

Nalin H Samarasinha, Béatrice EA Mueller, Michael JS Belton, and Laurent Jorda. Rotation of cometary nuclei. *Comets II*, pages 281–299, 2004.

G. Sarid, K. Volk, J. K. Steckloff, W. Harris, M. Womack, and L. M. Woodney. 29p/schwassmann–wachmann 1, a centaur in the gateway to the jupiter-family comets. *The Astrophysical Journal*, 883(1):L25, September 2019. doi: 10.3847/2041-8213/ab3fb3. URL https://doi.org/10.3847/2041-8213/ab3fb3.

Frederick L Scarf, Ferdinand V Coroniti, Charles F Kennel, Donald A Gurnett, Wing-Huen Ip, and Edward J Smith. Plasma wave observations at comet giacobini-zinner. *Science*, 232 (4748):377–381, 1986.

D. Schleicher. Deep impacts target comet 9p/tempel 1 at multiple apparitions: Seasonal and secular variations in gas and dust production. *Icarus*, 190(2):406–422, October 2007. doi: 10.1016/j.icarus.2007.04.013. URL https://doi.org/10.1016/j.icarus.2007.04.013.

D. Schleicher and A. Bair. Chemical and physical properties of comets in the Lowell database: Results from 35 years of narrow-band photometry. In K. Muinonen, A. Penttilä, M. Granvik, A. Virkki, G. Fedorets, O. Wilkman, and T. Kohout, editors, *Asteroids, Comets, Meteors 2014*, July 2014.

D. G. Schleicher. The Fluorescence Efficiencies of the CN Violet Bands in Comets. *AJ*, 140: 973–984, October 2010. doi: 10.1088/0004-6256/140/4/973.

D. G. Schleicher and M. F. A'Hearn. The fluorescence of cometary OH. *ApJ*, 331:1058–1077, August 1988. doi: 10.1086/166622.

D. G. Schleicher and A. N. Bair. The Composition of the Interior of Comet 73P/Schwassmann-Wachmann 3: Results from Narrowband Photometry of Multiple Components. 141:177, June 2011. doi: 10.1088/0004-6256/141/6/177.

D. G. Schleicher and T. L. Farnham. Photometry and Imaging of the Coma with Narrowband Filters. In Festou, M. C., Keller, H. U., & Weaver, H. A., editor, *Comets II*, pages 449–469. University of Arizona Press, Tucson, 2004.

D. G. Schleicher, R. L. Millis, and P. V. Birch. Photometric observations of comet P/Giacobini-Zinner. *A&A*, 187:531–538, November 1987.

D. G. Schleicher, R. L. Millis, D. J. Osip, and P. V. Birch. Comet Levy (1990c) - Ground-based photometric results. *Icarus*, 94:511–523, December 1991. doi: 10.1016/0019-1035(91) 90244-N.

D. G. Schleicher, R. L. Millis, and P. V. Birch. Narrowband Photometry of Comet P/Halley: Variation with Heliocentric Distance, Season, and Solar Phase Angle. *Icarus*, 132:397–417, April 1998. doi: 10.1006/icar.1997.5902.

D. G. Schleicher, N. Eisner, M. M. Knight, and A. Thirouin. CN Jet Morphology and the Very Rapidly Changing Rotation Period of Comet 41P/Tuttle-Giacobini-Kresak. In *AAS/Division for Planetary Sciences Meeting Abstracts*, volume 49 of *AAS/Division for Planetary Sciences Meeting Abstracts*, page 305.07, October 2017.

D. G. Schleicher, M. M. Knight, and B. A. Skiff. A Smorgasbord of Recent Comet Narrowband Imaging and Photometry: Results from NEOWISE (C/2020 F3), ATLAS (C/2019 Y4), PanSTARRS (C/2017 T2), and 88P/Howell. In *AAS/Division for Planetary Sciences Meeting Abstracts*, volume 52 of *AAS/Division for Planetary Sciences Meeting Abstracts*, page 111.05, October 2020.

David Schleicher and Matthew Knight. Narrowband Observations of Comet 21P/Giacobini-Zinner During Its Excellent 2018 Apparition. In *AAS/Division for Planetary Sciences Meeting Abstracts*, page 210.12, Oct 2018.

David G. Schleicher. Compositional and physical results for rosetta's new target comet 67p/churyumov–gerasimenko from narrowband photometry and imaging. *Icarus*, 181(2): 442 – 457, 2006. ISSN 0019-1035. doi: https://doi.org/10.1016/j.icarus.2005.11.014. URL http://www.sciencedirect.com/science/article/pii/S0019103505004628.

David G. Schleicher. The Extremely Anomalous Molecular Abundances of Comet 96p/Machholz 1 from Narrowband Photometry. *AJ*, 136(5):2204–2213, November 2008. doi: 10.1088/0004-6256/136/5/2204.

I. F. Schneider, O Dulieu, and A Giusti-Suzor. *J. Phys. B: At. Mol. Phys.*, 24:L289, 1991.

I. F. Schneider, C. Strömholm, L. Carata, X. Urbain, M. Larsson, and A. Suzor-Weiner. Rotational effects in dissociative recombination: theoretical study of resonant mechanisms and comparison with ion storage ring experiments. *Journal of Physics B: Atomic, Molecular and Optical Physics*, 30(11):2687, 1997.

I. F. Schneider, A. E. Orel, and A. Suzor-Weiner. Channel mixing effects in the dissociative recombination of H_3^+ with slow electrons. *Phys. Rev. Lett.*, 85:3785–3788, Oct 2000. doi: 10.1103/PhysRevLett.85.3785. URL https://link.aps.org/doi/10.1103/PhysRevLett.85.3785.

Megan E. Schwamb, Matthew M. Knight, Geraint H. Jones, Colin Snodgrass, Lorenzo Bucci, José Manuel Sánchez Pérez, Nikolai Skuppin, and Comet Interceptor Science Team. Potential Backup Targets for Comet Interceptor. *Research Notes of the American Astronomical Society*, 4(2):21, February 2020. doi: 10.3847/2515-5172/ab7300.

R. Schwenn, W.-H. Ip, H. Rosenbauer, H. Balsiger, F. Buhler, R. Goldstein, A. Meier, and E. G. Shelley. Ion Temperature and Flow Profiles in Comet Halley's Close Environment. In H. Kikuchi, editor, *Laboratory and Space Plasmas*, page 583, 1989.

M J Seaton. Quantum defect theory i. general formulation. *Proceedings of the Physical Society*, 88(4):801, 1966. URL http://stacks.iop.org/0370-1328/88/i=4/a=302.

M J Seaton. Quantum defect theory. *Reports on Progress in Physics*, 46(2):167, 1983. URL http://stacks.iop.org/0034-4885/46/i=2/a=002.

Z. Sekanina and D. K. Yeomans. Orbital motion, nucleus precession, and splitting of periodic Comet Brooks 2. *AJ*, 90:2335–2352, November 1985. doi: 10.1086/113939.

Matthew C. Senay and David Jewitt. Coma formation driven by carbon monoxide release from comet Schwassmann-Wachmann 1. *Nature*, 371(6494):229–231, Sep 1994. doi: 10.1038/371229a0.

F. Shelly, L. Brown-Manguso, M. Blythe, M. Bezpalko, M. Elowitz, R. Huber, J. Stuart, H. Viggh, R. Sayer, J. B. Evans, J. Ticha, M. Tichy, Z. Moravec, and G. Hug. Comet C/2000 G1 (LINEAR). *IAU Circ*, 7396, April 2000.

Yoshiharu Shinnaka and Hideyo Kawakita. Nitrogen Isotopic Ratio of Cometary Ammonia from High-resolution Optical Spectroscopic Observations of C/2014 Q2 (Lovejoy). *AJ*, 152 (5):145, Nov 2016. doi: 10.3847/0004-6256/152/5/145.

Yoshiharu Shinnaka, Hideyo Kawakita, Hitomi Kobayashi, Emmanuël Jehin, Jean Manfroid, Damien Hutsemékers, and Claude Arpigny. ORTHO-TO-PARA ABUNDANCE RATIO (OPR) OF AMMONIA IN 15 COMETS: OPRs OF AMMONIA VERSUS14n/15n RATIOS IN CN. *The Astrophysical Journal*, 729(2):81, February 2011. doi: 10.1088/0004-637x/729/2/81. URL https://doi.org/10.1088/0004-637x/729/2/81.

Yoshiharu Shinnaka, Hideyo Kawakita, Hitomi Kobayashi, Masayoshi Nagashima, and Daniel C. Boice. $^{14}NH_2/^{15}NH_2$ Ratio in Comet C/2012 S1 (ISON) Observed during its Outburst in 2013 November. *ApJL*, 782(2):L16, Feb 2014. doi: 10.1088/2041-8205/782/2/L16.

Yoshiharu Shinnaka, Hideyo Kawakita, Emmanuël Jehin, Alice Decock, Damien Hutsemékers, Jean Manfroid, and Akira Arai. Nitrogen isotopic ratios of NH_2 in comets: implication for ^{15}N-fractionation in cometary ammonia. *MNRAS*, 462:S195–S209, Nov 2016. doi: 10.1093/mnras/stw2410.

Yoshiharu Shinnaka, Hideyo Kawakita, and Akito Tajitsu. High-resolution optical spectroscopic observations of comet 21p/giacobini–zinner in its 2018 apparition. *The Astronomical Journal*, 159(5):203, April 2020. doi: 10.3847/1538-3881/ab7d34. URL https://doi.org/10.3847/1538-3881/ab7d34.

Colin Snodgrass, Jessica Agarwal, Michael Combi, Alan Fitzsimmons, Aurelie Guilbert-Lepoutre, Henry H. Hsieh, Man-To Hui, Emmanuel Jehin, Michael S. P. Kelley, Matthew M. Knight, Cyrielle Opitom, Roberto Orosei, Miguel de Val-Borro, and Bin Yang. The main belt comets and ice in the solar system. *The Astronomy and Astrophysics Review*, 25(1), nov 2017. doi: 10.1007/s00159-017-0104-7. URL https://doi.org/10.1007/s00159-017-0104-7.

L. A. Soderblom. Observations of comet 19p/borrelly by the miniature integrated camera and spectrometer aboard deep space 1. *Science*, 296(5570):1087–1091, April 2002. doi: 10.1126/science.1069527. URL https://doi.org/10.1126/science.1069527.

Michael Solontoi, Željko Ivezić, Mario Jurić, Andrew C. Becker, Lynne Jones, Andrew A. West, Steve Kent, Robert H. Lupton, Mark Claire, Gillian R. Knapp, Tom Quinn, James E. Gunn, and Donald P. Schneider. Ensemble properties of comets in the Sloan Digital Sky Survey. *Icarus*, 218(1):571–584, Mar 2012. doi: 10.1016/j.icarus.2011.10.008.

A. Sosa and J. A. Fernández. Dynamical evolution of comet pairs. In *AAS/Division for Planetary Sciences Meeting Abstracts 48*, volume 48 of *AAS/Division for Planetary Sciences Meeting Abstracts*, page 301.02, October 2016.

J. A. Stansberry, J. Van Cleve, W. T. Reach, D. P. Cruikshank, J. P. Emery, Y. R. Fernandez, V. S. Meadows, K. Y. L. Su, K. Misselt, G. H. Rieke, E. T. Young, M. W. Werner, C. W. Engelbracht, K. D. Gordon, D. C. Hines, D. M. Kelly, J. E. Morrison, and J. Muzerolle. Spitzer observations of the dust coma and nucleus of 29p/schwassmann-wachmann 1. *The Astrophysical Journal Supplement Series*, 154(1):463–468, September 2004. doi: 10.1086/422473. URL https://doi.org/10.1086/422473.

I. A. Steele, R. J. Smith, and J. Marchant. C/2019 Y4 ATLAS - confirmation of nuclear change. *The Astronomer's Telegram*, 13622:1, April 2020.

H. Stoerzer, J. Stutzki, and A. Sternberg. COˆ+ˆ in the Orion Bar, M17 and S140 star-forming regions. *Astronomy & Astrophysics*, 296:L9, April 1995.

K S Krishna Swamy. *Physics of Comets*. WORLD SCIENTIFIC, 3rd edition, 2010. doi: 10.1142/7537. URL https://www.worldscientific.com/doi/abs/10.1142/7537.

H. Takagi. Rotational effects in the dissociative recombination process of h 2 + +e. *Journal of Physics B: Atomic, Molecular and Optical Physics*, 26(24):4815, 1993. URL http://stacks.iop.org/0953-4075/26/i=24/a=014.

T. Tanabe, I. Katayama, H. Kamegaya, K. Chida, Y. Arakaki, T. Watanabe, M. Yoshizawa, M. Saito, Y. Haruyama, K. Hosono, K. Hatanaka, T. Honma, K. Noda, S. Ohtani, and H. Takagi. Dissociative recombination of hd$^+$ with an ultracold electron beam in a cooler ring. *Phys. Rev. Lett.*, 75:1066–1069, Aug 1995. doi: 10.1103/PhysRevLett.75.1066. URL https://link.aps.org/doi/10.1103/PhysRevLett.75.1066.

G. Tancredi, J. A. Fernández, H. Rickman, and J. Licand ro. A catalog of observed nuclear magnitudes of Jupiter family comets. *AAS*, 146:73–90, Oct 2000. doi: 10.1051/aas:2000263.

M. G. G. T. Taylor, N. Altobelli, B. J. Buratti, and M. Choukroun. The rosetta mission orbiter science overview: the comet phase. *Philosophical Transactions of the Royal Society A: Mathematical, Physical and Engineering Sciences*, 375(2097):20160262, May 2017. doi: 10.1098/rsta.2016.0262. URL https://doi.org/10.1098/rsta.2016.0262.

Jonathan Tennyson. R -matrix calculation of rydberg states of co. *Journal of Physics B: Atomic, Molecular and Optical Physics*, 29(24):6185, 1996. URL http://stacks.iop.org/0953-4075/29/i=24/a=024.

Nicolas Thomas. *An Introduction to Comets*. Springer International Publishing, 2020. doi: 10.1007/978-3-030-50574-5. URL https://doi.org/10.1007/978-3-030-50574-5.

P. C. Thomas, M. F. A'Hearn, J. Veverka, M. J. S. Belton, J. Kissel, K. P. Klaasen, L. A. McFadden, H. J. Melosh, P. H. Schultz, S. Besse, B. T. Carcich, T. L. Farnham, O. Groussin, B. Hermalyn, J.-Y. Li, D. J. Lindler, C. M. Lisse, K. Meech, and J. E. Richardson. Shape, density, and geology of the nucleus of Comet 103P/Hartley 2. 222:550–558, February 2013. doi: 10.1016/j.icarus.2012.05.034.

Stefan Tinck and Annemie Bogaerts. Computational study of the CF4 /CHF3 / h2 /cl2 /o2 /HBr gas phase plasma chemistry. *Journal of Physics D: Applied Physics*, 49(19):195203, apr 2016. doi: 10.1088/0022-3727/49/19/195203. URL https://doi.org/10.1088/0022-3727/49/19/195203.

D. Tody. The IRAF Data Reduction and Analysis System. In D. L. Crawford, editor, *Society of Photo-Optical Instrumentation Engineers (SPIE) Conference Series*, volume 627 of *Society of Photo-Optical Instrumentation Engineers (SPIE) Conference Series*, page 733, January 1986.

D. Tody. IRAF in the Nineties. In R. J. Hanisch, R. J. V. Brissenden, & J. Barnes, editor, *Astronomical Data Analysis Software and Systems II*, volume 52 of *Astronomical Society of the Pacific Conference Series*, page 173, January 1993.

J. L. Tonry, C. W. Stubbs, K. R. Lykke, P. Doherty, I. S. Shivvers, W. S. Burgett, K. C. Chambers, K. W. Hodapp, N. Kaiser, R.-P. Kudritzki, E. A. Magnier, J. S. Morgan, P. A. Price, and R. J. Wainscoat. The pan-starrs1 photometric system. 750(2):99, 2012. doi: 10.1088/0004-637X/750/2/99.

J. M. Trigo-Rodríguez, E. García-Melendo, B. J. R. Davidsson, A. Sánchez, D. Rodríguez, J. Lacruz, J. A. de Los Reyes, and S. Pastor. Outburst activity in comets. I. Continuous monitoring of comet 29P/Schwassmann-Wachmann 1. 485:599–606, July 2008. doi: 10.1051/0004-6361:20078666.

B. Vâlcu, I.F. Schneider, M. Raoult, C. Strömholm, M. Larsson, and A. Suzor-Weiner. Rotational effects in low energy dissociative recombination of diatomic ions. *The European Physical Journal D - Atomic, Molecular, Optical and Plasma Physics*, 1(1):71–78, 1998.

J. Vernet, H. Dekker, S. D'Odorico, L. Kaper, P. Kjaergaard, F. Hammer, S. Randich, F. Zerbi, P. J. Groot, J. Hjorth, I. Guinouard, R. Navarro, T. Adolfse, P. W. Albers, J.-P. Amans, J. J. Andersen, M. I. Andersen, P. Binetruy, P. Bristow, R. Castillo, F. Chemla, L. Christensen, P. Conconi, R. Conzelmann, J. Dam, V. De Caprio, A. De Ugarte Postigo, B. Delabre, P. Di Marcantonio, M. Downing, E. Elswijk, G. Finger, G. Fischer, H. Flores, P. François, P. Goldoni, L. Guglielmi, R. Haigron, H. Hanenburg, I. Hendriks, M. Horrobin, D. Horville, N. C. Jessen, F. Kerber, L. Kern, M. Kiekebusch, P. Kleszcz, J. Klougart, J. Kragt, H. H. Larsen, J.-L. Lizon, C. Lucuix, V. Mainieri, R. Manuputy, C. Martayan, E. Mason, R. Mazzoleni, N. Michaelsen, A. Modigliani, S. Moehler, P. Møller, A. Norup Sørensen, P. Nørregaard, C. Péroux, F. Patat, E. Pena, J. Pragt, C. Reinero, F. Rigal, M. Riva, R. Roelfsema, F. Royer, G. Sacco, P. Santin, T. Schoenmaker, P. Spano, E. Sweers, R. Ter Horst, M. Tintori, N. Tromp, P. van Dael, H. van der Vliet, L. Venema, M. Vidali, J. Vinther, P. Vola, R. Winters, D. Wistisen, G. Wulterkens, and A. Zacchei. X-shooter, the new wide band intermediate resolution spectrograph at the ESO very large telescope. *Astronomy & Astrophysics*, 536:A105, December 2011. doi: 10.1051/0004-6361/201117752. URL https://doi.org/10.1051/0004-6361/201117752.

J. Veverka, K. Klaasen, M. A'Hearn, M. Belton, D. Brownlee, S. Chesley, B. Clark, T. Economou, R. Farquhar, S. F. Green, O. Groussin, A. Harris, J. Kissel, J.-Y. Li, K. Meech, J. Melosh, J. Richardson, P. Schultz, J. Silen, J. Sunshine, P. Thomas, S. Bhaskaran, D. Bodewits, B. Carcich, A. Cheuvront, T. Farnham, S. Sackett, D. Wellnitz, and A. Wolf. Return to Comet Tempel 1: Overview of Stardust-NExT results. 222:424–435, February 2013. doi: 10.1016/j.icarus.2012.03.034.

E. Vigren and M. Galand. Predictions of Ion Production Rates and Ion Number Densities within the Diamagnetic Cavity of Comet 67P/Churyumov-Gerasimenko at Perihelion. *ApJ*, 772:33, July 2013. doi: 10.1088/0004-637X/772/1/33.

E. Vigren, K. Altwegg, N. J. T. Edberg, A. I. Eriksson, M. Galand, P. Henri, F. Johansson, E.Odelstad, C.-Y. Tzou, and X. Valliéres. Model–observation comparisons of electron number densities in the coma of 67p/churyumov-gerasimenko during january 2015. *The Astronomical Journal*, 152(3):59, 2016. URL http://stacks.iop.org/1538-3881/152/i=3/a=59.

M. Vojnovic, M. Popovic, M.M. Ristic, M.D. Vicic, and G.B. Poparic. Rate coefficients for electron impact excitation of co. *Chemical Physics*, 423:1 – 8, 2013. ISSN 0301-0104. doi: http://doi.org/10.1016/j.chemphys.2013.06.007.

Tycho T Von Rosenvinge, John C Brandt, and Robert W Farquhar. The international cometary explorer mission to comet giacobini-zinner. *Science*, 232(4748):353–356, 1986.

F. O. Waffeu Tamo, H. Buhr, O. Motapon, S. Altevogt, V. M. Andrianarijaona, M. Grieser, L. Lammich, M. Lestinsky, M. Motsch, I. Nevo, S. Novotny, D. A. Orlov, H. B. Pedersen, D. Schwalm, F. Sprenger, X. Urbain, U. Weigel, A. Wolf, and I. F. Schneider. Assignment of resonances in dissociative recombination of hd^+ ions: High-resolution measurements compared with accurate computations. *Phys. Rev. A*, 84:022710, Aug 2011. doi: 10.1103/PhysRevA.84.022710. URL https://link.aps.org/doi/10.1103/PhysRevA.84.022710.

R. J. Wainscoat, L. Wells, M. Micheli, and H. Sato. Comet C/2017 K2 (Panstarrs). *Central Bureau Electronic Telegrams*, 4393, May 2017.

V. Wakelam, E. Herbst, and F. Selsis. The effect of uncertainties on chemical models of dark clouds. *A&A*, 451(2):551–562, 2006. doi: 10.1051/0004-6361:20054682. URL https://doi.org/10.1051/0004-6361:20054682.

M. K. Wallis. Weakly-shocked flows of the solar wind plasma through atmospheres of comets and planets. *planss*, 21:1647–1660, October 1973. doi: 10.1016/0032-0633(73)90156-6.

W. Waniak, G. Borisov, M. Drahus, T. Bonev, K. Czart, and M. Küppers. Rotation of the Nucleus, Gas Kinematics and Emission Pattern of Comet 8P/Tuttle: Preliminary Results from Optical Imaging of the CN Coma. *Earth Moon and Planets*, 105:327–342, September 2009. doi: 10.1007/s11038-009-9326-7.

Brian D. Warner. Near-Earth Asteroid Lightcurve Analysis at CS3-Palmer Divide Station: 2016 January-April. *Minor Planet Bulletin*, 43(3):240–250, July 2016.

H. A. Weaver, M. F. A'Hearn, C. Arpigny, D. C. Boice, P. D. Feldman, S. M. Larson, P. Lamy, D. H. Levy, B. G. Marsden, K. J. Meech, K. S. Noll, J. V. Scotti, Z. Sekanina, C. S. Shoemaker, E. M. Shoemaker, T. E. Smith, S. A. Stern, A. D. Storrs, J. T. Trauger, D. K. Yeomans, and B. Zellner. The Hubble Space Telescope (HST) Observing Campaign on Comet Shoemaker- Levy 9. *Science*, 267(5202):1282–1288, March 1995. doi: 10.1126/science.7871424.

H.A. Weaver, G. Chin, D. Bockelee-Morvan, J. Crovisier, T.Y. Brooke, D.P. Cruikshank, T.R. Geballe, S.J. Kim, and R. Meier. An infrared investigation of volatiles in comet 21p/giacobini-zinner. *Icarus*, 142(2):482 – 497, 1999. ISSN 0019-1035. doi: https://doi.org/10.1006/icar.1999.6218. URL http://www.sciencedirect.com/science/article/pii/S0019103599962188.

M. Weiler. The chemistry of c3and c2in cometary comae. *Astronomy & Astrophysics*, 538:A149, February 2012. doi: 10.1051/0004-6361/201117480. URL https://doi.org/10.1051/0004-6361/201117480.

Paul R. Weissman. The oort cloud. *Nature*, 344(6269):825–830, April 1990. doi: 10.1038/344825a0. URL https://doi.org/10.1038/344825a0.

F. L. Whipple. A comet model. I. The acceleration of Comet Encke. *ApJ*, 111:375–394, March 1950. doi: 10.1086/145272.

Fred L Whipple. *The rotation of comet nuclei.* Univ. of Arizona Press, Tucson, 1982.

L.M. Woodney, M.F. AHearn, David G. Schleicher, Tony L. Farnham, J.P. McMullin, M.C.H. Wright, J.M. Veal, Lewis E. Snyder, Imke de Pater, J.R. Forster, Patrick Palmer, Y.-J. Kuan, Wendy R. Williams, Chi C. Cheung, and Bridget R. Smith. Morphology of HCN and CN in comet hale–bopp (1995 o1). *Icarus*, 157(1):193–204, May 2002. doi: 10.1006/icar.2001.6798. URL https://doi.org/10.1006/icar.2001.6798.

Karl Wurm. *Die Natur der Kometen.* Gräfe & Sillem, 1943.

Bin Yang, Damien Hutsemékers, Yoshiharu Shinnaka, Cyrielle Opitom, Jean Manfroid, Emmanuël Jehin, Karen J. Meech, Olivier R. Hainaut, Jacqueline V. Keane, and Michaël Gillon. Isotopic ratios in outbursting comet C/2015 ER61. *A&A*, 609:L4, Feb 2018. doi: 10.1051/0004-6361/201732100.

Bin Yang, Emmanuël Jehin, Francisco J. Pozuelos, Youssef Moulane, Yoshiharu Shinnaka, Cyrielle Opitom, Henry H. Hsieh, Damien Hutsemékers, and Jean Manfroid. Comet 66P/du Toit: not a near-Earth main belt comet. *A&A*, 631:A168, November 2019. doi: 10.1051/0004-6361/201936469.

Bin Yang, Emmanuël Jehin, Francisco J. Pozuelos, Youssef Moulane, Yoshiharu Shinnaka, Cyrielle Opitom, Henry H. Hsieh, Damien Hutsemékers, and Jean Manfroid. Comet 66p/du toit: not a near-earth main belt comet. *Astronomy & Astrophysics*, 631:A168, November 2019. doi: 10.1051/0004-6361/201936469. URL https://doi.org/10.1051/0004-6361/201936469.

Q. Ye, Q. Zhang, J. Brewer, M. Knight, and M. Kelley. Atomic and molecular emissions of bright comet C/2020 F3 (NEOWISE) at 0.5 au. In *AAS/Division for Planetary Sciences Meeting Abstracts*, volume 52 of *AAS/Division for Planetary Sciences Meeting Abstracts*, page 111.02, October 2020.

Quan-Zhi Ye, Peter G. Brown, and Paul A. Wiegert. COMET 252p/LINEAR: BORN (ALMOST) DEAD? *The Astrophysical Journal*, 818(2):L29, February 2016. doi: 10.3847/2041-8205/818/2/l29. URL https://doi.org/10.3847/2041-8205/818/2/l29.

Quanzhi Ye and Man-To Hui. Continuing Fragmentation of C/2019 Y4 (ATLAS). *The Astronomer's Telegram*, 13651:1, April 2020.

Quanzhi Ye and Qicheng Zhang. Possible Disintegration of Comet C/2019 Y4 (ATLAS). *The Astronomer's Telegram*, 13620:1, April 2020.

Quanzhi Ye, Michael S. P. Kelley, Dennis Bodewits, Bryce Bolin, Lynne Jones, Zhong-Yi Lin, Eric C. Bellm, Richard Dekany, Dmitry A. Duev, and Steven Groom. Multiple Outbursts of Asteroid (6478) Gault. *ApJ*, 874(2):L16, Apr 2019. doi: 10.3847/2041-8213/ab0f3c.

H. W. Zhang, G. Zhao, and J. Y. Hu. A catalogue of emission lines in spectra of comet c/1995 o1 (hale-bopp). *Astronomy and Astrophysics*, 367(3):1049–1055, March 2001. doi: 10.1051/0004-6361:20010008. URL https://doi.org/10.1051/0004-6361:20010008.

V. Zhaunerchyk, A. Al-Khalili, R. D. Thomas, W. D. Geppert, V. Bednarska, A. Petrignani, A. Ehlerding, M. Hamberg, M. Larsson, S. Rosen, and W. J. van der Zande. Rotational state effects in the dissociative recombination of h_2^+. *Phys. Rev. Lett.*, 99:013201, Jul 2007. doi: 10.1103/PhysRevLett.99.013201. URL https://link.aps.org/doi/10.1103/PhysRevLett.99.013201.

Evgenij Zubko, Maxim Zheltobryukhov, Ekaterina Chornaya, Anton Kochergin, Gorden Videen, Gennady Kornienko, and Sungsoo S Kim. Polarization of disintegrating comet c/2019 y4 (ATLAS). *Monthly Notices of the Royal Astronomical Society*, 497(2):1536–1542, June 2020. doi: 10.1093/mnras/staa1725. URL https://doi.org/10.1093/mnras/staa1725.